Crop development monitoring from Synthetic Aperture Radar (SAR) imagery

Cristian J. Silva-Perez

September 2021

A thesis submitted

for the degree of Doctor of Philosophy

Biological & Environmental Sciences

School of Natural Sciences

University of Stirling
Scotland

Supervisors:

Armando Marino and
Iain Cameron (external)

General abstract

Satellite remote sensing plays a vital role in providing large-scale and timely data to stakeholders of the agricultural supply chain. This allows for informed decision-making that promotes sustainable and cost-effective crop management practices. In particular, data derived from satellite-based Synthetic Aperture Radar (SAR) systems, provide opportunities for continuous crop monitoring, taking advantage of its ability to acquire images during day or night and under almost all weather conditions. Moreover, an abundance of SAR data can be anticipated in the next 5 years with the launch of several international SAR missions. However, research on crop development monitoring with data from SAR satellites has not been as widely studied as with data derived from passive multi-spectral satellites and contributions can be made to the current state-of-the-art techniques.

This thesis aims at improving the current knowledge on the use of satellite-based SAR imagery for crop development monitoring. This is approached by developing novel methodologies and detailed interpretations of multitemporal SAR and Polarimetric SAR (PolSAR) responses to crop growth in three different test sites.

Chapter two presents a detailed analysis of the Sentinel-1 SAR satellite response to asparagus crop development in Peru, investigating the capabilities of the sensor to capture seasonality effects as well as providing an interpretation of the temporal backscatter signature. This is complemented with a case study where a multiple-output random forest regression algorithm is used to successfully retrieve crop growth stage from Sentinel-1 data and temperature measurements.

Following the limitations identified with this approach, a methodology that builds upon ideas of Bayesian Filtering Frameworks (BFFs) for crop monitoring is proposed in chapter three. It incorporates Gaussian processes to model crop dynamics as well as to model the remote sensing response to the crop state. Using this

approach, it is possible to derive daily predictions with the associated uncertainties, to combine in near-real-time data from active and passive satellites as well as to estimate past and future crop key events that are of strategic importance for different stakeholders.

The final section of this thesis looks at the new developments of the SAR technology considering that future open access missions will provide Quad Polarimetric SAR data. An algorithm based on multitemporal PolSAR change detection is introduced in chapter four. It defines a Change Matrix to encode an interpretable representation of the crop dynamics as captured by the evolution of the scattering mechanisms over time. We use rice fields in Spain and multiple cereal crops in Canada to test the use of the algorithm for crop monitoring. A supervised learning-based crop type classification methodology is then proposed with the same method by using the encoded scattering mechanisms as input for a neural-network-based classifier, achieving comparable performances to state-of-the-art classifiers.

The results obtained in this thesis represent novel additions to the literature that contribute to our understanding and successful use of SAR imagery for agricultural monitoring. For the first time, a detailed analysis of asparagus crops is presented. It is a key crop for agricultural exports of Peru, the largest exporter of asparagus in the world. Secondly, two key contributions to the state of the art BFFs for crop monitoring are presented: a) A better exploitation of the SAR temporal dimension and an application with freely available data and b) given that it is a learning-based approach, it overcomes current limitations of transferability among crop types and regions. Finally, the PolSAR change detection approach presented in the last thesis chapter, provides a novel and easy-to-interpret tool for both crop monitoring and crop type mapping applications.

Declaration

I, Cristian Jose Silva Perez, declare that this thesis has been composed by myself and that it embodies the results of my own research. Where appropriate, I have acknowledged the nature and extent of work carried out in collaboration with others.

Signed: Cristian S. Date: 27/09/2021

Agradecimientos

A mi familia, por la ayuda invaluable no solo para terminar esta tesis, sino por su ayuda siempre. Papi, mami, Neis and Pao, gracias por estar ahi siempre y por el amor incondicional.

Acknowledgements

This research was funded by the Project EO4cultivar, led by Environment Systems Ltd and funded by the UK Space Agency under the International Partnership program (https://www.envsys.co.uk/projects/eo4cultivar/).

I would like to thank my PhD supervisors, friends and colleagues who made this journey very enjoyable. Armando, thank you for believing that I could deliver this PhD when I had no prior training in remote sensing or agriculture. Also, for the patience and the great advice these four years, the very nice informal chats and the invitation to join the unexpected but exciting journey to Scotland. Iain, thank you for the interesting discussions and advice regarding more applied problems in the field and for the guidance navigating the EO4c project. I would like to thank prof. Alistair Jump for the mentorship sessions and for granting me access to his research group. It was a pleasure to work with Prof. Juan M. Lopez-Sanchez of University of Alicante. Thank you for the advice to complete the PolSAR chapter and the datasets, I feel lucky to have had access to his extensive knowledge. I would like to also thank Alan Gay of Aberystwyth university for the instructive conversations about asparagus crops.

To friends and colleagues that in one way or another, in one place or another, stayed with me along the way. Pedro, Omar and Javi at the Open university, it was a pleasure to start the PhD life with you guys. Vanessa, Carlos and Ester for all the adventures and for the chats at Ferrari's 'pub' that made the first lockdown much easier. Mortimer and Nonglak, for the entertaining chats about work and life and Sam and Sonny for the enjoyable days at the office. Special thanks to our new but promising research group in SAR remote sensing, Armando, Vahid, Sonny, Morgan, Peter and Javi. Thank you for the enriching discussions and I look forward to the exciting challenges and opportunities that lie ahead. Liliana and Angela whose

PhD journeys started with me in the EO4c project. Thank you for the chats about asparagus, remote sensing, Colombia and about Latin America.

Finally, I'd like to thank Victoria. You brought love, happiness, balance and fun, altogether. I can't wait for the new adventures to come.

Contents

List of Figures

List of Tables

Chapter 1

General introduction

1.1 Motivation

As humanity tries to reduce the inequalities in wealth distribution, guarantee access to food and improve nutrition worldwide, changes in food consumption can be expected (Fan et al., 2021). In addition, population growth forecasts predict that the world's population will reach 8.5 billion in 2030 and 9.7 billion in 2050 (DESA, 2019). According to the United Nations (UN), in order to produce the resources needed to preserve our present lifestyle, the equivalent of nearly three planets may be needed (DESA, 2019). This places a significant pressure on our current food production system. Furthermore, the predominantly unsustainable agricultural management practices used nowadays cause degradation and infertility of cultivated soils, natural vegetation clearing and unsustainable water consumption (Shukla et al., 2019a). In fact, agriculture accounts for the world's largest water consumption sector (69%), for activities including irrigation, livestock and aquaculture (Smith et al., 2007). This represents more than the industrial and household sectors combined (31%)(Smith et al., 2007). Similarly, approximately 30% of the world's energy consumption is related to agricultural management practices, which often come from non-renewable sources that emit green house gases. Moreover, studies show that between 10% and 12% of green house emissions can be attributed to the agricultural sector (Smith et al., 2007). The combination of these factors are projected to reduce the productivity of our food production systems, challenging our ability to meet the increasing food demand.

Agriculture is also an important source of income and employment, particularly for small farmers in developing countries (Fan et al., 2021). Consequently, the sector represents a critical opportunity for attaining economic transformation and growth (Fan et al., 2021). In recent decades, a new agriculture paradigm known as precision agriculture has emerged as a way to increase farm productivity by employing technology to accurately gather field data and make more efficient and informed intra-field management decisions (Finger et al., 2019; McBratney et al., 2005; Valle & Kienzle, 2020). An example of this is applying agricultural inputs to a crop according to specific spatial and temporal variations within the field (Finger et al., 2019; Valle & Kienzle, 2020). In this sense, precision agriculture for croplands aims at maximising crop yields while optimizing production costs (McBratney et al., 2005).

Considering the aspects discussed above, current initiatives aim at obtaining a holistic solution to global problems including food security, malnutrition and reduction of Green House Gases (GHG) from agricultural activities, while optimizing returns from financial investments by increasing productivity of food producers (Leahy et al., 2020; Shukla et al., 2019b; Smith et al., 2008). These initiatives, including among others the UN sustainable development goals (numbers 2 and 12) ([UNDP], 2021), also try to ensure a multi-level approach to guarantee that actions are taken from the small scale food producers and stakeholders of the supply chain, to governmental, national and international levels.

Research and technological development have been considered key tools for achieving sustainable food production systems, resilient to climate change and helpful in maintaining ecosystems diversity and productivity (Leahy et al., 2020; McBratney et al., 2005). The use of satellite-based remote sensing imagery constitutes one such technological advancement that can be used to increase efficiency in food production systems (Gebbers & Adamchuk, 2010; Karthikeyan et al., 2020). Images of the agricultural fields are acquired with certain temporal and spatial resolution by several satellite types. Taking advantage of the large area covered, images have been used to remotely derive information about crop status and health and management practices (Karthikeyan et al., 2020). Applications aiming at contributing to food security, ranging from crop inventories (Thenkabail et al., 2010), land change

and degradation analysis (Rogan & Chen, 2004), soil moisture retrieval (L. Wang & Qu, 2009), yield estimation (Doraiswamy et al., 2003), vegetation and biomass monitoring (Lu, 2006; X. Zhang et al., 2003), have been reported.

More recently, thanks to the launch of new satellite constellations with improvements in spatial and temporal resolution and freely available data, novel applications have been developed to monitor croplands at parcel scale level, allowing its integration to precision agriculture applications. In this regard, remote sensing as part of farming management systems, can also be used to increase productivity and profitability of croplands, contributing to economical growth.

1.2 Satellite-based remote sensing for crop development monitoring

The contributions of remote sensing to ensuring sustainable management practices and to precision farming in croplands, can be initially categorised based on the stakeholders. Three major levels of stakeholders are considered in this thesis with their associated applications. These include, a) small scale food producers, b) agribusinesses (mid and large scale food producers, food traders, retailers, etc) and c) governments and food security agencies.

For small scale farmers, applications for crop monitoring have been reported using very high spatial resolution from satellite data providers. Using this input data, however, is difficult for small farmers given the costs associated with purchasing the imagery. Freely-available imagery can be used, but the spatial resolution is not sufficiently good in some cases e.g. for intra-field crop monitoring. On the other hand, applications for governments and food security agencies have been constantly increasing in the last decade (as introduced in the previous section) particularly due to the growing number of satellite constellations available and the open data policies that space agencies have adopted recently. However, ground data normally used for validation of crop monitoring applications at regional or national scale is expensive to collect and is not always available. Therefore, in this thesis we concentrate in applications that would initially benefit agribusinesses and have the possibility to be down-scaled to small farmers once high spatio-temporal resolutions are freely

available or up-scaled for large areas once the developed monitoring methodologies have been validated operationally.

Similarly, contributions of satellite-based remote sensing for cropland monitoring, can also be classified according to the type of technology used to acquire the imagery from space. The information captured by the satellite instruments can be acquired in different regions of the Electromagnetic (EM) spectrum, including microwave, infrared (IR), visible, and ultraviolet. Likewise, different sensors may use different source of EM radiation or illumination. Active systems use their own antenna or laser to send and receive EM radiation. These sensors include radars and they capture backscattered EM energy in the microwave regions of the spectrum. Passive systems use solar radiation as the source of EM energy, capturing the ultraviolet, visible, and near infrared regions of the EM spectrum, that are reflected in the direction of the satellite. A sub category of passive sensors can also capture radiation emitted from the earth surface, capturing thermal infrared, microwave emissions, x rays and gamma rays. Furthermore, as data from passive systems have a more close connection to human vision, they have been more investigated for crop monitoring than data from active systems.

In terms of crop monitoring, the use of the infrared energy acquired by passive systems has been extensively investigated and several vegetation indices that rely on this part of the spectrum have been developed to successfully retrieve information about vegetation condition (Xue & Su, 2017a). Note however that, as passive systems capture the solar radiation reflected from the earth surface, clouds and gases in the atmosphere disrupt the image acquisition. This limits the use of this type of system to acquire images only when no clouds are present. Therefore, acquisitions are irregular and can contain data gaps. Active radar systems on the other hand, are designed in such a way that the wavelength of the microwave energy emitted by the antenna in the satellite platform is significantly larger than the size of the particles suspended in the atmosphere and clouds. This allows the emitted radiation to penetrate them, providing acquisitions regardless of cloud coverage. As these systems do not use solar radiation, they can also capture images at night time. These advantages result in the capability of providing systematic acquisitions for monitoring earth processes.

In active systems, other aspects of image acquisition arise that may reduce the image quality. A broadly investigated issue with radar is 'speckle', which is a noise-like effect, visible in the images as a result of the coherent combination of the backscattered radiation from within a resolution cell (see more details in sections 1.3.3 and 1.3.4). However, different spatial and temporal filters can be used to reduce the impact of this effect (Oliver & Quegan, 2004a).

Research and use of satellite-based Synthetic Aperture Radar (SAR) systems are increasingly gaining attention due to the recent adoption of policies that offer free access to the available imagery. A key example of this is the European Space Agency (ESA) with the C-band dual polarimetric SAR satellite, and the constellation known as Sentinel-1 launched in 2015 (E. S. Agency, ESA 2015). Additionally, new constellations such as ALOS-4 (JAXA, 2021), the RADARSAT Constellation (C. S. Agency, 2021), Biomass (E. S. Agency, 2021), NISAR ((JPL), 2021) and the increasing number of high resolution smaller satellites (NovaSAR-S), will provide unprecedented access to SAR data (in some cases with open policy as for NISAR) for research and operational monitoring of earth processes. This opens a broad set of possibilities for using remote sensing for monitoring the implementation of sustainable management practices in croplands. As well as developing information decision systems to increase crop productivity, based on this data as sole source or as a part of a larger network of sensors to monitor agricultural fields. Given these factors, this thesis focuses on the exploitation of temporal and polarimetric dimensions of SAR data for crop monitoring.

1.3 Introduction to spaceborne SAR systems

A spaceborne SAR consists of a system of antennas mounted over a moving platform, orbiting our planet between 500 km to 800 km of altitude. Pulses of electromagnetic energy are sent to the earth surface and the backscattered EM energy is measured. Since it uses its own EM energy, it can capture signals during the day and at night, and given that it operates in the microwave region of the EM spectrum, it is able to go through particles in the atmosphere due to clouds, smoke and rain (Campbell & Wynne, 2011). This provides a key opportunity to observe earth processes almost

without interruptions. As shown in figure 1.1, the antennas on the moving platform are installed so that the instrument scans the earth surface in perpendicular direction to the direction of movement, also known as the azimuth direction. The angle that is formed between the wave direction and the normal to idealised the earth surface, is known as the incidence angle. This angle has an important effect in determining the intensity of the backscattered energy. In order to measure the backscattered EM

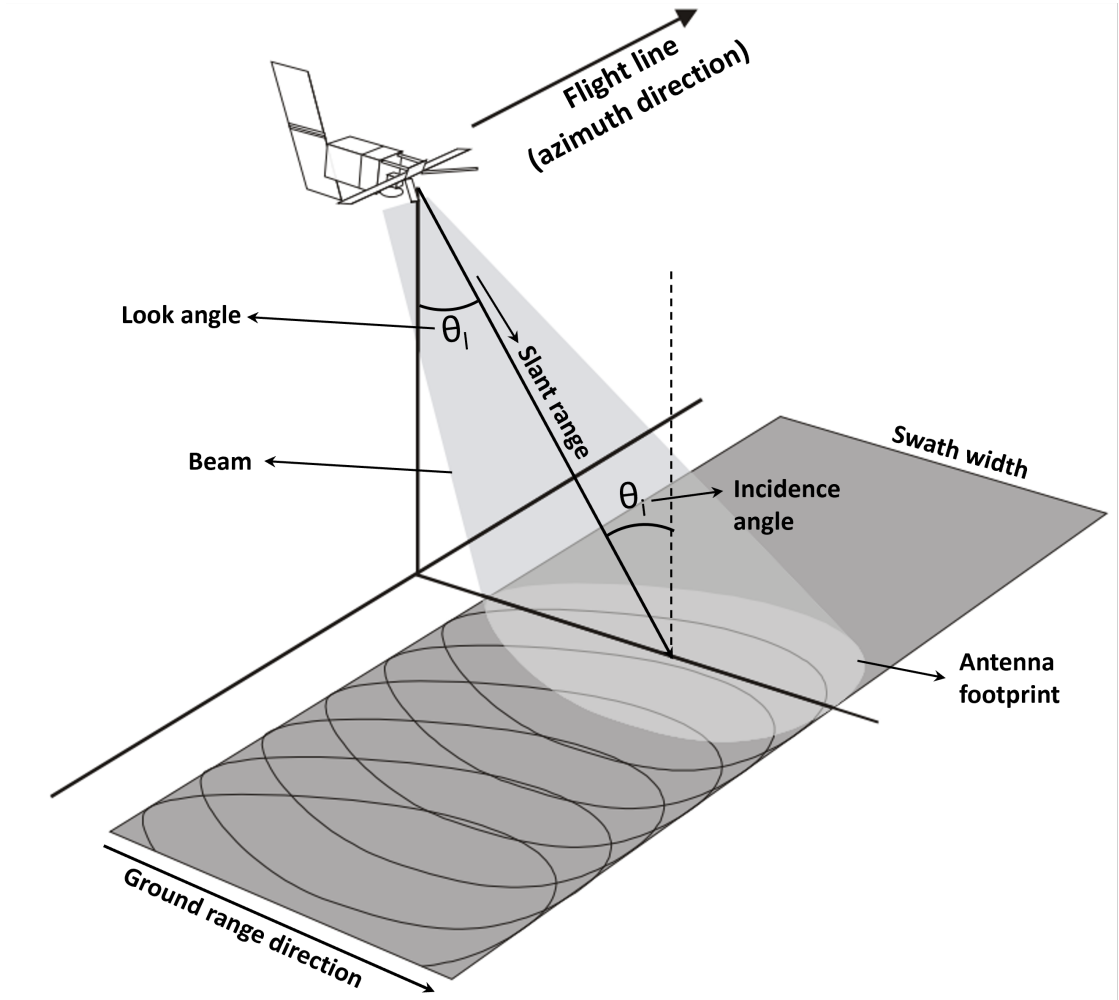

Figure 1.1: Side-looking Synthetic Aperture Radar (SAR) system geometry. Adapted from (Woodhouse, 2017).

energy, a SAR system uses the echolocation principle. This consists of measuring distance based on the time that an emitted pulse traveling at the speed of light takes to hit the target and return to the antenna (Campbell & Wynne, 2011; Richards et al., 2009). This provides the slant range distance to the target as shown in figure 1.1. The ground range dimension of a two dimensional image is constructed as the

projection of the slant range over the horizontal plane. The azimuth direction of the image is constructed by transmitting and receiving pulses as the platform moves along the orbit.

The image resolution in the case of SAR systems depends on different factors for the range and azimuth dimensions and it is therefore different in each dimension. This implies that a pixel in the image is generally not squared. A resolution cell (figure 1.2) is defined as the minimum area that a landscape on the ground can be resolved or separated in, and is determined by the ground range and azimuth resolutions (Richards et al., 2009).

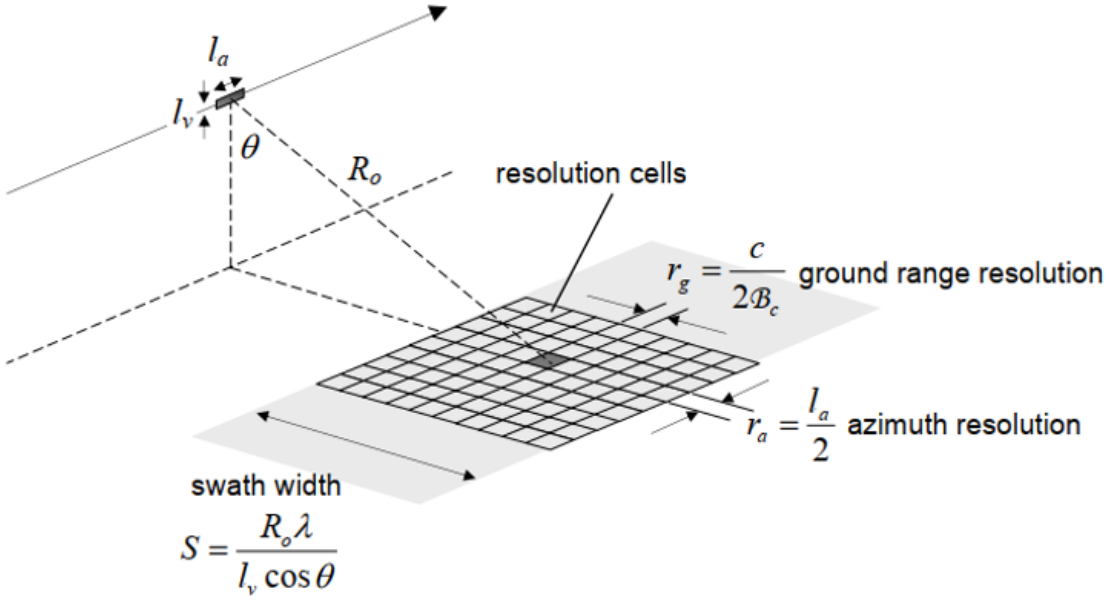

Figure 1.2: Schematic of a SAR image divided into resolution cells. The dimensions of each resolution cell are determined by the azimuth and range resolutions. Adapted from (Richards et al., 2009)

1.3.1 Resolution in range

SAR resolution can be defined as the ability of the system to resolve or distinguish neighbouring targets in a received signal. In the range direction, in a simple architecture, the resolution r_g depends on the characteristics of the emitted unmodulated pulse. This is considering that two targets on the ground can only be resolved if the distance between them is larger than half of the pulse duration as shown in equation

1.1 (Richards et al., 2009):

$$r_g = c\frac{\tau_p}{2} \tag{1.1}$$

where c is the speed of light and τ_p is the pulse duration. Accordingly, a naive way of achieving high range resolution would be to use short pulses. However, given that short pulses carry low energy it would be harder for the system to detect returning signals. On the other hand, it is complex to build a system capable of transmitting much higher power. A pulse compression technique is utilised to approach this problem by using pulse modulation. It consists of transmitting a so-called 'chirp' or a long pulse in which the frequency of the signal increases linearly over time (Richards et al., 2009). With the frequency modulation technique and expressing the pulse duration in equation 1.1 as a function of its bandwidth, which is defined as the range of frequencies over which the chirp sweeps, the resulting range resolution can be then expressed as:

$$r_g = \frac{c}{2B_c} \tag{1.2}$$

where B_c represents the bandwidth of the transmitted pulse. In this sense, the pulse bandwidth is a key feature that defines the image resolution in the range dimension. Once a 'chirp' impinges on a target on the ground and returns to the antenna, the signal must be passed through a matched filter to remove the modifications introduced with the frequency modulation (Richards et al., 2009).

1.3.2 Resolution in azimuth

In the azimuth dimension and considering the case of a Real Aperture Radar (RAR), the resolution is dependent on the distance of the platform to the target (R_0), the signal wavelength λ and the antenna length l_a as described in equation 1.3 (Richards et al., 2009):

$$\delta_{RAR} = R_0\frac{\lambda}{2l_a} \tag{1.3}$$

In RAR systems, higher azimuth resolutions can be achieved by increasing the antenna length l_a. This is because the longer the antenna, the narrower the antenna's beam width is, therefore, the easier it is for the system to separate targets. However, due to space and weight constraints in the moving satellite platform, the desired lengths are impractical (order of km). A different solution which gives origin to

the name of Synthetic Aperture Radar is to take advantage of the movement in the azimuth direction to synthesize and artificially create a longer antenna. This is done by using signal processing algorithms that coherently combine multiple views of the same target as the platform moves to greatly improve the azimuthal resolution. The study of the aperture or antenna synthesis is beyond the scope of this document and for a detailed description please refer to the textbooks by Curlander and McDonough (1991), Cumming and Wong (2005), Woodhouse (2017) and Richards et al. (2009). Concisely, the azimuth resolution resulting using the principle of synthetic aperture (antenna) L_e is:

$$r_a = R_0 \frac{\lambda}{2L_e} \tag{1.4}$$

The length of the synthetic aperture (antenna) L_e depends in turn on the real antenna size, wavelength and distance to a target in the ground as follows (Richards et al., 2009):

$$\text{Ł}_e < \frac{\lambda R_0}{l_a} \tag{1.5}$$

Therefore, replacing equation 1.5 in equation 1.4, the azimuth resolution is:

$$r_a = \frac{l_a}{2} \tag{1.6}$$

Note that according to equation 1.6, the azimuth resolution depends only on the antenna size and implies that the lower its length, the finer the resolution is. In principle this is counter intuitive considering that with a small antenna the beam-width is larger. However, having a large beam-width also means that the time that a target is seen by the synthetic aperture increases. On the other hand, since the azimuth resolution is independent of the distance between platform and target, space-borne SAR systems can easily obtain very high resolutions in azimuth quite independently of their orbital position.

1.3.3 Single-polarisation SAR image statistics

The size of a resolution cell is determined by the range and azimuth resolutions. A SAR image contains the landscape of a region divided into resolution cells as shown in figure 1.2. A resolution cell contains the response to the interaction between the microwave EM emitted and the targets on the ground. This response

represents a wave and therefore it is composed by an amplitude and phase (Woodhouse, 2017). The amplitude and phase are collected by the receiver using a I/Q modulation which converts them into a complex number format. This can therefore be written in Cartesian form with a real and an imaginary component, in polar form as amplitude and phase or in exponential form, also describing amplitude and phase (Woodhouse, 2017). When analysing a single-polarisation image (see section 1.3.5), if a single target is present or is dominant with respect to other objects within a resolution cell, the measured amplitude and phase correspond to the microwave response of this object. This case is known as having a point or single target. However, in practice this is normally not the case considering that the microwave pulse transmitted will interact with objects of the same size or bigger than the signal wavelength (Campbell & Wynne, 2011). Since the resolution in range and azimuth are significantly larger than the wavelength, the emitted pulse interacts with several objects simultaneously as shown in figure 1.3a. Therefore, the phase and amplitude received, correspond to the coherent combination of responses from individual objects within the resolution cell as shown in figure 1.3b. This case is commonly known as having a distributed target. The red vector represents (in the complex plane) the resulting coherent combination of complex vectors (waves with amplitudes and phases) from individual targets. Normally, adjacent resolution cells in a

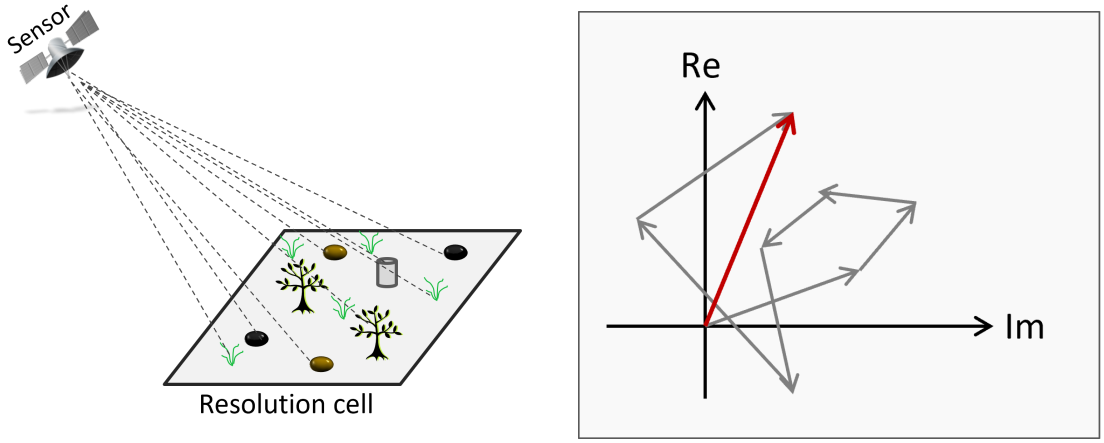

(a) Emitted EM pulse interacting with several scatterers in a resolution cell

(b) Coherent combination of responses from individual scatterers.

Figure 1.3: EM pulse interaction with distributed targets on the ground. Adapted from (Salepci et al., 2017)

SAR image have different arrangements of individual targets within each resolution cell. This causes the coherent combination of distributed targets to be different for neighbouring cells. Consequently, a SAR image will have variations in amplitude and phase even in areas of the ground that are homogeneous, such as in an agricultural field. This is because even small variations in the distribution of targets on the ground (i.e. leaves, branches, surface roughness, etc) will cause the interference pattern to change and hence, the received signal to be different (Woodhouse, 2017). The above-mentioned variations in the image are referred to as speckle and produce a noise-like effect in the SAR image as presented in figure 1.4. However, even if the speckle effect in a SAR image looks like noise, it cannot be defined simply as random noise. This is because it is an effect that could be repeated if for instance a SAR system could acquire two images over the same area with identical observation and target conditions (Woodhouse, 2017), as opposed to pure random noise effects where the exact noise cannot be reproduced by repeated experiments. If a random

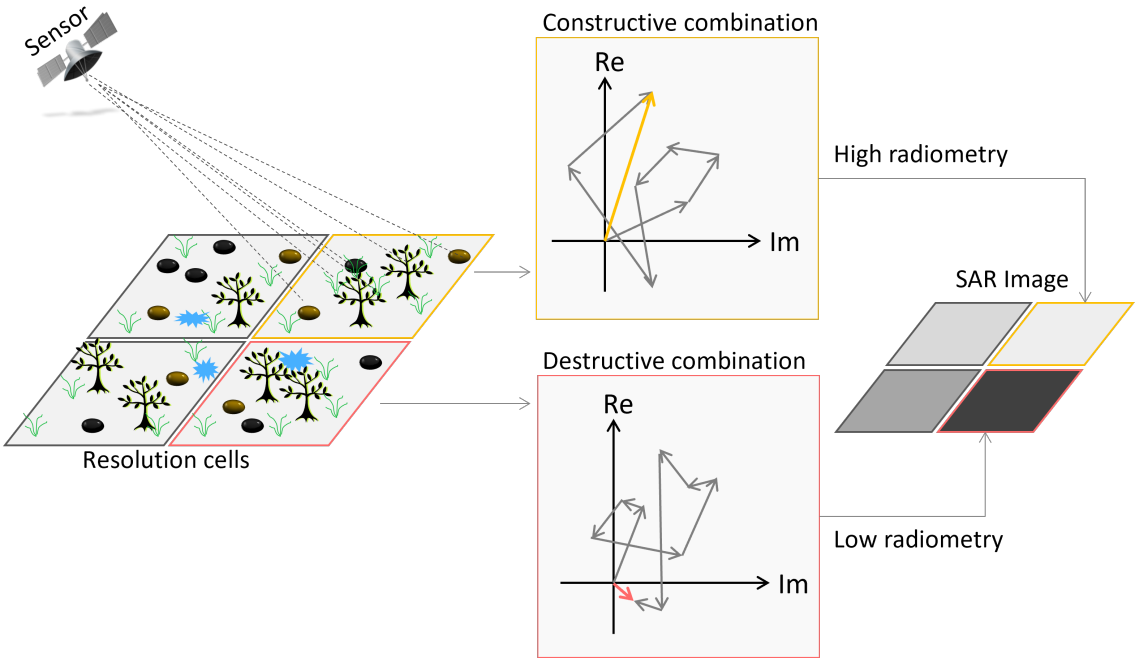

Figure 1.4: Resolution cell intensity variations due to speckle. Adapted from (Salepci et al., 2017).

arrangement of N scatterers is assumed to be within a resolution cell, the return from the $i-th$ element in the cell (expressed as a complex number in its exponential form) is $Z_i e^{j\theta_i}$. The coherent sum of the responses from all the scatterers in a cell

is:

$$Z = \sum_{i=1}^{N} Z_i e^{j\theta_i} = Z_{Re} + jZ_{Im} = \sum_{i=1}^{N} Z_i cos\theta_i + j\sum_{i=1}^{N} Z_i sin\theta_i \tag{1.7}$$

In SAR systems, the range and azimuth resolutions are normally significantly larger than the signal's wavelength, therefore the signal interacts with several scatterers. In this case, N can be assumed to be large ($N \to \infty$) and the central limit theorem can be applied. Consequently, the real and imaginary parts of the total return from a resolution cell are assumed to be independent (uncorrelated), identically distributed Gaussian random variables with zero mean: $Z_{Re} \sim \mathcal{N}(0,\, \sigma^2)$ and $Z_{Im} \sim \mathcal{N}(0,\, \sigma^2)$. In this context, their corresponding probability density functions (PDF) are described by:

$$P(Z_{Re}) = \frac{1}{\sqrt{2\pi\sigma^2}} \exp\left(-\frac{Z_{Re}^2}{2\sigma^2}\right) \tag{1.8}$$

$$P(Z_{Im}) = \frac{1}{\sqrt{2\pi\sigma^2}} \exp\left(-\frac{Z_{Im}^2}{2\sigma^2}\right) \tag{1.9}$$

A key point in statistically characterizing a SAR image is to identify the distribution of the amplitude (A) and phase (θ) of the returned signal from a resolution cell. This is done by firstly obtaining the joint PDF of the real and imaginary parts, shown in equations 1.8 and 1.9 as follows (Oliver & Quegan, 2004a):

$$P_z(Z) = \frac{1}{2\pi\sigma^2} \exp\left(-\frac{Z_{Re}^2 + Z_{Im}^2}{2\sigma^2}\right) \tag{1.10}$$

$$P_z(A, \theta) = \frac{1}{2\pi\sigma^2} \exp\left(-\frac{Z^2}{2\sigma^2}\right) \tag{1.11}$$

Secondly, the individual distributions for the amplitude and for the phase can be extracted from equation 1.11 by marginalizing the joint PDF. For the amplitude, the marginalisation results in the Rayleigh distribution:

$$P_A(A) = \int_{-\pi}^{\pi} P_A(A, \theta) d\theta = \frac{A}{\sigma^2} \exp\left(-\frac{A^2}{2\sigma^2}\right), \quad A \geq 0 \tag{1.12}$$

Equation 1.12 provides the probability that the returning coherent signal is of amplitude A (note that it is independent of the phase angle). Evaluating the moments of the PDF in Equation 1.12, the mean $\sqrt{\frac{\pi}{2}}\sigma$ and variance $\frac{4-\pi}{2}\sigma^2$ are extracted (Oliver & Quegan, 2004a). For the phase, the marginalisation results in the uniform distribution:

$$P_A(\theta) = \frac{1}{2\pi}, \quad -\pi \geq \theta \geq \pi \tag{1.13}$$

which indicates that the phase is independent of the amplitude and that all phases between $-\pi$ and π are equally likely, hence not providing any information about the target (Oliver & Quegan, 2004a). In some cases, the amplitude is not the quantity of interest, but the intensity or power of the signal which can be computed as the square of the amplitude ($I = A^2$). It can be demonstrated that the intensity (I) is then determined by the negative exponential distribution (Oliver & Quegan, 2004a):

$$P_I(I) = \frac{1}{2\sigma^2} \exp(-\frac{I}{2\sigma^2}) = \frac{1}{m} \exp(-\frac{I}{m}), \quad I \geq 0 \tag{1.14}$$

with $m = 2\sigma^2$. Note that the variance σ^2 of the real and imaginary components from equations 1.8 to 1.13 can be described as a function of the parameter m with $\sigma^2 = m/2$. Also note that according to equation 1.14, the intensity distribution for each resolution cell in an image can be characterised by the parameter m only which contains all the information about the distributed targets (Oliver & Quegan, 2004a). From the moments of an exponential distribution such as in equation 1.14, the mean can be extracted and is equal to the parameter m. This parameter is then known as the average intensity and is the key value we are interested in. Another important result is that the standard deviation for the exponential distribution also corresponds to the parameter m ($2\sigma^2$) (Oliver & Quegan, 2004a). This implies that the standard deviation is as large as the mean and increases in linear fashion with respect to it. These large variations around the mean help to statistically explain the speckle effect. In fact, the coefficient of variation for this distribution is equal to 1 or 100% (Oliver & Quegan, 2004a). An important implication of this result is that any calculations done using the intensity of a single resolution cell may include large errors. This is because the true intensity differs from the observed intensity as it is being mixed by the coherent sum of returns from individual scatterers (Woodhouse, 2017).

1.3.4 Reducing SAR image variability due to speckle

To reduce the variability present in the intensities of a SAR image, the average of L independently measured samples can be computed. As mentioned above in equation 1.13, for a single-polarisation and a single image the phase does not provide information about the target and can be discarded. The process of averaging the L

independent intensity samples without considering the phase is known as incoherent average. The independent samples can be obtained in two ways: a) during the acquisition process by splitting the azimuth beam into L sub-beams and acquiring L images or looks (Woodhouse, 2017) or b) during data processing by spatially averaging a set of L neighbouring resolution cells assuming that they all correspond to the same target. In both cases the resulting statistical distributions after the incoherent average are the same. The incoherent average is given by the expression

$$\overline{I} = \frac{1}{L}\sum_{k=1}^{L} I_k \tag{1.15}$$

where I_k corresponds to the intensity which follows the exponential distribution given by equation 1.14 for each of the L averaged resolution cells. The PDF of the resulting L-averaged resolution cell follows a Gamma function and is determined as (Oliver & Quegan, 2004a):

$$P_{\overline{I}}\overline{I} = \frac{1}{\Gamma(L)}(\frac{L}{m})^L I^{L-1}\exp(-\frac{LI}{m}) \tag{1.16}$$

where $\Gamma(L) = (L-1)!$ for integer values of L. Note, however, that number of looks is normally not an integer number given that the sub-apertures are processed so that they overlap and thus are not fully independent measurements. It has been shown that the moments of the average intensity obtained in equation 1.16 are (Oliver & Quegan, 2004a):

$$\mathbf{E}[\overline{I}] = m \quad var[\overline{I}] = \frac{m^2}{L} \tag{1.17}$$

where $\mathbf{E}$ corresponds to the expected value operator. Note that the variance $var[\overline{I}] = \frac{m^2}{L}$ has important implications. First of all, it indicates that the variability of the intensity decreases when more independent samples or looks (L) are averaged, hence reducing speckle. Since the L number of looks or neighbour pixels considered for reducing speckle are not necessarily independent, it is common to refer to this number as the Equivalent Number of Looks (ENL). In this context, another important property of the variance is that it provides us with a tool to empirically estimate ENL with the relationship $ENL = \frac{m^2}{var}$.

It is important to highlight that this subsection presented the image statistics for the single-polarisation and a single image case. If more polarisations are considered, the same assumptions apply for each polarisation separately, however, the statistics

of the combined information are not fully exploited. Polarimetric speckle statistics should then be considered (e.g. modelling the covariance matrix using a Wishart distribution). Please refer to (Lee & Pottier, 2009; Oliver & Quegan, 2004a) for an in-depth discussion. Similarly, if more than one image is considered, discarding the phase information is not always adequate, for instance for applications such as SAR interferometry or coherent change detection, among others. These cases exploit the difference in the phase between images or spectral portions of images and therefore phase needs to be preserved during the pre-processing and speckle filtering (Woodhouse, 2017).

1.3.5 Introduction to SAR Polarimetry

This subsection is intended to present only a brief introduction to the use of polarimetric data acquired by a space borne SAR system. Please refer to (S. Cloude, 2009; Lee & Pottier, 2009; Richards et al., 2009) for a thorough review.

In Polarimetric SAR (PolSAR), the intention is to analyse the geometrical shape and orientation of the emitted and received electromagnetic pulses, before and after interacting with the target on the ground. The EM wave orientation is determined by the direction of the oscillating electric field and is also known as polarisation or polarisation state. The aim of PolSAR is to exploit additional information in the data as each polarisation state used may interact differently with a target. In this context, a SAR image component can be acquired for each combination of transmitted-received polarisations used by the SAR sensor (see section 4.1). Similarly, the correlations between these SAR image components provide a separate source of information to characterise the target. In general, by characterising the polarimetric properties of objects on the ground, we may be able to gain insight into their physical characteristics.

1.3.5.1 Wave polarimetry

In this subsection, the derivation of the change in polarisation of a wave after interacting with the target is presented. This is closely related to the theory of electromagnetism and wave propagation. Here however, the derivation will start from the far field hypothesis, which states that far from its origin of propagation, a wave can

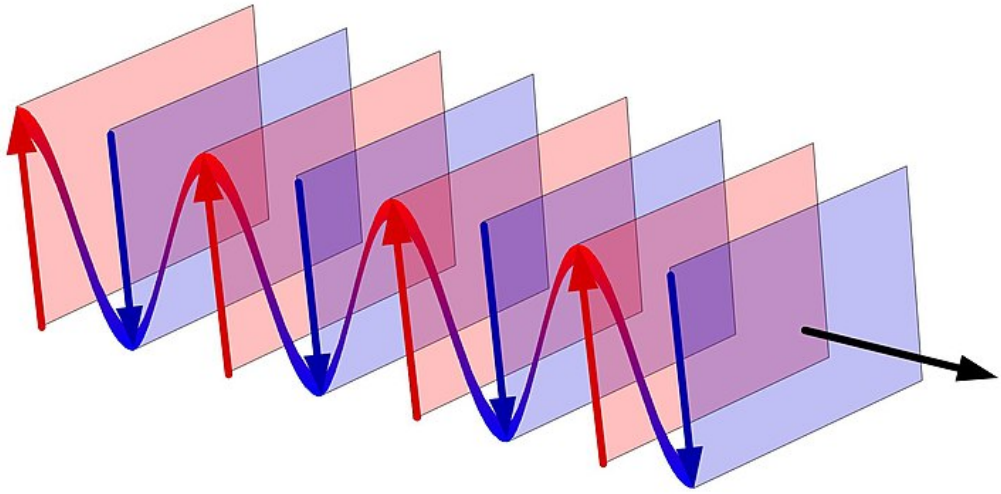

Figure 1.5: Propagation of a plane wave's electric field. Adapted from: A representation of a plane wave's electric field shown from an oblique angle, (https://commons.wikimedia.org/wiki/File:Plane_Wave_Oblique_View.jpg), 2010. In the public domain.

be approximated as a plane wave as shown in figure 1.5. Under this assumption, the front of the wave can be seen as a plane and the electric and magnetic fields oscillate orthogonally to the propagation direction. Wave polarisation is defined in terms of the geometrical shape that the electric field draws in the plane wave-front (Woodhouse, 2017). Different geometrical patterns such as lines, circles and ellipses can be identified (figure 1.6).

Since it is a vector laying on a plane, the electric field of an EM wave is modelled as the superposition of two vector components. If the direction of propagation is along the Z-axis, the two electric field components are given in the X and Y directions as shown in figure 1.7. This can mathematically be defined as:

$$\underline{E}] = E_x\underline{u_x} + E_y\underline{u_y} \tag{1.18}$$

where u_x and u_y are two generic and orthogonal unitary vectors perpendicular to the propagation direction. After transforming to polar coordinates and including the appropriate terms to describe the wave propagation in time, equation 1.18 can be re-written as:

$$\underline{E} = |E_x|cos(\omega t - kz + \phi_x)\underline{u_x} + |E_y|cos(\omega t - kz + \phi_y)\underline{u_x} \tag{1.19}$$

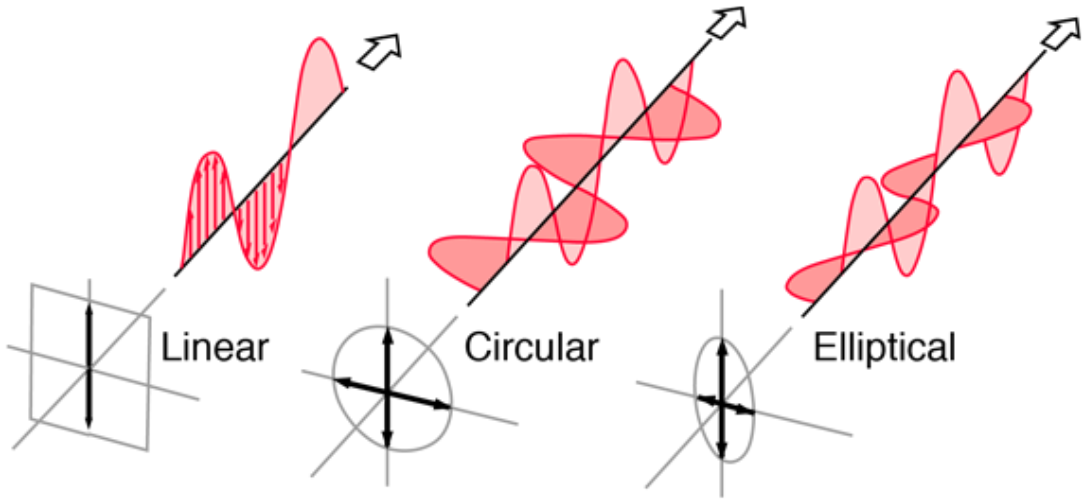

Figure 1.6: Geometric shape described by the orientation of the wave's electric field. Adapted from: Classification of Polarization, (http://hyperphysics.phy-astr.gsu.edu/hbase/phyopt/imgpho/polcls.png), 2010. In the public domain.

where ω represents the angular frequency $\omega = 2\pi f$ with f being the temporal frequency measured in hertz (Hz), t represents the time, k is the wavenumber $k = \frac{\omega}{c}$ and c is the speed of light. ϕ_x and ϕ_y correspond to the initial phase angle of each vector component. It is possible to create any EM wave polarisation state by modifying either the amplitude of the two vector components E_x and/or E_y, their phase difference, or both.

1.3.5.2 Linear Polarisation

The geometric shape drawn on the wavefront by a wave whose electric field has only one direction of displacement (either X, or Y or an in-phase linear combinations of those) is a line. This happens for instance if the amplitude of the component in the X direction of the electric field is zero, E_x=0, as only oscillations in the Y direction are present. Then the EM wave has vertical polarisation. Similarly, when the amplitude of the component in the Y direction is zero, E_y=0, only oscillations in the X direction are present, making the wave horizontally polarised.

The linear vertical and horizontal polarisations are frequently utilised by space-borne radars. In addition, by modifying the phase difference between the two vector components, elliptical and circular polarisations can be generated.

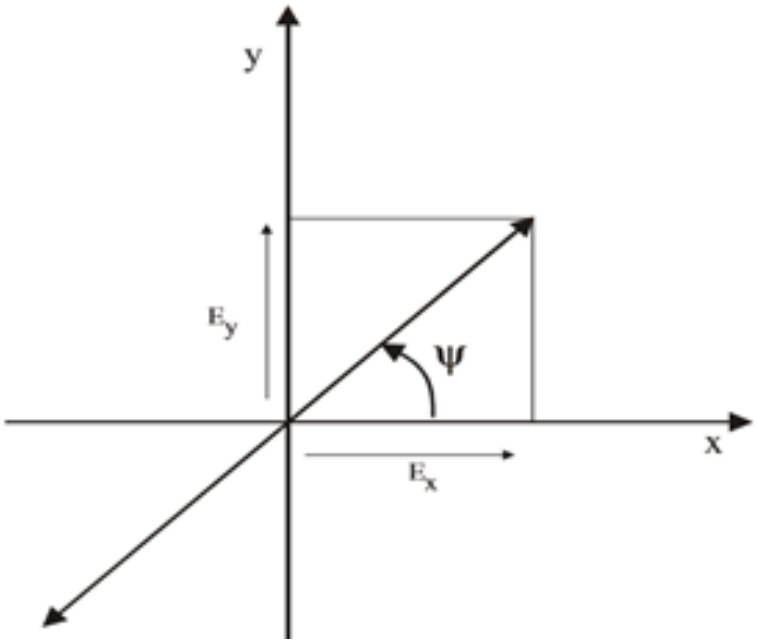

Figure 1.7: Electric field vector components of a wave propagating in the Z direction. From (Woodhouse, 2017)

1.3.5.3 The scattering matrix

When a polarised EM wave transmitted by the SAR satellite impinges on a target, part of the energy is reflected back to the receiver antenna. The polarisation of the reflection depends on the transmitted polarisation and the physical properties of the object such as shape, orientation and dielectric properties. Therefore, understanding the polarimetric behaviour of the target may help to characterise its physical properties. The target properties modify the incident wave polarisation such that we can assume that the scattering process converts the incident waves E^i into the scattered waves E^s. This relationship is described by:

$$E^S = [S]E^i \tag{1.20}$$

where $[S]$ represents the target properties that modify the wave polarisation. The vector form of the incident and scattered wave electric fields can be written as:

$$E^i = \begin{bmatrix} E_x^i \\ E_y^i \end{bmatrix} \quad E^s = \begin{bmatrix} E_x^s \\ E_y^s \end{bmatrix} \tag{1.21}$$

In this case, equation 1.23 becomes:

$$\begin{bmatrix} E_x^s \\ E_y^s \end{bmatrix} = \begin{bmatrix} S11 & S12 \\ S21 & S22 \end{bmatrix} \begin{bmatrix} E_x^i \\ E_y^i \end{bmatrix} \tag{1.22}$$

where the components $S11$, $S12$, $S21$ and $S22$ form the $[S]$ matrix, also known as the scattering (or Sinclair) matrix. It describes the scattering process in terms of the relationship between incident and scattered electric fields. The calculation of $[S]$ permits one to obtain information about the physical properties of the target and to create physical models for identification and/or separation of scattering mechanisms taking place inside the same resolution cell. Therefore, the interest is in $[S]$ rather than simulating E^s starting from E^i, since $[S]$ allows to describe the polarimetric behaviour of a target (assuming that it does not change in either space or time, i.e. it is a stationary point target). When considering the received waves E^s by the radar, the power drop due to the distance between the target and the radar must be considered:

$$\begin{bmatrix} E_x^s \\ E_y^s \end{bmatrix} = \frac{1}{\sqrt{2\pi R_0^2}} \begin{bmatrix} S11 & S12 \\ S21 & S22 \end{bmatrix} \begin{bmatrix} E_x^i \\ E_y^i \end{bmatrix} \tag{1.23}$$

where R_0 represents the distance between the sensor and the target. SAR systems that are able to acquire the full scattering matrix $[S]$ in one pass are known as quad-polarimetric systems. If $[S]$ is partially acquired, i.e. only one of its columns is acquired, the system is known as a dual-polarimetric system. Note that in order to characterise the polarimetric properties of a target, the full matrix is required (S. Cloude, 2009).

1.3.5.4 Coordinate systems: FSA and BSA

A SAR system can be utilised in monostatic or in bistatic configuration. In a monostatic radar, both the receiver and the transmitter are physically located sharing the same antenna (figure 1.8, right) while in the bistatic configuration they are spatially separated by a considerable distance (figure 1.8, left) (Woodhouse, 2017). Different reference coordinate systems can be utilised for the transmitted and received electromagnetic waves. These define the coordinates relative to the position of the transmitting and receiving antennas and relative to the target, as shown in figure 1.9. In this context, in the Forward Scattering Alignment (FSA) shown in figure 1.9(a), the reference direction given to the propagating wave scattered from the target points towards the antenna receiver. This type of reference coordinate system is normally used in bistatic configurations (Lee & Pottier, 2009). This is opposite to the IEEE convention known as Backward Scattering Alignment (BSA) of figure

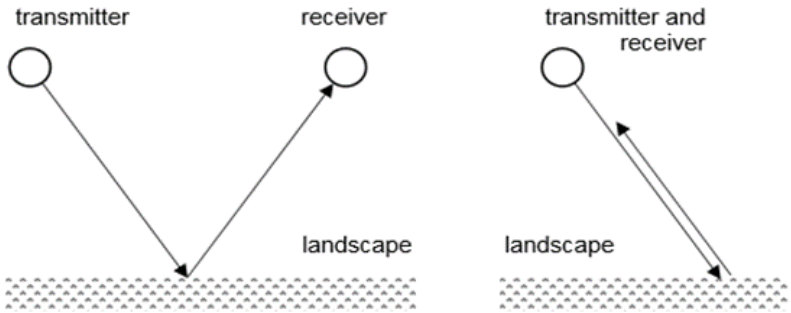

Figure 1.8: Monostatic and bistatic radar configurations. From (Richards et al., 2009)

1.9(b), in which the direction of the scattered propagating wave points towards the target or opposite to the antenna receiver. This reference system is particularly useful for monostatic configurations such as in figure 1.9(c), since the transmitter and receiver share the same antenna and the reference direction given to the emitted and received propagating wave coincides (Lee & Pottier, 2009).

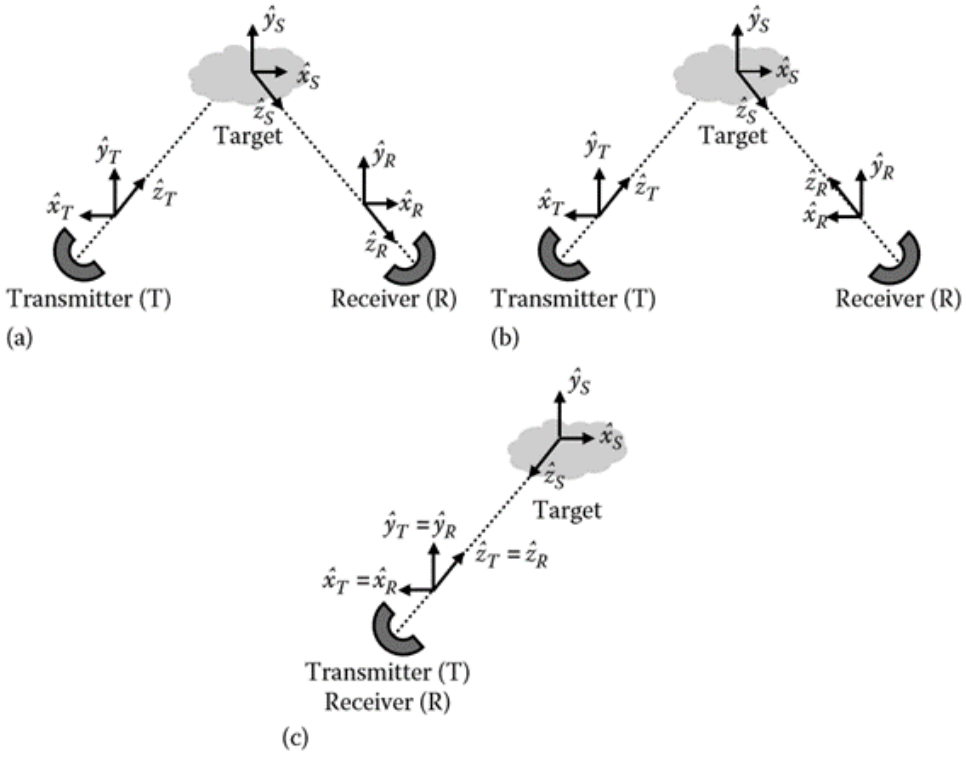

Figure 1.9: Coordinate systems: (a) FSA bistatic, (b) BSA bistatic, and (c) BSA monostatic coordinate systems. From (Richards et al., 2009)

Commercial SAR satellites commonly employ the monostatic (or quasi-monostatic) configuration and consequently, the most convenient coordinate system to utilise is

the BSA monostatic system. In this scenario and under the principle of reciprocity, the components $S12$ and $S21$ in the scattering matrix can be assumed to be the same ($S12 = S21$) except for thermal noise. This allows the reduction in the number of independent components in the $[S]$ matrix from four to three complex measurements in a fully polarimetric system (Lee & Pottier, 2009; Richards et al., 2009; Woodhouse, 2017).

1.3.6 PolSAR Image statistics

Section 1.3.3 introduced the statistical modelling applicable for a single-polarisation SAR image. If a SAR system is able to acquire imagery in more than one polarisation, the statistical exploitation of the SAR data needs to simultaneously consider the information available in all polarisations. For the case of distributed targets and linear polarisations, the scattering matrix of equation 1.23 can be represented as:

$$S = \begin{bmatrix} S_{HH} & S_{HV} \\ S_{VH} & S_{VV} \end{bmatrix} \tag{1.24}$$

where H and V stand for linear horizontal and vertical and the double letter corresponds to transmitter–receiver. A vectorisation of the scattering matrix is commonly utilised in order to aid the statistical characterisation and provide a geometrical interpretation of a target (Lee & Pottier, 2009; Richards et al., 2009). The resulting vector, also known as the scattering vector, is obtained using the vectorisation operatior $V(S)$ as follows:

$$\underline{\mathbf{k}}_4 = V(S) = \frac{1}{2} tr\{SH\} = [k_1, k_2, k_3, k_4]^T \tag{1.25}$$

where tr is the matrix trace, ^{T} represents the vector transpose and H is a set of 2x2 complex basis matrices. The vectorisation algebraically corresponds to forming linear combinations of the scattering matrix elements (Strang et al., 1993). A widely used set of basis matrices is the lexicographic set, defined as:

$$H_L = \left\{ \begin{bmatrix} 2 & 0 \\ 0 & 0 \end{bmatrix}, \begin{bmatrix} 0 & 2 \\ 0 & 0 \end{bmatrix}, \begin{bmatrix} 0 & 0 \\ 2 & 0 \end{bmatrix}, \begin{bmatrix} 0 & 0 \\ 0 & 2 \end{bmatrix} \right\} \tag{1.26}$$

from where the lexicographic scattering vector can be obtained, corresponding to:

$$\underline{\mathbf{k}}_{4L} = [S_{HH}, S_{HV}, S_{VH}, S_{VV}]^T \tag{1.27}$$

The Pauli base of equation 1.28 is another typically used matrix base to vectorise the scattering matrix, considering that the resulting components of the scattering vector can be associated with physical targets (Lee & Pottier, 2009; Richards et al., 2009).

$$H_P = \left\{ \sqrt{2}\begin{bmatrix} 1 & 0 \\ 0 & 1 \end{bmatrix}, \sqrt{2}\begin{bmatrix} 1 & 0 \\ 0 & -1 \end{bmatrix}, \sqrt{2}\begin{bmatrix} 0 & 1 \\ 1 & 0 \end{bmatrix}, \sqrt{2}\begin{bmatrix} 0 & -j \\ j & 0 \end{bmatrix} \right\} \tag{1.28}$$

The Pauli scattering vector then corresponds to:

$$\underline{\mathbf{k}}_{4P} = \frac{1}{\sqrt{2}}[S_{HH} + S_{VV}, S_{HH} - S_{VV}, S_{VH} + S_{HV}, j(S_{VH} - S_{HV})]^T \tag{1.29}$$

The elements of the Pauli scattering vector are normally associated with scattering mechanisms caused by physical targets (S. Cloude, 2009; Lee & Pottier, 2009). The element $S_{HH} + S_{VV}$ is associated with odd bounce or surface scattering caused by isotropic scatterers that may include surfaces or spheres. The element $S_{HH} - S_{VV}$ is related to even or double bounce caused by targets such as a dihedral element with one of the planes being horizontal. The elements $S_{VH} + S_{HV}$ and $j(S_{VH} - S_{HV})$ are associated with volume scattering caused by a 45 degree oriented dipole.

As mentioned in section 1.9 for the monostatic case and assuming the BSA convention, the scattering matrix can be simplified to three components and hence the lexicographic scattering vector become:

$$\underline{\mathbf{k}}_{3L} = [S_{HH}, \sqrt{2}S_{HV}, S_{VV}]^T \tag{1.30}$$

and the Pauli Scattering vector:

$$\underline{\mathbf{k}}_{3P} = \frac{1}{\sqrt{2}}[S_{HH} + S_{VV}, S_{HH} - S_{VV}, 2S_{VH}]^T \tag{1.31}$$

In order to exploit the polarimetric information contained in the scattering vectors, all polarisations need to be considered simultaneously and coherently as well as considering the statistical correlation among the polarisation channels. The derivation follows the same assumption as for the case of a single-polarisation SAR image introduced in section 1.3.3. It was assumed that the coherent signal returning from a resolution cell with distributed targets, follows a zero mean complex Gaussian distribution. Considering the same assumption for each of the SAR images acquired in

every polarisation, a multidimensional zero mean complex Gaussian distribution is obtained to characterise the distribution of the returning signals in all polarisations:

$$P_k(k) = \frac{1}{\pi^p |\Sigma|} \exp(-\underline{k}^{*T} \cdot \Sigma^{-1} \cdot \underline{k}) \tag{1.32}$$

where p represents the number of elements in the scattering vector, the ^{*T} symbol represents the conjugate transpose, Σ is a standard covariance matrix and $|\Sigma|$ is the matrix determinant. Note that this distribution representing the data acquired for a resolution cell is completely characterised by its covariance matrix. This is given that all of the higher order moments can be computed from Σ. Using the scattering vector in the lexicographic form of equation 1.30, the covariance matrix can be estimated as:

$$[\Sigma_L] = \langle \underline{k}_{3L} \cdot \underline{k}_{3L}^{*T} \rangle = \begin{bmatrix} \langle |S_{HH}|^2 \rangle & \sqrt{2}\langle S_{HH} S_{HV}^* \rangle & \langle S_{HH} S_{VV}^* \rangle \\ \sqrt{2}\langle S_{HV} S_{HH}^* \rangle & 2\langle |S_{HV}|^2 \rangle & \sqrt{2}\langle S_{HV} S_{VV}^* \rangle \\ \langle S_{VV} S_{HH}^* \rangle & \sqrt{2}\langle S_{VV} S_{HV}^* \rangle & \langle |S_{VV}|^2 \rangle \end{bmatrix} \tag{1.33}$$

For the scattering vector in the Pauli basis of equation 1.31, the covariance matrix, also known as coherency matrix, can be estimated as:

$$\begin{aligned} [\Sigma_P] &= \langle \underline{k}_{3P} \cdot \underline{k}_{3P}^{*T} \rangle \\ &= \begin{bmatrix} \langle |S_{HH} + S_{VV}|^2 \rangle & \sqrt{2}\langle (S_{HH} + S_{VV})(S_{HH} - S_{VV})^* \rangle & \dots \\ \sqrt{2}\langle (S_{HH} - S_{VV})(S_{HH} + S_{VV})^* \rangle & \langle |S_{HH} - S_{VV}|^2 \rangle & \dots \\ 2\langle (S_{HV}(S_{HH} + S_{VV})^* \rangle & 2\langle (S_{HV}(S_{HH} - S_{VV})^* \rangle & \dots \end{bmatrix} \\ &\dots \quad 2\langle (S_{HH} + S_{VV})(S_{HV})^* \rangle \\ &\dots \quad 2\langle (S_{HH} - S_{VV})(S_{HV})^* \rangle \\ &\dots \quad 4\langle |S_{HV}|^2 \rangle \end{aligned} \tag{1.34}$$

Considering that the amplitude and phase of a resolution cell for each polarisation are the coherent and linear combination of backscattered signals from individual scatterers within it (see figures 1.3a and 1.3b), the measurements are also affected by speckle. To reduce the image variability due to speckle, L number of *iid* resolution cells can be averaged (or speckle filtered), and the matrix of equation (3) becomes the L-looked coherency matrix:

$$T = \frac{1}{L} \sum_{i=1}^{L} \underline{k}_{pi} \underline{k}_{pi}^{*T} \tag{1.35}$$

where i=1,2, .., L, are the number of averaged samples or realizations. L-look PolSAR data. Note that the spatial averaging assumes that the averaging is performed over homogeneous areas or samples. In cases where this assumption is not met, it results in loss of spatial resolution. This is in practice a common case and trade off between spatial averaging to reduce speckle effects and spatial resolution loss.

The L-looked covariance or coherency matrix of equation 1.35 is normally used to represent the polarimetric information of a SAR image resolution cell. As such, several studies have proposed methods to exploit the information contained in it. A review of covariance and coherency matrix decomposition was presented in S. R. Cloude and Pottier (1996). Also, please refer to section 4.4.1, where the eigenvalue/eigenvector decomposition of the coherency matrix is presented as part of a novel approach for crop monitoring using multitemporal PolSAR data. It is also worth noting that, the probability distribution of the L-looked covariance or coherency matrix of equation 1.35 can then be modelled with a complex Wishart distribution. Please refer to Lee and Pottier (2009) for a detailed explanation of the formulation and applications of the Wishart distribution to statistically model PolSAR data.

1.3.7 Scattering Mechanisms for Vegetated Soils

A SAR system measures the EM waves scattered from a target on the ground. This scattering depends on the physical properties of the target, including roughness, moisture, dielectric constant, shape and geometry (Campbell & Wynne, 2011; Woodhouse, 2017). In order to analyse the interaction of incident EM waves and the target properties that produce the scattered waves, some scattering processes or as more commonly known, scattering mechanisms (SMs) have been introduced in the literature. In the following, a brief overview of these scattering mechanisms is provided and its applicability for agricultural fields monitoring. This is not intended to be a complete literature review on scattering mechanisms and the reader is referred to (S. Cloude, 2009; Lee & Pottier, 2009; Richards et al., 2009; Woodhouse, 2017) for more details. The three most common and widely accepted scattering mechanisms include:

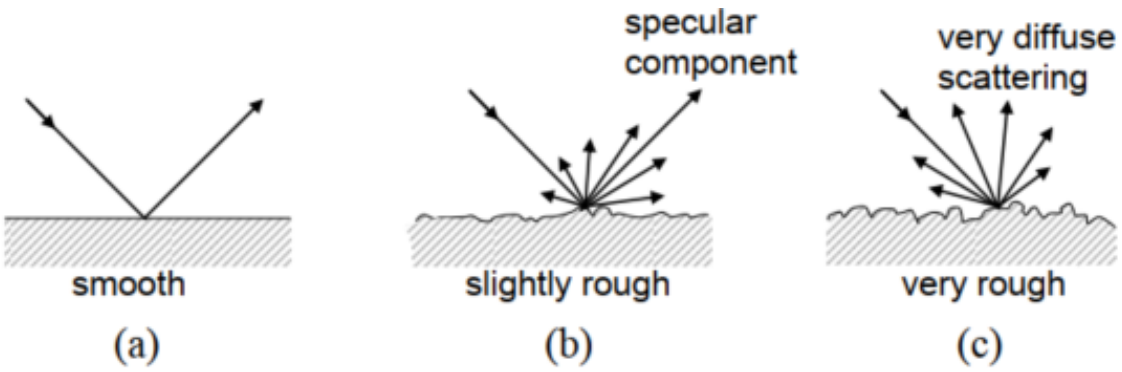

Figure 1.10: Specular and diffuse surface scattering and its relationship with surface roughness. From (Richards et al., 2009).

- Surface or odd scattering: From a natural surface, the intensity of the scattering is highly affected by the dielectric constant of the surface, which in turn is related to the surface moisture content. The direction of the scattered waves, which also influences the intensity, depends on the surface roughness as follows. In a smooth surface, for example, the EM waves are scattered away from the SAR sensor with the same angle of the incident waves. This effect is known as specular scattering (Richards et al., 2009) and since only a small part of the EM waves is scattered back to the satellite, these types of surfaces appear dark in a SAR image. In a rougher surface, a part of the scattered waves can have specular scattering while another part can scatter back to the satellite. The proportion of energy that presents specular reflection or that scatters back towards the spacecraft, is highly dependent on the amount of surface roughness, as shown in figure 1.10. This in addition is dependent on the system wavelength, considering that the signal interacts with targets that have its same or greater size (Campbell & Wynne, 2011). In this context a surface may appear rougher for an X-band system of 3 cm wavelength than for an L-band system with 12 cm wavelength. Since in rougher surfaces a part to of the energy is reflected to the satellite, these regions will appear brighter in the image than the smooth surfaces. Importantly, the combination of surface roughness and the SAR system incidence angle also influences the scattering from surfaces as presented in figure 1.11. It is possible to see that this angle influences more scattering from smooth forces than from rougher ones. In fact, scattering in the latter case is almost unaffected by the incidence angle due to

the surface roughness scattering the incident waves in several directions (right of figure 1.11.

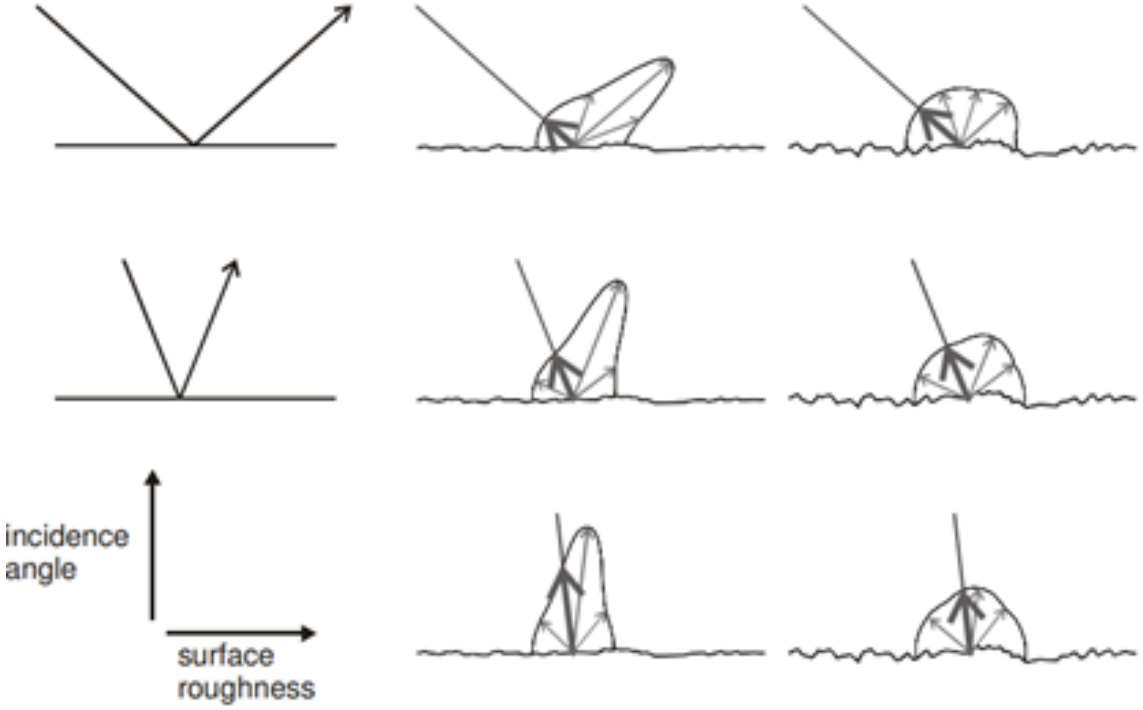

Figure 1.11: Surface scattering and its relationship with incidence angle and surface roughness. From (Woodhouse, 2017)

- Volume scattering: Under this type of scattering, a complex scattering response is assumed in which the reflected EM waves come from several scatterers rather than from a single one. A typical land surface used to describe volume scattering is a forest, where the SAR signal from a resolution cell is scattered from different elements of the forest canopy such as leaves, branches and/or trunk, which in turn may have different orientations and dielectrical constants (Richards et al., 2009; Woodhouse, 2017)

- Double or even bounce scattering: In ideal conditions, double bounce occurs with scattering between two neighbour surfaces that form an angle between them. A typical example of this is observed in situations where EM waves present specular reflection from the ground that then bounces in a vertical target such as a tree trunk or a building and subsequently reflects the EM

waves back to the satellite. Note however that the bouncing can also occur first in the vertical surface and subsequently in the horizontal surface. In real cases, factors such as the incidence angle, the orientation of the two intervening surfaces and their material properties (i.e. roughness, moisture), influence the scattering characteristics and therefore the observed double bounce.

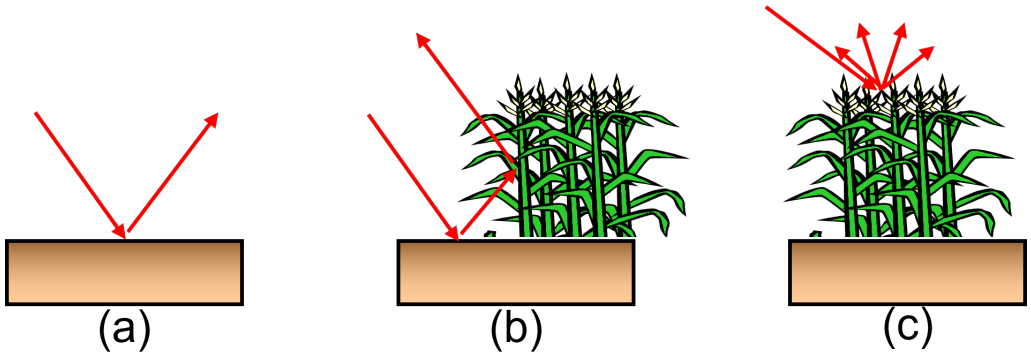

Figure 1.12: Typical scattering mechanisms in agricultural fields : (a) Surface scattering, (b) Double bounce, and (c) Volume scattering.

For the specific case of croplands, the same scattering mechanisms are assumed to occur and are depicted in figure 1.12. In this context, surface scattering is normally observed when a crop does not have a canopy and the incident EM waves interact with the soil directly. This occurs for instance before sowing stages or after a canopy has been mechanically removed for harvest. The soil characteristics including soil moisture, roughness and row orientation determine the scattered signals. With regards to the satellite system, an important factor that impacts the scattered EM waves is the incidence angle, and in particular, its combined effect with surface roughness (Woodhouse, 2017). In the practice, surface scattering from crops is observed for example in rice crops when the soil is flooded and the incident EMs interact with the water surface (Lopez-Sanchez et al., 2014) and in general for other crop types when the SAR signal interacts with a crop on very early growth stages or after harvest (C.-a. Liu et al., 2019; Steele-Dunne et al., 2017a). Similarly, volume scattering is normally observed in a crop when a canopy is present and the waves emitted by the SAR sensor interact with leaves, branches, vertical and oriented stems and the soil. The effect of the incidence angle when a canopy is present producing volume scattering is less evident than for surface scattering provided the use of a

short wavelength such as C-band. This is since C-band signals do not penetrate the canopy significantly but are mostly reflected from the canopy top layer (De Roo et al., 2001; Hosseini & McNairn, 2017; Skriver et al., 2011; Skriver et al., 1999). When a longer wavelength is used such as L- or P-band, the penetration of the SAR signal is greater and interaction of the signal with the main vertical stems and soil can be expected. In this sense, the wavelength constitutes an important system parameter when analysing SAR response from a crop canopy. Double or even bounce is observed in a crop for instance when vertical stems are emerging from the ground and vertically elongate resembling the presence of vertically oriented dipoles. As will be introduced in next section, several crops present this type of behaviour including rice and cereal crops (C.-a. Liu et al., 2019; Lopez-Sanchez et al., 2014; Steele-Dunne et al., 2017a).

1.4 Spaceborne SAR for crop biophysical variables estimation and monitoring

In the literature for agricultural applications using SAR data we can identify five general categories: crop type mapping (Bargiel, 2017; Shang et al., 2009; Van Tricht et al., 2018), cropping practices monitoring (Bégué et al., 2018), assimilation of SAR data into crop growth models (Huang et al., 2019; Kasampalis et al., 2018; Steele-Dunne et al., 2017b), crop yield prediction (LIU et al., 2019; Steele-Dunne et al., 2017b; Weiss et al., 2020a) and crop biophysical variables estimation and monitoring. Since this thesis is concerned with crop development monitoring, this section provides a review on crop biophysical variables extraction and monitoring. The reader is directed to the above presented references for the other categories.

In terms of the crop variables themselves, in the literature among other the following variables have been reported: crop phenology, Leaf Area Index (LAI), above ground biomass (AGB), crop height (Erten et al., 2016a; Lopez-Sanchez, Ballester-Berman, & Hajnsek, 2011; McNairn et al., 2018; Vicente-Guijalba et al., 2015). Most studies focus on investigating the interaction between the SAR signal and crop vegetation during one or more agricultural seasons. This is done by implementing modelling techniques to retrieve the state of crop parameters given a SAR

image and by investigating the statistical correlation between SAR observables and ground samples of the crop biophysical variables. Please note that the terms crop parameters, crop biophysical variables and crop variables are used in this section interchangeably.

With respect to the SAR imagery, the backscatter response to crop development has been widely studied, particularly testing different system parameters such as acquisition geometry, wavelength, and polarisations. Polarimetric data has been used by exploiting quad-polarisation imagery modelled with a pixel covariance matrix as presented in section 1.3.6. Other studies use features derived from eigenvalue/eigenvector decomposition of the covariance matrix as well as model based covariance matrix decompositions (S. R. Cloude & Pottier, 1996). Interferometric data has been used by studying the behaviour of the interferometric coherence as the crop evolves over time (Jacob et al., 2020; Mestre-Quereda et al., 2020; Nasirzadehdizaji et al., 2021) and for crop height retrieval (Erten et al., 2016b; Romero-Puig & Lopez-Sanchez, 2021) as will be introduced later in this chapter. Similarly, the combined Polarimetric and interferometric features for crop monitoring have been studied as described by Lopez-Sanchez and Ballester-Berman (2009) and Romero-Puig et al. (2021). The following lines present a review of the main works reported in the field and that are relevant for this thesis, however, an extensive and systematic literature review of the field as whole is out of the scope of this thesis. Please refer to (Erten et al., 2016b; McNairn & Shang, 2016b; Steele-Dunne et al., 2017b; Weiss et al., 2020a) for more detailed reviews.

1.4.1 Correlating SAR observations with crop parameters

The SAR signal received by the system antenna after interacting with a target is sensitive to target properties such as roughness, moisture, dielectric constant, shape and geometry (Campbell & Wynne, 2011; Woodhouse, 2017). This Since the crop morphological parameters, including soil moisture and roughness, crop height, canopy density, biomass and plant water content etc, change as the agricultural season progresses, the SAR signature changes accordingly. It is based on this principle that SAR data can be exploited for agricultural applications. Several studies have focused on observing the correlation between crop morphological parameters

and the corresponding SAR observables. Using models to understand the response of SAR observations to these parameters is key to develop applications that allow operational retrieval of the crop biophysical variables using SAR imagery as input.

1.4.1.1 Semi-empirical models

Early research in the field relied on scattering models to explain the observed backscatter given a crop condition and environmental factors. The Water Cloud Model (WCM) is considered a seminal work for this approach and was developed by Attema and Ulaby (1978). It proposes to model a vegetation canopy as a cloud of water droplets that are supported by vegetation matter. It considers the scattering and attenuation from the droplets and soil to derive the equations that estimate backscatter intensity from three vegetation parameters: Soil moisture, plant water content and plant height. Since the original experiment considered several incidence angles, system frequencies and polarisations, these system parameters can also be included in the mathematical expressions. This way, knowing the crop and SAR system parameters, the backscatter intensity can be simulated. Since the backscatter is measured by the satellite and the interest is to retrieve the crop parameters, several calibration and inversion strategies have been proposed to invert (or estimate) the crop parameters from the observed backscatter (Graham & Harris, 2003). Ordinarily, retrieving the parameters is done in two steps: WCM calibration and model inversion. In the calibration step, the crop parameters are measured in the ground truth for a set of training fields in order to calibrate the WCM equations in such a way that they correctly simulate the observed backscatter over the same fields. Then, in the inversion step, the backscatter observations are used on the test fields together with the calibrated model, to invert the crop biophysical variables.

The WCM model has been substantially used to retrieve crop parameters from SAR data. De Roo et al. (2001) used the WCM to retrieve vegetation water content and soil moisture of soybean fields using C and L band SAR imagery. Bériaux et al. (2011) used the WCM to estimate surface soil moisture and LAI from SAR data for maize crops. The applicability for LAI and biomass retrieval in corn and wheat fields was tested successfully by Hosseini et al. (2015) and Hosseini and McNairn (2017), respectively. Baghdadi et al. (2017) show the potential of retrieving soil

moisture using the WCM, by replacing the canopy component of the required ground samples with the optical NDVI and deriving the soil moisture samples for the integral equation model (Fung et al., 1992). Then after the model inversion, the authors show that the VV polarisation provides better estimations of soil moisture than the VH, since the VH reacts more to the canopy layer than the VV.

Note, however, that given the simplifications assumed to develop the WCM, several studies have found situations where the performance of the model is low and have proposed modifications to it. These includes modelling more elaborated scattering mechanisms or more geometrical properties of the vegetation (Paris, 1986; Tao et al., 2016a). Additionally, other investigations have reported instability problems when calibrating the WCM model. Bériaux et al. (2015) introduces problems of transferring the calibrated model coefficients of the WCM in space and time as well as to other crop types or SAR sensors. Bériaux et al. (2015) also introduces a Bayesian method to combine the WCM-based LAI predictions from the VH and VV polarisations in such a way that the predictions with high uncertainty are given lower averaging weight. Similarly, experimental data has shown that the assumption of modelling the canopy as a cloud of uniformly distributed droplets does not always hold true. Steele-Dunne et al. (2017b) report experimental measurements of vegetation water content which show that the water content changes with plant height, and therefore, it is not uniformly distributed during the whole season. This assumption combined with instability problems for calibration and problems for transferability in space and time, may reduce the applicability of the WCM.

1.4.1.2 Physical models

Physical models have also been developed forward and inverse models for the backscatter from a vegetated surface. These models exploit physics knowledge of the interaction between electromagnetic waves and vegetation, where the vegetation is normally assumed to be composed of geometrical shapes such as vertical or oriented cylinders for stems and branches and ellipsoids or disks for leaves. Similarly, canopy parameters such as height, dielectric constant, number of layers and leaves, leaf angle and size, stem width etc, are used to describe the canopy (Della Vecchia et al., 2006; Steele-Dunne et al., 2017b; Weiß et al., 2020). The microwave backscatter is gen-

erally modelled using radiative transfer theory (Chandrasekhar, 2013). A popular example of a physics based model is the Michigan Microwave Canopy Scattering Model (MIMICS) (Ulaby et al., 1990). Although it was designed originally for forest scattering modelling by dividing the vegetation layer into three layers (crown, trunk and under), it has been adapted for agricultural applications for its use in wheat and canola crops vegetation parameters extraction (Toure et al., 1994). This was done to retrieve LAI by removing the trunk layer of the model and representing crop parameters by cylinders, discs and rectangles. A similar approach was used by De Roo et al. (2001) to retrieve soil moisture from soybean crops. Also for soybean, outputs from the MIMICS were used by P.-W. Liu et al. (2016) as input for a crop growth model for soil moisture and biomass retrieval in a Kalman filter-based data assimilation application. A fully polarimetric multiple scattering model for crops was also introduced by Bracaglia et al. (1995).

L.-F. Wang et al. (2005) proposed a rice growth model based on a microwave scattering theory and supported by Monte Carlo simulations to solve Maxwell's equations. The model considers the geometrical structures of rice plants and rice fields and allows to simulate the backscatter response produced by growth of rice crops using L- and C-band SAR data, and different incident angles. More recently and also for rice, Y. Liu et al. (2016) proposed another radiative transfer model to simulate the microwave scattering mechanisms of rice crops at different growth stages and SAR system parameters. The authors used this model to show that canopy backscatter from stems is more important than from leaves and that, during stem elongation, intensity of VH and HH polarisations increase while the VV increases at the start of the season and then decreases. A wheat canopy scattering model was introduced by Yan et al. (2018) based on first order microwave radiative transfer equation using time series of C-band quad- (Radarsat-2 and GaoFen-3) and dual-polarization (Sentinel-1) SAR data. The authors report good agreement between observations and simulations and highlight the importance of considering the incidence angle as a key variable within an operational retrieval context. Also for wheat, X-band data from the COSMO-SKYMED satellite has been used in a physical based approach to retrieve canopy parameters and soil moisture.

Note that despite having a strong theoretical foundation, physical models still

face challenges regarding accuracy of the retrieved results, partly due to the assumptions and approximations about the geometrical shapes used to model the canopy and to solve the mathematical equations. The theoretical background required as well as the computational cost to run the models are seen as a barrier for the operational adoption of these approaches (Della Vecchia et al., 2006; Steele-Dunne et al., 2017b).

1.4.1.3 Statistical correlation of backscatter and crop biophysical variables

This subsection provides a brief review on the studies that empirically investigate the relationship between SAR backscatter measurements and crop biophysical parameters. Considering the vast amount of studies published in the last two decades and particularly after the freely available Sentinel-1 imagery, an exhaustive literature review is out of the scope of this section. Here we present the papers most relevant to this thesis and some seminal works that are widely recognized in the field. Although the WCM and other physical based models had provided initial insights on the sensitivity of SAR measurements to crop parameters, several studies based on empirical comparisons of SAR response to ground truth, further enhanced knowledge on the interaction between microwave signals and agricultural fields. For example, in Le Toan et al. (1997) the authors use C-band SAR data for flooded rice fields monitoring. They show how the backscatter intensity from the fields changes as the season progresses, highlighting that the temporal variation of the radar response is due to the wave-vegetation-water interaction. It is demonstrated how different growth stages have different responses and how the backscatter increases from the transplanting stage to reproductive stage. Skriver et al. (1999) study the temporal response of HH and VV polarisations over spring and winter crops using L- and C-band polarimetric SAR data. They conclude that the impact of variations in the incidence angle is stronger for images acquired early in the agricultural season. This effect is less pronounced, according to the authors, once the canopy is fully developed. Comparing the response from different fields, authors conclude that the planting direction and tillage practices are the two key factors that change the backscatter response. Similarly, the correlation coefficient

between HH and VV polarisations was found to be key for discriminating between winter crops and spring crops, especially at C-band. Macelloni et al. (2001) study the influence of the shape and size of the canopy on the backscatter response, and demonstrated that the response is different between broad and narrow leaves crops. The authors also conclude that the leaves make a significant contribution to scattering and reduce the contribution of stems at C-band SAR, while stalks dominate the response at L-band. Mattia et al. (2003) discuss the sensitivity of different polarisations and incidence angles of C-band SAR to retrieve wheat biomass and soil moisture. The authors show the potential of VV polarisation channel to retrieve above ground biomass before the heading stage and also show the potential for soil moisture retrieval after the heading stage with the HH polarisation channel. They also highlight that there is no simple relationship between above ground biomass retrieval after heading, and soil moisture before heading, and a more complicated model needs to be developed as well as highlight the need to test the potential of the VH polarisation. Della Vecchia et al. (2008) study the sensitivity of VV, HV, and HH radar backscatter intensities to maize crop height, biomass and soil moisture for several incidence angles and frequencies. The study concludes that VV is sensitive to soil moisture, while the VV/HV ratio shows an important sensitivity to crop canopy parameters and is moderately affected by soil-moisture conditions. Similarly, Lin et al. (2009) study the C-band SAR backscatter response from sugarcane fields and the potential for operational retrieval of leaf area index at different growth stages. Results show that the ratio HH/HV highly correlates with leaf area index and reduces the soil backscattering effects. Based on this findings, the authors present an empirical model to retrieve LAI from SAR imagery. On the other hand, the polarisation ratio HH/VV was reported to be key for mapping rice cropping systems given that VV is significantly lower than HH for most of the rice season, which generates a characteristic pattern. This is because of the attenuation of the microwave signals by the vertical structure of the plants (Bouvet et al., 2009). A similar finding was reported by Larranaga et al. (2013) using RADARSAT-2 data over cereal crops. Here, they observed a significant attenuation of the VV backscatter intensity which is stronger than the one seen for HH due to the vertical orientation of stems. In this same study a strong response for Rapeseed and peas was reported

with the HV polarisation channel, presumably due to the canopies being more heterogeneous. Moran et al. (2011) study the response of dense RADARSAT-2 C-band quad-polarized SAR imagery for wheat, barley, oat, corn, onion, and alfalfa in Barrax, Spain. Preliminary results showed that the cross-polarized HV backscatter was sensitive to crop growth, particularly for identifying heading in cereal crops and leaf growth and reproduction in corn and onion. The HV was also found the least sensitive to differences in beam incidence angle. Interestingly, the authors discuss the importance of the temporal resolution and report that having 3 to 6 days resolution was acceptable for crop type mapping and for crop phenology monitoring if quad-pol imagery are used. If only dual-polarization data is available with this temporal resolution, mapping crop green biomass was possible. For soil moisture applications, however, the authors recommend daily image acquisitions.

Fieuzal et al. (2013) present the results of a large experiment that combines X-, C- and L-bands SAR data from the TerraSAR-X, RADARSAT-2 and ALOS satellites, including HH, VV, VH and HV polarisation channels and several incidence angles during the growing season of winter rapeseed and wheat. Results show that the best correlation between leaf area index and crop height with the SAR observations are obtained with C-band SAR for rapeseed and with X-band data for wheat crops. Authors present a novel method for normalizing the system incidence angles while highlighting the opportunities of SAR to complement optical data, for crop parameters monitoring. Inoue et al. (2014) present the results of a 4 year experiment in Japan that tests the potential of rice crop biophysical variables monitoring using C-band backscatter. Here, VH polarisation channel has a high sensitivity to crop height, however, authors suggest that it is more an indirect effect of the changes in the leaves biomass and structure. Authors also report an indirect or not a significant relationship between backscatter and chlorophyll content (Fraction of Absorbed Photosynthetically Active Radiation - FAPAR), while stating that there is no sensitivity to the canopy water content.

- **Launch of the Sentinel-1 Constellation**

The launch of the Sentinel-1 constellation enabled a wider use of SAR data for agricultural monitoring. A noticeable increase in the amount of research published in the field is evident. Although some studies make use of the dual-polarimetric and

interferometric data, the majority of the studies focus on exploiting the VH and VV backscatter intensities. An early study by Bousbih et al. (2017), uses two years of ground measurements of soil roughness and water content as well as vegetation parameters including leaf area index, and vegetation height for cereal crops to evaluate the sensitivity of Sentinel-1 to these crop variables. Authors show that the sensitivity of the VV polarisation channel to soil moisture is stronger than that of VH, and decreases as the above ground canopy starts to form and establish. Both polarisation channels are sensitive to increase in soil roughness. Interestingly, authors report not finding an evident correlation between the VH channel and the vegetation parameters, while the correlation to VV decreases with vegetation growth. Veloso et al. (2017) analyse time series of Sentinel-1 data for wheat, rapeseed, maize, soybean and sunflower, and compare them with Landsat-derived NDVI time series. Supported by rainfall, temperature and ground measurements of green area index and fresh biomass, authors correlate crop growth with the corresponding VV and VH backscatter intensities and VH/VV ratio trends. They found the VH/VV ratio to provide key information for identifying maize, soybean and sunflower during the heading and the flowering phases. The authors also demonstrate that there is a strong correlation between VH/VV time series and both green area index and fresh biomass measurements. Furthermore, the VH/VV ratio is found to be less influenced by rainfall events than either the VH and VV polarisation channels individually. Therefore, authors report that VH/VV is suitable for biophysical parameters retrieval, for biomass assimilation in crop models and that the backscatter intensities may be complementary to NDVI during cloudy periods. Vreugdenhil et al. (2018) introduce a study exploiting time series of Sentinel-1 data using the VV and VH backscatter intensities as well as the ratio VH/VV for evaluating the potential for vegetation monitoring. In particular, authors focus on SAR sensitivity to Vegetation Water Content (VWC), biomass, Leaf Area Index (LAI) and height, for oilseed-rape, corn and winter wheat during two growing seasons. Results show that it is difficult to separate vegetation water content from growth of leaves, stem extension and head development. Similarly, exponential models that use the VH/VV ratio as input are found to be better predictor of VWC than linear models, confirming a non-linear relationship between the SAR observations and crop parameters. The

feature importance tool of the random forest algorithm is then used to demonstrate that the VH/VV ratio is a more important feature than any individual polarisation for retrieving VWC. Authors also report the sensitivity of the VH/VV ratio to estimate the time of occurrence of heading and flowering in winter cereals, confirming what was reported in Veloso et al. (2017). Also using time series of Sentinel-1 data, Harfenmeister et al. (2019b) show an analysis of the SAR temporal profile driven by the evolution of wheat and barley crops biophysical parameters. According to the authors, an observed SAR signal attenuation can be explained by vegetation growth in spring and by a more volume scattering, attributed to the crop reaching certain height and due to the appearance of the flag leaves. Continuing the work on wheat fields, Nasrallah et al. (2019) also study the Sentinel-1 time series as a function of the phenological stages and investigate the potential for estimation of dates for wheat main growth stages. These stages include germination, heading, soft dough and harvesting. Authors identify that the ratio VV/VH at low incidence angle (32–34°) was able to detect the germination and harvesting dates. Similarly, it is reported that the VV polarization channel was able to detect the heading phase, while VH at high incidence angle (43–45°) was better than that at low incidence angle (32–34°), in detecting the soft dough phase. Supported by a Gaussian fitting and smoothing algorithms, authors report the ability to estimate germination with a root mean square (RMSE) error of 2.9 days, heading with RMSE of 5.5 days, soft dough RMSE of 5.1 days and approximately 4 days for harvesting. Wali et al. (2020) reports an analysis over paddy rice fields in Japan using C-band Sentinel-1 backscatter time series to study the sensitivity to plant height, green vegetation cover, leaf area index, and total dry biomass. The authors find that a polynomial regression accurately model the non-linear relationship between crop parameters and SAR observables, particularly for the VH channel. They also propose to fit a linear regression model separately to the beginning of the season and another linear model for the end of the season, in order to represent the relationship between crop parameters and both the VH and VV polarisation channels. Interestingly, authors report that all the considered crop variables can be linearly estimated in the first half of the season from the SAR backscattering observations (particularly for the VH polarization channel), this is, from transplanting to the mid-reproductive stage. However, they also in-

dicate that accurate monitoring after the mid reproductive stage is difficult since the backscatter saturates and become insensitive to the further crop development. Schlund and Erasmi (2020) study the occurrence of phenological stages using the local extrema and breakpoints of smoothed VH, VV, and VH/VV SAR time series collected over wheat crops for three consecutive years. Authors report the retrieval of the date when shooting occur using the VH/VV ratio with an RMSE of 4.6, 5.3 and 9.5 days for each of the years monitored. For retrieving harvest date, accuracy of 5.1, 8.2 and 10.4 days are reported while ripeness stages could not be detected with high accuracy. Bhogapurapu et al. (2021) introduce three vegetation descriptors using the Sentinel-1 backscatter intensities. Authors designed them as the pseudo scattering-type parameter, the pseudo scattering entropy parameter, and the co-pol purity parameter from dual-pol S1 GRD SAR data. The usefulness of the proposed vegetation descriptors is tested in wheat and canola crops. Authors demonstrate that the indices are highly dynamic as the agricultural season progresses while highlighting the relationship between the indices and the crops phenological stages. They also proposed a clustering algorithm using these three vegetation descriptors as input, showing that the sample pixels moves in between the feature space zones of the clustering algorithm according to the crop phenological stage. According to the authors, the proposed indices can then be used to classify crop phenological stages.

- **Use of Polarimetric SAR data**

In general, the potential of polarimetric SAR observables for crop monitoring has been widely tested and several studies report its successful use. However, due to an added degree of complexity, lack of freely available imagery, a higher computational cost and storage space, and a the trade-off between quad-polarisation systems and image resolution, quad-polarimetry is not frequently reported in operational applications. As mentioned in section 4.1, the target scattering matrix collects the information about the interaction between the polarisations sent and received by a SAR system and a target on the ground. This matrix describes the changes in polarisation between the incident and scattered waves. To aid the interpretation and analysis of PolSAR data and inversion of target parameters from it, several target methodologies have been proposed. A review of these can be found in S. R. Cloude and Pottier (1996) and Lee and Pottier (2009). A general objective of the

PolSAR decompositions is to extract information about the physical properties of a target from the scattered waves, by understanding whether the response comes from a surface or a volume structure, or a combination of both. Similarly, the aim is to understand whether the target causes a single dominant scattering mechanism, or more than one scattering mechanisms are present in the observed area. For agricultural applications, the aim is to analyse how the scattering mechanisms derived from PolSAR data change over time as a crop develops, plants grow and a canopy forms and reaches maturation and how the soil and vegetation water content influence them. This information is then related to the state of crop biophysical parameters. An example of this can be seen in C. Liu et al. (2013) where the authors vectorise the scattering matrix and use the Pauli components of equation 1.31 to study the intensity of the surface scattering, double-bounce, and volume scattering in corn, spring wheat, and soybeans using quad-Pol C-band RADARSAT-2 data. It is found that since each crop type has specific structural characteristics, the evolution of the Pauli components changes accordingly. They also found that for each crop type, the dominant scattering mechanism changes depending on the crop growth stage, noting particularly strong changes in the PolSAR response when plants emerge and after harvest. Lopez-Sanchez, Cloude, et al. (2011) interpret the radar response of rice fields by deriving a set of dual polarimetric observables from TerraSAR-X data including the Pauli components and features derived from target decomposition techniques such as the eigenvector decomposition. Authors found that even though the dual-PolSAR response changes during the season, some growth are difficult to discriminate since they present a similar PolSAR response. Adams et al. (2013) propose the Cloude–Pottier (S. R. Cloude & Pottier, 1996) and Freeman–Durden scattering decompositions (Freeman & Durden, 1998) to characterize scattering mechanisms from mature crops and harvested fields. They found that the PolSAR features from before harvest are statistically significantly different from post-harvest PolSAR response. Also using Freeman-Durden and Cloude-Pottier decompositions, Cable et al. (2014) found that PolSAR response to soybean and canola crops generally shows an increase in volume scattering as the crops approximate senescence. They also highlight the importance of considering the row orientation as well as incidence angle, since they are strongly related to penetration of the SAR signal into the

canopy. Wiseman et al. (2014b) study the response of 21 PolSAR parameters to dry biomass growth in canola, corn, soybean, and spring wheat. It is demonstrated that the intensity of the PolSAR observables increased more rapidly at the beginning of the season as biomass accumulation accelerated, partially fitting a nonlinear model (logarithmic). Similarly, it is shown that volume scattering and pedestal height can help identify milking and dough stages in wheat. In Lopez-Sanchez et al. (2014), the response of C-band backscattering coefficients and several polarimetric observables computed using the Eigenvalue/Vector decomposition, the Freman-Durden decomposition and compact polarimetry is presented as a function of rice crop phenology. As part of the analysis, it is concluded by the authors that features such as the Entropy, Anisotropy and alpha angle derived from the Eigenvalue/Vector decomposition clearly describe the polarimetric behaviour in this crop. Each growth stage presents a different behaviour for these features, for instance, moderate entropy, dominant surface scattering (low alpha angle values), and high anisotropy for early vegetative stage and high entropy, low anisotropy, and dominant alpha angle below 45 degrees for maturation. This enables the discrimination of the growth stage in a SAR imagery by analysing these three PolSAR features. Canisius et al. (2018) also study PolSAR features derived from C-band quad-Pol data from the RADARSAT-2 satellite for retrieving canola and spring wheat plant height and LAI. Results show that there exist for this test site a linear correlation between plant height and the alpha angle and that LAI for both crop types is strongly correlated with the beta angle (derived from Eigenvalue decomposition of the covariance matrix). A different approached based on change detection has been presented by Alonso-González et al. (2016) and recently expanded in Alonso-González et al. (2020). It consists in correlating the PolSAR changes with the changes that the crop undergoes as it evolves during the season.

Although the dual-polarimetric properties offered by the Sentinel-1 satellite have not been widely used so far, few studies have tested its potential for crop monitoring. Mandal et al. (2020) propose to exploit the information contained in the dual-pol covariance matrix, and specifically, the degree of polarization and the eigenvalue behaviour to estimate a novel vegetation index from Sentinel-1 imagery. The authors compare the proposed index with the so-called dual-pol radar vegetation index

and the cross-polarisation ratio to evaluate their sensitivity to canola, soybean, and wheat crop growth. The statistical analysis reported demonstrates that there is significant correlation between the proposed index and the crop parameters for the three crops. Harfenmeister et al. (2021) analyse time series of entropy, anisotropy, and alpha angle computed from decomposition of the dual-polarimetric covariance matrix formed with Sentinel-1 data for monitoring wheat and barley. Single and multiple linear regression models and exponential models are utilised to invert plant height, wet biomass, dry biomass, and vegetation water content from the backscatter and dual-pol features. This study reports that the dual-polarimetric features provide additional information for crop parameters retrieval, in contrast to using backscatter intensities only. This was shown by comparing the R^2 results for multiple regression which includes all features and linear regression models by individual features separately. It is also shown that the retrieval accuracy of the regression models is different for each phenological stage, with performances being more accurate early in the season, possibly because the structural changes in the canopy are more significant. A study by Xie et al. (2021a) presents retrieval of corn crop height from Multitemporal C-band quad-Pol RADARSAT-2 data. It uses a Random Forest Regression and a Support Vector Regression as well as a set of 27 features derived from the PolSAR imagery. The root mean square error between predicted and observed values is 40 to 50 cm throughout the growth cycle (corn plants can reach up to 3 meters) and conclude that the features that contain information regarding double-bounce and volume scattering are key for corn height estimation.

- **Use of Interferometric SAR (InSAR), Polarimetric-interferometric SAR (PolInSAR) SAR data**

A study by Zalite et al. (2016) analyse the potential of X-band interferometric coherence from the CosmoSkyMed satellite to detect mowing events and estimate vegetation height and biomass on agricultural grasslands. Interestingly, it is found that the vegetation height and wet biomass are negatively correlated with the coherence while the backscatter intensities are not correlated with these two vegetation parameters. Rossi and Erten (2015) demonstrate an application on the use of bistatic (separated transmitter and receiver) InSAR using Tandem-X data for monitoring paddy rice crop height. This is done by generating Digital Elevation Models DEM

over the fields for all crop stages, apart from the emergence stage when the fields are flooded and without vegetation.

With regards to the use of Sentinel-1 data, Khabbazan et al. (2019b) study the potential of the interferometric coherence to monitor crop biophysical variables of sugar beet, potato, maize, wheat and English rye grass. Based on statistical analysis the authors show a strong correlation between time series of SAR backscatter intensities and changes in the crop structure and vegetation water content. It is also demonstrated that the interferometric coherence increases as the vegetation grows and the canopy develops while, showing that after harvest the coherence increases again. Based on this, it is highlighted that this feature can be used as a metric for identifying crop harvest. A similar conclusion is reached by Kavats et al. (2019) where the date when harvest occurs is inferred from Sentinel-1 imagery for soybean and sunflower crops. Authors show that for the test site the interferometric coherence increases as plants ripen and dry out while drooping after harvest. This effect seems to be maximised for crops planted in rows. Authors then design a bespoke threshold-based algorithm from InSAR coherence to retrieve the harvest date achieving mean average errors of about 6 days. Also for harvest detection and expanding to seeding detection, a paper by Shang et al. (2020) presents an algorithm which establishes the rules to estimate dates for crop seeding and harvest from InSAR coherence for cereal crops, canola and hay, from Sentinel-1 data. The algorithm achieves an accuracy of 85% for harvest detection and 56% for seeding detection. In addition, it is discussed that issues may arise using InSAR coherence for key dates estimation due to rainfall, excess of soil moisture and other events such as post-harvest residue removal and field ploughing.

Although the PolInSAR technique has also been proposed for deriving forest canopy height and crop canopy height, the applications have so far been limited to airborne campaigns rather than spaceborne SAR systems as for the interest of this thesis. A detailed analysis in this topic is out of the scope of this thesis but can be found in Ballester-Berman et al. (2005) and Lopez-Sanchez and Ballester-Berman (2009). In essence, the advantage of using PolInSAR observations, represented by the complex InSAR coherence for different polarisations, is to be able to acquire information about the vertical structure of the plants in a field. This is done eval-

uating the localization of the scattering centers and it is in addition to providing information of dielectric properties, shape and orientation of the canopy as when using backscatter intensities and PolSAR data. Additionally, as described in (Lopez-Sanchez & Ballester-Berman, 2009), PolInSAR allows the identification of different scattering mechanisms along the vertical dimension (e.g. plant height). This means that it is possible to separate scattering contributions from the soil and canopy. Note however, that ideally, PolInSAR observations need to come from a single-pass system with bi-static configuration and with long spatial baselines to have good vertical sensitivity. Since satellites systems with this configurations are not common, PolInSAR applications are more limited for operation monitoring.

- **Methodologies to monitor and estimate crop parameters from SAR imagery**

As introduced previously in this section, the WCM and radiative transfer model approaches have been used for inverting crop biophysical parameters from SAR imagery (Baghdadi et al., 2017; Graham & Harris, 2003; Hosseini & McNairn, 2017; Hosseini et al., 2015; Y. Zhang et al., 2014). Similarly, a meta-modeling approach has been proposed, specifically for rice fields in order to retrieve growth stage and height (Yuzugullu et al., 2016; Yuzugullu et al., 2017). Recently, separate methodologies have proposed the use of linear, polynomial and exponential models to invert crop height, green vegetation cover, leaf area index, and dry biomass using SAR backscatter intensities for rice (Chakraborty et al., 2005; Wali et al., 2020), and with dual-polarimetric data for wheat and barley (Harfenmeister et al., 2021).

Machine learning algorithms have also been tested in recent years for estimating crop parameters from SAR imagery. In Küçük et al. (2016) a method for rice phenology monitoring was presented. It tests the performance of support vector machines (SVM), k-nearest neighbors (kNN), and decision trees (DT) to classify rice growth stage from dual-PolSAR derived features as inputs for the classifier. Issues including the correct selection of features and the number of classes are discussed. A study by Ndikumana et al. (2018) reports the retrieval of rice height and biomass from Sentinel-1 data by training algorithms including Multiple Linear Regression (MLR), Support Vector Regression (SVR) and Random Forest (RF), with the RF achieving coefficient of determination R^2 above 0.9. In H. Wang, Magagi, Goïta,

et al. (2019) authors proposed polarimetric features from covariance matrix decompositions as inputs for random forest, neural network and K-nearest neighbours for classifying the crop stage from a SAR image for canola, wheat and soybean. Authors report that the algorithms successfully learn the non-linear mapping functions that estimate phenology, with the Random Forest being the most accurate using a combination of multiple polarimetric features. A hybrid approach which seeks to integrate the best of machine learning with current knowledge on the WCM, has been similarly introduced in the literature. A study by Mandal, Hosseini, et al. (2019) compares four approaches to invert LAI of corn using the WCM: iterative optimization, Look-up table search, Support Vector Regression (SVR) and Random Forest Regression, concluding that the SVR results in more accurate estimations while the Look-up table search is the least accurate. Similarly, Mandal, Kumar, McNairn, et al. (2019) proposed an approach to estimate, based on the water cloud model, plant area index and wet biomass simultaneously, supported by a multiple output random forest regression. Authors claim that retrieving the two variables at the same time improve the retrieval accuracy compared to retrieving the crop variables individually. The Gaussian Process Regression algorithm (Rasmussen, 2003) has been used to fuse Sentinel-1 data with optical data from the Sentinel-2 satellite in order to retrieve leaf area index. In Pipia et al. (2019) a method to retrieve leaf area index was proposed, which combines time series of Sentinel-1 backscatter intensities to fill the gaps of Sentinel-2 vegetation indices due to clouds. The advantage of this method is, according to the authors, that the Gaussian process algorithm is able to learn the statistical correlations between the two satellites, so that even if Sentinel-2 data are absent, using Sentinel-1 and the trained model, leaf area index can be retrieved. Based on the results, authors demonstrate the benefits of the synergy of the two sensors. Similarly, a study by Mercier et al. (2020) uses Gaussian processes to retrieve LAI, biomass, and water content of wheat and rapeseed crops from Sentinel-1 and Sentinel-2 imagery. Authors test several combinations of features for each sensor, identifying the SAR and vegetation indices that provide the most accurate LAI, biomass, and water content, and conclude that even though Sentinel-2 is more accurate, polarimetric SAR features greatly increase the performance of SAR based models. The authors, also highlight the potential for

simultaneous exploitation of the two sensors in an operational context. Statistical and probabilistic approaches have been introduced in the literature to estimate crop biophysical variables from SAR imagery. Mascolo et al. (2016) present an algorithm for classification of crop stage (phenology) in oats, barley, wheat and corn from quad-PolSAR RADARSAT-2 data. Rather than using a polarimetric decomposition, the algorithm computes the Wishart distance between training and test pixel covariance matrices in order to classify the crop phenology. A procedure is introduced to select the covariance matrices that are used as training for each crop phenological stage. Then a threshold is applied to the computed distance to decide what training crop stage is the most similar to the observed in the SAR image. A novel paradigm was proposed by Vicente-Guijalba et al. (2014) and Vicente-Guijalba et al. (2015) which considers the crop development as a dynamic process and utilises a Bayesian Filtering Framework (BFF) for monitoring the crop development. In this case, it specifically uses an Extended Kalman Filter (EKF) to classify rice crop phenological stages. The methodology is then expanded by De Bernardis et al. (2014a) to replace the EKF with a Particle Filter (PF) and use the dynamic model for forecasting key dates, specifically, forecasting when the crop will be ready for harvest. Authors conclude that the PF provides better phenology estimation accuracy given that it is not restricted to model a crop state with normal distributions but with any arbitrary distribution. They also show that the proposed method can forecast harvest dates with errors between 5 and 10 days. The same methodology is further expanded to combine SAR data with optical data from the Landsat satellite in De Bernardis et al. (2016a). It is concluded that a data fusion approach increases the retrieval accuracy of phenology and is further enhanced if temperature measurements are considered alongside. A study by McNairn et al. (2018) uses a particle filtering for estimating canola phenology. In this case, the use of a phenology retrieval algorithm is justified since it is important for canola growers to timely detect when flowering is reached. This is since the moisture levels at this stage need to be controlled. This application considers fusion of C- and X-band SAR sensors (RADARSAT-2 and TerraSAR-X, respectively), however, forecasting is not approached.

The BFF algorithms are currently considered state of the art, since they are able to retrieve crop parameters accurately, integrate several active and passive sensors

as well as to nowcast and forecast the state of the biophysical variables.

1.5 Literature review concluding remarks

Although a significant amount of research has been devoted to understanding the interaction between SAR microwaves and croplands, most of the studies have focused on cereal crops and rice fields. Accordingly, research on other crop types could expand and enhance our current knowledge. Similarly, the test sites involved in most of the research are located in developed countries, where the fields tend to be large and the land flat. This may not transfer easily to developing countries, dominated by growers with small farms, difficult geographical conditions and less ground truth available for experiments. Therefore, research in crops located in developing countries should be encouraged. An important part of this thesis is the use of PolSAR data for agricultural applications. A common challenge that researchers have when starting an application for retrieving crop variables, is selecting the appropriate PolSAR decomposition(s) to use. Options include: the Eigenvalue decomposition, Freeman-Durden, Yamaguchi, Tutzi or other bespoke model-based decompositions. Each one provides a different set of PolSAR observables conveying similar or complementary information. Moreover, the analysis and interpretation of the time series for all these features simultaneously can be challenging and prone to error. This hand-crafted analysis may not be appropriate for large scale applications. Therefore, methodologies to better analyse and interpret multiple time series of polarimetric features simultaneously, would benefit users looking to exploit multitemporal PolSAR data. Additionally, there is evidence from recent studies that the InSAR coherence may provide complementary information from backscatter intensities and PolSAR data. Based on this, and although not explored in this thesis, research exploiting InSAR coherence can be expected in the near future. PolInSAR and Tomographic SAR, on the other hand, are more restricted due to requirements of the SAR systems to have multiple observation baselines. These are still seen as pilot applications as part of airborne SAR campaigns, rather than large scale and operational monitoring systems from spaceborne SAR. Due to this limitation, these approaches are not considered in this work. In relation to the methods for inver-

sion or estimation of crop biophysical variables from SAR imagery, as mentioned in the previous subsection, the performance of the WCM model may suffer due to the simplifications assumed, numerical problems for model calibration and problems of transferability in space and time. Similarly, physical models derived from radiative transfer theory, along with requiring a strong theoretical foundation, face challenges regarding accuracy of the retrieved results. This is due to assumptions around the geometrical shapes used to model a canopy to solve the mathematical equations, and the computational cost to run the models. These represent barriers for wider adoption of this approach. Recent applications based on machine learning algorithms have shown promising results in terms of retrieval accuracy. These algorithms exploit regression or classification methods using random forests, support vector machines and/or neural networks. Although, these approaches can be highly accurate with the possibility of learning the non-linear mapping functions between SAR data and ground truth, some issues still remain unsolved. In particular, most methodologies reported so far do not consider the crop development as an evolving process monitored in real or near-real time. This applies to studies that estimate a crop biophysical variable without considering the preexisting information from previous predictions. Although in some cases this can still be accurate, it may be beneficial to include knowledge of the previous crop state when making a new prediction. Similarly, current approaches would need to design a separate subsystem for each SAR acquisition geometry and other sensors (e.g. optical sensors). An algorithm to harmonise the subsystems would be beneficial, but has not yet been designed. Despite a few recent methodologies attempting to address this, not considering the crop development as an evolving process presents a further limitation which still reduces accuracy of approaches. This limitation involves not being able to forecast the crop biophysical variables given the previous and current crop state. As this is a very informative characteristic, key to understanding when a growth stage will occur, or when a field will be ready for harvest, adding it to the retrieval algorithms is of strategic importance. The BFFs are considered to be state of the art. They consider the crop development as a dynamical process and use dynamic filtering techniques to monitor the crop. This provides the advantage of performing monitoring in near-real time, combining sensors and forecasting the dates of key

occurrences. Note however, that the freely available data offered by Sentinel-1 and complemented by Sentinel-2 has not yet been used within the BFFs frameworks. This is partly due to quad-polarimetric data being preferred in previous studies. Note also, that two of the key elements of the BFFs, namely the dynamic and observation models, have been designed in a crop and location specific manner, which makes the transferability of these methodologies to other applications difficult. In summary, despite significant efforts to improve techniques for retrieval of crop biophysical variables from SAR data, methodological issues remain and opportunities for enhancement are foreseen.

1.6 Thesis aims and contributions

As pressure in current food production systems increases, a synoptic and holistic solution is needed to worldwide challenges that include food security and reduction of green house gases from agricultural activities, while maximizing revenues from financial investments. Remote sensing constitutes a key technology to provide tools to mid and large-scale food producers, food traders, retailers, and agribusinesses in general, for informed decision making that promote sustainable and cost-effective crop management practices. SAR systems in particular, provide opportunities for large scale crop monitoring without interruption, due to the added ability to acquire images during day or night and under almost any weather conditions. An abundance of SAR data can be anticipated in the next 5 years with the launch of several international missions. Crucially, research on crop development monitoring with data from SAR satellites has not been as widely studied as data from passive systems and although significant amount of research has been devoted to understand the relationship between crop development and SAR imagery, applications to retrieve crop biophysical variables in near-real time have been less studied and as mentioned in the previous subsection, improvements can still be made. Consequently, the overall aim of this thesis is to contribute to current knowledge about the use of spaceborne SAR imagery for crop development monitoring and biophysical variables retrieval. This is approached in this thesis by processing large multitemporal and polarimetric SAR datasets, interpreting SAR responses to crop growth, designing

novel methodologies for crop monitoring built on state of the art statistical and machine learning techniques, and using ground truth data for training and validation purposes.

An initial objective of the thesis is to understand the SAR response to crop development in both our test sites (see section 1.8). We achieve this in chapters 2 and 3 by interpreting time series of SAR backscatter intensity together with knowledge about the physiology of asparagus crops and field data related to management practices. This is similarly done in chapter 4 for rice fields, however, here we use multitemporal quad-polarimetric change detection instead of dual-polarimetric time series.

A second objective is to develop novel algorithms that allow monitoring crop biophysical variables for these crops as new SAR images are acquired by satellites and become available. In this regard, a multi-output random forest regression is proposed in chapter 2 to retrieve asparagus crop growth stage. In chapter 3, a Bayesian filtering algorithm is proposed to retrieve and to track below ground asparagus carbohydrates, and to estimate the crop age or the number of days since the season started. Multitemporal quad-pol change detection based on optimisation of the difference of covariance matrices is proposed in chapter 4 to monitor rice growth. A further step is taken in chapter 4, by using the same approach for crop type mapping, which is vital for crop inventories applications.

An additional specific objective that falls within the overall aim is for the proposed algorithms to be able to incorporate data from other sensors to work alongside SAR imagery. This is achieved in chapter 2 with the inclusion of temperature data and in chapter 3 with the incorporation of multi-spectral satellite data in a sensor fusion algorithm. In the latter, a modelling approach is taken for gap filling, which is a recurrent problem when working with multi-spectral sensors, and also allows for daily prediction of biophysical variables and for forecasting. The obtained results represent novel additions to the literature that contributes to our understanding and successful use of SAR imagery for agricultural fields monitoring.

1.7 Outline of thesis chapters

Chapter 2: Monitoring Agricultural Fields Using Sentinel-1 and Temperature Data in Peru: Case Study of Asparagus (*Asparagus officinalis*)

In this chapter, we investigate with an unprecedented level of detail, the response of the freely available Sentinel-1 satellite SAR data to the asparagus crop development in the north coast of Peru. We analyse how the time series of backscatter intensities changes due to the crop growth and management practices. We also consider several consecutive agricultural seasons to study the temperature effects on the crop growth and the potential for estimating the crop stage from SAR imagery and temperature using a Multiple-output machine learning model.

Chapter 3: Learning-based tracking of below ground asparagus carbohydrates and key dates estimation from fusion of sparse remote sensing observations

This chapter is built upon the understanding gained about the asparagus crop and the limitations identified in chapter 2. We propose the use of a Bayesian filtering framework, which was identified in the literature review as the current state of the art method for crop monitoring and sensor fusion. However, we propose to improve this methodology by using Gaussian processes to model the crop dynamics and the multitemporal satellite sensor response to crop growth. We then integrate these models into a Bayesian filtering framework which allows us to perform Sentinel-1 and Sentinel-2 sensor fusion in near-real time. This reduces the temporal resolution and enables the integration of complementary information derived from multi-spectral vegetation indices. Based on the model of the crop dynamics, we are also able to make daily predictions, even when no images are available (i.e., now-casting and gap filling), and to forecast asparagus below ground carbohydrates thus providing the ability to estimate the occurrence of future crop key dates.

Chapter 4: Multi-Temporal Polarimetric SAR (MT-PolSAR) Change Detection for Crop Monitoring And Crop Type Classification

In preparation for future constellations of satellites that will provide freely available Quad-PolSAR data, we propose a multi-temporal PolSAR change detection-based method for crop monitoring that builds upon recently proposed methodolo-

gies. We present an intuitive interpretation of the PolSAR response to the crop growth stage and monitor its changes over time as the crop develops. We validate the results obtained with the proposed method using field data from rice fields in Spain and several other crop types in the Indian head, Canada. This allows us to see how, under the proposed method, each crop type forms a unique signature which we then exploit to train neural network-based classifiers for crop type mapping.

1.8 Test sites and datasets

Three different locations were utilised in this thesis as shown in figure 1.13. The asparagus crops studied in chapters two and three are located in the north coast of Peru, near the city of Trujillo. The site was chosen as part of the EO4 cultivar project (https://www.envsys.co.uk/data-services/eo4cultivar/). This project, co-funded by the UK space agency and managed by Environment systems LTD (https://www.envsys.co.uk/), relies on a close international cooperation with local growers and food traders in Peru and Colombia. It aims at providing crop insights for informed decision making derived from freely available earth observation data in near-real time and at multiple scales (field level, regional and national scales). The EO4 cultivar project enabled close collaboration with farmers, including coordination of ground campaigns where field data is collected by local farmers and shared with different project stakeholders. The project also enabled direct communication with lead agronomists and visits to asparagus farms in May of 2019. For chapters two and three which focus on development of algorithms for asparagus monitoring, the Level-1 Sentinel-1 SAR analysis ready data provided by the Google Earth Engine platform (Gorelick et al., 2017) was used.

In chapter four, rice fields in the Isla Mayor town, near Seville, in the south of Spain were utilised to develop a multitemporal and quad-polarimetric change detection based method for monitoring the crop. The field data available for analysis was collected in 2014 and is accompanied by 16 quad-polarimetric images from the Single look complex (SLC) format of the RADARSAT-2 satellite in three different incidence angles. Similarly, field data collected during the AGRISAR 2009 campaign (team, 2009) in the Indian head, Canada, was utilised. This campaign was carried

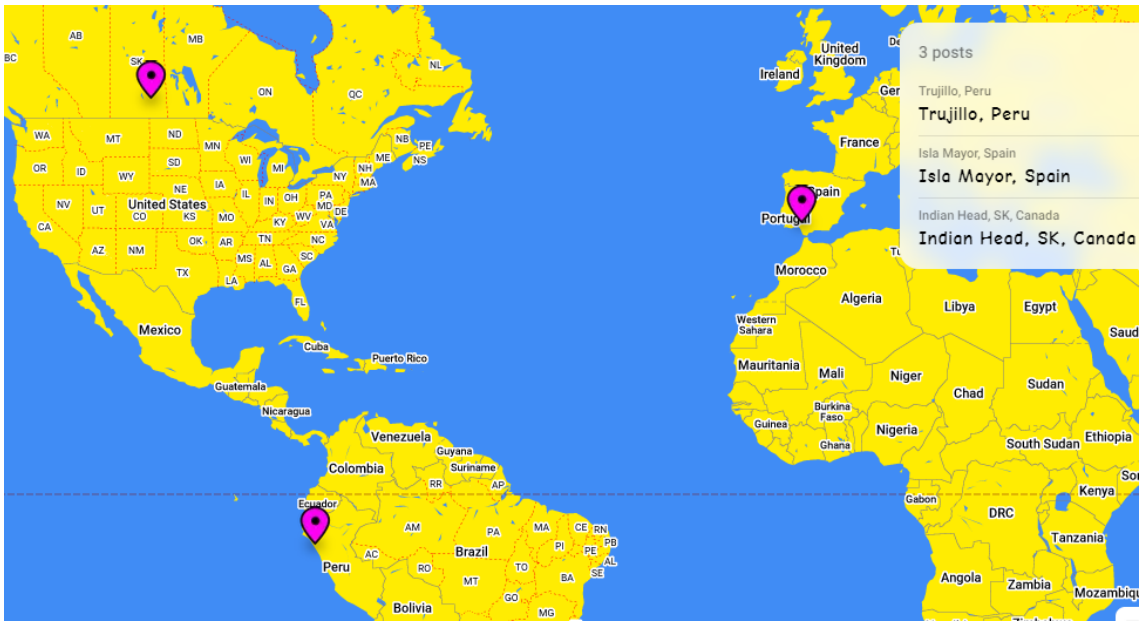

Figure 1.13: Location of test sites used in this thesis as follows: Trujillo, Peru, chapters two and three. Isla Mayor, Spain and Indian Head, Canada, in chapter four.

out using the C-band SAR data from RADARSAT-2 to demonstrate the potential for several monitoring applications, focusing mainly in agriculture. This demonstration was part of a series of studies to motivate the development of the C-band Sentinel-1 mission by the European Space Agency. This dataset, which included ground data and SLC RADARSAT-2 imagery, is used in chapter four to test a crop type mapping application including.

1.9 Publications

1.9.1 Peer-reviewed publications:

- Silva-Perez, C., Marino, A., & Cameron, I. (2021). Learning and near-real time monitoring of crop dynamics from noisy and sparse remote sensing observations (**In preparation JSTARS/TGRS**. Pre-print available upon request).

- Silva-Perez, C., Marino, A., Lopez-Sanchez, J. M., Cameron, I. (2021). Multi-Temporal Polarimetric SAR Change Detection for Crop Monitoring and Crop Type Classification. IEEE Journal of Selected Topics in Applied Earth Obser-

vations and Remote Sensing. https://doi.org/10.1109/JSTARS.2021.3130186

- Silva-Perez, C., Marino, A., & Cameron, I. (2020). Monitoring Agricultural Fields Using Sentinel-1 and Temperature Data in Peru: Case Study of Asparagus (Asparagus officinalis L.). Remote Sensing, 12(12), 1993. https://doi.org/10.3390/rs12121993

1.9.2 Conference proceedings and oral presentations:

- C. Silva, A. Marino and I. Cameron, "Using C-Band SAR and Temperature to Monitor Tropical Agricultural Fields," IGARSS 2020 - 2020 IEEE International Geoscience and Remote Sensing Symposium, Waikoloa, HI, USA, 2020, pp. 4894-4897, doi: 10.1109/IGARSS39084.2020.9324542.

- C. Silva, A. Marino, J. M. Lopez-Sanchez and I. Cameron, "Agricultural Fields Monitoring with Multi-Temporal Polarimetric SAR (MT-POLSAR) Change Detection," IGARSS 2020 - 2020 IEEE International Geoscience and Remote Sensing Symposium, Waikoloa, HI, USA, 2020, pp. 4554-4557, doi: 10.1109/IGARSS39084.2020.9324626.

- C. Silva, A. Marino, J. M. Lopez-Sanchez and I. Cameron, "Multi-temporal quad-Polarimetric change matrix for agricultural fields monitoring," POLINSAR 2019, 28 January—1 February 2019, ESA-ESRIN, Frascati (Rome), Italy: http://polinsar2019.esa.int/agenda/

- C. Silva, A. Marino, J. M. Lopez-Sanchez and I. Cameron, "Monitoring Agricultural Fields Using an Optimisation of the Difference of Covariance Matrices for PolSAR," IGARSS 2018 - 2018 IEEE International Geoscience and Remote Sensing Symposium, Valencia, 2018, pp. 6619-6622. doi: 10.1109/IGARSS.2018.8519267

Chapter 2

Monitoring Agricultural Fields Using Sentinel-1 and Temperature Data in Peru: Case Study of Asparagus (*Asparagus officinalis* L.)

This chapter presents the analysis and a methodology for monitoring asparagus crops from remote sensing observations in a tropical region, where the local climatological conditions allow farmers to grow two production cycles per year. To perform the analysis, the freely available dual-polarisation GRD data provided by the Sentinel-1 satellite were used together with temperature from a ground station and crop phenology ground truth from January to August of 2019. A multi-output machine learning regression algorithm was trained on a rich spatio-temporal dataset. Each output estimates the number of asparagus stems that are present in each of the pre-defined crop phenological stages. This analysis shows that particularly the VH polarisation can be used for monitoring the canopy formation, density and growth rate, revealing connections with temperature. Several scenarios to evaluate the importance of each input data source and features were tested. Results show that the methodology was able to retrieve the number of asparagus stems in each crop stage when using information about starting date and temperature as predictors

with coefficients of determination (R^2) between 0.84 and 0.86 and root mean squared error (RMSE) between 2.9 and 2.7. For the multitemporal SAR scenario, results showed a maximum R^2 of 0.87 when using up to 5 images as input and an RMSE that maintains approximately the same values as the number of images increased. This suggests that under the conditions considered, the use of multitemporal SAR data only improved mildly the retrieval when the season start date and accumulated temperature are used to complement the backscatter.

2.1 Introduction

Due to the recent and future growth of freely available satellite remote sensing data, there is an opportunity to implement near real time agricultural monitoring systems to increase yield and crop management efficiency. This is based on informed decision making with information derived fully or partially from satellite sensors.

Such a system is particularly important in tropical regions which highly contribute to the global food production but for many crops with considerably lower yields per hectare compared with temperate regions (West et al., 2010). It is also essential given the necessity in the tropics to preserve natural ecosystems by increasing yield in existing crop areas rather than transforming tropical forests to low yield croplands (West et al., 2010). A distinctive operational characteristic in tropical and subtropical regions for several crop types is the uninterrupted production cycles, with cultivation of more than one cycle per year. Each of these production cycles or campaigns may be under slightly different meteorological conditions due to a "soft seasonality", e.g., mild winters, thus modifying to a certain extent the crop growth rate and structure. This leads to the different responses captured by the satellites at each campaign. This chapter considers the above-mentioned conditions for agricultural monitoring, particularly analysing the case of asparagus crops in Peru. *Asparagus officinalis* L. is a key crop for the country's agricultural exports, being the largest exporter in the world, the second largest producer after China (Food & agriculture organization of the united Nations, FAO 2019) and an important source of job (Terán-Velazco, 2017).

In this context, crop phenology has been used as a tool to measure crop status

at any given time during the cultivation period and to measure the development rate relative to previous campaigns or relative to neighbour plots (Hodges, 1990). Accordingly, monitoring phenological evolution and accurately knowing crop status and development rate, the farmers can strategically plan the management.

Given the importance of monitoring phenology during the campaign without interruptions, synthetic aperture radar (SAR) emerges as a potential technology for this task. The capabilities to acquire images at day and night and under nearly all-weather conditions of SAR satellites offer significant opportunities for systematic monitoring regardless of cloud coverage (Lee & Pottier, 2009). On the other hand, to consider the impact of different climatological conditions on each campaign of a year, temperature records can be analysed to support the crop development monitoring.

2.1.1 Related Work

An initial step for crop monitoring from SAR data is to understand the time series evolution of the features derived from SAR imagery over time. To this end, biophysical crop variables collected in ground truth surveys are used as a reference for validation and for correlating measurements in the field with the SAR response. In the case of Quad-polarimetric data, multi-temporal polarimetric SAR (PolSAR) analysis is used to characterise a crop signature in terms of evolution of scattering mechanisms along the season identifying key moments (Alonso-Gonzalez et al., 2016; Lopez-Sanchez et al., 2014; Wiseman et al., 2014a).

Recently, more attention is being given to dual polarimetric systems given the free access to these data (Sentinel-1). Research to understand the interaction of Sentinel-1 signal response to crop evolution has been presented for several crop types. Researchers have reported the VH, VV backscatter and the ratio between the two polarisations to be sensitive to the development of different crop biophysical parameters (Harfenmeister et al., 2019a; Khabbazan et al., 2019a; Steele-Dunne et al., 2018; Veloso et al., 2017).

A common method to monitor crop development is to determine the crop growth stage when a new SAR image becomes available (De Bernardis et al., 2016b; Lopez-Sanchez et al., 2014; McNairn et al., 2018). In a general context, phenology is defined

as the observation of life cycle phases and their time of occurrence in plants and animals (Lieth, 2013; Meier, 1997; Schwartz et al., 2003). In the current context, crop phenology refers to the division of the crop development cycle into distinguishable growth phases (Schwartz et al., 2003) to be detected from SAR imagery. Accurate knowledge of crop phenology can aid farmers to plan timings for irrigation and applications of fertilisers and pesticides (Schwartz et al., 2003). This knowledge can also be used to make forecasts of crop development and harvest dates.

In order to retrieve crop phenology from SAR data, an initial step is usually to understand time series of SAR observables, and then use them as inputs to a statistical or a machine learning model. These models are trained with SAR and ground truth from past agricultural seasons such as in the works by Küçük et al. (2016) and H. Wang, Magagi, Goıta, et al. (2019). Other authors have proposed the use of distance measures to compare the covariance matrix of a given SAR resolution cell inside a parcel with a set of previously characterised covariance matrices that are associated with a phenological stage (Mascolo et al., 2016). The aim is to find the most similar predefined covariance matrix and assign the pixel under analysis, the crop stage with the most similar covariance matrix.

However, these approaches consider the phenology retrieval as a classification application, aiming at classifying the current parcel state as one of the previously defined pool of possible states (e.g., emergence, vegetative stage, maturation, etc.). This generates inconveniences selecting the appropriate boundaries for each stage in a process that may be subjective, often selecting ones (biasing) that the algorithm can actually identify. On the other hand, if standard phenological scales are used, such as the BBCH scale (Meier, 1997), the algorithm may not be able to disentangle every stage since the SAR response may not be sensitive to all these agronomic processes. Likewise, previous approaches ignore the fact that it is possible to have simultaneously more than a single stage in a parcel due to different plant growth rates and the fact that in the real evolution adjacent stages overlap (e.g., a parcel with some plants in flowering and some in fructification simultaneously). These approaches predict current phenology based on a single SAR image without considering the multi-temporal information. This leads for instance to stages at the beginning of the season being miss-classified by the model with final crop

stages as they may have similar SAR response, as occurred in (Küçük et al., 2016; Lopez-Sanchez, Ballester-Berman, & Hajnsek, 2011).

To overcome this, a hidden Markov model technique was proposed in (Cota et al., 2015; Siachalou et al., 2015) so that a prediction of the current stage is dependant on the previous stage, following a Markov property. However, the problem of subjectively selecting the boundaries for the crop stages still remains. Other authors have proposed a different approach whereby they consider the crop evolution as a time dependant dynamical process that follows a trajectory governed by the crop underlying dynamics (De Bernardis et al., 2016a; McNairn et al., 2018; Vicente-Guijalba et al., 2015). The aim of these methodologies is to retrieve the crop state in that trajectory when a new SAR image is analysed. However, these last methods have only been proven using polarimetric SAR data, which provides a much richer amount of information to characterise a target compared to the freely available data from Sentinel-1. Studies associated with the potential of space borne radar remote sensing concerning asparagus fields have been presented in (Arias et al., 2020; Bargiel et al., 2010; Sabour et al., 2008; Tavakkoli & Lohmann, 2006), although all of them focus on the crop type classification problem rather than in the analysis of individual crop stages as we present in this chapter. In (Sabour et al., 2008; Tavakkoli & Lohmann, 2006), C-band ENVISAR ASAR satellite data in VH and VV polarisations are used to identify land use of two agricultural regions, with asparagus being one of several crop types to identify. However, neither description of the crop stages nor the backscatter response over time is presented. In (Bargiel et al., 2010), time series of HH and VV polarisations of X-band data from TerraSAR-X satellite are reported. This study aims to evaluate the potential for classification of agricultural areas by analysing the crop signature of several crop types. Among them, 12 parcels of asparagus are studied and both the HH and the VV polarisations using X-band data are presented. The backscatter seems to increase during the period of vegetation growth, with a widespread distribution among the 12 parcels. This increase happens during the summer similar to several other crop types which was identified as an inconvenient to classify asparagus. This same effect was reported in (Tavakkoli & Lohmann, 2006), where asparagus response is particularly similar to sugar beet. In (Arias et al., 2020), among other 13 crop types, the multitemporal

response of asparagus was evaluated to use the crop signature for agricultural fields classification purposes using Sentinel-1 data. The authors report an increase of the VH backscatter during the periods of vegetation growth. Interestingly, the authors also report a more constant backscatter response during the whole cultivation period using the VV polarisation. This is aligned to what is presented in Section 2.2.6.1 of this chapter and in contrast to Bargiel et al. (2010) (although X-band data was used in this case). The authors, also report low accuracies for classifying asparagus due to similarities to summer crop types as reported in (Tavakkoli & Lohmann, 2006).

Crucially, none of the reported work in asparagus focuses on monitoring growth development or crop stages classification from SAR imagery. Also note that since the climatological conditions in Peru are different to those reported in the works by Tavakkoli and Lohmann (2006),Sabour et al. (2008), Bargiel et al. (2010) and Arias et al. (2020), direct comparisons are not straight forward. For instance, in (Arias et al., 2020), authors report that the agricultural season length is more than a year, which is significantly different from our test site (6 months average). Similarly, the crop signature is inherently different since the senescence periods for crops located in temperate regions are not present in our Peruvian test site.

2.1.2 Objectives of the Study

The main objectives of this chapter are the following:

1. To analyse the SAR response to the asparagus crop evolution.

2. To present examples of how the seasonal climatological conditions influence the crop development in the test site (tropical conditions).

3. To present the implementation of a data-driven methodology that captures the recurrent patterns in the SAR response and the temperature to provide an approximation of the crop development at every new SAR acquisition. It consists of a Multi-output machine learning regression algorithm in which each output estimates the number of asparagus stems that are present in each of the predefined phenological stages at a given date.

2.2 Materials and Methods

2.2.1 Asparagus Crop Development and Production Cycles

In this section, we briefly introduce the asparagus crop and the main phases of development. For a more detailed description of the asparagus growth and physiology the reader is directed to (Wien & Stützel, 2020; Wilson et al., 2005). Asparagus is a vegetable perennial crop which once is in a productive phase, re-emerges after harvest without the need to re-plant it. The cultivation process begins by transplanting to the fields the seedlings grown in a nursery. The roots system below ground, also known as the crown, and the fern above ground begin to grow and after approximately 2 years of development and establishment, the ferns are cut, the asparagus spears emerge and the crop is lightly harvested for the first time (Casas, 2004; Wilson et al., 2001).

After the first harvest, at the emergence crop stage, the next stems that emerge from the buds of the crown develop into a fern as shown in Figure 2.1. The asparagus stems grow vertically and will start producing the horizontal branches in a crop stage known as ramification. From this point, the cladophylls (leaf-like structures in the branches) will develop during the aperture stage. The aggregation of several consecutive individual asparagus stems that emerged from the root system, with their respective side branches and cladophylls compose the fern.

Subsequently, the fern thickens and covers the sandy soil intercepting light and beginning the production of carbohydrates which are sent down via translocation to replenish the roots system and be stored (Wilson et al., 2005). The fern development is followed by the short appearance of small yellow flowers and a maturation period, which corresponds to the longest crop stage. In total, each production cycle takes between four to five months before the crop is ready to be harvested.

During harvest, the spears that emerge from the buds are manually cut (harvested) when they reach approximately 20 cm of height. The root system produces new spears that are again harvested causing the depletion of the carbohydrates stored from previous seasons. The harvest is carried on until a minimum level of carbohydrates is reached in the root system to maintain the plant's healthy condition. At this point, the new asparagus stems are left to develop and grow again to

begin a new production cycle, in a life cycle that can last up to 15 years (Casas, 2004; Wilson et al., 2001). The crop stages in Figure 2.1 are the same stages that are recorded during the ground surveys and that are estimated in Section 2.2.7.

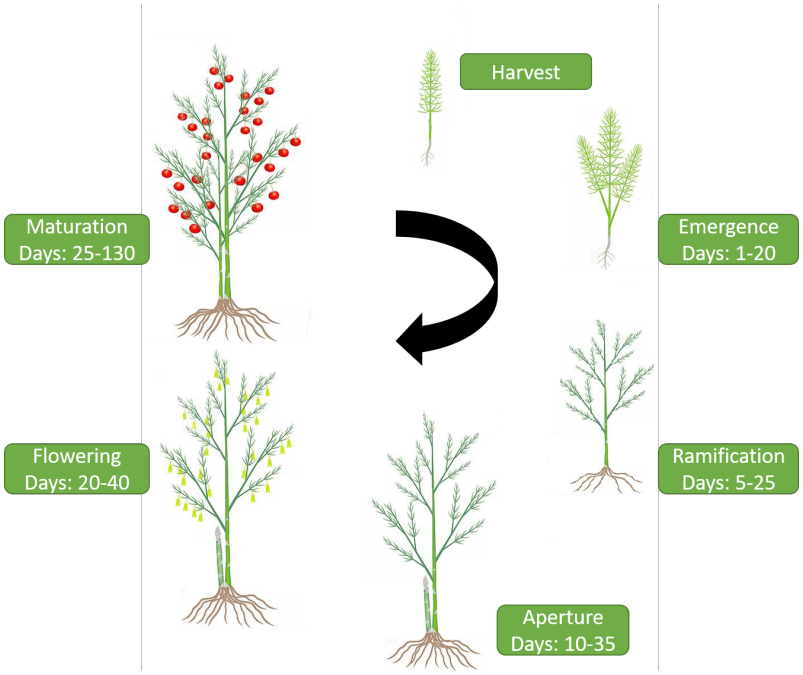

Figure 2.1: Asparagus crop growth and production cycles. Every season after harvest, new asparagus stems emerge to begin a new production cycle

2.2.2 Test Site

The asparagus fields (Figure 2.2) are located in the north of Peru in a dry coastal zone with sandy soil, divided in plots of an average of two hectares. We considered approximately 442 parcels in total, where timing and management practices such as starting and harvest dates as well as application of nutrients and pesticides among other activities, are performed simultaneously in groups of around four to six neighbouring parcels.

2.2.3 Climatological Conditions

The temperature and solar radiation present the maximum variability in the local test site, following the seasons of the southern hemisphere with a maximum peak of temperature around mid-February (summer) reaching up to 26 degrees Celsius and

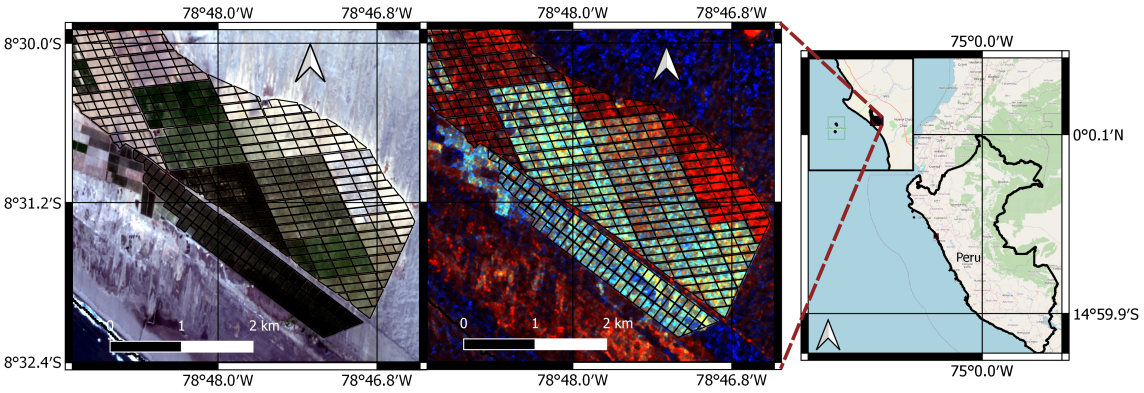

Figure 2.2: Test site. (**Left**): Sentinel 2 RGB image acquired the 29/09/2018. (**Center**): Sentinel-1 RGB image acquired the 30/09/2018. (**Right**): Location of test site in Peru

lowest values in August (winter) with temperatures of around 15 degrees (Figure 2.3).

Since the winter never reaches extremely low temperatures, the asparagus crop does not reach a dormant stage which permits growers to have two productive cycles per year. However, since the conditions along the year are not exactly the same, there may be a difference in the crop evolution of the same plot in two consecutive productive cycles, in response to these changing conditions. This is an important factor that will be analysed in Section 2.2.6.2.

The rainfall levels are extremely low given the desert conditions where the parcels are located with an average of less than 1 mm per month.

2.2.4 Ground Truth

As a part of the EO4 cultivar project (section 1.8), a survey campaign to collect asparagus phenological information was carried over a period of 8 months, from January to August of 2019, for 442 asparagus parcels. For each parcel evaluated, field surveyors randomly selected two transects to assess, with each transect being a metre in length. Within each transect the surveyors identified the phenological stage of each stem and counted the total number of stems in each stage present. Results for the two transects were averaged and recorded. In this way, the proportion of stems per parcel in any of the phenological stages identified in Figure 2.1 can be recorded, and a proxy for the evolution of crop stage over time can be established.

The average temporal evolution of asparagus stems in each crop stage is presented in Figure 2.4 for all the production cycles covered in the ground truth. Please note that after the asparagus stems have emerged from the ground, the total number of stems remains approximately the same throughout the season while the number of stems present at each stage changes as the crop develops.

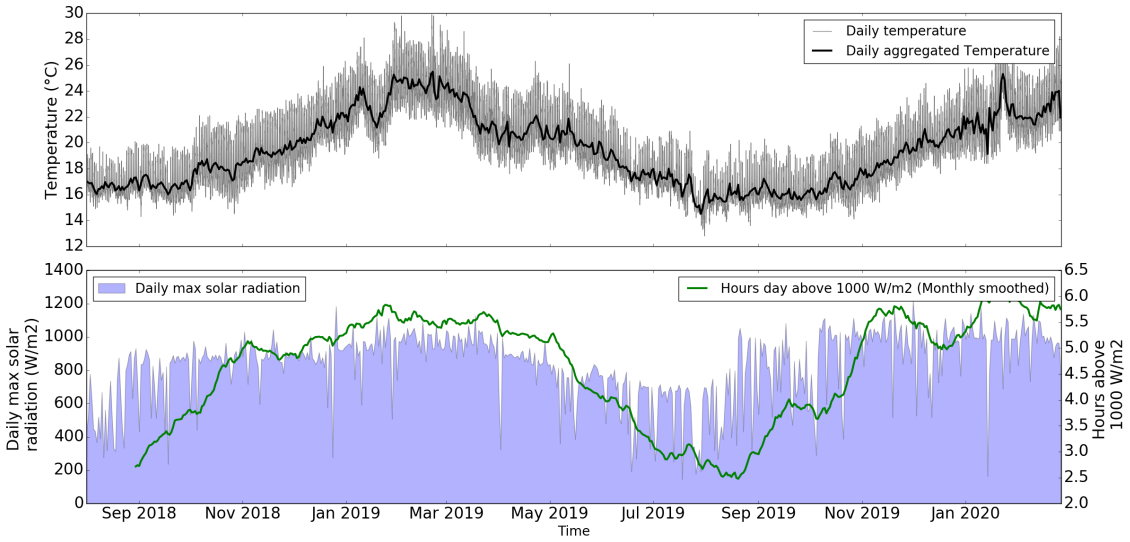

Figure 2.3: Average temperature and solar radiation in the test site. Chart generated from data collected by the farm's meteorological station.

An average of 36 surveys were performed per parcel during the eight months of the ground data collection, i.e, approximately one survey per week per parcel. However, given the complexity of the operation not all surveys were carried on systematically, e.g., exactly every week, but rather with irregular sampling. Also, note that given the climatological conditions as explained in the previous section, it is possible to grow up to two production cycles per year independently of the starting month and consequently the resulting surveys contain information to characterise multiple times an entire asparagus campaign or season. This enable us to create a rich spatio-temporal dataset to characterise the crop development.

2.2.5 SAR Datasets

The Sentinel-1 dataset used for the analysis was built using the Level-1 Ground Range Detected (GRD) and the Interferometric Wide swath (IW) acquisition mode, with VV and VH polarisation channels. The data was collected using the Google

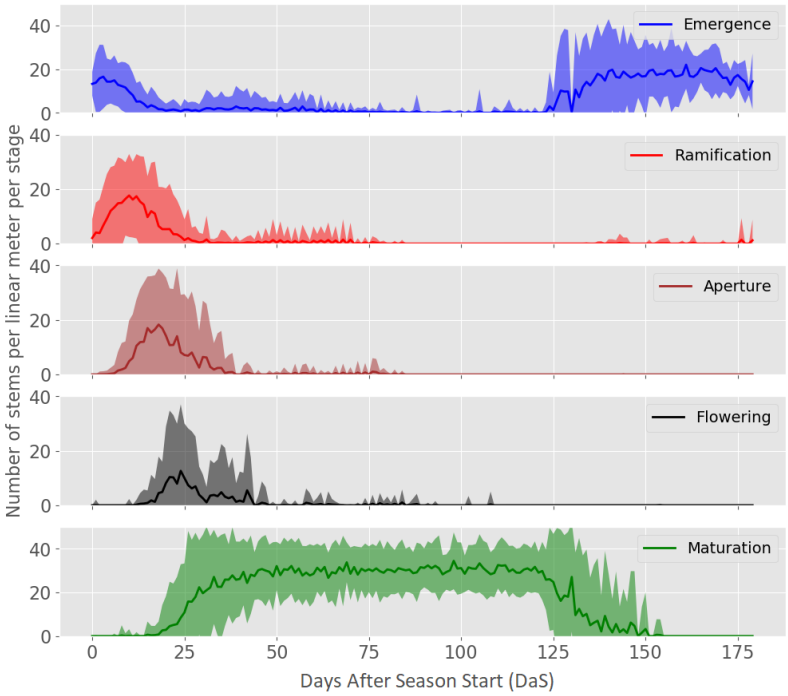

Figure 2.4: Number of asparagus stems in each of the crop stages. The solid lines represent the averages of all the ground measurements collected in 442 plots during the first 8 months of 2019. The shaded regions represent plus and minus 1.96 standard deviations.

Earth Engine (GEE) platform (Gorelick et al., 2017) in which the data pre-processing steps include applying orbit file, GRD border noise removal, thermal noise removal, Radiometric calibration and terrain correction. After obtaining the data from the GEE, a 3×3 boxcar averaging window was used as speckle filter.

Table 3.1 shows the three acquisition geometries available for the test site with the corresponding average incidence angles and acquisition times, including the orbit 142 in descending pass direction and the orbits 18 and 91 in ascending pass. Using the three available orbits the revisit frequency corresponds to between 3 and 5 days while it is 12 days using a single incidence angle. In order to analyse the long-term behaviour of the backscatter signal (e.g., seasonality), a time series of nearly two years was built from Sentinel-1 data over a typical parcel of asparagus where the ground truth is known and which includes four consecutive agricultural seasons. For the methodology to monitor asparagus development presented in Section 2.2.7 data from January to August of 2019 was used for the 442 plots when ground truth is available. Figure 2.5 shows the average temporal evolution of the backscatter for

Table 2.1: Sentinel-1 acquisition geometries available in the test site

Pass Direction	Relative Orbit	Inc. Angle	Acquisition Time
Descending	142	35	10:54
Ascending	18	31	23:34
Ascending	91	45	23:42

all the production cycles covered in the ground truth. The crop characteristics that cause the SAR observations in Figure 2.5 will be further explained in Section 2.2.6.1. Please note that the VH polarisation presents more significant changes through time and with less statistical variance than the VV polarisation as described in Section 2.2.6.1. Also note that after the day 125 there is a significant increase in the variance of the response. This is due to different cultivation period lengths as will be explained in Section 2.2.6.2. Figure 2.7 shows the VH backscatter profile with the corresponding ground truth of a typical asparagus parcel over time, covering 4 consecutive production cycles.

2.2.6 Methodology for Estimating Asparagus Stems Per Stage

To design the methodology of this chapter, three main steps are undertaken: (1) Understanding of Sentinel-1 signal interaction and sensitivity with the asparagus temporal evolution, (2) Analysis of the impact that the local climatological conditions, particularly the temperature, have over the canopy development and (3) the multi-output machine learning regression model training and use to estimate the number of asparagus stems in the phenological stages of Figure 2.1.

2.2.6.1 SAR Sensitivity to Crop Evolution

Due to the mild winters with minimum temperatures of around 16 degrees Celsius, the asparagus crop does not reach a dormant stage naturally and there is not a harvest time forced by the climatological conditions. This allows growers to plan the starting and ending dates of the season (occasionally for individual parcels) so

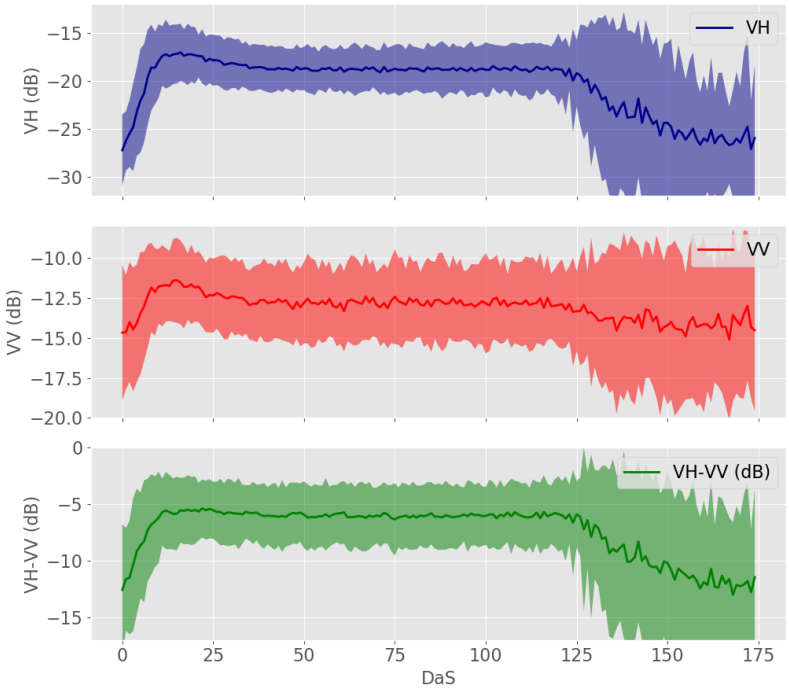

Figure 2.5: Sentinel-1 temporal backscatter evolution for the orbit 142. This chart shows the mean backscatter plus/minus two standard deviations of 442 parcels backscatter time series. The backscatter of each parcel is sorted by the DaS so that backscatter of all parcels can be combined.

that is possible to have more than one production cycles per year (normally two) and if required, adjust to the market needs and contractual planning. Given this, at a single SAR acquisition there are plots at almost all possible crop stages.

The photographs presented in Figure 2.6 were taken the same date as a SAR acquisition (28/05/2019). Based on this, it is possible to locate in the time series of each parcel where the picture was taken, what the SAR response to the crop is and compare it with the crop status recorded in the footage. Please note that all the images were taken the same date to parcels at different growth stages, a possibility enabled by the local climatological conditions. Since the parcels are at different crop stages, the backscatter is also different as shown in the VH polarisation time series of Figure 2.6, in which the lowest backscatter of the season is present during the harvest periods given that the fern has been mechanically removed and the new emerging spears are being harvested (Figure 2.6, images 1 and 2). At this point, the SAR signal interacts only with the soil presumably with a predominant surface scattering mechanism. For a description of the main SMs in crops please refer to

section 1.3.7).

The SAR response to these conditions has been shown to depend on the dielectric and geometric properties of the soil, e.g., surface moisture and roughness (Davidson et al., 2000; Oh et al., 1992). In the test site, the moisture is mainly dependant on the irrigation since the rainfall levels are extremely low given the desert conditions. On the other hand, the roughness is determined by the ridges and furrows created by the rows where the plants were sowed. In this case, the height of these rows, the plot age (the younger the crop, the more sand present), together with the row orientation and the incidence angle define the soil-SAR signal interaction. This effect is particularly evident with the VV polarisation (although not shown here).

Both polarisations, but particularly the VH polarisation increase significantly as the asparagus stems start emerging and vertically elongating up to two meters height. This increase may be a consequence of the double bounce created with the SAR signal reaching the soil and bouncing off the vertical spears back to the satellite (Figure 2.6, image 3), although a more detailed polarimetric analysis would be required to confirm it. Please note that as shown in Figure 2.5, the VV backscatter has less increment in time than the VH backscatter possibly due to the VH being more sensitive to the quasi-horizontal branches that grow sideways from the main vertical asparagus stems. A similar result was reported in (Arias et al., 2020) where authors present an almost constant VV response during the periods of vegetation growth.

However, when the crop reaches approximately the peak of the aperture stage (see Figure 2.7), the backscatter also reaches the peak in the entire cultivation period. At this point, the fern already has developed branches and the leaf-like structures in the stems are developing. From this moment, the contact of the SAR signal with the soil decreases thus also reducing the backscatter measured.

Subsequently, at the flowering stage (image 5 of Figure 2.6) the fern is fully developed and denser covering the soil and presumably creating a volume scattering response. The latter is less intense than the previous double bounce at the aperture stage since the SAR signal is radiated in several directions rather than being reflected back to the satellite, causing a decrease in the overall backscatter. Once the crop has reached the mature stage (images 6 to 8 of Figure 2.6), no significant changes happen in the biomass of the canopy hence the SAR signal remains at approximately

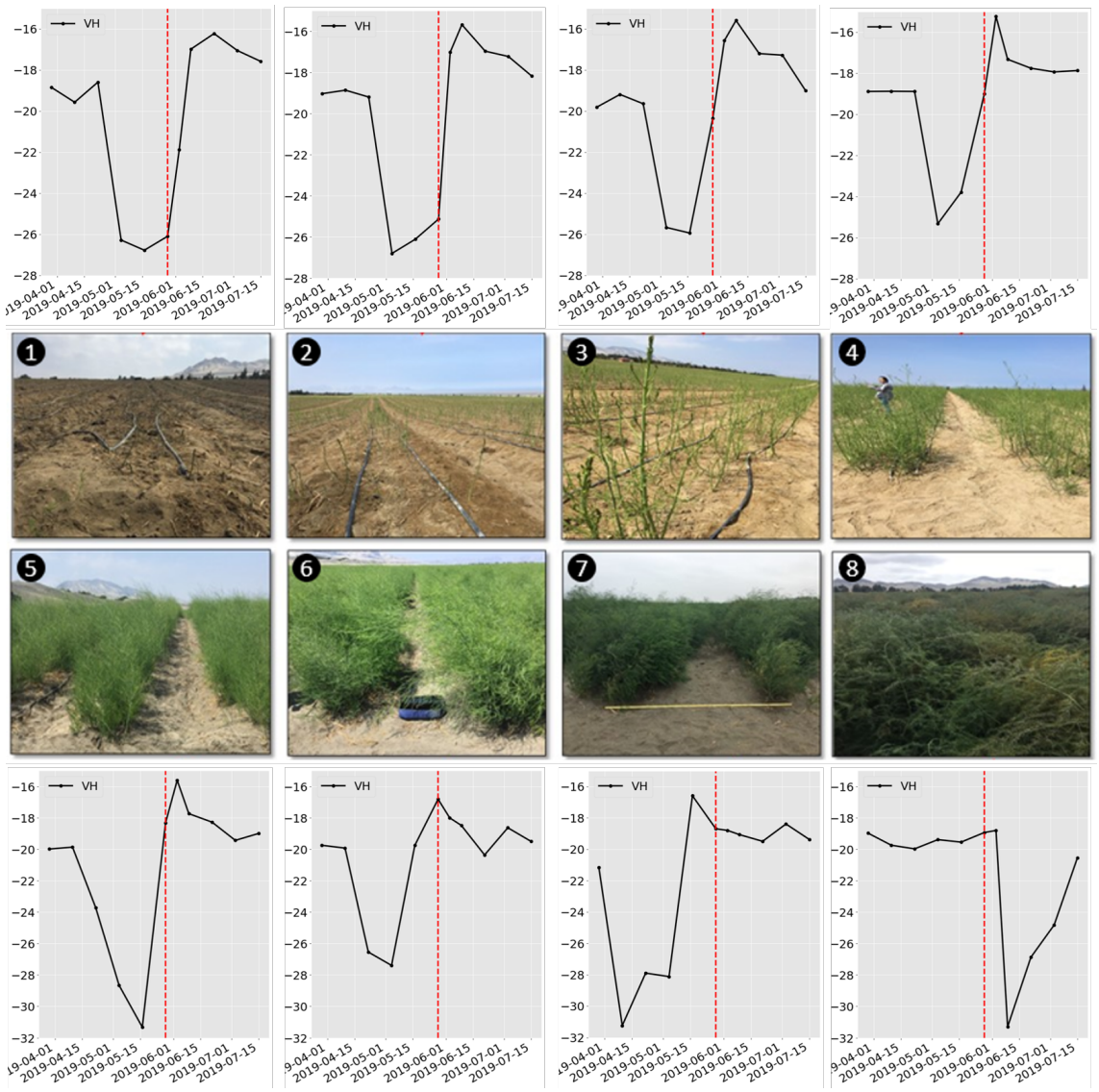

Figure 2.6: Images taken in the fields the 28/05/2019 (red vertical line) when a Sentinel-1 image was also acquired. The time series correspond to the VH backscatter for the orbit 142. Each pair of image and time series correspond to a different parcel. The parcels are at different growth stages taking advantage of the local climate.

the same level until the end of the season. An additional aspect to highlight is that as presented in Figure 2.4 and mentioned in Section 2.2.5, during the maturation stage the VV channel presents more statistical variation presumably since the VV backscatter still has an important contirbution coming from the soil as opposed to the VH backscatter which after the fern develops and stabilises, seems to have a strong contribution from the canopy and less from the soil. As a consequence,

the VV may capture features related to the soil, such as changes in moisture or roughness that are not captured by the VV polarisation.

2.2.6.2 Impact of Temperature on the Crop and the SAR Response

In this section, we analyse the impact of the seasonality and the variable climatological conditions on the crop evolution. This analysis is relevant to build a phenology retrieval algorithm since these factors change the crop behaviour and/or the SAR response in time thus modifying the inputs for an algorithm and affecting the accuracy results. Please note that in this analysis of effect of temperature, we have used the VH channel given that it is more sensitive to vegetation growth and canopy establishment than the VV polarisation as shown in figure 2.5 and reported for different crop canopies C.-a. Liu et al., 2019; Steele-Dunne et al., 2017a; Weiss et al., 2020b.

Based on empirical observations, growers have noticed that the crop evolution during a "winter" and a "summer" campaign in the same year are different, in terms of canopy volume and development rate, possibly due to the different climatological conditions. Similarly, previous research showed that temperature influences asparagus plant growth rates and may cause growth depression (Wilson et al., 1997; Yen, 1993). On the other hand, mechanistic models of asparagus shoots height have been developed as a function of the temperature (Wilson et al., 1997).

To investigate this effect in our test site using remotely sensed observations, time series of meteorological information, ground truth and SAR backscatter were analysed. Figure 2.7 shows the VH polarisation channel backscatter intensity with the corresponding phenology ground truth samples for a typical parcel during four consecutive campaigns.

The bottom plot of Figure 2.7 shows that the number of asparagus stems in maturation recorded during surveys are lower in the first semesters of 2018 and 2019 compared to the corresponding second semesters of the same years. Looking closely at the backscatter level for the same periods in the plot of the same figure, it is possible to see that the same pattern is followed in the time series of the VH polarisation once the crop has reached the maturation stage. This provides initial evidence of sensitivity of the SAR signal to the changes in the canopy volume (mea-

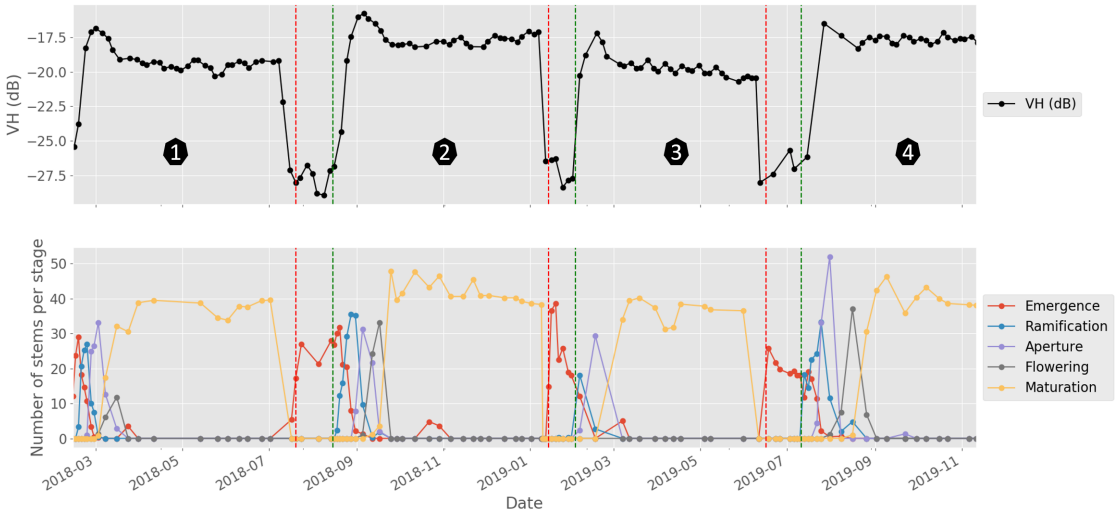

Figure 2.7: VH polarisation and ground truth observations for a typical parcel during four consecutive campaigns. Both the backscatter and the ground truth show a seasonal behaviour. The green and red vertical lines represent the start and end of the cultivation period respectively. The campaigns 1 and 3 correspond to summer season while the campaigns 2 and 4 represent winter campaigns.

sured as number of stems in maturation, which would represent the total number of stems in the parcel for this period).

On the other hand, the left side of Figure 2.8 shows the VH backscatter response for the same parcel, during the winter campaign (second semester of 2018) and the summer campaign (first semester of 2019) as a function of the number of days after the cultivation started (DaS). It is possible to see the difference in the growth rate at the beginning of the cultivation, where in the summer campaign (red line) the crop reaches the peak of the VH time series faster relative to this same point in the cold season (blue line).

In order to confirm that the temperature impacts the crop growth rate, a test was done using the temperature as independent variable instead of the number of days after the campaign start. A measure of daily accumulated heat has been previously used in the literature for this purpose. It considers an averaged measure of the daily maximum and minimum temperature to determine how much heat the crop receives in a day (Growing Degree Day - GDD) and how much it accumulates day after day during a period of time (McMaster & Wilhelm, 1997a). For the present study, 10 degrees Celsius was considered to be base temperature (Wilson et al.,

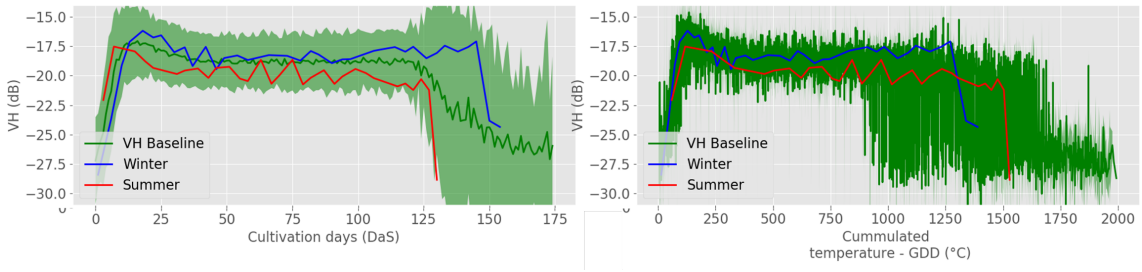

Figure 2.8: SAR backscatter of two consecutive campaigns aligned as function of cultivation days (DaS) and accumulated Growing Degree Days (GDD). The blue line corresponds to the campaign one that grew during the colder season ("winter") and red line corresponds to one in the warmer season ("summer"). The plots at the bottom show the cultivation period length measured as a function of time (**left**) and temperature (**right**).

2001). By accumulating GDD and using it as independent variable, the plot on the right side of Figure 2.8 shows that the VH backscatter observed for the winter and summer campaigns are approximately aligned. This suggests that the temperature drives the rate of canopy formation as suggested in other studies (Wilson et al., 1997; Yen, 1993), and that it is observable with the VH polarisation measurements. It also provides insights about the potential usefulness of the temperature as input feature to complement a remote sensing algorithm to retrieve canopy development and thus crop stage information.

The boxplot of Figure 2.9 presents the median accumulated temperature in all the campaigns registered in the ground truth, from the campaign start to harvest. It can be seen that depending on the month when the cultivation started, there is a seasonal trend in the accumulated temperature. This information is key to for example estimate the harvest date given the campaign starting month, based on the accumulated temperature.

To summarise, in principle there are three visible effects of the temperature on the crop. The first one, corresponds to the canopy volume developed, being less biomass during hotter temperatures. The SAR backscatter signal is sensitive to this by measuring lower backscatter intensity during the maturation period (Figure 2.7).

The second effect is associated with the growth rate, since as shown in the left side plot of Figure 2.8, it causes the stages at the beginning of the season to de-

velop faster in a warmer campaign (red line). This effect is also visible from the backscatter response. The third effect is related to the season length depending on the accumulated temperature during the cultivation period (Figure 2.9). This accumulated temperature in turn depends on the month of the year when the campaign started.

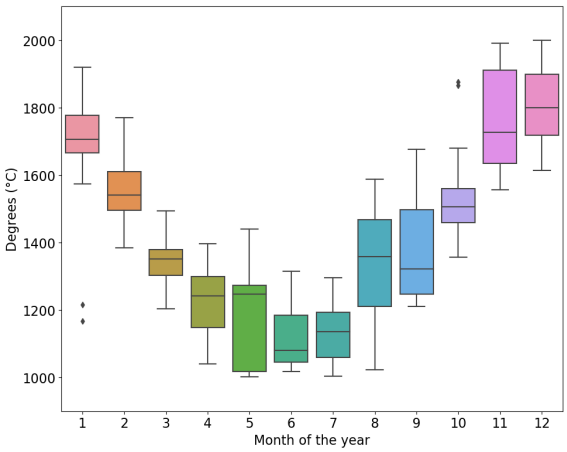

Figure 2.9: Campaign length measured in degrees Celsius (accumulated temperature) as a function of the production cycle starting month. As an example, if a campaign starts in January it normally accumulates around 600 degrees more than a campaign that starts in July. A total 442 campaigns were considered to generate this plot.

2.2.7 Estimation of Number of Asparagus Stems in Each Crop Stage

This section presents the methodology used for monitoring asparagus development as described by the number of asparagus stems in each of the stages of Figure 2.1. We use a data-driven model to estimate ground truth measurements from SAR image. Please note that a deterministic physical model inversion is an ill posed problem since the number of unknowns are greater than the number of independent SAR measurements (Liang, 2008; Oliver & Quegan, 2004b). However, we exploit the patterns and correlations found in the SAR observations and temperature together with the ground truth to build empirical models.

We consider the retrieving the number of asparagus stems as a regression problem since it is possible to avoid selecting crop stage boundaries and allow soft transition

between adjacent phenological stages. Please note that the ground truth used for training corresponding to phenological information is given by multiple and correlated variables (Figure 2.4). These variables do not evolve in time independently but rather they have temporal co-variation since they are produced by the same underlying process, i.e., the crop growth.

To exploit this structure in the output data, we use a multi-task or multi-output regression algorithm. It considers this interdependence of the individual outputs before making predictions. In this context, multitask learning (MTL) has been used in several applications precisely with this objective (Caruana, 1997; Ruder, 2017).

It is expected that not only the accuracy of a single multi-task learner increases compared to individual single-task learners (i.e., fitting an individual model for each output), but also since the model captures the structure of the data, it is able to generalize or interpolate better when the model is presented with unseen data (Caruana, 1997; Ruder, 2017).

In the remote sensing community multitask-learning has been previously implemented using different machine learning algorithms (Camps-Valls et al., 2018; Leiva-Murillo et al., 2013). Specifically for the case of SAR, in (Camps-Valls et al., 2018) the authors show how a multitask learner is able to make more accurately predictions of soil moisture and plant water content than individual learners.

2.2.7.1 Model Development

We chose initially a multi-task Random Forest Regressor (Segal & Xiao, 2011) from the available MTL algorithms due to its power for capturing both the non-linear relationships and the correlation between multiple outputs. A Random Forest Regressor (Breiman, 2001) is known as an ensemble algorithm in which several individual decision regression trees (n-estimator trees) are built from individual bootstrapped datasets (datasets in which the samples are randomly selected from the original training dataset) (R. W. Johnson, 2001). Each regression tree uses a random subset of the input feature variables (m-features) from the original number of input features, and from this subset an optimal feature with an associated threshold is selected for each node (Breiman et al., 1984). In the single output case of a regression decision tree, both the optimal feature and the node threshold (i.e., the threshold

that decides whether to go to the left or right child node) are found by minimizing a split function (also known as node cost) based on a euclidean distance error measure (Breiman et al., 1984). In the case of a multiple-output regression decision tree, an additional term is added to the node cost to account for the correlations in the output data. Specifically, in the framework proposed by (Segal & Xiao, 2011), a Mahalanobis distance (Mahalanobis, 1936) is added to the split function to consider the multiple dimensions in the output data in the minimization cost function to select the corresponding thresholds. Please note that other split functions have been developed (Kim, Lee, et al., 2003) but in this chapter the framework proposed in (Segal & Xiao, 2011) is used. A final estimation is obtained from the multi-task Random Forest Regressor by averaging the estimations provided by the leaf nodes in each individual tree in the forest.

In this chapter, the objective is to estimate the number of asparagus stems in each of five possible stages. Each of these five estimations corresponds to an output predicted by the multi-output random forest regression. On the other hand, the algorithm uses historical SAR, temperature and ground truth data to learn the corresponding mapping functions. For this purpose, the scenarios in Table 2.2 have been considered in this chapter.

2.2.7.2 Inputs

An initial category identified as category A, does not use remote sensing as input for the multi-task regression but only uses ground data. In the scenario A1 the number of days after the cultivation started (DaS) is used to estimate the number of asparagus stems present in each phenological stage at every image (Table 2.2), similar to how farmers traditionally execute their planning in the test site and in general for farms with low adoption of technology. Considering that multiple production cycles per year occur and grow under different climatological conditions, as shown in Figures 2.8 and 2.9, the day of the year (DoY) when the cultivation season starts impacts the canopy development. We tested the value of using this information as input for the algorithm, given that for instance, 20 days of cultivation in summer may differ from 20 days of cultivation in winter. This corresponds to the scenario (A2).

Table 2.2: Scenarios considered for asparagus growth estimation. Please note that each of the scenarios in B and C categories is tested using one image as well as sequence of multiple images.

Category	**Scenario**	**Input**	**Description**
A	A1	DaS	Only number of days after cultivation started.
A	A2	DaS, DoY	Days after cultivation started and, Day of year when cultivation started.
A	A3	DaS, DoY, GDD	Days after cultivation started and, Day of year when cultivation started and, accumulated temperature.
B	B1	VH	Only VH polarisation
B	B2	VH, VV, VH/VV	VH, VV polarisations and the VH/VV ratio
C	C1	VH, VV, VH/VV, DaS	VH, VV, Ratio, Days after cultivation started.
C	C2	VH, VV, VH/VV, DaS, DoY	VH, VV, Ratio, Days after cultivation started, Day of year when cultivation started.
C	C3	VH, VV, VH/VV, DaS, DoY, GDD	All previous features

A more robust scenario, the scenario A3, uses additionally the accumulated temperature during the cultivation period (from cultivation start to the SAR acquisition date) or accumulated growing degree-days, since as it was shown in Section 2.2.6.2, the temperature drives the growth rate and canopy volume. Several other methodologies have used GDD to account for the impact of climatic conditions in the crop growth (d'Andrimont et al., 2020; McNairn et al., 2018; Skakun et al., 2019). Please note that by using these input data sources the model learns the mapping function to give a theoretical estimation of the number of asparagus stems in each growth stage. This estimation may be accurate only if no external abnormal conditions

affect the crop, such as extreme weather events including droughts, hail, etc., plant diseases, pests or changes in the management practices. Similarly, it does not provide any spatial information of crop status but a single prediction for the entire field. Although this information may be valuable for planning, it is not sufficient for operational crop monitoring.

A remote sensing-based approach that uses SAR images was considered to be the second category (B), where the Sentinel-1 backscatter including VH and VV polarisation channels with their corresponding ratio was used. This was tested using a single image and a sequence of images, from two to five. In this case, the near-real time data acquired by the satellite provides the capabilities for operational monitoring. In this scenario the VH polarisation was tested individually as well as together with the VH and VV ratio (scenarios B1 and B2). This scenario only uses SAR data as input for the multi-output regression.

A third category (C), includes each of the previous data sources SAR, DaS, DoY, and GDD as input for the algorithm hoping to integrate their individual advantages (scenarios C1 to C3). Please note that the scenario C1 is included with the aim of quantifying the usefulness of the DaS feature when using multi-temporal SAR data and the scenario C2 quantifies the usefulness of the DoY feature.

2.2.7.3 Outputs

In all the scenarios, the aim is to produce estimates of the number of asparagus stems present in each of the following phenological stages: Emergence, ramification, aperture, flowering and maturation at any given SAR acquisition (same stages shown in Figure 2.1). Because in this case we require to simultaneously predict the multiple outputs, we chose the model described in Section 2.2.7.1. On the other hand, as described in Section 2.2.4, these values would correspond to measurements taken in a randomly selected linear meter within the parcel. Here we assume that the ground data collected in this way is representative of the entire parcel.

2.2.7.4 Training and Testing Data

The ground truth described in Section 2.2.4 collected between January and August 2019, Sentinel-1 data and temperature measurements from the same periods are

used to create the datasets. The dataset D takes the form $D = (X, y)$ where X is a matrix of dimension mxn, m is the number of ground truth measurements available, n is defined by the features being used according to each scenario of Table 2.2 and y is the matrix of ground truth data with dimension $mx5$, where the number 5 corresponds to the number of asparagus stems in each stage of Figure 2.1 recorded in the ground truth surveys.

In order to separate training and testing data, we randomly select plots based on their unique identifier tag. Then approximately 70% of plots are grouped in a training dataset and 30% in a testing dataset. This guarantees the unseen data required for the testing phase. In total, from the 442 plots (of 2 Ha on average) with available ground truth, approximately 309 plots randomly selected are used for training and the remaining 133 plots for testing. Given that the ground sampling is not performed every day, several ground truth measurement dates do not coincide with the Sentinel-1 acquisition dates. Consecuently, a three order spline interpolation was used to interpolate and obtain daily samples of ground truth so that an associated ground truth measurement can be obtained for every SAR observation. In total, there exist 4023 training data-points and 1739 testing data-points.

2.2.7.5 Model Hyper Parameters

Tuning of the optimal model hyper-parameters was done using 5-fold cross-validation with grid search. Table 2.3 presents the selected hyperparameters for the scenario C3.

Table 2.3: Selected model hyperparameters

Hyperparameter	Selected
Bootstrap	True
The number of trees in the forest	800 (a)
Split funciton	Mahalanobis Distance
max-depth	30 (a)

(a): Tunned hyper-parameter.

2.2.7.6 Accuracy Metrics

The coefficient of determination R^2 computed with Equation 2.1 (Krause et al., 2005; Pedregosa et al., 2021) was used to measure the model performance, both for the individual outputs and for the model as a whole, by averaging the scores of the five outputs.

$$R^2 = 1 - \frac{\Sigma_{i=1}^{n}\left(y_i - \widehat{y_i}\right)^2}{\Sigma_{i=1}^{n}\left(y_i - \widehat{y}\right)^2} \tag{2.1}$$

where y_i corresponds to the $i-th$ ground truth test sample, $\widehat{y_i}$ a prediction made with the model for this sample after training, and $\widehat{y}$ the mean value of the n-ground truth test samples.

Similarly, the root mean squared error RMSE calculated with Equation (2.2), was computed between predicted and testing values.

$$RMSE = \sqrt{\frac{1}{n}\Sigma_{i=1}^{n}\left(y_i - \widehat{y_i}\right)^2} \tag{2.2}$$

where y_i corresponds to the $i-th$ ground truth test sample, $\widehat{y_i}$ a prediction made with the model for this sample after training.

2.3 Results

2.3.1 Single SAR Image Results

The obtained results when using a single SAR image as input for the model are reported in Tables 2.4 and 2.5. When using one SAR image (see Table 2.4), particularly the scenarios A2, A3, C2 and C3 achieve satisfactory predictive capabilities with overall coefficients of determination R^2 between 0.84 and 0.89. This is confirmed with the RMSE's that are also the lowest for these scenarios.

Regarding individual outputs of the multi-task regression for these same scenarios, the maturation phase has the best performance achieving an R^2 of more than 0.9 in almost all of them and flowering the lowest accuracy between 0.70 and 0.8. Note from Figure 2.4 that comparing flowering to any other stage the temporal shape described in the ground truth by this measurement is more irregular and reaches on average fewer stems than the other stages. This could be due to an agronomic reason that requires further analysis or due to a systematic error affecting flowering

Table 2.4: Summary of coefficients of determination R^2 for the predicted number of stems in each crop stage when using a single SAR image.

Stage	**A1**	**A2**	**A3**	**B1**	**B2**	**C1**	**C2**	**C3**
Emergence	0.72	0.83	0.88	0.54	0.68	0.78	0.83	0.84
Aperture	0.65	0.9	0.92	0.04	0.27	0.71	0.87	0.9
Ramification	0.74	0.9	0.9	−0.22	0.11	0.81	0.9	0.9
Flowering	0.41	0.79	0.82	−0.36	−0.06	0.49	0.7	0.76
Maturation	0.79	0.91	0.94	0.36	0.52	0.82	0.89	0.9
Overall	0.66	0.87	0.89	0.07	0.3	0.72	0.84	0.86

when surveying the fields. This is also possibly the reason causing the predictions of asparagus stems in flowering less accurate than in the other stages.

On the other hand, the results of scenario C1 are substantially higher than the scenarios in category B. By providing to the regressor the number of days after the season started (DaS) as in scenario C1, the algorithm improves the retrieval with respect to category B potentially since it would be possible to disentangle similar backscatters at different dates.

An additional increase in R^2 (from 0.72 to 0.84) and reduction of RMSE (from 3.73 to 2.9) is achieved in the scenario C2 only by specifying the day of the year when the agricultural season starts. This feature indirectly provides information about the seasonality present in the test site and shown in Figures 2.7 and 2.8. The R^2 and RMSE are further improved and decreased respectively in the scenario C3 after the addition of the GDD feature, although not significantly. This low increase may be explained by considering that providing DoY (as in scenario C2) we already provide information about seasonality and given that as mentioned in Section 2.2.6.2, the impact of higher and lower accumulated temperature in the canopy is perceived by the VH backscatter as shown in Figures 2.7 and 2.8. Consequently, the algorithm indirectly receives information about the accumulated temperature through the use of VH and DoY. This is an important result as it implies that temperature from a ground station (as in scenario C2) may not be needed, without sacrificing

Table 2.5: Summary of root mean square error RMSE for the predicted number of stems in each crop stage when using a single SAR image.

Stage	**A1**	**A2**	**A3**	**B1**	**B2**	**C1**	**C2**	**C3**
Emergence	4.16	3.23	2.72	5.36	4.42	3.69	3.25	3.13
Aperture	3.18	1.67	1.54	5.26	4.61	2.87	1.96	1.66
Ramification	2.2	1.34	1.34	4.78	4.09	1.87	1.36	1.35
Flowering	2.91	1.74	1.61	4.43	3.92	2.71	2.08	1.85
Maturation	6.48	4.34	3.48	11.39	9.88	6.08	4.63	4.36
Overall	4.07	2.72	2.3	6.77	5.84	3.73	2.9	2.72

substantially the model performance.

Figure 2.10 summarises the model performance for the scenario C3. For this same scenario, Figure 2.11 shows the test and predicted data-points as a function of the days after the season started (using the cultivation days associated with the test data-points as x-axis). It can be seen that in general the predicted values (in red) follow the timing and the expected number of stems of the testing data-points (in blue). It is also possible to see however, that they are not exactly the same, indicating that although the model is accurately making predictions, it does not over fit to produce identical values as the testing points and does not predict extreme values that may correspond to outliers.

2.3.2 Multi-Temporal SAR Results

In order to quantify the performance of all the scenarios considered when using multiple Sentinel-1 images, we tested increasing the number of images to create the training time series, e.g., from only using the latest SAR image to using the 5 latest available images. In this case, the dataset $D = ([X_t, X_{t-1}, X_{t-2}, X_{t-3}, X_{t-4}], y_t)$ where t represents the index of the date when the ground truth was collected or in a prediction setting, when the prediction is desired. Figure 2.12 show the corresponding overall, R^2 scores and RMSE for each scenario of Table 2.2 when using from one to five Sentinel-1 images to estimate the number of asparagus stems in

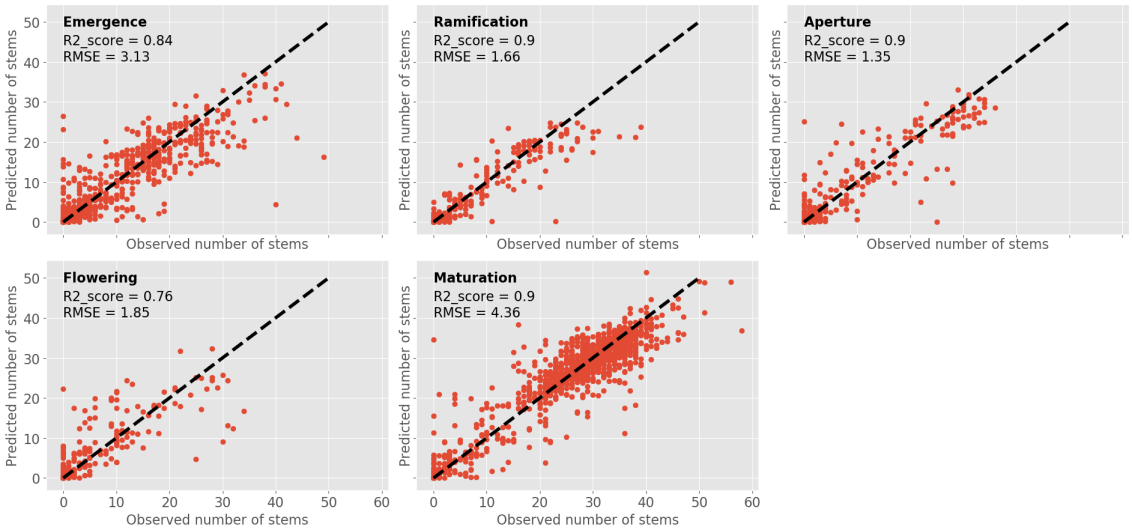

Figure 2.10: Observed vs Predicted number of asparagus stems per stage, with the corresponding overall coefficient of determination and root mean squared error, using features of scenario C3 to train the model .

each phenological stage. Please note that since the scenarios of the category A do not use Sentinel-1 data, we only consider the categories B and C for this part of the analysis.

In this case, the scenarios that use the VH, VV and ratio as features (B1 and B2), increase their performance when more images are used, with the scenario B2 achieving an R^2 of 0.66. This is not surprising since by using the sequence of the backscatter evolution provides additional information for the algorithm to disentangle similar backscatter present at different time of the season. An additional significant result obtained here is that no substantial improvement is achieved when more than 4 images are used.

However, all the other scenarios considered in this chapter do not increase the performance when increasing the number of images used as it would be expected, but rather maintain the same accuracy achieved when using a single SAR image, temperature and the start of the season information as input features. This may be due to the fact that the information provided by DaS, DoY and GDD is sufficient for helping to disentangle the backscatter of a single image and thus no further images are required for this purpose.

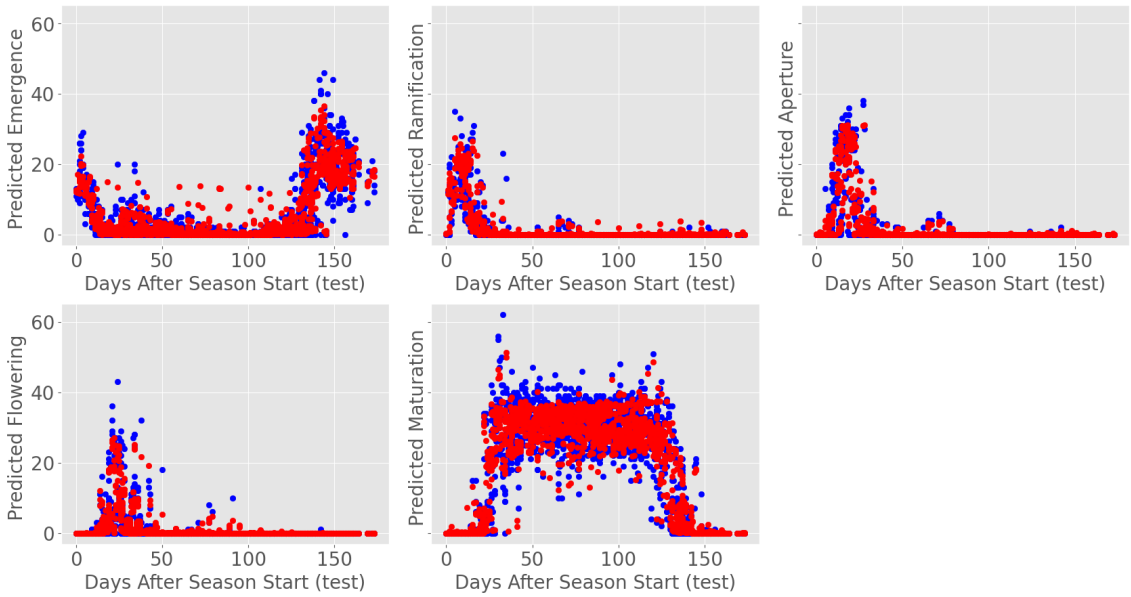

Figure 2.11: Predicted (red) vs test (blue) number of asparagus stems per stage, using the cultivation days associated with the testing data-points as x-axis.

2.3.3 Growth Stage Estimation Maps

Figure 2.13 shows for all the parcels in the test site, the estimation of asparagus stems present in each phenological stage, obtained using the trained multi-task random forest of the scenario C3, for the Sentinel-1 image acquired the 2018/10/12. This is the same acquisition date as in Figure 2.2 and the intermediate subplot of Figure 2.14, which in turn shows an RGB composite of the same information using the predicted asparagus stems in emergence in the blue channel, the predicted asparagus stems in maturation in the green channel and the sum of the predicted asparagus stems in ramification, aperture and flowering in the red channel (given their short duration).

Figure 2.14 shows additionally the RGB composites of 4 other Sentinel-1 acquisitions in order to visualise the change in time of the predicted crop stages due to crop development. This composite reveals the crop stage of each parcel in an intuitive and fast way while the number of asparagus stems predictions map of Figure 2.13 shows more detailed information for every individual crop stage.

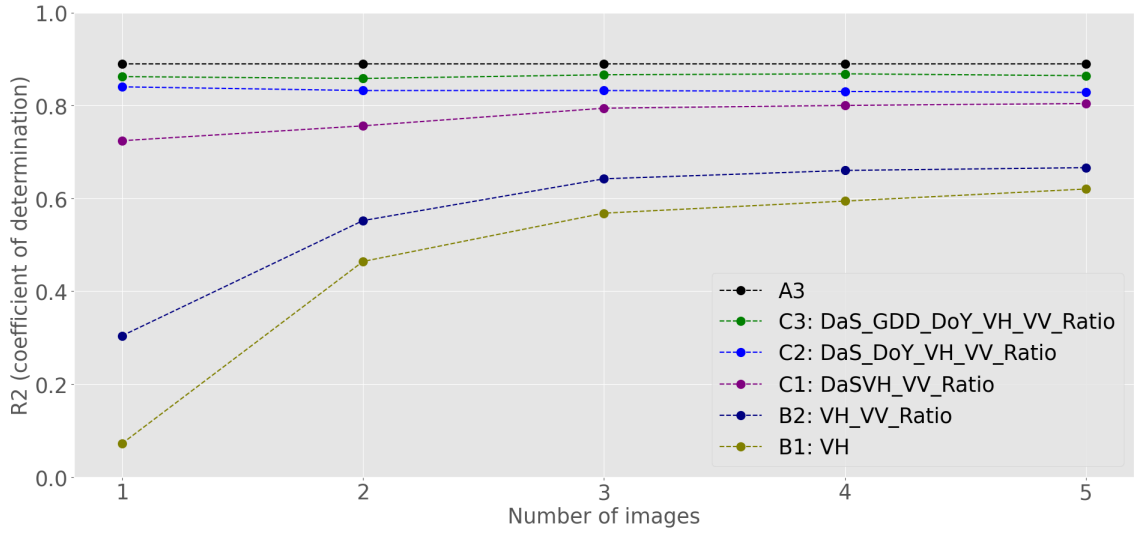

(**a**) Coefficient of determination ((R^2))

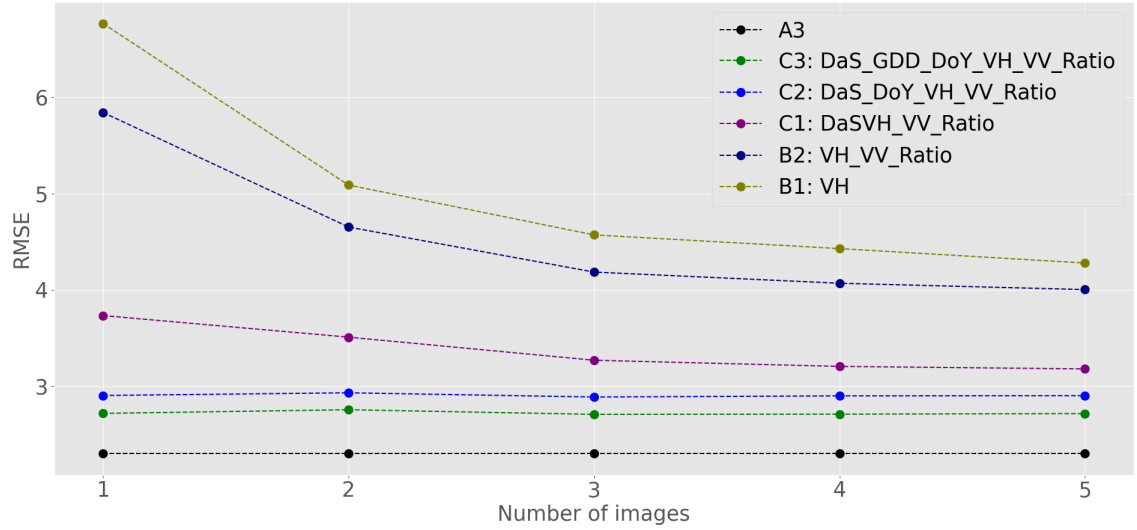

(**b**) Root mean square error (RMSE)

Figure 2.12: Multi-task regression performance metrics as a function of the number of images used to train the model for each of the scenarios of Table 2.2.

2.4 Discussion

We have provided the analysis of the SAR backscatter response to asparagus growth development and canopy formation as shown in Figure 2.4. Similarly, Figure 2.7 presents the seasonality effect both in the sensor response and the ground truth due to consecutive production cycles that grow under different meteorological conditions.

Figure 2.8 shows how the VH polarisation is used for crop monitoring in order to visualise the canopy growth rate, revealing that it is faster in summer than in

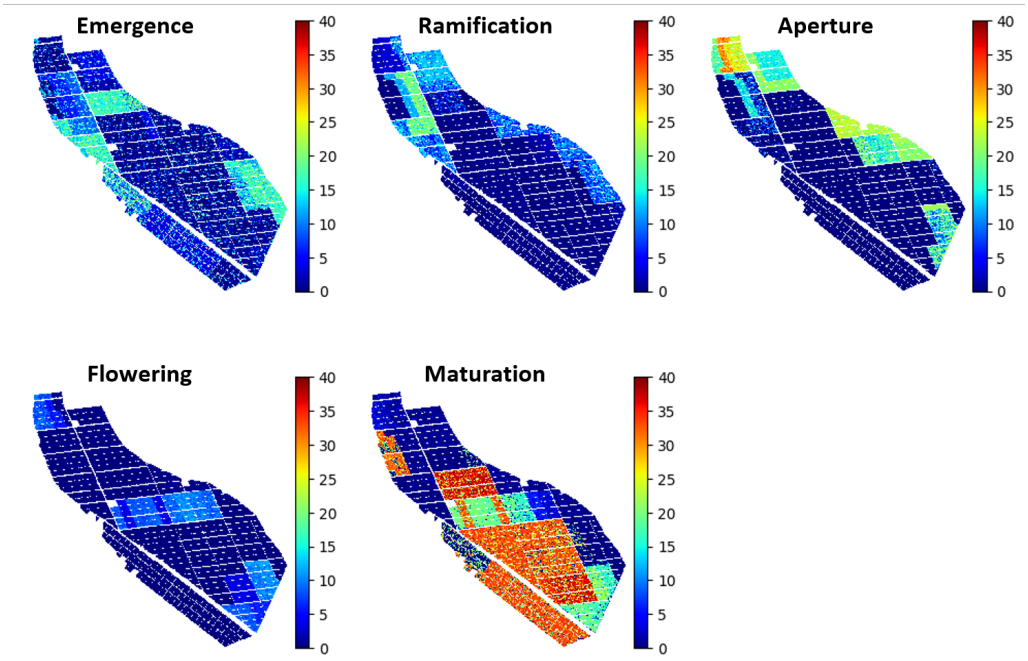

Figure 2.13: Number of asparagus stems estimated for each of the crop stages for the 2018/10/12 Sentinel-1 image (Same as Figure 2.2 and intermediate plot of Figure 2.14).

winter, but with less canopy volume (biomass). It also shows that although the production cycles in winter are longer, those cycles accumulate less temperature measured in GDD compared to the summer campaigns. Based on this information, the season length varies depending on the cycle starting month as shown in Figure 2.9. The backscatter response is sensitive to all these events as shown in Section 2.2.6.2.

With respect to the algorithm to retrieve the crop stage algorithm, several scenarios were considered in the analysis to understand the relevance of each data source and input feature and to determine the best way to combine the available information. The scenarios of category A, which do not include remote sensing data, show that using accumulated growing degree days improves the predicting capabilities of an algorithm given that temperature is an important factor driving the crop evolution. In fact, the scenario A3 provides the highest R^2-scores as well as the lowest RMSE's of the scenarios tested (0.89 and 2.3 respectively). This is aligned with the well known techniques to estimate the timing of phenological events using thermal calendars (Ahmad et al., 2017). However, this estimation may be accurate only if

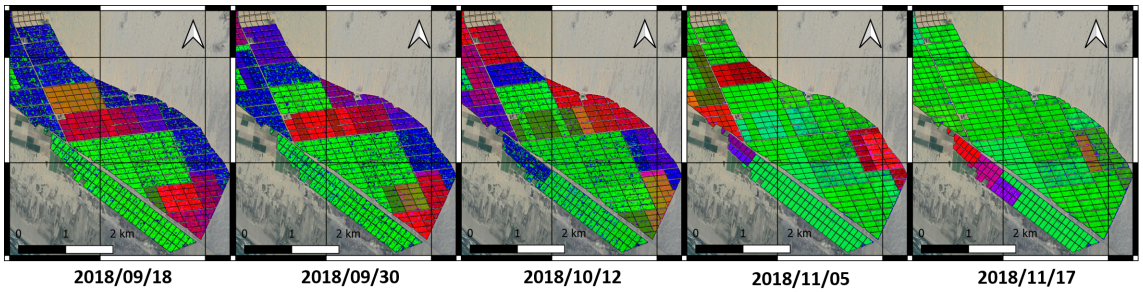

Figure 2.14: RGB composites of the estimated crop stage. Red: (Ramification+Aperture+flowering), Green: Maturation, Blue: Emergence.

no external anomalous conditions affect the crop, such as extreme weather events, diseases or changes in the management practices. Similarly, it does not provide pixel-wise spatial information of crop status as remote sensing can, but a single prediction for the entire field. In consequence, although this information may be valuable for planning, it is not sufficient for operational crop monitoring. With regards to the scenarios of category B (SAR only), although by using multiple images as input for a model the predictive capabilities improve significantly, it achieves poorer results than the categories A and C. The scenarios in category C which use all available input sources, achieve similar accuracy retrieving the number of asparagus stems in each phenological stage than the scenarios of category A (Tables 2.4 and 2.5). Note that in addition, these scenarios provide pixel-wise spatial resolution and the ability to determine growth anomalies. Focusing particularly in scenarios C2 and C3, while C3 performs better than C2 confirming the value of using temperature measurements, the difference in their performance is not significant. Considering that scenario C2 does not use temperature, it would reduce the hardware and software that the monitoring system requires, at the expense of some retrieval accuracy being lost.

Note that although results when using the K-nearest neighbour (KNN) algorithm and Support Vector Machines (SMV) were not reported, preliminary tests suggests that there is not a significant difference in accuracy when compared to the Random Forest used in this chapter. In this sense, pixel-based algorithms are not expected to improve significantly the R2 scores or reduce the RMSE. On the other hand, the use of a deep learning approach (i.e. semantic segmentation), which includes contextual information may improve performance. This will be further studied in future work.

With regards to the current literature available, although previous studies have considered the possibility of identifying asparagus from other crops using radar remote sensing data (Arias et al., 2020; Bargiel et al., 2010; Sabour et al., 2008; Tavakkoli & Lohmann, 2006), they did not focus on analysing the backscatter response relative the crop evolution due to the transition between phenological stages as was presented in Sections 2.2.6.1 and 2.2.6.2. Similarly, no previous study evaluated the possibility to retrieve the crop stage. In this context, the present study contributes to the literature with a more detailed analysis of asparagus providing an interpretation of backscatter evolution that may offer tools for better crop classification (since so far low accuracy have been reported (Arias et al., 2020; Tavakkoli & Lohmann, 2006)), through a better understanding of the temporal crop signature.

The VV backscatter throughout the agricultural season does not have significant changes relative to the VH polarisation channel. This has been previously reported in (Arias et al., 2020) and it differs from what was presented in (Bargiel et al., 2010) using TerraSAR-X. This suggest that X-band is able to capture events in the crop development not visible in C-band as happens for instance in rice fields (Lopez-Sanchez et al., 2014).

It is important to highlight that the current methodology is limited in part by the availability of the season starting date information as input, being used for calculating the GDD as well as input for the multitemporal regressor (DaS). A potential solution to this is the estimation of starting dates from remote sensing as it has been previously investigated with satisfactory results in (Boschetti et al., 2009; De Bernardis et al., 2014a; Mascolo et al., 2019; Ozer, 2003; Phan et al., 2018b; Tan et al., 2008). A further limitation in the current analysis is the lower accuracy of retrieving the number of asparagus stems in flowering, with respect to other stages such as emergence and maturation (Tables 2.4 and 2.5), which as mentioned in Section 2.3.1 might be caused by the unclear ground truth samples used to train the model. Statistical tests to better understand the characteristics of the training data and variations between measurements in each stage may be used to make decisions about better strategies to use the same data.

In order to scale up and transfer the methodology of this chapter to regional or national scale asparagus monitoring, it is necessary to understand if the asparagus

crop signature is maintained in other farms and regions or the country. Having the same crop signature would mean that the ground truth already collected is applicable to other locations and therefore the model trained can be used too. However, in case this signature is different, it is recommended to expand the current dataset by adding ground truth phenology samples of different test sites. Two additional factors that may impact on the use of the current model for asparagus phenology monitoring are the incidence angle that the satellites uses to observe the crop in different locations and crop orientation respect to the sensor line of sight. In this context, it is ideal and recommended as future work, to either normalise the SAR incidence angle for training and use of the normalised imagery to train the machine learning algorithms. A different approach could be to use a sensor fusion method in which each of the acquisition geometries (i.e. orbits) is considered as a different sensor.

Crucially, deploying a machine learning model for operational monitoring such as the multiple-output random forest used here, is not computationally expensive. This is because once the model has been trained, it can be loaded and used for phenology predictions almost instantly.

Based on all the limitations identified, future research will focus on the automatic detection of starting date from SAR and the use of quad-polarimetric data to better understand the scattering mechanisms throughout the season. Additionally, the use of better ways to deal with the sequential nature of data generated from agricultural fields and multitemporal remote sensing data will be considered including dynamical modelling (McNairn et al., 2018; Vicente-Guijalba et al., 2015) and more advanced machine learning models . A better way to deal with the inclusion of different SAR observation geometries should also be investigated.

2.5 Conclusions

In this chapter, an interpretation of the SAR backscatter response to asparagus crop growth was provided with an analysis of the impact that temperature has on the canopy volume, its development rate, and the cultivation length. It was shown that the VH backscatter is sensitive to all these effects. Then, a multi-output machine

learning regression algorithm was trained to retrieve the number of asparagus stems present in each of five possible phenological stages. Several operational scenarios were tested finding that the temperature and DoY when the season starts, provide the best predictive performance of crop phenology at a parcel level with an overall R2 of 0.89 and RMSE of 2.3. This is provided that no anomalies occur in the fields and no pixel-wise phenology estimation is required. This agrees with methods that employ well-known thermal calendars to estimate crop phenology (Ahmad et al., 2017). Using SAR remote sensing for near-real time, pixel-wise monitoring which include the VH, VV, VH/VV, and information about season start date (scenario C2), the model is able to retrieve the number of asparagus stems with an overall R2 of 0.84 and RMSE of 2.9. Adding the accumulated temperature (AGDD) as in the scenario C3, improved slightly the accuracy resulting in overall R2 of 0.86 and RMSE of 2.7. However, given that this increase is not substantial, the scenario C2 might be preferred since the temperature feature is not required and therefore this additional data source could be removed without losing significant model performance. Additionally, as shown in Figure 2.12, for the conditions evaluated in this paper, the use of multitemporal SAR data is not critical when using information about the season start date and temperature as crop stage predictors to complement the backscatter, since these features provide similar information for the algorithm to disentangle events in the temporal dimension

Chapter 3

Learning-based tracking of below ground asparagus carbohydrates and key dates estimation from fusion of freely available spaceborne SAR and optical data

3.1 Abstract

The yield of asparagus crops is highly associated with the amount of carbohydrates stored below ground in the plant's root system. This amount defines the crop capacity to grow asparagus spears during harvest and to establish a healthy canopy when the harvest ends (Wilson et al., 2001; Wilson et al., 2005). However, current methods for measuring carbohydrates in the fields require expensive and destructive sampling. In this paper, we propose a novel dynamic filtering framework which uses Gaussian Process based dynamic and observation models, an Unscented Kalman filter (GP-UKF) and fusion of freely available multitemporal Sentinel-1 and Sentinel-2 data to track the below ground carbohydrates, the season crop age and to forecast crop key dates. The proposed method complements state of the art filtering frameworks given its ability to learn the models and uncertainties from data and to exploit the temporal dimension of the remote sensing observations. This enables the method

proposed here to be transferable to other crop biophysical variables, crop types and locations. We validated the proposed filtering framework with ground truth data and found that the method can successfully track below ground carbohydrates, retrieve season crop age and forecast harvest. It was also found that the use of more than one Sentinel-1 acquisition geometries combined with Sentinel-2 data when available, provided the best tracking performances and a reliable system for handling missing data from an individual sensor. Under this configuration, the method achieves a Mean Absolute Error (MAE) of 1.802 brix degrees (i.e. a surrogate for carbohydrates). Similarly, it is able to retrieve crop age and forecast the date when a parcel will be fit for harvest, with MAE of 6 days. Tracking the below ground carbohydrates as proposed here, the method provides farmers the possibility to drastically reduce the amount of destructive sampling required in this high valued crop.

3.2 Introduction

In line with population growth, demand for agricultural commodities is also increasing. Technological tools to ensure sustainable management practices are key to reduce the negative impact on people and the environment (Shukla et al., 2019b). Thanks to its large area coverage and the growing availability of free data, satellite remote sensing has been increasingly used in recent decades for agricultural information extraction. These insights are then used to inform decision making by different stakeholders in the agricultural supply chain (C.-a. Liu et al., 2019; Steele-Dunne et al., 2017a; Weiss et al., 2020b). Agricultural fields monitoring with satellite-based Synthetic Aperture Radar (SAR) has gained substantial importance in recent years (C.-a. Liu et al., 2019). This is due to the ability of these sensors to acquire images under moderately adverse weather conditions, including the presence of clouds and irrespective of day light. Consequently, we can achieve a systematic acquisition system able to avoid data gaps and create consistent time series.

For the case of monitoring crop development with SAR, several methodologies have been reported in the literature. These include methods in which the SAR response to a given crop stage is manually analysed and insights are extracted based on expert knowledge (Lopez-Sanchez, Ballester-Berman, and Hajnsek, 2011; Phan

et al., 2018a). More recent methods use machine learning algorithms trained on ground truth and SAR data to create a mapping function between the SAR images and the crop stages (Küçük et al., 2016; H. Wang, Magagi, Goıta, et al., 2019). Wishart distance-based crop stage classifiers (Mascolo et al., 2016) have also been proposed with the aim of exploiting the Quad-Polarimetric SAR information of a resolution cell when available. However, these methods cannot be easily combined with other sensor technologies such as multispectral satellites and lack the ability to properly exploit the data's temporal dimension. Similarly, these methods lack the ability to model the crop dynamics to be able to hind-cast and forecast crop development.

To overcome these limitations, other studies proposed to retrieve crop biophysical variables as a problem of tracking the state of a dynamic system and used well established tracking algorithms such as Kalman filters and particle filters. An example of this method is presented by De Bernardis et al. (2016b) who perform sensor fusion by using TerraSAR-X backscatter in combination with Landsat-derived GNDVI to estimate rice phenology. The authors report successfully tracking phenology, however, the dynamic and observation models used within the filtering strategy are parametric models based on double logistic functions, which despite offering results for rice fields in a specific location, are not likely to be transferable to other biophysical variables, crop types or locations. Vicente-Guijalba et al. (2015) adopted another tracking application which avoids this issue by deriving the crop dynamic model from historical data. However, the authors in this case, do not provide a way to fuse multiple sensors, but only limit the application to the RADARSAT-2 satellite. Similarly, no forecast of key dates is attempted. De Bernardis et al. (2014b) presented a particle filter-based rice phenology tracking approach, which uses the same method to derive the required dynamic model from historical data, with the additional capabilities to forecast key dates. However, in this method they do not propose a straightforward way to utilise other sensors and the forecasting process may be computationally expensive.

McNairn et al. (2018) utilise a particle filter to track canola phenology. The algorithm fuses data from the RADARSAT-2 and TerraSAR-X satellites and temperature. In this case the attention is focused on the potential of the model of

predicting flowering, since it is a key point in this crop type to guarantee certain conditions of humidity and trigger other management practices. In this application however, the dynamic model is not derived from data, but it is assumed that the phenology can be estimated from the accumulated temperature in the year or in the agricultural season, measured in growing degree days (GDD) (McMaster and Wilhelm, 1997b). Under this assumption for the dynamic model, the framework works exclusively for phenology, but is not possible to use it for other crop biophysical variables. In this application, temperature is the most critical measured variable, more than the remote sensing observations to such an extent that if temperature is not measured, the algorithm cannot work. In addition, the authors do not present a way to forecast crop phenology as part of the tracking methodology, partly because the dynamic model which allows this capability is based on temperature rather than based on remote sensing observations. This is a well-known procedure in agriculture, using the so-called thermal calendars, however, here the capabilities of remote sensing are not exploited.

All the previously described methods for tracking the state of crop variables, use only one image to extract information about the crop development. Specifically, the vector of observations considers only features extracted from the latest image. While this might be enough when using quad-PolSAR data, which provides a richer set of information to characterise a target on the ground, it can be more challenging when utilising dual-polarimetric datasets. Additionally, given the strength of the SAR technology to systematically acquire images avoiding data gaps, the temporal dimension may offer additional advantages.

In this chapter, we propose a Gaussian Process-based, Unscented Kalman Filtering Framework (GP-UKF) that uses freely available multitemporal Sentinel-1 data and learns the non-linear and not parametric dynamic and observations models of the filter using Gaussian Processes (GPs) (Rasmussen, 2003). Learning these models and their predictive uncertainties allows the GP-UKF to be transferable to other crop variables, locations, and crop types. The framework also performs active-passive satellite sensor fusion, incorporating multitemporal Sentinel-2 data when available. The GP-based dynamic model is utilised to fill gaps due to missing remote sensing observations and to forecast the crop development. We present

an application for tracking below ground asparagus plants carbohydrates (highly related to the crop yield) and the seasonal crop age (also known as the Days After Season start – DaS). In addition, the forecasting capabilities of the GP-UKF framework are tested to determine when a field will be ready for harvest.

The remainder of the paper is organised as follows: Section 3.3 presents a brief introduction to the theoretical background required by the GP-UKF. Section 3.4 introduces the test site and ground and remote sensing datasets used in this study. Section 3.5 presents the results obtained tracking below ground asparagus plants carbohydrate and seasonal crop age and the results of forecasting when a field will be ready for harvest. The strengths and limitations of the current study are discussed in section 3.6 and the conclusions are presented in section 3.7.

3.3 Methodology

Crop development monitoring can be seen as a particular case of monitoring a dynamical system, in which the crop development is considered a time varying process observed through noisy and/or missing remote sensing observations (Vicente-Guijalba et al., 2015; Vicente-Guijalba, 2016). A set of D biophysical variables such as phenology, leaf area index (LAI), biomass (among others) is assumed to describe the crop condition at a given point in time. Specifically, the crop state can be described by knowing the state of these variables, which are in turn known as the state variables. Typically, and throughout this paper, the state variables are represented by the D-dimensional random vector x_k where k refers to the time step in which the system is.

This approach enables the use of widely known tools for dynamical systems state estimation by means of the well-known Bayesian filtering algorithms (Särkkä, 2013). The Kalman filter (Kalman, 1960) is the most used in practice, for example for systems with linear evolution in time and process states that are Gaussian distributed. For the concrete purpose of this paper, a filtering algorithm aims at tracking the crop state variables by fusing observations from freely available active-passive multitemporal satellite data sources and data-driven models of the crop state variable dynamics. As shown in figure 3.1, the filter does this by updating or modifying

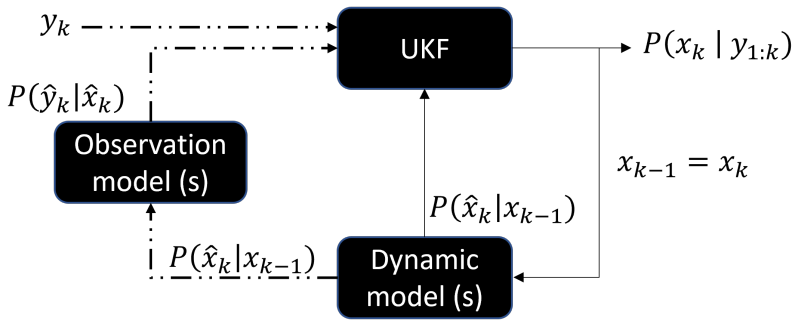

Figure 3.1: Schematic of a dynamic filtering algorithm to track the state variables. The filter (UKF) updates the dynamic model predictions based on deviations between observations and predicted observations. Dashed lines are optional paths executed only when a new vector of remote sensing observations y_k arrives (new image).

the predicted distribution from the dynamic models $P(x_k|x_{k-1})$, by a factor derived from the deviations between the vector of remote sensing observations received at time step k (y_k) and these same observations predicted given the dynamic model predictions $P(\hat{y}_k|\hat{x}_k)$.

The filter output $P(x_k|y_{1:k})$ is the state at time step k given all observations available up to time k. This is achieved by assuming that the Markovian property for estate estimation applies (Särkkä, 2013), or in other words, assuming that a future state only is dependent on the present state. Note however, that this is different from exploiting multitemporal data as will be shown in section 3.3.3.2. The difference between $\hat{x}_k$ and x_k is that $\hat{x}_k$ represents predictions from the dynamic model and x_k is the filter output, this is, the predictions after being updated by the filter. The same rationale applies for the vector of remote sensing observations y_k and the predictions of remote sensing observations $\hat{y}_k$ from the observation model. After a filter output, the previous state is updated to the current state ($x_{k-1} = x_k$), providing the filter with the ability to perform recursive state estimation. In figure 3.1, the dashed lines indicate that these paths are optional and are executed only when the vector of remote sensing observations y_k is available, this is, when a new image arrives. In this sense, if no remote sensing observations are available, the filter output corresponds directly to the dynamic model predictions. This enables estimation of the crop state variables between remote sensing images (nowcasting

and/or gap filling) and through recursive estimation, forecasting of the crop state variables.

Apart from the filter itself, two key components of the filtering algorithms are the dynamic and the observation models (Särkkä, 2013). The state variables evolution over time is modelled with a probabilistic dynamic model, represented by:

$$x_k = f(x_{k-1}) + q_k \tag{3.1}$$

In equation 3.1 the system state at a given date k can be estimated as a function of the previous state x_{k-1} using the non-linear function $f(.)$ and considering the additive Gaussian process noise $q_k \sim \mathcal{N}(0, Q_k)$ accounting for the uncertainty when modelling the system dynamics with the process noise covariance matrix Q_k. The non-linear function $f(.)$ describes the laws that govern the dynamic system evolution, which is a function deriving future states following from the current states. Also note that the dynamic model of equation 3.1 results in the conditional probability distribution $P(x_k|x_{k-1})$.

The observation model is in charge of modelling a sensor response to a given crop state and is represented by the E-dimensional vector of sensor observations y_k. The E dimensions in this case correspond to the number of features used to observe the crop state with sensors, which corresponds in this paper to backscatter indices derived from Sentinel-1 data and/or the vegetation indices from Sentinel-2 data. The sensor response y_k can be predicted as a function of the system state x_k by means of the probabilistic observation model:

$$y_k = g_{ith}(x_k) + r_k \tag{3.2}$$

Where $g_{ith}(.)$ is a non-linear function mapping from system state to remote sensing observations measured by the sensor ith, and $r_k \sim \mathcal{N}(0, R_k)$ is the additive Gaussian measurement noise accounting for the uncertainty around the predicted observations. Note that the probabilistic observation model of equation 3.2 results in the conditional probability distribution $P(y_k|x_k)$ describing the likelihood of getting the observations y_k given the state x_k. The under-script ith stresses the fact that there should be as many non-linear functions $g_{ith}(.)$ as sensors observing the crop development. This is to ensure the correct fusion of sensors.

3.3.1 Learning dynamic and observations models

Typically, the dynamic and observations models are represented by parametric models (i.e. equations) derived from having in depth knowledge of the forces driving the evolution of system states and the response of each of the satellite sensor to the system states (Särkkä, 2013). For crop monitoring, this is associated to knowledge regarding the dynamics of each state variable, for each individual crop type and under the specific conditions of each location. It requires identifying the adequate number of factors impacting the evolution of state variables over time and the complex relationship between them. Unfortunately, even if this process can be done for a test site, it is difficult and/or expensive to scale everywhere this may be needed. Given the large variety of variables (e.g. crop type, location, wavelength in the case of SAR measurements), models are very specific and not transferable to other crop types or locations.

Instead of using parametric models that may experience the above-mentioned issues, a Gaussian process regression (GPR) has been proposed in engineering applications with the so-called Gaussian process state space (GPSS) models to learn the transition and observation models from data (Deisenroth et al., 2013; Ko and Fox, 2009). A key advantage of using statistical modelling tools such as the GPR to learn these models, beside their non-parametric form and flexibility, is that they provide uncertainty with each predicted estimation. This is a vital requirement of the Bayesian filtering algorithms. In fact, it provides a state-dependant uncertainty, for instance with increased uncertainty in those regions where the variability increases or in those regions where insufficient data is used to train the models.

3.3.2 Gaussian process regression (GPR)

Given the importance of the GPR to learn dynamic and observations models, this section presents a basic introduction to its foundations. For an in-depth study of GPRs, the reader is referred to Rasmussen (2003). Note that in the literature, the X and y variables are normally used to denote, respectively, the inputs and outputs of a Gaussian Process regression. In this paper, however, since these variables are used for the system states and vector of observations, the training inputs for the GPR are

represented by the matrix $\boldsymbol{\chi}$ while the outputs are represented by the vector $\underline{\psi}$. In this context, given a set of inputs $\boldsymbol{\chi} = [\underline{d}_1, \underline{d}_2, \ldots, \underline{d}_n]^T$ where $\underline{d}_i$ is a D-dimensional input vector example and a set of outputs $\underline{\psi} = [\psi_1, \psi_2, \ldots, \psi_n]^T$ with ψ_i being the corresponding scalar output, a GPR considers the following non-parametric model for regression:

$$\psi_i = h(d_i) + \varepsilon \tag{3.3}$$

where h represents the unknown mapping function between d_i and ψ_i and $\varepsilon \sim \mathcal{N}(0, \sigma_n^2)$ corresponds to the additive noise model with variance σ_n^2 assumed to be corrupting the observed values. Rather than using a parametric model and estimating its parameters from the data in order to obtain a regression function, $h(.)$ is assumed to be a Gaussian process (i.e. a Gaussian distribution over functions) (Rasmussen, 2003). A Gaussian process (GP) is fully specified by a mean function $m(.)$ and a positive semidefinite covariance function $K(.)$ (also known as the kernel). The covariance function determines the key characteristics that the mean function takes, such as smoothness, periodicity, etc, and is chosen depending on the modelling problem at hand (Rasmussen, 2003). In this paper, we consider the exponentiated quadratic kernel $k(\underline{d}_i, \underline{d}_j)$:

$$k(\underline{d}_i, \underline{d}_j) = \sigma_f^2 exp(-\frac{1}{2}(\underline{d}_i - \underline{d}_j)^T \Lambda^2 (\underline{d}_i - \underline{d}_j)) \tag{3.4}$$

where Λ is a diagonal matrix of the length-scales hyperparameters, and σ_f^2 is the variance of the function h defined in equation 3.3. At a test point(s) $\underline{d}_*$ evaluated with the model $h(.)$, the GP estimates an output ψ_* with mean and variance using the predictive equations 3.5 and 3.6 respectively, shown below. These equations are derived from the conditional distribution of the test points $\underline{d}_*$, given the observed values $\boldsymbol{\chi}$ and $\underline{\psi}$. The reader is directed to (Rasmussen, 2003) for the complete derivation:

$$m_h(\underline{d}_*) = GP_\mu = k_*^T (K + \sigma_n^2 I)^{-1} \underline{\psi} = k_*^T \boldsymbol{\beta} \tag{3.5}$$

$$\sigma_h^2(\psi_*) = GP_{var} = k_{**} - k_*^T (K + \sigma_n^2 I)^{-1} k_* \tag{3.6}$$

In equations 3.5 and 3.6, the term $k_* = k(\boldsymbol{\chi}, \underline{d}_*)$ is a vector defined by kernel values between the inputs $\boldsymbol{\chi}$ and test point(s) $\underline{d}_*$, $K = k(\underline{d}_i; \underline{d}_j)$ is the $n \times n$ kernel matrix of the training input values, and $k_{**} := k(\underline{d}_*; \underline{d}_*)$ is the kernel function evaluated at the test points $\underline{d}_*$. In equation 3.5, $\boldsymbol{\beta}$ is often used in the literature to shorten

the equation, with $\boldsymbol{\beta} := (K + \sigma_n^2 I)^{-1}\underline{\psi}$. The length scale hyperparameters Λ and the variance σ_n^2 in the kernel function are learned by maximizing the log marginal likelihood of the training outputs given the inputs (Rasmussen, 2003).

3.3.3 Training dynamic and observation models

This section explains how the crop dynamic model and the crop observation models can be learned with Gaussian process regressions. GPRs are particularly suited for this task since not only they provide model predictions but also the uncertainty associated with the predictions. This is in turn a key requirement in Bayesian filtering algorithms as will be introduced in section 3.3.4.

3.3.3.1 Training the dynamic model

Within a filtering framework, the purpose of the dynamic model is to advance the state of the system one step at a time. This can also be seen as a one step-ahead state forecast given the current state. The dynamic model must predict the conditional distribution $P(x_k|x_{k-1})$ corresponding to the prediction of the current state given the previous state, because at all times the state is represented by a probability distribution. In this paper we use Gaussian processes to obtain the prediction of this probability distribution. The output of the GPR is a Gaussian distribution thus, $P(x_k|x_{k-1}) \sim \mathcal{N}(x_k|\mu_k, \Sigma_k)$. Training of the dynamic model is achieved in two steps: First we obtain the typical state variables behaviour over time and secondly, we learn to predict a state distribution at time step k given the state distribution at step $k-1$.

In order to estimate a typical state variable behaviour over time, we collect a training set of ground truth samples from several agricultural seasons, either several parcels or more than one season of the same parcel (i.e. for perennial crops). Then we fit a non-linear, non-parametric GPR using this set as output and using the crop age or Days after the season started (DaS) as input. This also allows us to gain insight about the process that we are monitoring as will be presented in section 3.5.2.1. Once the typical evolution is obtained, the key role of the dynamic model is to predict a state distribution at step k given the state distribution at time step $k-1$. In this paper, we propose to do this by training a second GPR model that

learns to predict the expected change to the current state in order to advance to a subsequent state following the typical dynamics previously obtained. To train this model a dataset of the form $D_{dyn} = [x_{k-1}, (x_k - x_{k-1})]$ is required, where the input x_{k-1} corresponds to the expected value of the crop state variables at time step $k-1$, and the output expression $(x_k - x_{k-1})$ is the expected change to advance to a subsequent state. The conditional probability distribution $P(x_k|x_{k-1})$ can be obtained as:

$$\begin{aligned} P(x_k|x_{k-1}) &\sim \mathcal{N}(\mu_k, \Sigma_k) \\ \mu_k &= \mu_{k-1} + \Delta\mu \\ \mu_k &= \mu_{k-1} + GP_\mu([\mu_{k-1}], D_{dyn}) \\ \Sigma_k &= GP_{var}([\mu_{k-1}], D_{dyn}) \end{aligned} \tag{3.7}$$

where GP_μ and GP_{var} corresponds to the prediction obtained from a Gaussian process model using the dataset D_{dyn} and the equations 3.5 and 3.6. Note that using this procedure results in a "one-step ahead" prediction. However, by recursively using equation 3.7, multiple steps ahead predictions can be obtained. This is a key property since it allows us to predict values of the state variables when no remote sensing observations are available (i.e., in a daily basis), allows us to fill gaps for instance for Sentinel-2 and/or to forecast the expected evolution of the state variables given the current states. An additional key property at this point is the ability to propagate uncertainty. This enables the model to convey the uncertainty associated with a prediction. For instance, increased uncertainty should be seen when interpolating between images or when performing multiple steps ahead forecasting (given the lack of remote sensing observations). This is done by considering the whole input distribution $P(x_{k-1}/y_{1:k-1})$ as input for the dynamic model as opposed to only its mean (mu_{k-1}). Note that the notation $1:k-1$ indicates indexes from 1 to $k-1$.

This property of the GPs with respect to uncertainty propagation has been studied in the literature (J. E. Johnson et al., 2019; McHutchon and Rasmussen, 2011). In this paper, the unscented transform (Julier and Uhlmann, 1997) is used to characterise the distribution $P(x_{k-1}|y1:k-1)$ using the so-called sigma points, and these points are propagated through the dynamic model. Then a weighted combination of the outputs obtained for each sigma point is performed to obtain

the propagation of the whole distribution through the dynamic model. A more detailed explanation of this is presented in section 3.3.4.

3.3.3.2 Training the observation models

As mentioned previously in this section, the observation model oversees modelling a sensor response to a given crop state (represented by the state variables). A GPR is trained to predict the conditional probability $P(y_k|x_k) \sim \mathcal{N}(y_k/\mu_k, \Sigma_k)$ of the remote sensing observations given the crop state at time step k. The remote sensing observations predicted by this model are the same remote sensing observations used to monitor the crop. In previous works, authors have reported the use of several features derived from backscatter and PolSAR decompositions of a single image (16 features in De Bernardis et al., 2014b and 12 features in McNairn et al., 2018 or more generally, p PolSAR features). In this paper, we propose to use the temporal dimension of the observations to compensate for the lack of Quad-PolSAR data. This way a vector of remote sensing observations contains a sequence of the last N past available images instead of the p PolSAR features of a single image. Considering a sequence of observations is in fact desired since it provides information of not only the crop state in a single date but in the period covered. In this sense, the observation model predicts the sequence of the past N observations available in a pre-defined period (e.g., the previous N-VH backscatter or N-GNDVI measurements available in the past 100 days) given the current crop state. It is important for the observation models to be able to predict the observations and their uncertainty for any arbitrary day in the past (within the pre-defined period). This way we do not constrain the model to predict exclusively every 6 or 12 days for the case of Sentinel-1 or 5 days for Sentinel-2. This is beneficial for optical Sentinel-2 data, where there may be gaps in the observations acquired in cloudy days resulting in irregular number of days between observations. To train this model a dataset of the form $D_{obs} = [(x_k^T, DaS_{k-j}), y_{k-j}]$ is required, where x_k^T in the input expression (x_k^T, DaS_{k-j}), corresponds to the expected value of the crop state variables at time step k, DaS_{k-j} is the number of days in the past when we wish to predict an observation, and the output y_{k-j} are the predicted remote sensing observations acquired $k-j$ days before. Note that the model is used N times to form the sequence

of the past N observations, for j that goes from zero to the N past observations. In this case, zero corresponds to the observation at time k and N the oldest of the N observations in the sequence. The output of an observation model is then: $P(x_k|x_{k-1})$ can be obtained as:

$$\begin{aligned} P(y_k|x_k) &\sim \mathcal{N}(\mu_{k-j},\, \Sigma_{k-j}) \\ &\text{for j} = 0, ..., N: \\ \mu_{k-j} &= GP_{\mu}[(x_k^T, DaS_{k-j})] \\ \Sigma_{k-j} &= GP_{var}[(x_k^T, DaS_{k-j})] \end{aligned} \tag{3.8}$$

Sensor fusion is achieved by training separate models for each sensor and observable used (e.g., one for Sentinel-1 VH and another for Sentinel-2 GNDVI), and selecting the model to use for predicting the sequence of past N observations, to be the same as the sensor providing the new observation that arrives at time k. This will be further detailed in section 3.5.3.2.

3.3.4 Unscented Kalman filter (UKF) with Gaussian process dynamic and observation models

In this paper, the UKF is used in order to perform the near-real time dynamic filtering. This section presents a brief introduction to the UKF and how it is combined with GP derived predictions of dynamic and observation models. The UKF is an extension to the Kalman filter to applications where the dynamic and observation models are non-linear. This is the case in this paper since these models are learned with the non-linear and non-parametric GPRs.

The UKF first finds an approximation to a Gaussian function for the non-Gaussian distributions resulting from propagating the states x_{k-1} and x_k through the non-linear models of equations 3.1 and 3.2 respectively. Then, the analytical solution of the Bayesian filtering equations (Särkkä, 2013) for the case of linear and Gaussian systems, i.e., the Kalman filter equations, can be applied to compute the approximated system state. In the UKF the approximation to Gaussian distributions is made with the aid of the unscented transform (UT), hence the name unscented Kalman filter. The UT selects, in a deterministic rather than random manner, a set of points (known as sigma points) in the input distribution (x_{k-1} of

equation 3.1 or x_k in equation 3.2) in order to characterise it (Särkkä, 2013). These points are then propagated through the non-linear models, i.e., a prediction is made for each sigma point using a GP-based model, and a weighted mean and covariance of the output or target distribution is computed from them.

Algorithm 1 below combines the original UKF (Julier and Uhlmann, 1997) with the Gaussian processes based dynamic and observation models as presented in section 3.3.1 and adapted from Ko and Fox (2009) and Särkkä (2013):

Algorithm 1: GP-UKF algorithm

1 Algorithm GP-UKF$(\mu_{k-1}, \Sigma_{k-1}, y_k)$:

2 $\chi_{k-1} = (\mu_{k-1} \quad \mu_{k-1} + \gamma\sqrt{\Sigma_{k-1}} \quad \mu_{k-1} - \gamma\sqrt{\Sigma_{k-1}})$

3 for i = 0,...,2n: $\chi_k^{[i]} = \chi_{k-1}^{[i]} + GP_\mu([\chi_{k-1}^{[i]}], D_{dyn})$ (see equation 3.7)

4 $Q_k = GP_{var}([\mu_{k-1}, D_{dyn}])$

5 $\hat{\mu_k} = \sum_{i=0}^{2n} W_m^{[i]} \chi_k^{[i]}$

6 $\hat{\Sigma}_k = \sum_{i=0}^{2n} W_c^{[i]} (\chi_k^{[i]} - \hat{\mu_k})(\chi_k^{[i]} - \hat{\mu_k})^T + Q_k$

7 $\chi_k = (\hat{\mu_k} \quad \hat{\mu_k} + \gamma\sqrt{\hat{\Sigma}_k} \quad \hat{\mu_k} - \gamma\sqrt{\hat{\Sigma}_k})$

8 for i = 0,...,2n: $\hat{Y}_k^{[i]} = GP_\mu([\chi_k^{[i]}], D_{obs})$ (see equation 3.8)

9 $R_k = GP_{var}([\hat{\mu}_k, D_{obs}])$

10 $\hat{y_k} = \sum_{i=0}^{2n} W_m^{[i]} \hat{Y}_k^{[i]}$

11 $S_k = \sum_{i=0}^{2n} W_c^{[i]} (\hat{Y}_k^{[i]} - \hat{y_k})(\hat{Y}_k^{[i]} - \hat{y_k})^T + R_k$

12 $\hat{\Sigma}_k^{x,y} = \sum_{i=0}^{2n} W_c^{[i]} (\chi_k^{[i]} - \hat{\mu_k})(\hat{Y}_k^{[i]} - \hat{y_k})^T$

13 $K_k = \hat{\Sigma}_k^{x,y} S_k^{-1}$

14 $\mu_k = \hat{\mu_k} + K_k(y_k - \hat{y_k})$

15 $\Sigma_k = \hat{\Sigma}_k - K_k S_k K_k^T$

16 return(μ_k, Σ_k)

Bayesian filtering algorithms approach the filtering problem in two stages: prediction and update steps (Särkkä, 2013). The algorithm 1 begins the prediction in step 2 with the unscented transform, generating a set of $(2n + 1)$ so-called sigma points to characterise the normally distributed previous state $x_{k-1} \sim \mathcal{N}(m_{k-1}, P_{k-1})$. In this step, the parameter λ is associated with the spread of the sigma points around the distribution mean (Särkkä, 2013) and D is the number of state dimensions. In step 3 each of the sigma points are propagated through the GP-based dynamic model (section 3.3.3.1) while in step 4 the additive process noise is estimated from

the predicted uncertainty of the GP-based dynamic model. In steps 5 and 6, the predicted mean m_k and the predicted covariance P_k as originally proposed in the UKF (Julier and Uhlmann, 1997) are estimated. In these steps, $Wi(m)$ and $Wi(c)$ are constant weights required to perform a weighted combination of the propagated or predicted sigma points (Särkkä, 2013). The update stage of the GP-UKF algorithm begins in step 7 by generating again a set of sigma points, now characterising the predicted state distribution of steps 5 and 6. Then this set is propagated through the GP-based observation model in step 8 to obtain the expected observations given the state (see section 3.3.3.2), while the observation noise is also obtained from the GP-based observation model in step 9. Subsequently, in steps 10 and 11 again a weighted combination of the propagated sigma points is made to obtain the mean and covariance of the predicted observations. Step 12 computes the cross-covariance of the predicted state and predicted observations as proposed in the seminal UKF algorithm. Step 13 computes the so-called Kalman gain as in the original Kalman filter algorithm and steps 14 and 15 provide the state mean m_k and the covariance P_k, conditioned on the sensed observations y_k

3.4 Test site and Datasets

3.4.1 Test site

Figure 3.2 shows a Sentinel-1 and Sentinel-2 image of the test site acquired on 29-09-2018. The asparagus fields located in the Peruvian north coast considered a total of 432 parcels for the analysis. The plants (Asparagus officinalis L.) used in the crop were grown in a nursery and later transplanted to the fields, which consist of dry sandy soil with subtropical climatological conditions. The peak of temperature occurs in February reaching averages of up to 26 degrees Celsius and lowest values in August with average temperatures of 15 degrees. This synchronises with the highest and lowest solar radiation levels (Senamhi, 2021).

Given the mild winters, the crop does not naturally reach senescence and is instead able to grow all year round. Therefore, the test site experiences two agricultural seasons per year. The timing of each of the individual parcels is generally not synchronized, where different parcels could be in different growth stages.

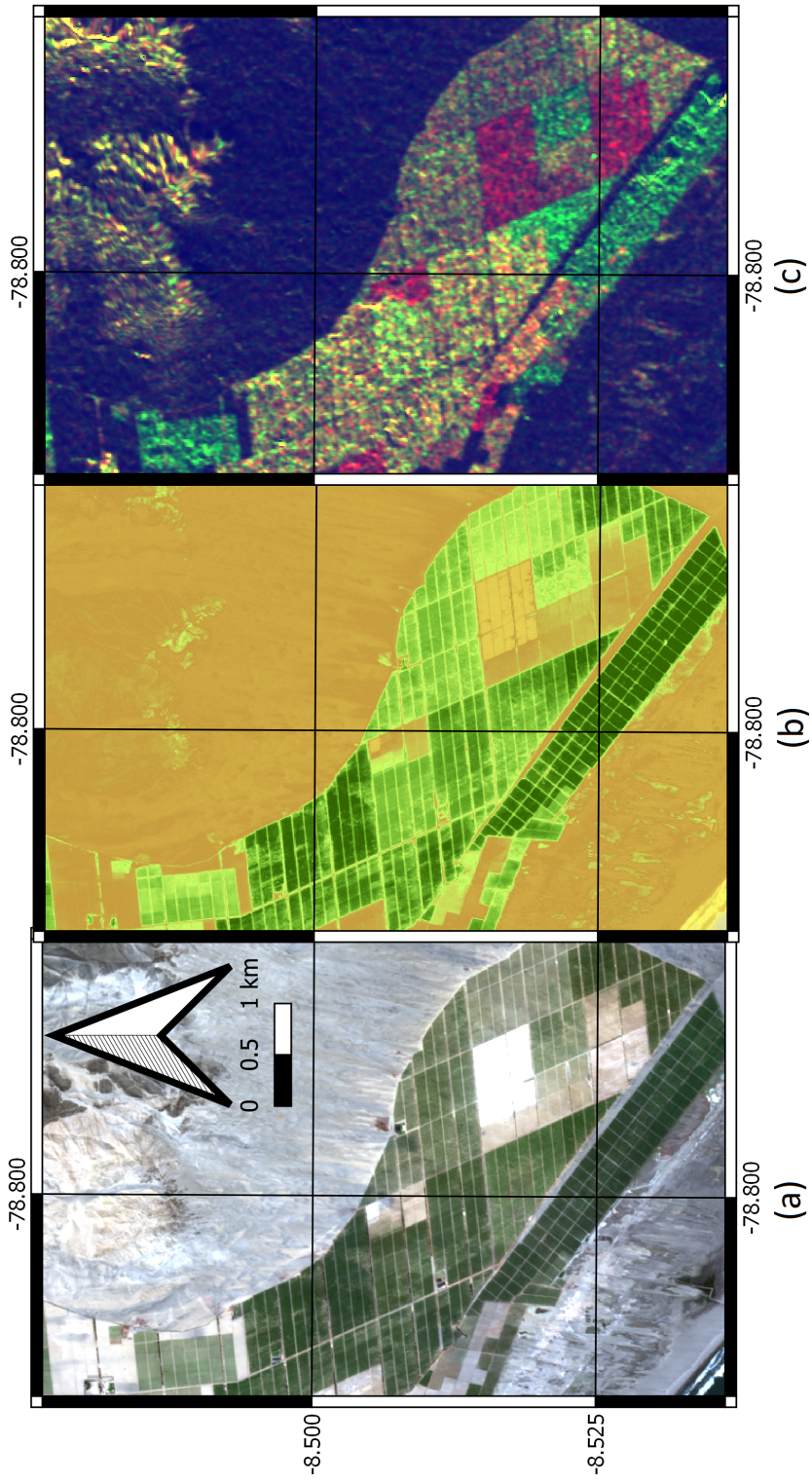

Figure 3.2: Test site. (a): Sentinel 2 RGB image acquired the 04/01/2019. (b): Sentinel-2 GNDVI image. (c): Multitemporal Sentinel-1 RGB composite, Red: VH on the 17/11/2018, green: VH on the 04/01/2019, blue: ratio between the 04/01/2019 and the 17/11/2018 VH images.

3.4.2 Asparagus crop growth cycle

Once the transplanted asparagus plants have matured and are in their productive period, the crop undergoes two main phases during each agricultural development cycle (season): fern establishment and harvest[1]. Phenological stages including emergence, aperture, ramification, flowering, maturation and harvest are typical in each season (Silva-Perez et al., 2020). As a perennial crop, this development cycle is repeated twice a year given the sub-tropical conditions of the test site, with a life-span of up to 25 years. Each above-ground development cycle drives an additional cycle of consumption and production of soluble carbohydrates (CHO) that are stored in the plant's below-ground root system Wilson et al., 2001; Wilson et al., 2005. CHO consumption is mainly happening during the above-ground spear and fern growth and during harvest. CHO production occurs once the fern canopy has established and is produced from photosynthesis in the ferns and translocated to the root system below-ground Wilson et al., 2000. When the crop is ready to be harvested, the canopy ferns are mechanically removed to initiate spear production. At this point, spears grow with a temperature dependant growth rate from the plant buds, enabled by the CHO produced and stored during the fern establishment in the previous season. Once the asparagus spears reach a desired length (between 20 and 25 cm), they are harvested and new spears develop from the root system. Since each spear that emerges and is harvested consumes stored CHO, the level of CHO decreases as the harvest progresses. This implies that the higher the level of CHO stored during the previous season, the higher the crop yield will be. At harvest completion, spears are left to grow reaching average heights of 1.8 meters, using the remaining CHO stored in the roots to develop a new canopy. In order to develop a healthy canopy, a minimum level of CHO is required, and therefore the harvest needs to be terminated before this minimum is reached. Farmers ensure this by constantly sampling the CHO levels in plants during harvest. Once the canopy is fully formed, the production of CHO begins and is stored in the roots to be used for harvest and to grow a healthy canopy in the subsequent season.

[1] A dormancy phase is additionally included for crops in temperate climates Wilson et al., 2001

3.4.3 Datasets

3.4.3.1 Ground truth

Given the key role that CHO plays in the crop yield, periodic samples are taken in the field to monitor a parcel's CHO evolution over time. However, the samples collected do not correspond directly to CHO. Although it exists an analytical method known as the anthrone method for measuring soluble carbohydrate in mg of CHO per g of dry weight (Allen et al., 1989), it is too demanding and not-commercially viable (Wilson et al., 2005). This led to the development of an approximation of root CHO content derived from the refractive index (Brix%) of asparagus root sap measured with a refractometer (Wilson et al., 2000; Wilson et al., 2005). According to this method, the CHO can be estimated by a linear regression model that uses Brix% as input (Feller & Fink, 2007; Wilson et al., 2000; Wilson et al., 2005). Authors of the method reported a Pearson correlation coefficient of 0.91 (r=0.91) for correlation between CHO estimated with the time and labour consuming analytical method and the model that uses the Brix% as input. This was obtained from an statistical analysis containing more than 400 samples.

The procedure considered to obtain the Brix% samples is as follows: avoiding row ends and external rows in the parcel, two random asparagus plants are selected. For each plant, two parallel vertical cuts of 40 cm deep are excavated and root pieces of approximately 10cm long are removed. Then, after washing and drying the root pieces, they are squeezed to obtain the root sap which is subsequently used to measure refraction with a digital refractometer. The Brix% level is then recorded from the refractometer scale. The mean Brix% level for the two plants is computed and used to represent the parcel Brix% level. This process was carried out as a tool to monitor the crop development in the 432 fields analysed in a period covering from June of 2018 to December 2020.

3.4.3.2 Sentinel-1 images

The level-1 GRD Sentinel-1 data utilised were downloaded from the Google Earth Engine platform Gorelick et al., 2017. The VH and VV polarisations are obtained in the Interferometric Wide swath (IW) acquisition mode. The pre-processing steps

Table 3.1: Sentinel-1 acquisition geometries available in the test site

Direction	Orbit	Inc. Angle	Acquisition Time	Total images
Descending	142	35	10:54	62
Ascending	18	31	23:34	66
Ascending	91	45	23:42	82

applied by GEE include orbit file update, GRD border noise removal, thermal noise removal, Radiometric calibration and terrain correction Gorelick et al., 2017. Three acquisition geometries are available in the study site as shown in table 3.1, covering the period from June 2018 to December 2020.

3.4.3.3 Sentinel-2 images

Orthorectified and radio-corrected Sentinel-2 level 1C data available in the GEE platform were used. A cloud masking pre-processing step was applied exploiting the Sentinel-2 QA60 band, masking out opaque clouds and cirrus clouds. A period covering from June 2018 to December 2020 is selected to generate vegetation indices time series at 10 metres resolution. This results in a total of 71 images used for the analysis. However, these images are concentrated in consecutive images for short periods of time (cloud-free months) and prolonged gaps in cloudy months as will be mentioned in section 3.5.4.2.

3.4.3.4 Remote sensing and ground truth time series

Figure 3.3 shows the mean values of VH backscatter intensity, Green Normalised Vegetation Index (GNDVI) (Bannari et al., 1995; Xue & Su, 2017b) and brix degrees (ground truth) time series. Three agricultural seasons for five typical parcels which have the same management practices are shown. The green and red vertical dashed lines mark the season beginning and end of the fern establishment, respectively. The time between a red and green vertical line corresponds to harvest. It can be seen in the VH backscatter shown in the top plot, that a significant decrease in intensity is measured during the harvest periods (between red and green lines).

This is considering that the canopy is mechanically removed when harvest starts and therefore, single bounce scattering predominates in the interaction between the SAR signal and the ground under the crop (Silva-Perez et al., 2020). The absence of canopy causes a similar effect in the Sentinel-2 data reducing the plant reflectance as can be inferred from the trends recorded in the GNDVI time series. Despite limited samples available in this example, the brix degree measurements have a negative trend as CHO are consumed when producing new spears during harvest as described in section 3.4.2. When harvest stops, and the spears emerge from the ground and are allowed to elongate vertically, the backscatter rapidly increases as a result of the double-bounce scattering with the signal reflecting from both the ground and the asparagus main vertical stalks (Silva-Perez et al., 2020). Once the leaf-like structures in the branches also known as cladophylls grow establishing the canopy fern, the backscatter moderately decreases since volume scattering is predominant at this point. This is a key point for the crop, since it marks the moment when the fern has fully established and GNDVI reaches its maximum value. Also, this is the moment when the CHO consumption stops and the production begins via photosynthesis as mentioned in section 3.4.2. After this point, since no important changes in the canopy biomass are observed, the VH backscatter remains almost constant (Silva-Perez et al., 2020). The GNDVI shows a marginal decrease until the end of the season, however, it is not as pronounced as it could be in a temperate climate when the crop senescence is more significant. The brix degrees, conversely, continue to increase until the end of the season when the crop is ready to be harvested. Figure 3.3 shows how the above-ground processes involving spear growth and fern establishment as recorded by the remote sensing observations, are connected with the below-ground carbohydrate stored in the plants root system. Based on these links and interactions, the methodology of section 3.3 is applied to track the parcel level CHO values over time.

3.5 Results

This section presents the results obtained using the proposed method for learning the dynamics of asparagus crop variables and tracking their state over time. We

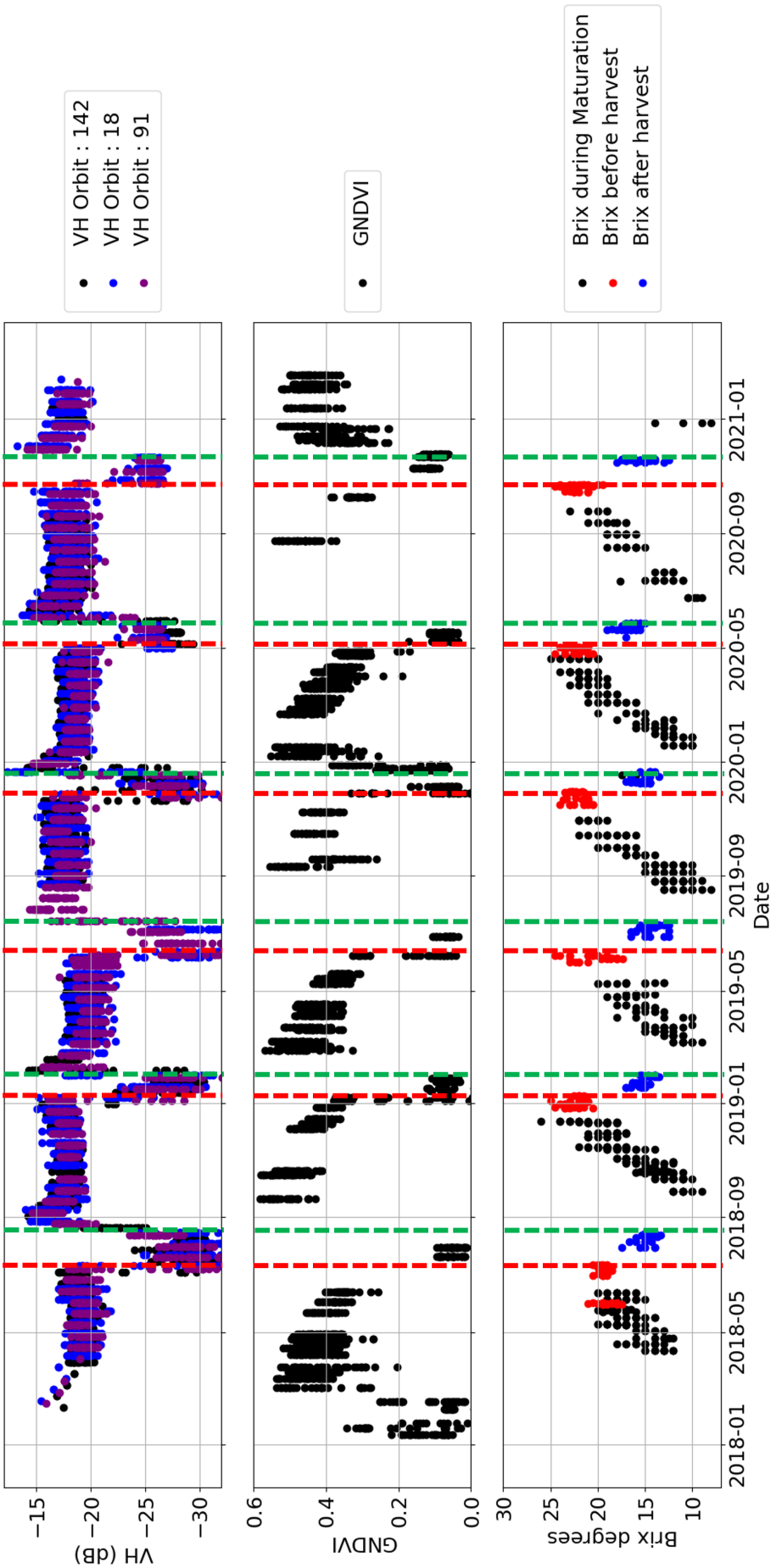

Figure 3.3: Time series for several parcels of Sentinel-1 VH backscatter (top) and GNDVI derived from Sentinel-2 data (middle). Time intervals between green and red dashed vertical lines corresponds with fern growth and establishment. Time between red and green lines correspond with harvest. A cycle of CHO charge and discharge, approximated with Brix% results from each above-ground development cycle or season (bottom).

first describe the variables that are being tracked, the results after training dynamic and observation models, and the results obtained using the filtering framework for tracking the variables for several consecutive seasons and for forecasting the harvest date.

3.5.1 State variables

Two informative variables are initially considered to characterise the crop over time and are of interest for farmers locally and other asparagus supply chain stakeholders. These include the below ground plant carbohydrates and the season crop age in days or also known as the number of days after the season started (DaS). This results in the state vector $x_k = (DaS_k, DaS_k)^T$

3.5.1.1 Below ground plant carbohydrates

As mentioned in sections 3.4.2, the crop yield is directly linked with the amount of plant carbohydrates stored in a plant root system (Wien and Stützel, 2020). The carbohydrates are in turn linked to the amount of canopy available to intercept sunlight, the solar radiation in the site and the efficiency of the plant transforming the latter into carbohydrates (Wien and Stützel, 2020). In this paper, we consider tracking the Brix% quantity since this is the variable taken in the field and available as ground truth. Note that as this quantity is constantly monitored, there are several samples available for training and testing, providing spatial and temporal diversity.

3.5.1.2 Crop Age or Days After the Season started (DaS)

Several stakeholders of the agricultural supply chains are interested in knowing the current season starting date. These include, for example, insurance companies and governments as a requirement prior to paying indemnity to farmers. This is also an informative feature required to compute the growing degree days (GDD) for cases when phenology is estimated with a thermal calendar $GDD_1997.Similarly, itprovidesroughestimati$ $BernardisEtal., 2014b; MascoloEtal., 2019).Inthispaper, weshowhowthiscanbeincludedasavariabl$

3.5.2 Dynamic model

As described in section 3.3.3.1, the dynamic model represents how the crop state variables evolve over time, one step at a time. The training of the dynamic model is achieved in two steps: First we obtain the typical state variable evolution over time and secondly, we learn to predict a state distribution at time step k given the state distribution at time step $k-1$.

3.5.2.1 Asparagus below ground carbohydrates typical dynamics

We first identify the typical dynamics of the variables being tracked. To achieve this, the ground samples available are used to train a GPR (described in section 3.3.2). The input for the GPR is the DaS when a sample is taken while the output is the corresponding brix degree measured. The result of this is shown in figure 3.4 and explained as follows.

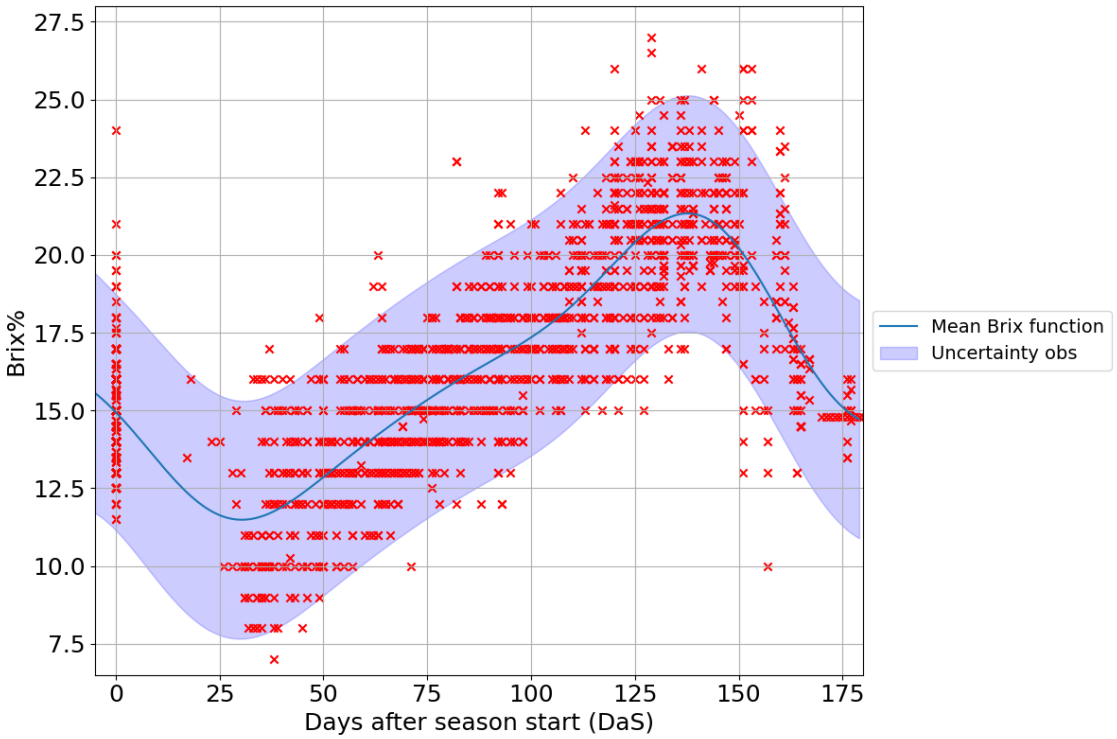

Figure 3.4: Typical Brix% dynamics and uncertainty. Red crosses are the ground truth samples.

The red crosses correspond to the brix degree sampled for several parcels plotted with the cultivation days (DaS) as a reference in the x axis. The solid blue line

represents the fitted GPR which corresponds to the typical brix evolution over time with its associated uncertainty shown in shaded blue. The interpretation of this typical model is given based on the agronomical and biological processes known for this crop type. After harvest of a season ends (DaS=0), the energy required to grow a new canopy is taken from the remaining carbohydrates stored in the root system after harvest in the previous season(s). As shown in fig x, from day zero the brix level decreases during this period as the carbohydrates in the roots are depleted. Note that around day 30 after the season started (DaS=30), a minimum brix level is reached. This point marks the end of the canopy formation as can be corroborated in the remote sensing observations of figure 3.3. The canopy has finished the production of cladophylls (leaf-like small structures in the canopy branches), the GNDVI reaches its maximum point in the season, and the double bounce effect in the VH polarisation has decreased and is transitioning to volume scattering, which is sustained until the end of the season (Silva-Perez et al., 2020). From this point, the brix level increases until the end of the season with different increase rates depending on the processes happening in the canopy above ground and environmental conditions, particularly solar radiation. The light that is intercepted by the now formed canopy is then transformed by the plant in carbohydrates and stored in the root system. However, note that the increase rate varies over time as well as the uncertainty associated with the ground samples. This is mainly due to changes in the canopy above ground, for instance when the plant spends CHO growing flowers and fruits which reduce the amount the CHO that is stored. Similarly, as the canopy gets more mature, the efficiency producing CHO may decrease altering the rate of CHO gain. By the end of the cultivation period (after DaS 130), when the canopy is cut prior harvest, new asparagus spears start to emerge and are harvested causing the CHO levels stored in the roots to rapidly decrease. Harvest is then stopped when a lowest level is reached. At this point, the new stems that emerge are allowed to regrow and form a new canopy to begin a new season.

3.5.3 Predicting asparagus crop state distribution at time step k given the state distribution at time step k-1

To estimate a crop state, the filter optimally blends a prediction obtained from the dynamic model and predictions made after acquiring new sensor observations. With regards to the DaS, the dynamic model consists in increasing by one day the previous prediction of DaS. For the brix state variable, the GP-based dynamic model uses as input the previous state and provides as output the change required to advance to the next brix state. In this sense, the model uses a training dataset of the form $D = [(DaS_{k-1}, Brix_{k-1}), \Delta Brix_k]$, where the model inputs DaS_{k-1} and $Brix_{k-1}$ correspond to the expected values of the state variables at time step $k-1$, and $\Delta Brix_k$ is the expected change given the previous state (obtained as $Brix_k - Brix_{k-1}$). Then, using equation 3.5 (GP mean), a prediction for this variable can be made and the current state is then approximated as:

$$
\begin{aligned}
P(x_k|x_{k-1}) &\sim \mathcal{N}(\mu_k, \Sigma_k) \\
\mu_k &= \mu_{k-1} + \Delta\mu \\
\mu_k &= \begin{bmatrix} DaS_{k-1} + 1 \\ Brix_{k-1} + GP_{mu}[DaS_{k-1}, Brix_{k-1}] \end{bmatrix} \\
\Sigma_k &= \begin{bmatrix} 1 & 0 \\ 0 & GP_{var}[DaS_{k-1}, Brix_{k-1}] \end{bmatrix}
\end{aligned}
\tag{3.9}
$$

In equation 3.9 the dynamic model for the DaS simply increases one day at each time step with uncertainty assumed to be 1 day. Since the dynamic models for the DaS and Brix are considered independently, the non-diagonal terms in equation 3.9 are zero. This can be solved with a multioutput Gaussian Process Regression (Álvarez et al., 2012; Pipia et al., 2019) which provides correlated outputs as will be detailed in the discussion section.

3.5.3.1 Dynamic model gap filling and forecasting

As first introduced in section 3.3.3.1, the dynamic model can be used recursively to obtain the value of the state variables between remote sensing observations (now-casting) and for multiple-step ahead prediction or forecasting. Figure 3.5 shows the result of this for several consecutive agricultural seasons.

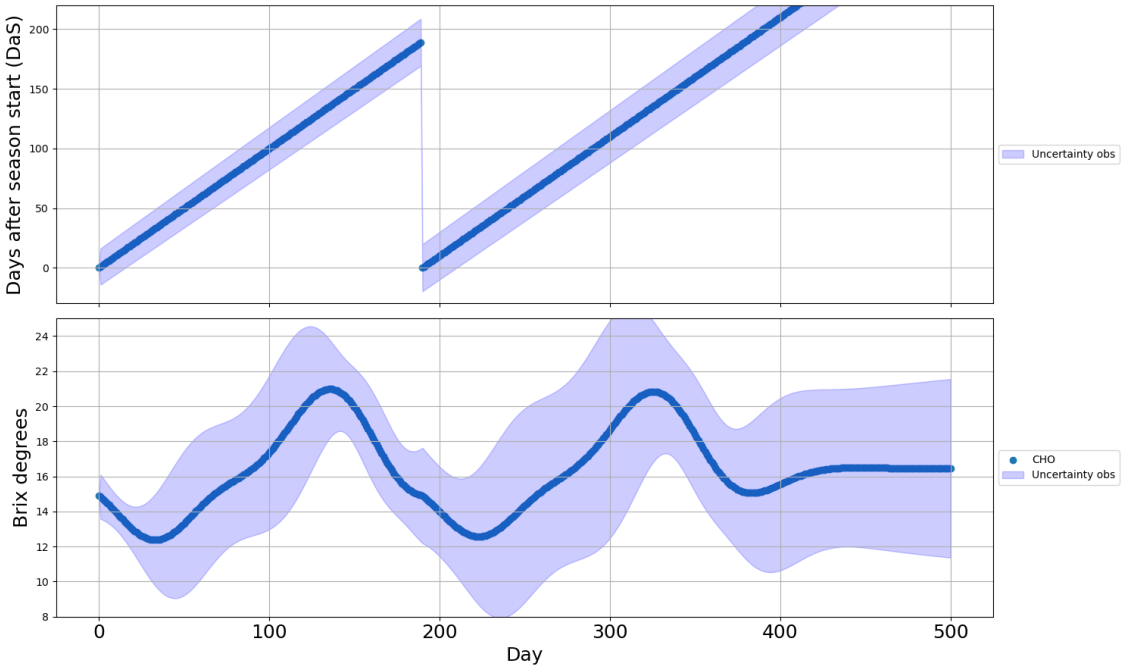

Figure 3.5: Recursive dynamic model predictions useful for gap filling and/or forecasting. Only the starting Brix% and DaS need to be provided, then the predictions from the dynamic model are fed-back for recursive estimation.

To generate this plot, only the initial value for Brix and DaS is provided and recursive prediction is then carried out for forecasting. An automatic detection of end of a season in real time is used with the expression:

$$\text{Season end detection if } brix_k < median\, brix_0 \text{ and } brix_{k-1} > median brix_0 \quad (3.10)$$

where the median $brix_0$ corresponds to the median of all brix ground samples at the beginning of the season. This detector estimates when the brix level goes below a typical starting brix level (median $brix_0$) to reset the DaS value to zero. This way, the forecast can be performed even beyond the current season. Note how the uncertainty associated with the predictions increases the more time steps are considered. This is achieved by the uncertainty propagation implemented with the help of the unscented transform and conveys the fact that the predictions are made using the model only, without new observations. Note that due to the uncertainty increase, the brix level does not go below the typical starting level after the second season and therefore there is no DaS reset.

3.5.3.2 Observation model

An observation model predicts the conditional probability distribution $P(y_k|x_k)$ corresponding to a sensor's response given the crop state (represented by the state variables). As introduced in section 3.3.3.2, in this paper we propose to use a vector of observations conformed by a sequence of N observations available in the past 100 days. The period of 100 days is chosen since it covers half or more of an agricultural season. Then, the sequence of N observations is predicted using equation 3.11 as follows:

$$\begin{aligned} P(y_k|x_k) &\sim \mathcal{N}(\mu_{k-i},\, \Sigma_{k-i}) \\ For\ i &= 0, \ldots, N \\ \mu_{k-i} &= GP_{mu}[DaS_k, Brix_k, DaS_{k-i}] \\ \Sigma_{k-i} &= GP_{var}[DaS_k, Brix_k, DaS_{k-i}] \end{aligned} \tag{3.11}$$

In order to achieve the fusion of active and passive satellite remote sensing data, separate models must be trained for Sentinel-1 and for Sentinel-2. Then during near-real time operation, a model is chosen to be compatible with the observations received, i.e. using model of Sentinel-1 when Sentinel-1 observations arrive or model of Sentinel-2 when Sentinel-2 observations arrive. Furthermore, given the variations captured by each acquisition geometry of Sentinel-1 (i.e., ascending, or descending passes and different incidence angles), individual models are trained for each of the three acquisition geometries available shown in table 3.1. It is important to highlight here that, if a single feature for each sensor is used, for instance, a sequence of the previous N-VH backscatter or N-GNDVI measurements, a single output GPR can be trained. If multiple features are considered, such as the VH, VH/VV, dual-Pol RVI or others for the case of Sentinel-1, an individual model for each feature is required or a multiple output GPR (Álvarez et al., 2012; Pipia et al., 2019) can be trained instead. Note that as in the case of the dynamic model, using independent models for each feature results in uncorrelated noise covariances or in other words, the matrix Σ_{k-i} is a diagonal matrix. In this paper, both the VH backscatter and the ratio VH/VV are considered, and individual models are trained to predict each feature. For the case of Sentinel-2, the green normalised difference vegetation index (GNDVI) and the Modified Chlorophyll Absorption in Reflective Index (MCARI) (Blackburn,

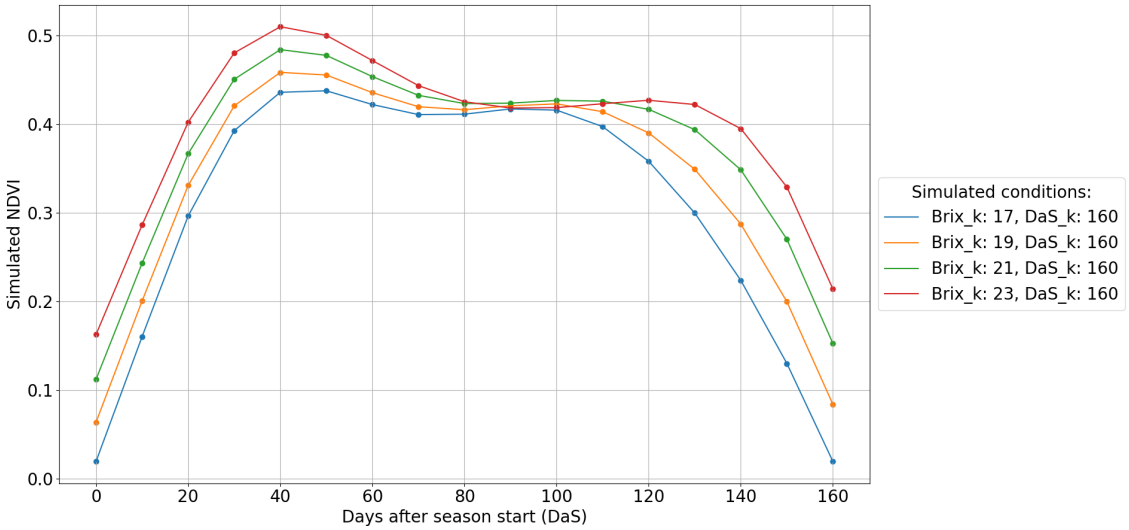

Figure 3.6: What-if simulation of an GNDVI typical season given different brix levels at the end of the season. Using these levels, a DaS=160, and the observation model, we can predict backwards the GNDVI season.

1999; Wu et al., 2008) are used, also training individual models to predict each feature. Other vegetation indices were not included since linear correlation between them and the GNDVI and MCARI were identified.

In order to test what the observation models learned based on the training data, figure 3.6 shows a 'what-if' analysis where the model for Sentinel-2 simulates the GNDVI response to different brix levels at the season end. In this case, we set the DaS_k to 160 (end of season), simulate several brix degrees for this same day, and use the model to predict the GNDVI backwards every ten days to form the history of GNDVI to reach these brix levels.

It can be seen in figure 3.6 that the higher the brix level is at the end of the season (i.e. $Brix_k$), the higher the GNDVI that the model predicts during the season. Similarly, with a high brix level, the season is expected to last longer than those cases with lower brix.

3.5.4 Unscented Kalman Filtering with GP-based dynamic and observation models

In section 3.3.4 the GP-UKF and its integration with Gaussian process dynamic and observation models was presented. In order to test the performance of the near-real

Table 3.2: Dynamic model and sensor combination cases. S1 is short for Sentinel-1 and S2 for Sentinel-2.

Case name	Dynamic model	S1 Orbit 18	S1 Orbit 142	S1 Orbit 91	S2
Dyn_model	X				
S1_18	X	X			
S1_142	X		X		
S1_91	X			X	
S2	X				X
S1_18+S1_142	X	X	X		
S1_18+S1_142+S2	X	X	X		X
S1_18+S1_91	X	X		X	
S1_18+S1_91+S2	X	X		X	X
S1_91+S1_142	X		X	X	
S1_91+S1_142+S2	X		X	X	X
S1_all Orbits	X	X	X	X	
S1_all Orbits + S2	X	X	X	X	X

time filtering framework with fusion of active and passive satellite sensors, several possible combinations between the available Sentinel-1 acquisition geometries and Sentinel-2 data were evaluated as shown in table 3.2.

Ground brix measurements collected in the fields from July 2018 to September 2019 are used for training the GP-UKF and data collected from October 2019 to December of 2020 for testing. The analysis is carried out at parcel level after averaging the pixel backscatter and reflectances. This is to match the ground truth also sampled at parcel level and considering that the management practices for the analysed fields are performed at parcel level. As described in equation 3.10, an automatic detection of the end of a season in near-real time is used to begin a new agricultural season. The observation models that use multitemporal data, considered the available images present in the previous 100 days to a given image using the VH and VH/VV backscatter as Sentinel-1 features, and the GNDVI and MCARI as

Sentinel-2 features. To initialise the filter, a prior belief of the crop state variables needs to be provided. An assumption based on the Sentinel-1 VH backscatter is made to provide an initial estimate of the DaS and the brix degrees. The starting date or DaS zero is the nearest date in the previous 100 days to the monitoring starting date, in which the VH backscatter was lower than -23 dB. If all values are higher than -23dB in the previous 100 days, the crop is assumed to be in maturation and a DaS of 120 is adopted. This is considering that the backscattering for C-band during harvest and at the moment of starting a new agricultural season is low (i.e. less than -23dB) due to the absence of canopy and the single bounce resulting from the SAR signal interacting with bare soil. The brix degrees are then initialised with the typical starting value of figure 3.4 (for DaS zero) estimated as the median of all the brix starting values collected in the ground truth. If a DaS of 120 is adopted, the typical brix value for DaS 120 is used. Since the filter is initialised with a Gaussian probability distribution, a standard deviation of 20 days for the DAS is used and a standard deviation 2.5 brix degrees for the below ground carbohydrates. Note that the described assumption is not necessarily required if large variances to the prior belief or initial probability distribution are adopted. In this case, after seeing new observations, the filter updates the state variables so that they are in agreement with the observations thus converging to the actual states. However, the described assumption allows the filter to converge faster. Similarly, the assumption that VH backscatter is low before beginning the agricultural season could be generalised to other crop types, again due to the absence of vegetation. The GP-UKF algorithm described in section 3.3.4 is then used for filtering. The algorithm updates predictions of the GP-based dynamic model when a new vector of observations arrives. This update is based on a weighted difference between the acquired vector of observations and the observations predicted by the GP-based observation model, given the dynamic model predicted state.

3.5.4.1 Tracking crop state variables only with the dynamic model

Figure 3.7 shows the result of running the GP-UKF filter without any remote sensing observations but only using the dynamic model to predict recursively and track the below ground plant carbohydrates and the crop age. As shown by the red dots, using

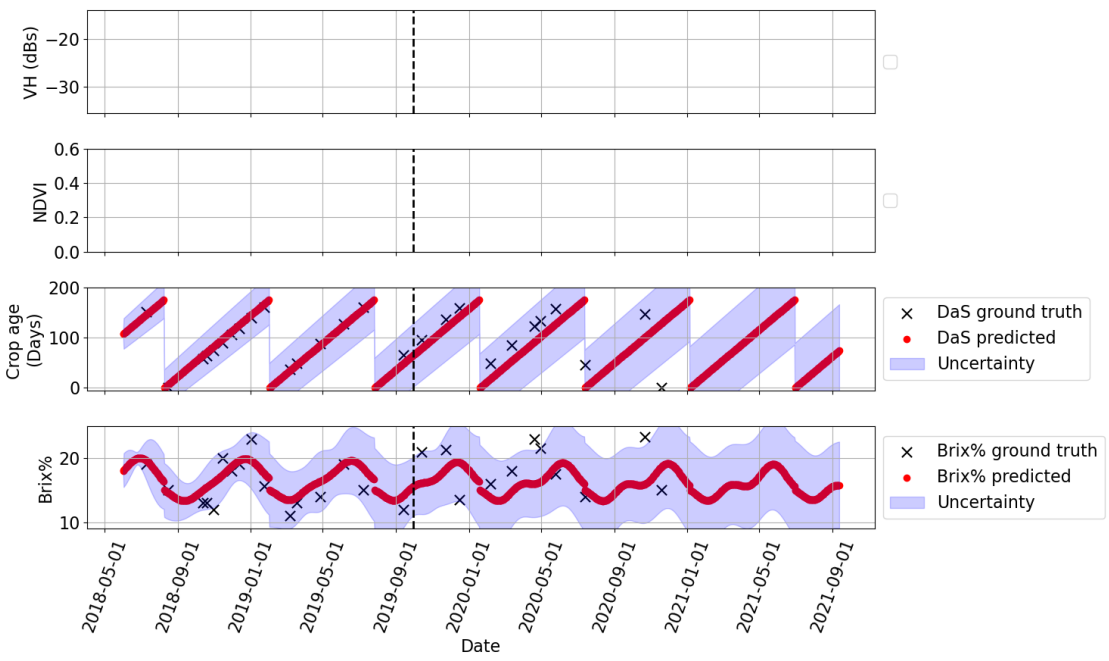

Figure 3.7: GP-UKF using dynamic model only, without remote sensing observations.

recursively the dynamic model to estimate brix degrees and DaS, the filter is able to provide daily predictions that are comparable to the ground truth samples (black crosses). The quantification of the error for these estimations will be introduced in section 3.5.5. These predictions follow the typical trends expected for the evolution of the state variables confirming that the dynamic model effectively captured their behaviour. Note that when the season end is detected, the DaS is reset to zero as well as the state initial uncertainty. Note however, that the predictions do not adapt to the particular conditions of every season as no remote sensing observations are being considered. These conditions could include among others, variations in management practices as well variations in crop development due to environmental conditions. Specifically in figure 3.7, note for example that after September of 2019 the dynamic model predictions are not synchronized with the ground truth. This is due to an atypical season start and end being changed according to management practices. This in turn reduces the overall GP-UKF performance if observations are not available.

3.5.4.2 Tracking crop state variables with Sentinel-2

In the case that Sentinel-2 observations are considered, the GP-UKF adapts better to the particularities of each agricultural season, as shown in figure 3.8. In this

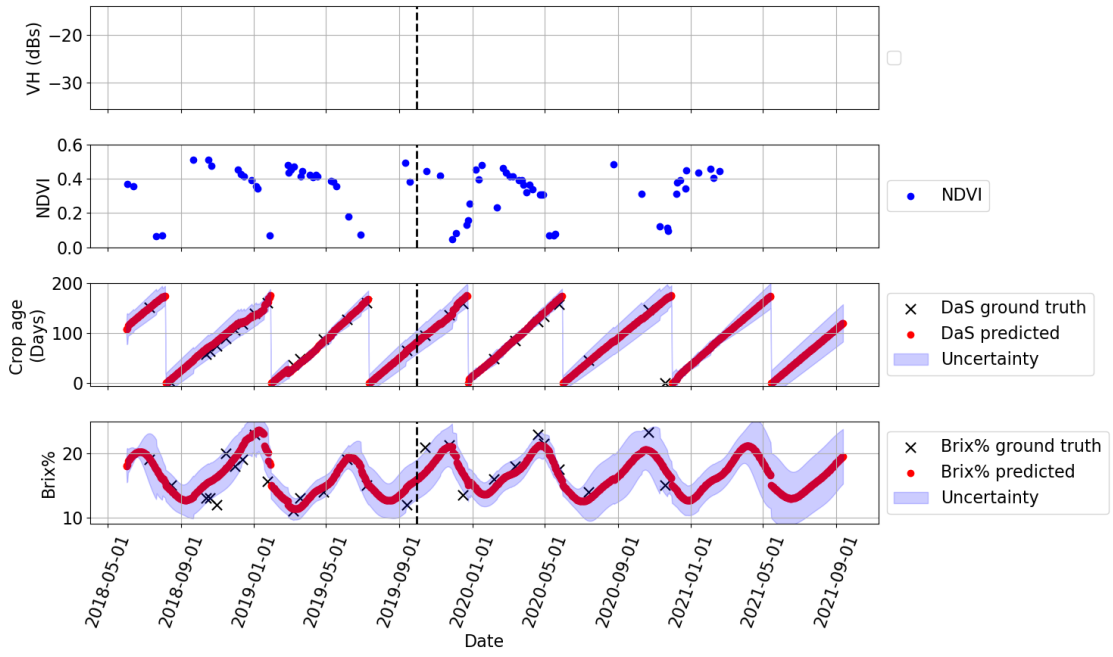

Figure 3.8: GP-UKF using dynamic model and Sentinel-2 data. Data from before the vertical dashed line is used for training, and data after is used for testing.

case, the filter uses the Sentinel-2 observations when available and based on the deviations between them and the predictions from the GP-based observation model for the Sentinel-2 features, adjusts the predictions of the dynamic model. If observations are not available, for instance due to cloudy days, the filter is still able to provide a prediction filling these gaps. The uncertainty in the predictions decreases significantly when several observations are consecutively received, such as between February and May of 2020. On the contrary, when a gap in the Sentinel-2 observations occurs, the filter fills the gaps and the uncertainty associated with these predictions increases as is the case between July and September of 2020. In fact, notice that a seasonal pattern can be observed in the uncertainty, where in the coldest months of the year when is also cloudier (second semester of each year), the uncertainty is larger than in the hotter months where less clouds are normally present. It is expected then that during cloudy months the GP-UKF relies mostly

on the dynamic model whereas in the cloud-free months relies in the observations. Note also that the uncertainty also increases when recursively using the dynamic model to forecast, as shown after the last observation available in February of 2021.

3.5.4.3 Tracking crop state variables with one acquisition geometry of Sentinel-1

Given the SAR capabilities of acquisition at day and night and almost all-weather conditions, long time series can be obtained. Figure 3.9 shows the result of the GP-UKF using one of the Sentinel-1 acquisition geometries available for the test site (orbit 91 in ascending pass).

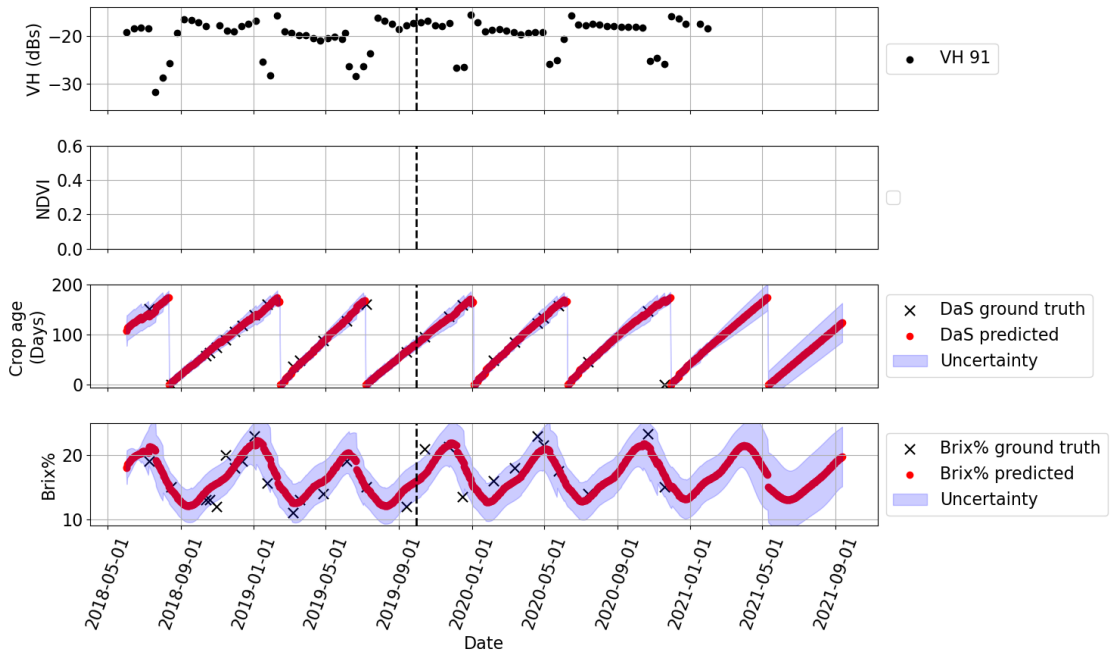

Figure 3.9: GP-UKF using dynamic model and Sentinel-1. Data from before the vertical dashed line is used for training, and data after is used for testing.

Visually inspecting figure 3.9, it can be seen that the predictions are close to the ground truth even though the observations can be noisy (see error for these predictions in section 3.5.5). If we focus on predictive accuracy, we can notice that Sentinel-1 seems to be less accurate than Sentinel-2 in cloud-free months. However, in the cloudy months, the more consistent time series of observations of Sentinel-1 provides better predictions than Sentinel-2. This suggests that the vegetation indices from a multispectral satellite may be more easily associated with the canopy

development than the backscatter from Sentinel-1 but this benefit is lost with the data gaps. Note that the predictive uncertainty using a single orbit of Sentinel-1 is relatively constant during the whole monitoring period.

3.5.4.4 Tracking crop state variables with one acquisition geometry of Sentinel-1 and Sentinel-2

Figure 3.10 shows the result of the GP-UKF combining both Sentinel-1 and Sentinel-2 data when available. To perform the data fusion, the crop state variables predictions from the GP-based dynamic model sit at the centre of the filtering strategy. These predictions are then adjusted after either of the data sources is available by using the adequate observation model to predict the expected remote sensing observations given the current crop state. The predicted remote sensing observations are then compared with the actual observations and based on their deviations, the state variable predictions of the dynamic models are adjusted.

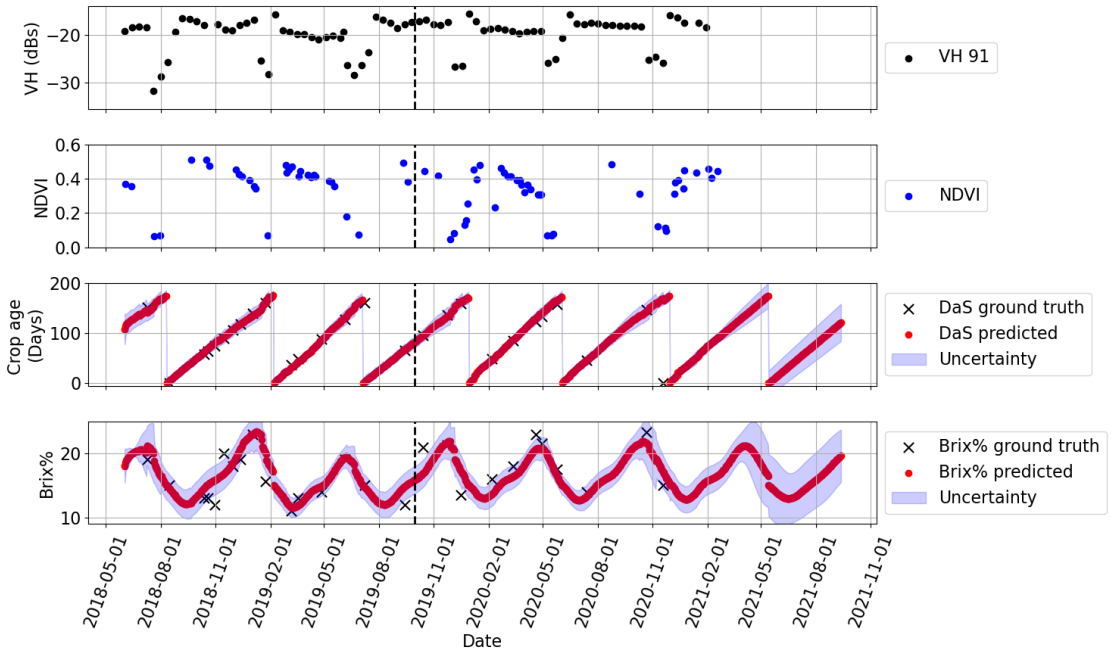

Figure 3.10: GP-UKF using dynamic model, Sentinel-1 and Sentinel-2.

The uncertainty that was high when filling the gaps if using Sentinel-2 data only, is now reduced thanks to the Sentinel-1 data being present. Note that the accuracy of the predictions with respect to each individual data source also improves. In a more general analysis, with the aid of the dynamic and observation models, the

GP-UKF learns to identify automatically when to start increasing or decreasing the plant carbohydrates given the remote sensing observations. This can be seen for instance in seasons shorter or longer than the typical season. Similarly, the brix degree starts to increase only after the canopy has been fully formed, this is, when the GNDVI reaches its highest point, and the double bounce reduces in the VH backscatter around DaS 30. This is a consistent behaviour to what was described in section 3.4.2 about the plant carbohydrates charge and discharge pattern.

3.5.4.5 Tracking crop state variables with all acquisition geometries of Sentinel-1

The results of the GP-UKF using the three Sentinel-1 acquisition geometries are shown in figure 3.11. In this case the temporal resolution is reduced such that on average every four days an image is obtained, provoking the uncertainty associated with predictions to be low throughout the monitoring period. Visually inspecting figure 3.11, it can be seen that it shows better performance than using only one orbit, however, compared for instance with the active-passive sensor fusion of figure 3.10 the difference in accuracy or uncertainty do not seem to be substantial.

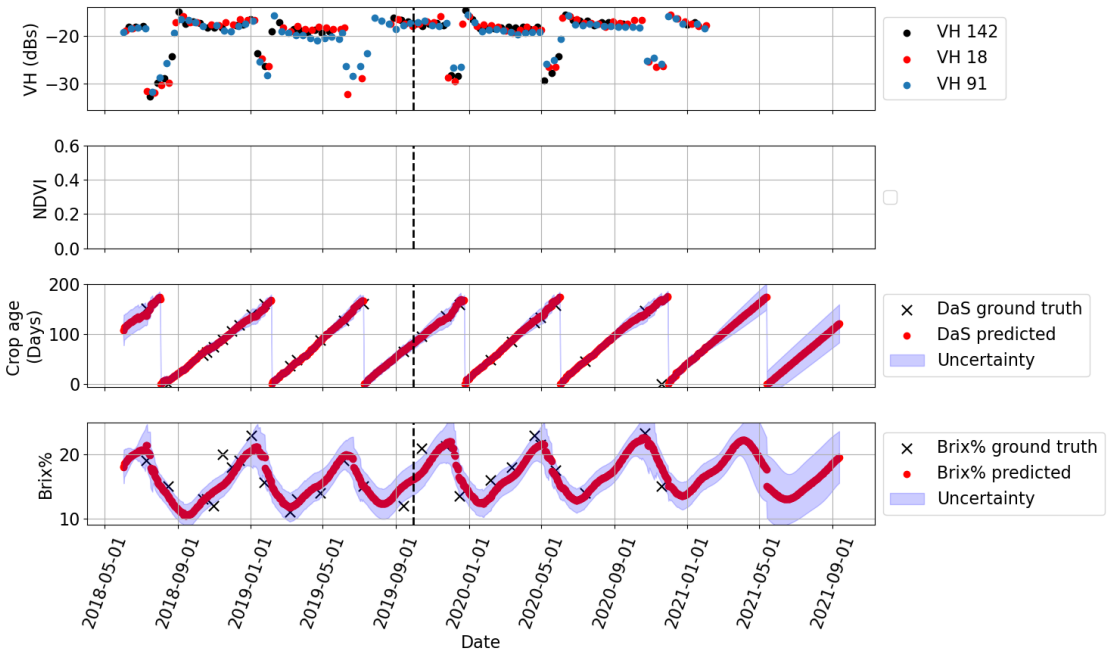

Figure 3.11: GP-UKF using dynamic model and all Sentinel-1 acquisition geometries.

3.5.4.6 Tracking crop state variables with all acquisition geometries of Sentinel-1 and Sentinel-2

When all acquisition geometries of Sentinel-1 and the Sentinel-2 data are used as shown in figure 3.12, the results obtained are more precise and the uncertainty when tracking the crop state variables is low. The accuracy in the season from January to June of 2020 improves compared to what is shown in figure 3.11, confirming the added value of Sentinel-2 to the three sentinel-1 Orbits. Similarly, an interesting synergy achieved using active-passive sensor fusion can be seen at the end of October 2020. The estimation of the accumulated brix degrees at the end of the season are better predicted than in any other case. In this case as in the other seasons, the brix degrees level at the end of the season prior harvest is a key informative factor about the potential asparagus yield in that season.

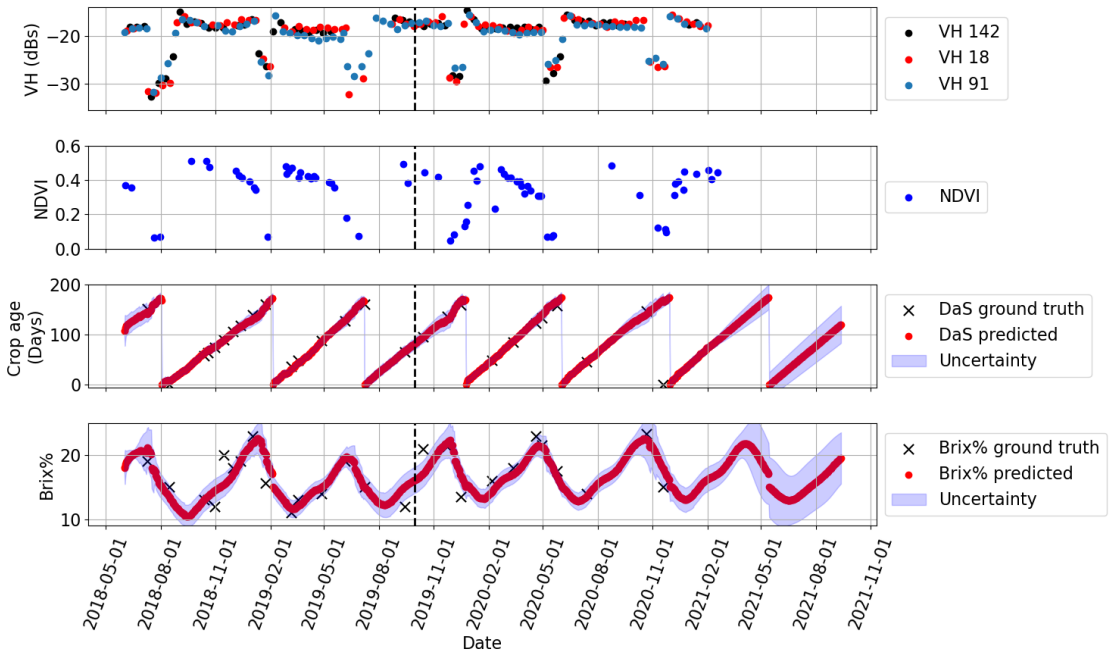

Figure 3.12: GP-UKF using dynamic model, all Sentinel-1 acquisition geometries and Sentinel-2.

3.5.5 Performance evaluation

This section presents the quantitative assessment of the GP-UKF for retrieving asparagus below ground carbohydrates and the season crop age. The ground dataset

is split in two parts for training and test. The performance is evaluated with ground truth from October 2019 to December 2020 covering more than two agricultural season for each of the 116 analysed parcels. Three metrics typically utilised for regression and time series assessment are used as indicators of performance: the Root Mean Square Error (RMSE), the Pearson correlation coefficient (r2) and the Mean Absolute error (MAE). The results of these metrics validating the performance of the GP-UKF applied to each of the analysed cases of table 3.2 is shown in table 3.3.

Table 3.3: GP-UKF performance evaluation. S1 is short for Sentinel-1 and S2 for Sentinel-2. Results are organised in descending order, from best to worst Mean Absolute error (MAE) brix performance.

Case	MAE Brix	MAE DaS	r2 Brix	r2 DaS	RMSE Brix	RMSE DaS
S1_all + S2	1.802	6	0.58	0.97	2.287	8
S1_18+S1_91+S2	1.805	6	0.59	0.97	2.278	8
S1_91+S2	1.808	6	0.58	0.97	2.295	8
S1_91+S1_142+S2	1.812	6	0.58	0.97	2.309	8
S1_all	1.905	6	0.53	0.97	2.401	8
S1_91	1.931	6	0.54	0.96	2.413	8
S1_18+S2	1.944	7	0.5	0.94	2.472	10
S1_18+S1_91	1.946	6	0.53	0.96	2.435	8
$S1_91 + S1_142$	1.953	5	0.51	0.97	2.46	7
S1_18+S1_142+S2	1.989	7	0.45	0.91	2.548	11
S2	2.083	8	0.43	0.91	2.649	12
S1_142+S2	2.14	9	0.32	0.83	2.745	12
S1_18+S1_142	2.243	8	0.33	0.83	2.862	13
S1_18	2.508	12	0.17	0.74	3.166	17
S1_142	2.531	15	0.07	0.52	3.278	22
Dyn_model	3.109	31	-0.27	-0.01	3.964	39
Line	16.88	44	-22.52	-0.34	17.252	52

As expected, using all the acquisition geometries of Sentinel-1 together with the Sentinel-2 data when available, provides the best results. In this case, the GP-UKF is able to track the asparagus crop state variables with a MAE of 1.802 brix degrees and 6 days. Note that while the r2 for DaS is high achieving 0.97, it is not as high for brix degrees achieving only 0.58. This difference may be related to the fact that the brix samples are significantly more prone to error when measuring them, resulting in noisy training and testing data. In fact, in order to reduce this error in the ground truth, more samples are required at parcel level for the sampled population to correctly represent the brix level. However, this process is expensive and resources consuming. The RMSE achieved in this case is 2.287 and 8 days, similar to the error obtained with the MAE.

In general, based on the results of table 3.3, adding more satellite sensors improves the performance partly due to the improvement to the temporal resolution observing the crop and partly due to the complementary information of the active-passive data fusion. This is even more evident in summer seasons when more Sentinel-2 images are available. The errors retrieving Brix degrees obtained with the other cases, are not substantially different as shown in table 3.3. The last row (line), represents the performance evaluation if all predictions corresponded to a line equal to the median of the training ground truth samples. This is only for testing that the filter is indeed better than predicting always the median brix and DaS values. The row Dyn_model represents the case when no remote sensing observations are considered but only the dynamic model as presented in section 3.5.4.1.

For the case of DaS as well as for brix degree, the poorest results are obtained when using the orbits 18 and 142 of Sentinel-1, both individually and in combination with other orbits or with Sentinel-2. This can be associated with the number of images available being considerably lower than for the orbit 91 as it can be seen in table 3.1. In fact, using Sentinel-2 data only (S2) even with the associated data gaps, has better performance than orbits 18 (S1_18) and 142 (S1_142), with a MAE of 2.083 compared to the 2.508 and 2.531 for these two Sentinel-1 orbits.

However, the orbit 91 (S1_91) individually presents better performance than Sentinel-2 data with a MAE of 1.931 and 6 Days. Note that this is practically the same performance achieved using all the acquisition geometries available (S1_all)

which achieves a MAE of 1.905 and 6 days, possibly meaning that the majority of the performance achieved corresponds to information provided by orbit 91 of Sentinel-1. The value of the active-passive sensor fusion can be seen when considering that the best four performances are achieved when using both Sentinel-1 and Sentinel-2. In these four cases the orbit 91 is always present confirming the value of a consistent flow of Sentinel-1 data (not fully achieved with orbits 18 and 142). An interesting case to highlight here is that using the orbit 91 and Sentinel-2 (S1_91+S2) performs better than using all Sentinel-1 acquisition geometries (S1_all), confirming the value of Sentinel-2 even with its data gaps in cloudy months. Note that this case (S1_91+S2) practically achieves the same performance as the best case. However using all orbits of Sentinel-1 (or more than one) and Sentinel-2 provides a more robust system in case of intermittent operation of any acquisition orbit, as was the case in this test site with orbits 18 and 142.

3.5.6 Multitemporal prediction maps: DaS and Brix degrees

Figures 3.13 and 3.14 show the results of retrieving the crop state variables with the GP-UKF when using the active-passive sensor fusion, for the whole farm where the ground truth was collected. These four dates show the evolution of both the brix degree and the days after the season started (or cultivation days). As it can be seen, not all the parcels are in the same development stage since farmers can manage this, taking advantage of the all year-round food production potential offered by the local climatological conditions.

3.5.7 Key dates estimation

As mentioned in sections 3.3.3.1 and 3.5.2, the same procedure to fill gaps or make one step ahead predictions can be recursively performed for multiple steps ahead prediction or forecast. This gives the GP-UKF the possibility to estimate the occurrence of future crop key dates. Accurately predicting the date when a parcel will be ready for harvest is essential to plan human and material resources required for harvest and to plan the capacity in the plant to process the harvested asparagus.

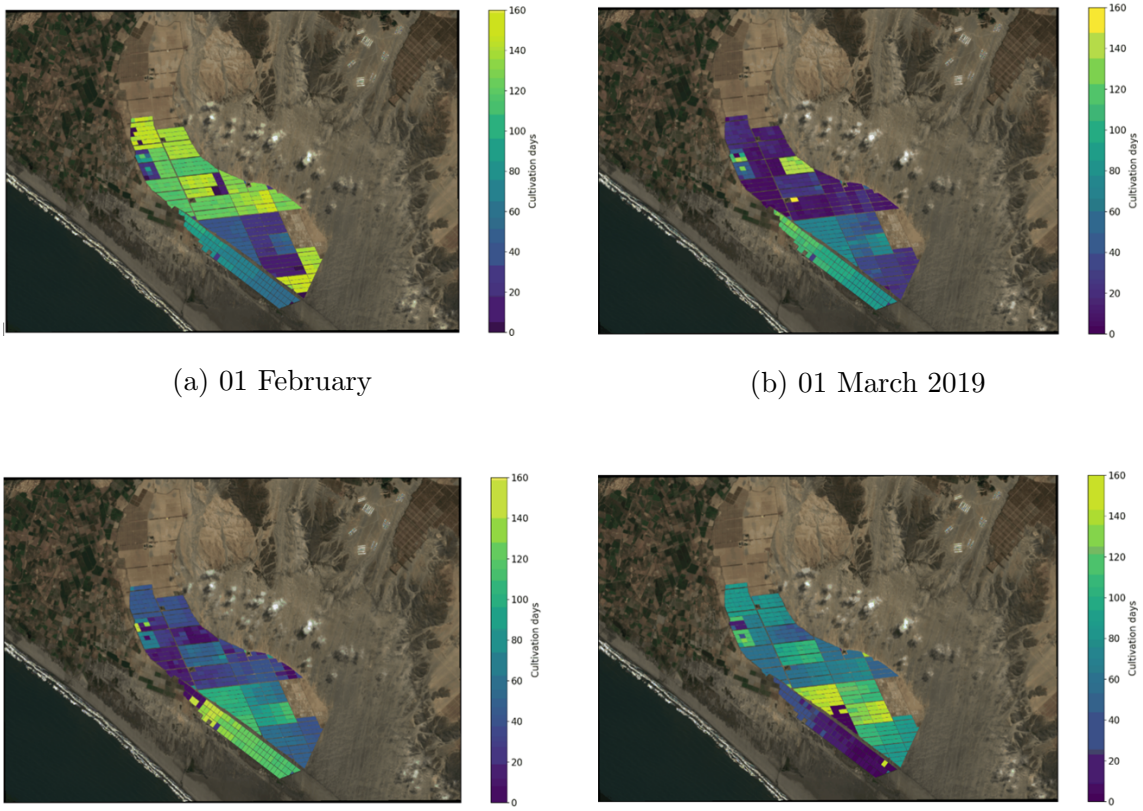

(a) 01 February

(b) 01 March 2019

(c) 29 March 2019

(d) 10 May 2019

Figure 3.13: Multitemporal DaS retrievied with the GP-UKF using Sentinel-1 and Sentinel-2 data. Image geo-coordinates not included to anonymize the fields location.

This is particularly important considering the all-year round production of asparagus. The crop is assumed to be ready for harvest when the accumulation of below ground plant carbohydrates in the roots system is maximum. Therefore, the procedure to test the GP-UKF capabilities for harvest date prediction is as follows: Using the case that provides the best results for tracking, i.e., using the three acquisition geometries of Sentinel-1 and Sentinel-2, the GP-UKF tracks the crop state variables until the last season in 2020. Then four cases are considered: the filter stops the tracking when the season crop age is 0, 30, 60 and 90 days. The GP-based dynamic model is utilised to recursively forecast from these points when the maximum brix degree in the next 200 days will occur. This date is then extracted as the expected harvest date for the parcels of asparagus included in the analysis. A key point to highlight is that this date in the practice can be affected by management decisions since it could be accelerated or delayed depending on contractual obligations or market intelligence. Therefore, since the date provided here is an estimation based

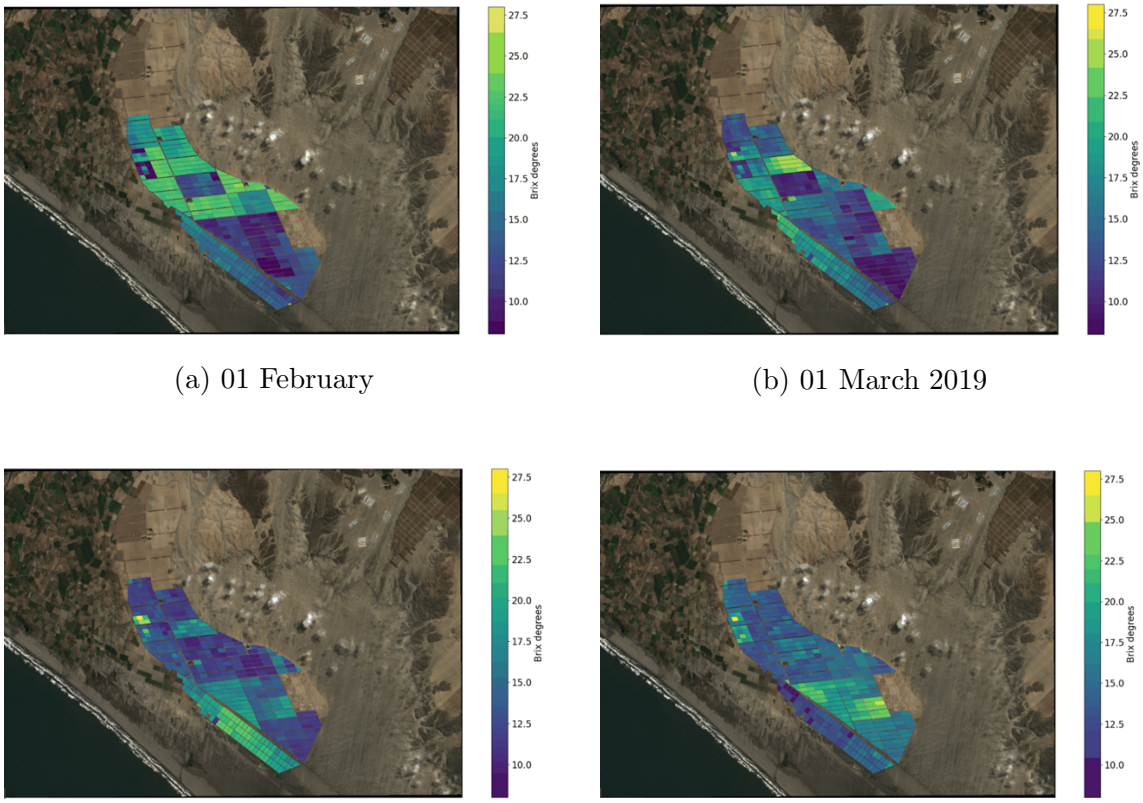

(a) 01 February

(b) 01 March 2019

(c) 29 March 2019

(d) 10 May 2019

Figure 3.14: Multitemporal Brix degrees retrieved with the GP-UKF using Sentinel-1 and Sentinel-2 data. Image geo-coordinates not included to anonymize the fields location.

only on the crop condition, it may in some cases disagree with the real date for days or in few cases even weeks. Table 3.4 shows the results from forecasting the harvest date for the three cases considered: As it can be seen, the error predicting harvest

Table 3.4: Forecast performance in days.

	DaS			
	0	30	60	90
MAE	17	6	4	4

date is lower the closer the parcel is to the real harvest (DaS=90). This is because the filter has seen more observations to correctly track the crop state variables up to that point. Conversely, forecasting the harvest date from DaS=0, corresponds to predicting without the aid of remote sensing observations, but only using the

dynamic model. Note than even when predicting harvest date 30 days after the season started, a MAE of 6 days is achieved. This is already an acceptable error for the practical purpose of this task.

Despite not accurately knowing when the season started but assuming a window of one month where it could have started, and after receiving observations for 2 months (60 days), the GP-UKF is able to forecast the date when the crop will be ready to harvest with an error (MAE) of 4 days.

3.6 Discussion

This paper introduced a filtering framework designed to track below ground asparagus plants carbohydrates and the season crop age with fusion of freely available and multitemporal Sentinel-1 and Sentinel-2 data. The method proposed complements what other studies have suggested are the advantages of a filtering framework, particularly in relation to accuracy, sensor fusion and key dates estimation (De Bernardis et al., 2016b; McNairn et al., 2018; Vicente-Guijalba et al., 2015).

As mentioned in section xx, there is evidence that suggests that if enough Sentinel-2 images are available the predictions using these observations may be more accurate than using Sentinel-1 (i.e. if no data gaps existed). However, if a Sentinel-1 acquisition geometry provides constant data (S_91) it is overall more accurate than Sentinel-2 as shown in table 3.3. In this regard, current work is focused on evaluating the accuracy metrics by considering the local climate seasonality. The aim is to quantify the gain in accuracy in the summer months with respect to the winter months when less acquisitions are available. This will also help to analyse the contribution of Sentinel-2 to the overall accuracy when the active-passive sensor fusion is used. Crucially, even when Sentinel-2 data gaps exist, the GP-based dynamic model is able to fill these gaps and provide an estimation of the tracked crop state variables and to forecast crop key dates. The combination of active-passive data provided the best performances and was found to be valuable to better predict the brix degree of a parcel at the end of the season. This is one of the most important moments in the season for this prediction, since it is highly correlated to the crop yield (Wilson et al., 2001; Wilson et al., 2005). As it can be seen in table 3.3, us-

ing one orbit of Sentinel-1 that provides systematic acquisitions and in fusion with Sentinel-2 (S1_91+S2) provides better performance than using all three available acquisition geometries of Sentinel-1. This helps corroborate the value of the active-passive sensor fusion. Additionally, including more than one Sentinel-1 orbit with Sentinel-2, besides of providing the best performance, contributes to having a more reliable operational system.

Note that an important advantage of the method proposed is the potential for transferability to other crop biophysical variables, crop types and Satellite sensors (i.e. other SAR wavelengths or multi-spectral satellites). This is a clear improvement with respect to previous approaches that use filtering frameworks with parametric models (De Bernardis et al., 2016b; McNairn et al., 2018). Since the GP-based dynamic and observation models are learnt from historical satellite and ground truth data, the only requirement for replicating this work to other sites is to have the training data for the state variables available (as in any other supervised approach). Since the GPs permit to learn a diverse range of functions and provide the associated uncertainties, the method can adapt to the different locations and crop types. In addition, previous work did not consider the use of several images to create a vector of observations as proposed here. However, in remote sensing the multitemporal information has been repeatedly shown to improve an algorithm's performance. Note also that in this paper we proposed to estimate the DaS directly as part of the filtering instead of designing a totally different algorithm as has been done in previous works (Mascolo et al., 2019; Phan et al., 2018a).

Compared to the traditional Kalman Filter, the GP-UKF is more accurate as it is able to learn non-linear dynamic and observation models. Compared to the Extended Kalman Filter (EKF) as in (Vicente-Guijalba et al., 2015), the UKF has been shown to be at least as accurate as the EKF (Julier and Uhlmann, 1997). Note that propagating the states through the GP-based models results in a non-Gaussian distribution (Deisenroth et al., 2013). However, the GP-UKF approximates them to Gaussian in order to use the original Kalman filter equations. In this regard, the GP-UKF may be at a slight disadvantage compared to the particle filters of (De Bernardis et al., 2014b; McNairn et al., 2018). Nevertheless, a pragmatic approach can be taken, accepting the error, as it allows for a significant improvement in

reducing the destructive sampling damage of this high value crop. Future work will address this potential disadvantage.

Previous papers have exclusively focused on tracking one individual crop state variable, particularly crop phenology. As we show in this paper, tracking more than one variable may imply having individual dynamic models for each crop state variable, which results in uncorrelated process noise covariance (section 3.5.3). This is a limitation of the current version of the GP-UKF that can be solved by training multiple outputs GPs (Álvarez et al., 2012; Pipia et al., 2019) instead of individual models. The same case is true for the measurement noise covariance in the observation models for each of the individual remote sensing features used. This will also be addressed in a future version of the GP-UKF.

Depending on the size of the training dataset, a GPR can become computationally expensive to handle. Several algorithms for efficient inference have been proposed (H. Liu et al., 2020). An upgrade to these approximations of GPs, such as sparse GPs (Quinonero-Candela and Rasmussen, 2005), may be recommended in large datasets. Including this also reduces the computational cost needed for near-real time monitoring.

In this paper, back-prediction (or hind-casting) was not performed using the dynamic model, however, it is possible to do so by adopting a straight forward modification of the training data and the equation 3.9. A practical application of this could be the ability to extrapolate (backwards), the initial date of canopy maturation. For asparagus physiological models this date is critical as it can be assumed as the point where the gain of carbohydrates starts (Wilson et al., 2001; Wilson et al., 2005). Although ground sensors were not included in the analysis, the GP-based dynamic model can handle them as control inputs (Deisenroth et al., 2013; Ko and Fox, 2009).The model can then learn to predict the response of a crop state to climatological signals and thus the crop dynamics. This includes factors such as temperature and solar radiation. A notable experiment that is being considered for future work is the use of different SAR wavelengths. The use of X-band for instance may enable earlier identification of emerging asparagus, from the soil than the C-band of Sentinel-1. This is a feature that would contribute to the automatic identification of the start of a new season, in a similar manner as have been reported

for other crop types (Lopez-Sanchez, Ballester-Berman, & Hajnsek, 2011; Lopez-Sanchez et al., 2014). Conversely, using a longer wavelength such as L-band may provide additional information during the crop maturation phase. This is because it may penetrate the canopy significantly more the C-band providing additional information about the soil status, such as moisture content. It is important to also understand the benefits of treating each SAR acquisition geometry (i.e. orbit) as a different sensor as treated here, rather than performing an incidence angle normalisation approach to combine them. Based on this a decision can be taken on which method is preferable for transferibility purposes. In principle, an incidence angle normalisation approach that does not require training data may be easier to implement in different locations. Similarly, it is important to corroborate that the SAR crop signature and the ground truth samples of brix degrees are similar in other fields and regions of the country. This will ease transferability of the current algorithm. However, expansion of the training dataset may be required to include more training diversity which would then allow scalability for larger area asparagus crop monitoring.

3.7 Conclusion

In order to provide an alternative to current, destructive and expensive field sampling of below ground asparagus plants carbohydrate, this paper presents a novel, data-driven, unscented Kalman filtering framework. It fuses multitemporal and freely available Sentinel-1 and Sentinel-2 data to track brix degrees as a surrogate of carbohydrates, the season crop age and to forecast crop key dates. Gaussian process regressions are trained with multi-year ground truth to learn the dynamic and observation models and their corresponding uncertainties. After testing the performance of the GP-UKF with unseen field samples, a MAE of 1.802 brix degrees is obtained fusing the three Sentinel-1 acquisition geometries available in the test site and the Sentinel-2 data when available. The GP-UKF achieved a MAE of 6 days for crop-age retrieval and a MAE of 6 days for forecasting the date for a parcel being fit for harvest.

The GP-UKF proposed here is also able to perform daily predictions, fill data

gaps and forecast key crop dates while remaining robust to individual sensor failures. As a data-driven approach, the method can be applied to other crop biophysical variables and crop types. Apart from overcoming the limitations discussed in section 4.9, future work will expand the GP-UKF for combination with asparagus growth physiology models and with ground sensors for temperature and for solar radiation. The algorithm may also be expanded for national scale monitoring.

3.8 Acknowledgment

This research was partially supported by the Project EO4cultivar, led by Environment Systems Ltd and co-funded by the UK Space Agency (https://www.envsys.co.uk/projects/eo4cultivar/). Sentinel data were downloaded thanks to the Copernicus mission of the European Space Agency (ESA).

Chapter 4

Multi-Temporal Polarimetric SAR (MT-PolSAR) Change Detection for Crop Monitoring And Crop Type Classification

4.1 Abstract

The interpretation of multidimensional Synthetic Aperture Radar data often requires expert knowledge. In fact, it requires to simultaneously consider several time series of polarimetric features to understand the physical changes of a target and its temporal evolution. In an effort to characterise the changes over time, Multi-temporal Polarimetric SAR (MTPolSAR) change detection was introduced in the literature by Lê et al. (2015) and Alonso-González et al. (2020). However, existing methods either only exploit intensity of changes or the resulting changed scattering mechanisms are not guaranteed to represent physical changes of the target.

This paper presents a variation in a previously published change detector (Alonso-González et al., 2020). It is based on the difference of covariance matrices that characterise the polarimetric information, allowing for an intuitive representation and characterisation of physical changes of a target and its dynamics. We show the results of this method for monitoring growth stages of rice crops and present a novel application of the method for crop type mapping from MT-PolSAR data. We

compare its performance with a neural network-based classifier that uses time series of PolSAR features derived from a target covariance matrix decomposition as input.

Experimental results show that the classification performance of the proposed method and the baseline method are comparable, with differences between the two methods in the overall balanced accuracy and the F1-macro metrics of around 2% and 3%, respectively. The method presented here achieves similar classification performances of a traditional PolSAR data classifier while providing additional advantages in terms of interpretability and insights about the physical changes of a target over time.

4.2 Introduction

Since a single satellite image cannot capture long-term variability, seasonality effects, or information described by the changes in a process state, multitemporal information has become a key tool in remote sensing. The day and night and all-weather capabilities of SAR satellites offer significant opportunities for continuous and remote monitoring regardless of cloud cover. Additionally, the information extracted from the acquired SAR data can be augmented by means of polarimetric analysis, exploiting the covariance between the different polarization channels measured by the satellite (S. Cloude, 2009; Lee & Pottier, 2009). However, the process of deriving information is often not intuitive due to the large amount of polarimetric features that change over time driven by natural or human-made processes. This analysis is essential for evaluating changes in earth processes, land cover and use, including applications such as forest (Antropov et al., 2011), agriculture (Lopez-Sanchez et al., 2014; McNairn et al., 2009), glacier changes (Akbari et al., 2013) and urban settlements monitoring, among others. Agricultural fields are just one of the examples of such dynamical behaviour since the morphological parameters of the plants evolve along the season varying the PolSAR response accordingly. The most widely used polarimetric analyses consider the simultaneous interpretation of several polarimetric time series, resulting from multitemporal backscatter measurements and PolSAR decompositions (S. R. Cloude & Pottier, 1996; Lopez-Sanchez et al., 2014). However, the process of identifying the adequate PolSAR decomposition to use, the

set of features that are best suited for the problem at hand and how to combine them to identify informative patterns is not straightforward.

Other methods focus on identifying the scattering mechanisms that are suffering the largest change by means of PolSAR change detection. Test statistic methods such as the likelihood ratio test focus on evaluating the equality of two covariance matrices that follow the complex Wishart distribution (Conradsen et al., 2003; Kersten et al., 2005). Likewise, the complex Hotelling-Lawley trace test statistic is used by Akbari et al. (2016) to evaluate the similarity between two complex covariance matrices which is subsequently thresholded to determine changes between images. Statistical information theory has also been applied to measure divergence between complex covariance matrices (Nascimento et al., 2018), as well as distance-based methods which evaluate the polarimetric similarities between images to identify changed regions (Inglada & Mercier, 2007; M. Liu et al., 2014). Note that although these methods exploit the PolSAR information to quantify the intensity of changes, they do not focus on identifying the type of changes between images. Therefore, they are not suitable for analyzing the scattering mechanisms dynamics and its temporal evolution. Marino et al. (2012) presented a method in order to detect polarimetric changes between two images. However, a way to combine this information with the changes in the backscatter amplitude is not directly embedded in the detection process. In terms of multitemporal change detection, the likelihood ratio test statistic was extended in order to handle multiple images and test the equality of several covariance matrices (Conradsen et al., 2016; A. Nielsen et al., 2017). In this case, the authors focused on detecting whether change occurred in any of the images in the stack and try to estimate when it happened. Note however that the interpretation regarding the type of change which is vital for change analysis is not considered in this approach. In A. A. Nielsen et al. (2019), the same authors propose to improve this method by adding the capability of identifying the change direction. This is done by computing the definiteness (positive or negative definiteness) of the difference of covariance matrices that model the PolSAR response in the two dates considered for the change detection. This way the method detects not only that there was a change and its associated intensity, but also the direction of the change, for example, whether the change was due to a target(s) that appeared or disappeared

between the two dates. A faster computation of the same method is presented in A. A. Nielsen (2019). Note that while knowing the direction of change provides more information, it does not explain in physical sense, i.e. as a scattering mechanism, the type of change. This may be sufficient for some applications, specifically for change analysis of man-made targets, however, understanding types of changes is crucial for example for environmental applications, such as understanding the physical changes in the vegetation development or degradation of a crop or a forest.

Other studies introduced the concept of change detection matrix to denote changes not only between consecutive images but also between all images in a stack. In Lê et al. (2014), the authors used it for speckle filtering by identifying the changed an unchanged areas over a time series, however, the analysis was limited to single polarization data and focused exclusively on the image filtering strategy. In Lê et al. (2015), the concept was extended for PolSAR data and included multitemporal change detection. However, besides being a supervised change detection methodology, the change matrix and the change maps only provide information about how dynamic or stable the resolution cells are over the time series, without giving information about the types of changes and the specific dates of occurrences.

In Marino and Hajnsek (2013), a PolSAR change detector inspired by the Polarimetric Match Filter (Novak et al., 1989) was introduced, which proposes to find changes between two images based on the optimization of the power ratio between them. In this case, focus is given to the intensity of the change for anomaly detection, although the scattering mechanisms are not analyzed. Based on the same concept, a method to analyse and characterize multi-temporal PolSAR changes was proposed recently by Alonso-González et al. (2020), also based on the maximization of the power ratio between acquisitions, with the aim of providing not only the intensity of changes between images, but also its type. A novel visualisation of the PolSAR changes, previously introduced in (Alonso-Gonzalez et al., 2016; Alonso-González et al., 2016) is also formalised.

The authors of Alonso-González et al. (2020) extend the method to not only analyse changes between consecutive images but also among all images in the stack and apply it to visually inspect changes in agricultural fields. Note however, that the projection vectors of the optimisation (i.e. eigenvectors of the optimisation) that

maximize the power ratio are not guaranteed to correspond to scattering mechanisms but are the vectors that provide the maximum contrast between the covariance matrices of the two dates. This implies that the type of changes detected may not correspond to physical changes in the target and can only be interpreted with the aid of transformation models which significantly restricts the potential of the method.

In this paper, a modified version of the change detector is proposed in order to improve the type of change interpretation so that the obtained changes represent PolSAR scattering mechanisms directly. This allows one to gain insight into the scene evolution without depending on transformation models that consider matrix multiplications. We also present the analysis for different crop types and test sites, confirming the transferability of the method presented here, and present a novel application of the same method, in which we test the potential for image classification. We exploit the fact that analysing the intensity and type of changes during the whole growing season and encoding them into a change matrix allows the characterization of a target, in this case a crop type, in terms of the increase and decrease of scattering mechanisms over time. In other words, we propose a classifier that is not only based on states (at different dates), but also on the dynamics (or changes) of such states directly embedded in the change matrix. Unlike other crop type classification algorithms, the method proposed here provides the advantage of having a single method for in-season phenology monitoring as shown by Alonso-González et al. (2020) and for crop type classification as will be presented here.

4.3 Test site and Data sets

The methods presented in this paper are tested on two separated test sites where ground truth has been collected. The sites are geographically distant and include several crop types in order to include crop and region diversity. In the first site the focus is on monitoring crop growth while in the second site, additional to crop growth the interest is to test the potential of the methods presented here for crop classification. The following is a short description of the two locations.

4.3.1 South of Spain

The site 1 corresponds to rice fields locate near Seville, in the south of Spain as shown in figure 4.1. The ground truth includes phenology data for validation collected weekly from May to September of 2014 covering one complete agricultural season. In this case the ground data is used for comparing and validating the results obtained from the proposed methodology, particularly for monitoring crop growth along the season as it will be shown in section 4.7. With regards to the satellite data, as shown in table 4.1, 16 Single Look Complex (SLC) Quad-Polarimetric images from the RADARSAT-2 satellite with three different incidence angles are available, with temporal resolution of approximately two weeks when combining incidence angles or one month for each incidence angle separately.

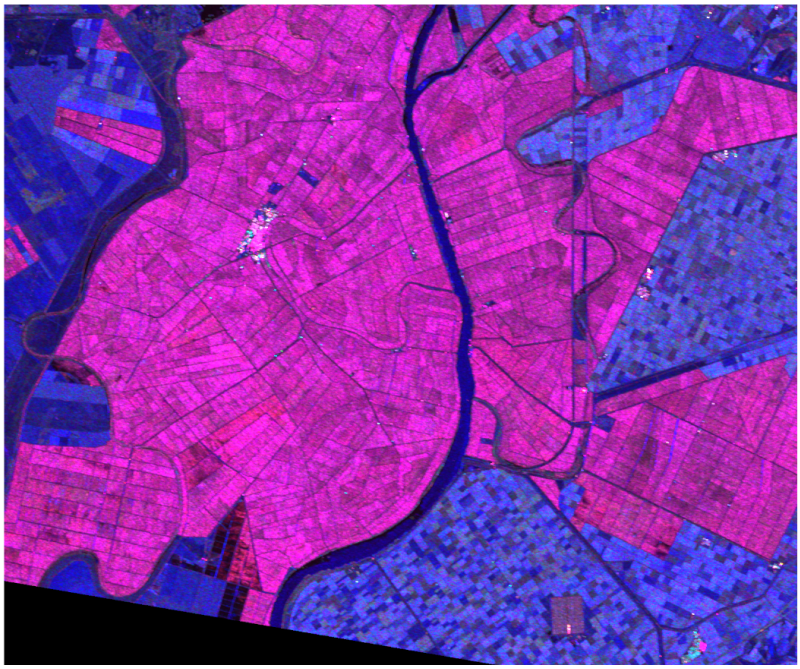

Figure 4.1: Rice fields in the South of Spain (Test site 1). Quad-Pol RADARSAT-2 image acquired the 02/08/2014. Blue:$\sqrt{\underline{\lambda}}\, cos(\underline{\alpha})$, Red: $\sqrt{\underline{\lambda}}\, cos(\underline{\alpha})sin(\underline{\beta})$, Green: $\sqrt{\underline{\lambda}}\, sin(\underline{\alpha})sin(\underline{\beta})$ (See equation 4.9).

4.3.2 Indian Head, Canada

This dataset includes several other crops types including barley, oats, wheat, canola, flax, lentils and field peas. These crops are located in the Indian head in Canada, where ground truth was gathered as part of the AgriSAR 2009 campaign, which

Table 4.1: South of Spain (Test site 1) RADARSAT-2 images used

Date (yyyymmdd)	**Beam**	**Inc. angle(deg)**
20140522	FQ8	28
20140605	FQ19	39
20140615	FQ8	28
20140622	FQ13	33
20140629	FQ19	39
20170709	FQ8	28
20170716	FQ13	33
20140723	FQ19	39
20170802	FQ8	28
20170809	FQ13	33
20140816	FQ19	39
20170826	FQ8	28
20170902	FQ13	33
20140909	FQ19	39
20170919	FQ8	28
20170926	FQ13	33

covers phenology among other biophysical variables. Images between June and September of the same year are selected, ensuring that the cultivation period is covered and removing images affected by severe rainfalls. Figure 4.2 presents the location of the fields and table 4.2 shows the 7 quad polarimetric images from the RADARSAT-2 satellite with the associated incidence angles that are considered for crop growth monitoring and crop type mapping (sections 4.7.2 and 4.8).

4.3.3 SAR data pre-processing

In both test sites, the covariance matrices utilised as input for the analysis are obtained after applying radiometric calibration, multi-looking and speckle filter. A 9x9 boxcar filter is used considering that parcels are sufficiently big and several pixels fall within a parcel. Then terrain correction and geocoding are performed, to ensure that all the images are geocoded over the same grid even if they are acquired by different beams or pass directions.

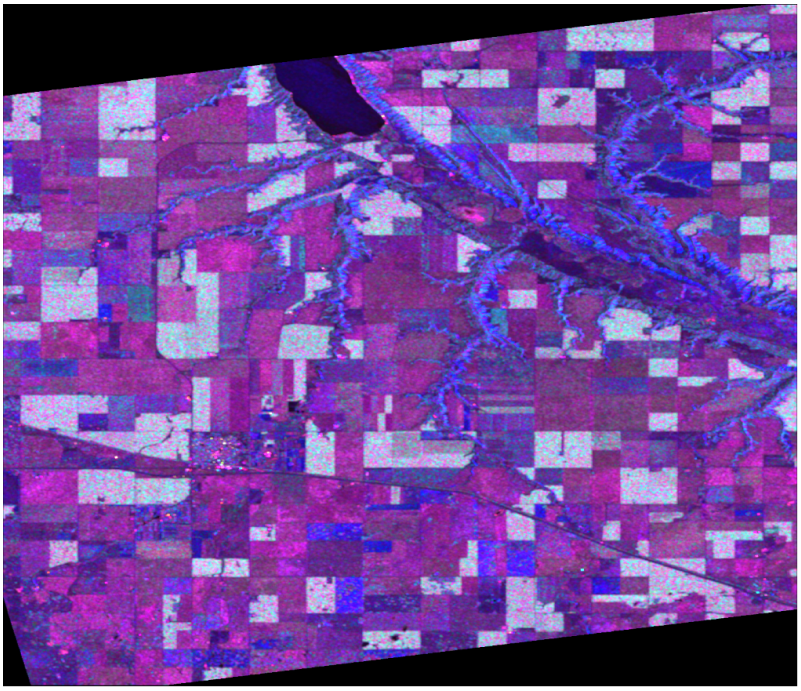

Figure 4.2: Indian Head, Canada (Test site 2). Quad-Pol RADARSAT-2 image acquired on the 22/08/2009. Blue:$\sqrt{\underline{\lambda}}\,cos(\underline{\alpha})$, Red: $\sqrt{\underline{\lambda}}\,cos(\underline{\alpha})sin(\underline{\beta})$, Green: $\sqrt{\underline{\lambda}}\,sin(\underline{\alpha})sin(\underline{\beta})$ (See equation 4.9).

Table 4.2: Indian Head, Canada (Test site 2) RADARSAT-2 images used

Date (yyyymmdd)	**Beam**	**Inc. angle(deg)**
20090604	FQ19	39
20090702	FQ2	22
20090712	FQ11	31
20090815	FQ19	39
20090822	FQ15	35
20090829	FQ11	31
20090908	FQ19	39

4.4 Methodology

The scattering process measured by a quad-polarimetric radar imaging system is conventionally represented for each resolution cell by the scattering matrix S (S. Cloude, 2009; Lee & Pottier, 2009)

$$S = \begin{bmatrix} S_{HH} & S_{HV} \\ S_{VH} & S_{VV} \end{bmatrix} \tag{4.1}$$

The elements S_{ij} of the matrix correspond to the complex scattering coefficients associated with the amplitude and phase of the backscattered signals, where H and V stand for linear horizontal and vertical and the double letter is for transmitter–receiver. The scattering matrix can also be represented in a vectorized form derived from a chosen set of 2x2 complex basis matrices, as $\underline{k} = \frac{1}{2}[Tr(S\Psi)]$, where Tr is the matrix trace operator, and Ψ is a set of 2x2 complex basis matrices (S. Cloude, 2009; Lee & Pottier, 2009).

If a monostatic backscattering system is used and assuming reciprocity (HV = VH), the polarimetric target vector in Pauli basis is given by:

$$\underline{k}_p = \frac{1}{\sqrt{2}}[S_{HH} + S_{VV}, S_{HH} - S_{VV}, 2S_{HV}]^T \tag{4.2}$$

where the superscript T denotes the vector transpose, and the $\sqrt{2}$ is required to preserve the total scattered power.

The polarimetric target vector presented in (4.2) corresponds to the case of a single look complex image. The central limit theorem can be applied assuming that the number of scatterers inside a resolution cell is large and thus $\underline{k}_p$ follows a multivariate complex circular Gaussian distribution with zero mean and probability density function (S. Cloude, 2009; Lee & Pottier, 2009):

$$f(\underline{k}_p) = \frac{1}{\pi^3 \|\Sigma\|} \exp(-\underline{k}_p^{*T} \Sigma \underline{k}_p) \tag{4.3}$$

where * represents the complex conjugate, $\|.\|$ represents the matrix determinant, and Σ is the covariance matrix of the PolSAR target vector in Pauli basis (also known as the coherency matrix), obtained as $\Sigma = \{\underline{k}_p \underline{k}_p^{*T}\}$, where $\{.\}$ is the statistical expectation operator.

Equation 4.3 corresponds to the distribution $\underline{k}_p \sim \mathcal{N}(0, \Sigma)$, where Σ is a Hermitian positive semi-definite matrix and contains the necessary information to characterize a target (S. Cloude, 2009; Lee & Pottier, 2009).

Since the amplitude and phase of a resolution cell are the coherent and linear combination of backscattered signals from individual scatterers within it, the measurements are affected by a random variation denoted as speckle (Oliver & Quegan, 2004a). To reduce the randomness of the acquired signals, L number of iid resolution cells can be averaged (or speckle filtered), and the matrix of equation (3) becomes the L-looked coherency matrix:

$$T = \frac{1}{L} \sum_{i=1}^{L} \underline{k}_{pi} \underline{k}_{pi}^{*T} \tag{4.4}$$

where i=1,2, .., L, are the number of averaged samples or realizations.

4.4.1 Covariance matrix eigenvector/eigenvalue decomposition

Several theorems have been proposed to decompose the target covariance matrix of equation 4.4 into simpler objects to aid its physical interpretation. These can be coherent decompositions to characterize the so-called coherent or pure targets, or

incoherent decompositions for partial or distributed targets (Lee & Pottier, 2009). In this paper, a brief introduction to the eigenvector/eigenvalues decomposition in the context of PolSAR data analysis (S. R. Cloude & Pottier, 1996; Lee & Pottier, 2009) is given since as it will be seen in section 4.5, it is linked to the optimization required in the change detector proposed. The coherency matrix T of equation 4.4 can be decomposed using the eigendecomposition theorem, as

$$T = U \cdot D \cdot U^{-1} \tag{4.5}$$

where D is a 3x3 diagonal matrix that contains the non-negative and real eigenvalues $diag(\lambda_1, \lambda_2, \lambda_3)$, and $U = [\underline{u_1} \quad \underline{u_2} \quad \underline{u_3}]$ is a 3x3 unitary matrix in which the column vectors $\underline{u}_1$, $\underline{u_2}$, and $\underline{u_3}$ are the three orthogonal eigenvectors.

In order to provide a physical interpretation of this decomposition, the eigenvectors $\underline{u}_1$, $\underline{u_2}$, and $\underline{u_3}$ or more generally, $\underline{v_i}$ with i=1,2,3 of T can be rewritten as

$$\underline{v}_i = \sqrt{\lambda_i}\,[\cos(\alpha_i) \quad \cos(\alpha_i)\sin(\beta_i) \quad \sin(\alpha_i)\sin(\beta_i)]^T \tag{4.6}$$

The average or dominant scattering mechanism of a resolution cell can then be obtained by combination of the three orthogonal eigenvectors as (Lee & Pottier, 2009)

$$\underline{v} = \sqrt{\underline{\lambda}}\,[\cos(\underline{\alpha}) \quad \cos(\underline{\alpha})\sin(\underline{\beta}) \quad \sin(\underline{\alpha})\sin(\underline{\beta})]^T \tag{4.7}$$

where $\underline{\lambda} = \sum_{i=1}^{3} P_i\lambda_i$, $\underline{\alpha} = \sum_{i=1}^{3} P_i\alpha_i$, $\underline{\beta} = \sum_{i=1}^{3} P_i\beta_i$. In the three later definitions, P_i corresponds to the pseudo probabilities

$$P_i = \frac{\lambda_i}{\sum_{k=1}^{3}\lambda_k}. \tag{4.8}$$

Using equation 4.7 it is possible to visualise the average or dominant scattering mechanism of each resolution cell of a PolSAR image as an RGB composite as shown in figure 4.1, using the following colour representation:

$$\begin{aligned} Blue: &\quad \sqrt{\underline{\lambda}}\,\cos(\underline{\alpha}) \\ Red: &\quad \sqrt{\underline{\lambda}}\,\cos(\underline{\alpha})\sin(\underline{\beta}) \\ Green: &\quad \sqrt{\underline{\lambda}}\,\sin(\underline{\alpha})\sin(\underline{\beta}) \end{aligned} \tag{4.9}$$

In equation 4.9 the expression in the blue channel corresponds to surface scattering, in the red channel to double bounce scattering and in the green channel to volume scattering (Lee & Pottier, 2009).

4.5 PolSAR change detection based on difference of covariance matrices

This section introduces the proposed PolSAR change detector which allows us to extract polarimetric changes between two acquisitions, identifying the occurrence of changes and providing interpretation about the type of change that a target suffered. Part of this method has been previously introduced by the authors in (Marino & Alonso-González, 2017; Silva et al., 2018). Note that previous works introduced only the algebraic part of the detector but it did not contain a way to intuitively visualise scattering mechanisms. Similarly, it did not explore the potential for crop type classification nor any of quantitative validation had been performed.

4.5.1 Pairwise change detection

For the case of bi-date change detection, we denote the pair of co-registered acquisitions to be compared as date1 and date2. The coherency matrices represented by equation 4.4 and denoted as T_1 and T_2 are used to characterize a resolution cell at date1 and date2, respectively. It is possible to write T_2 as the sum of T_1 plus an independent matrix including the added and subtracted components as

$$T_2 = T_1 + T_C \tag{4.10}$$

where the matrix T_C calculated as $T_C = T_2 - T_1$ is Hermitian symmetric, since it is produced by the linear combination of two hermitian matrices, but is not positive semi-definite. This means that the diagonal elements of Tc are real and the upper

triangular part is the complex conjugate of the lower triangular part (Marino & Alonso-González, 2017). However, there is a difference with ordinary coherency matrix, since it is not bound to be positive semi-definite. This means that its Trace and its quadratic form $P = \underline{\omega}^{*T} T_C \underline{\omega}$ (using a generic projection vector $\underline{\omega}$) can be negative. This is an expected feature since we need a matrix that is able to communicate if the change in the partial target has brought an increase or reduction of a) a specific scattering mechanism and b) the overall power of the final partial target (trace).

By representing T_C with its quadratic form $P = \underline{\omega}^{*T} T_C \underline{\omega}$ we can investigate the amount of change that a scattering vector represented by the projection vector $\underline{\omega}$ suffers. In this sense, by optimizing over all the possible projection vectors $\underline{\omega}$, it is possible to find the one that experiences the largest or smallest change. Note that the optima $\underline{\omega}$ also corresponds to the scattering mechanism that was added/subtracted to the partial target in date1.

4.5.2 Optimisation

To find the maximum and minimum projection vectors we can apply the well-known Lagrangian optimisation for the quadratic form $P = \underline{\omega}^{*T} T_C \underline{\omega}$. That is:

$$\underline{\omega}_{max} = \arg\max_{\underline{\omega} \in \mathcal{C}^3} [\underline{\omega}^{*T} T_C \underline{\omega}] \tag{4.11}$$

By constraining $\underline{\omega}$ to be unitary we can obtain the Lagrangian as:

$$L = \underline{\omega}^{*T} T_C \underline{\omega} - \lambda(\underline{\omega}^{*T} \underline{\omega} + C) \tag{4.12}$$

Differentiating with respect to ω^{*T} and setting the derivative equal to zero we obtain the equation:

$$\begin{aligned} \frac{dL}{d\underline{\omega}^{*T}} &= T_C \underline{\omega} - \lambda \underline{\omega} \\ T_C \underline{\omega} &= \lambda \underline{\omega} \end{aligned} \tag{4.13}$$

Note that equation 4.13 corresponds to the eigendecomposition theorem described in equation 4.5 and therefore the optimisation can be completed by a diagonalisation of the matrix T_C. Since T_C is Hermitian, the eigenvalues will be real

but as T_C is not positive semi-definite, the eigenvalues are not bound to be positive. This is because a change can increase or decrease the resulting power of a scattering mechanism (e.g. we could have that the surface scattering mechanism increases or decreases).

4.5.3 Change visualisation

After the optimisation procedure described in the previous section the eigenvalues and eigenvectors of T_C are obtained. In this case, the eigenvectors represent scattering mechanisms that change between a pair of acquisitions and the eigenvalues represent the intensity of such changes. Note that since the eigenvalues are not bound to be positive, the negative eigenvalues represent a scattering mechanism that has been removed from the scene.

The visualisation and interpretation can be performed in the same way as described in section 4.4.1. The dominant or average scattering mechanism for both cases, i.e. when is added or removed from a scene, can be represented with equation 4.9. However, equation 4.8 requires special consideration given that the eigenvalues can be negative. It is adjusted by separating the positive and negative eigenvalues, corresponding to added or removed scattering mechanisms respectively, which allows for their independent visualisation, as follows:

$$
\begin{aligned}
P_{i\ added} &= \begin{cases} 0 & \text{for } \lambda_i < 0 \\ \frac{\lambda_i}{|\lambda_1|+|\lambda_2|+|\lambda_3|} & \text{for } \lambda_i > 0 \end{cases} \\
P_{i\ removed} &= \begin{cases} \frac{|\lambda_i|}{|\lambda_1|+|\lambda_2|+|\lambda_3|} & \text{for } \lambda_i < 0 \\ 0 & \text{for } \lambda_i > 0 \end{cases}
\end{aligned}
\tag{4.14}
$$

Equation 4.14 indicates that if an eigenvalue is negative, the pseudo-probability that the associated eigenvector or scattering mechanism (SM) was added to the scene is zero and if the eigenvalue is positive, the pseudo-probability that the associated eigenvector or SM was removed to the scene is zero. We can then compute the average parameters $\underline{\lambda}$, $\underline{\alpha}$, $\underline{\beta}$ separately for added or removed scattering mechanisms which enable us to employ the RGB representation of equation 9, as follows:

$$\begin{aligned}
\underline{\lambda}_{\,added} &= \sum_{i=1}^{3} P_{i\ added}\,|\lambda_i| \\
\underline{\alpha}_{\,added} &= \sum_{i=1}^{3} P_{i\ added}\,\alpha_i \\
\underline{\beta}_{\,added} &= \sum_{i=1}^{3} P_{i\ added}\,\beta_i
\end{aligned} \tag{4.15}$$

$$\begin{aligned}
\underline{\lambda}_{\,removed} &= \sum_{i=1}^{3} P_{i\ removed}\,|\lambda_i| \\
\underline{\alpha}_{\,removed} &= \sum_{i=1}^{3} P_{i\ removed}\,\alpha_i \\
\underline{\beta}_{\,removed} &= \sum_{i=1}^{3} P_{i\ removed}\,\beta_i
\end{aligned} \tag{4.16}$$

Using equation 4.15 and 4.16 into equation 4.9, an RGB representation for the added and removed scattering mechanisms between a couple of acquisitions can be obtained.

4.6 Results and Interpretation of PolSAR Change Detection

Figure 4.3 shows the change detection results applied over four different pairs of images along the season in the test site 1. To describe the changes between images we will focus on the rice fields which are represented by the pink colour in figure 1. Although other interesting behaviour is observed in the smaller fields nearby, no description is given since ground truth for these fields is not available in this dataset. A single incidence angle is considered to provide an interpretation of the observed PolSAR changes between the following set of pairs of images:

- Pair 1: From 2014-06-05 to 2014-06-29 (fig 4.3a)
- Pair 2: From 2014-06-29 to 2014-07-23 (fig 4.3b)
- Pair 3: From 2014-07-23 to 2014-08-16 (fig 4.3c)

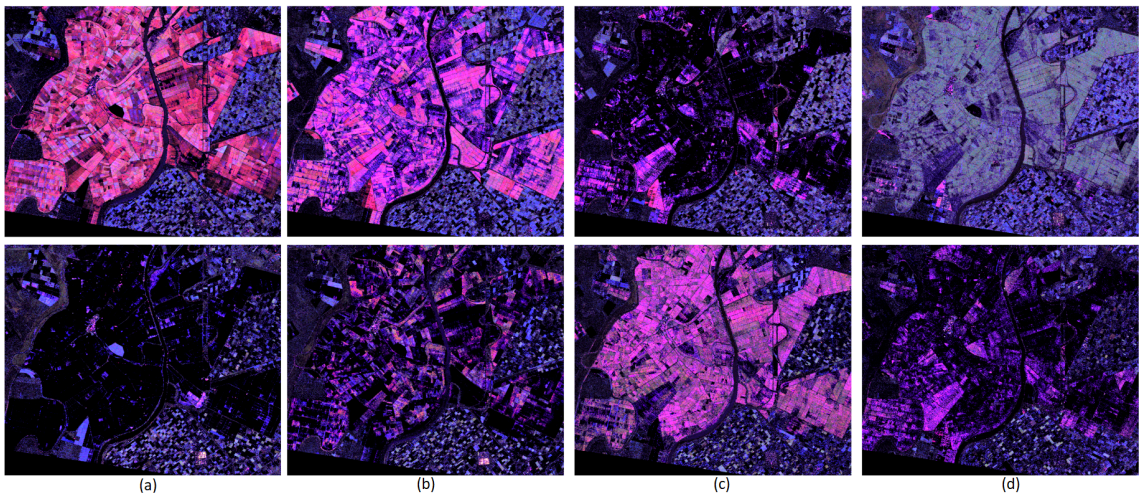

Figure 4.3: RGB composite of changes detected in test site 1. The colours represent Red: Double bounce, Green: volume scattering, Blue: Surface scattering. The brightness of the pixel corresponds to intensity of change. Top row: Scattering mechanisms added to the scene. Bottom row: Scattering mechanisms removed from the scene. Changes from: a) 2014-06-05 to 2014-06-29, b) 2014-06-29 to 2014-07-23, c) 2014-07-23 to 2014-08-16, d) 2014-08-16 to 2014-09-09

- Pair 4: From 2014-08-16 to 2014-09-09 (fig 4.3d)

Pair 1: Figure 4.3a shows the change in scattering mechanisms from the beginning to the end of June when the phenological information confirms that on 2014-06-05 most of the parcels have been already flooded while on 2014-06-29, the majority of the parcels reached the tillering stage. In the top plot of figure 4a, we can see a strong increase in double bounce (red) mostly due to the SAR signal bouncing in the water surface, then to the emerging plants in tillering and back to the satellite. Few parcels also depict blue colour since not all parcels share the same starting date or might be shortly delayed in the growth process. Note at the bottom plot of figure 4a that mostly dark areas are present meaning that the scattering mechanisms that are removed from the scene are not strong. This can be associated with the fact that the parcels transitioned from flooded fields to fields with short vegetation and therefore the power of the acquisition is stronger at the end of June than at the beginning, causing the majority of the SMs to be added rather than removed.

Pair 2: A similar behaviour can be observed for change in SMs from the 29th

of June to the 23th of July when the fields reach the vegetative stage and plants continue to get more vigorous. However, the intensity of the SMs that are added to the scene is not as strong as the change between the previous pair since the overall change in the backscatter power is not as high. Note that the colour depicted in fig4b resembles more a pink colour rather than only red, indicating a combination of added double bounce and surface scattering. This might be explained since stronger and more vegetative structures are added to the scattering scene due to the increase in the plants height and the number of tillers. Note that this does not necessarily mean that surface scattering is predominant in the scene but that the surface scattering in July was stronger than in June. As a consequence, there is an increase in the intensity of both surface scattering and double bounce. Similar to the previous pair, the SMs that are removed from the scene are not strong, however, some weak red colour can be seen in the bottom plot of figure 4.3b, indicating the removal of double bounce in those parcels.

Pair 3: The pair from the 23th of July to the 16th of August shows mostly dark areas indicating no added scattering mechanisms to the scene (figure 4.3c). This can be explained since the plants are reaching the advanced vegetative state in the 16th of August image therefore starting to lose the vigour and vertical structure and producing a less strong backscatter response than in the 23th of July image. On the contrary, the bottom plot shows that the combined double bounce and surface scattering that had been added from June to July, are now being removed from the scene given the weaker structure of the plants once they reach late vegetative stages. This is the only pair of images in which the removed scattering mechanisms are stronger than the added ones.

Pair 4: Figure 4.3d shows an increase in green colour in the top plot, corresponding to the addition of volume scattering from the 16th of August to the 9th of September. By the latter date, plants have reached maturation, lost water content and the vigorous vertical structure allowing the SAR signal to interact with plants, soil and simultaneously with both in a combination of the three scattering mechanisms. In the bottom plot of figure 4.3d, it is possible to see that it is mostly characterised by dark areas with again weak pink color being removed from some parcels, in this case due to these parcels being delayed in the growth process and

showing the same effect than the removed SMs in the previous pair.

4.7 Change matrix and target dynamics

Since the information about the crop evolution is obtained from the analysis of pairs of acquisitions, it is possible to evaluate not only changes from consecutive dates but also to see how any given acquisition differs with respect to all the other acquisitions in the stack of co-registered images. This process identifies the evolution of the scattering mechanisms throughout the season.

Inspired by Alonso-González et al. (2020), we organised the PolSAR changes not only between consecutive images but between all the images in the stack as a NxNx3 square matrix, with N being the number of images in the stack, and three given the RGB representation of equation 4.9. The off-diagonal elements correspond to the evaluation of polarimetric changes between the available dates. The upper triangular part is designed to represent the scattering mechanisms that are added to the scene between a given pair of images and the lower triangular part to represent the ones that have been removed. Note that the diagonal elements of this matrix can also be employed if desired, by obtaining the dominant or average scattering mechanism in the scene for a given date as introduced in section 4.4.1.

It is worth noticing that the color representation of added or removed scattering mechanisms in the square matrix is in the same way as described in section 4.9. Therefore, the change matrix is an RGB composite that depicts with the color the type of change and with the contrast the intensity of the change between a given pair of dates.

4.7.1 Target dynamic analysis

To illustrate the evolution of a target scattering mechanisms over time and relate them to physical changes, figure 4.4 shows the SMs throughout the season of a rice parcel in the test site 1, where the ground truth is known. The colours and intensities of the change matrix can be interpreted as a conventional Pauli RGB composite, that is, red for double bounce, green for oriented dihedral or volume and blue for surface scattering.

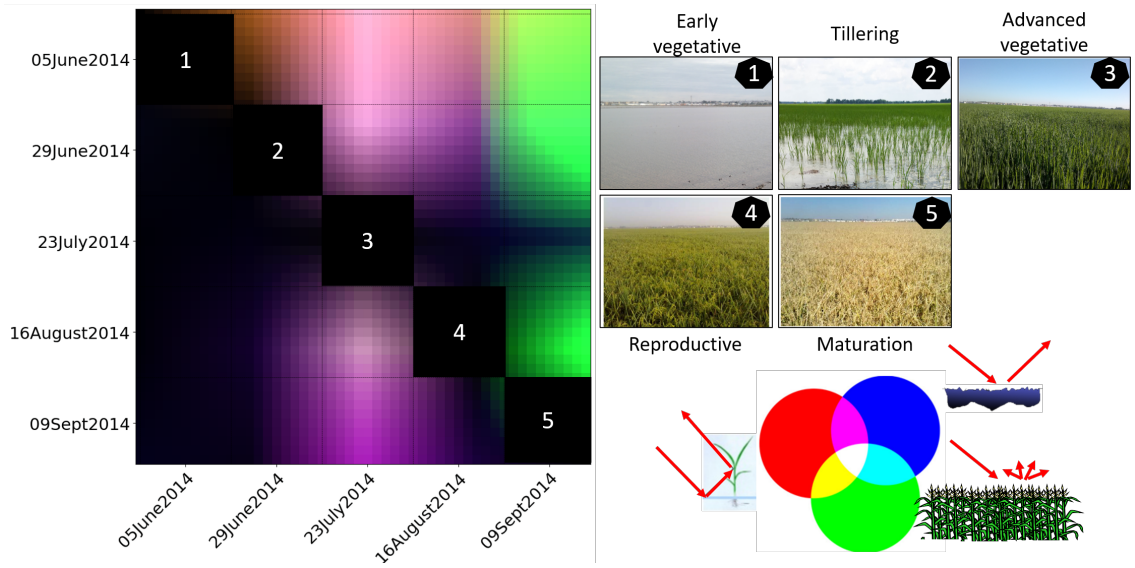

Figure 4.4: Typical rice change matrix. Left: Change matrix. Top right: Main rice growth stages. Bottom right: RGB interpretation of added and removed scattering mechanisms (SMs). The added and removed SMs between two stages correspond to their intersecting squares in the upper and lower triangular part, respectively.

Due to the rice crop cultivation practices in which the season starts with seeding over flooded soils with low backscatter returned to the satellite, the multitemporal change detection process mostly identifies increase in scattering mechanisms when compared to this initial stage. This is reflected by the upper triangular elements of the change matrix of figure 4.4, having marginally stronger intensity than the lower triangular part. In figure 4.4, the squares and circles with the numbers 1 to 5 correspond to the main growth stages of rice. The SMs added between two growth stages can be seen as the intersection between the squares of both stages in the upper triangular part. The intersection of these stages in the lower triangular part represents the SMs that are removed from the scene. It is possible to see for instance, that double bounce is added to the scene between stages 1 and 2 represented by the red colour, which is assumed to be caused by the interaction of the SAR signal with the plant stems emerging from the water at tillering stage. Although is almost imperceptible, dark blue appears in the leftmost column of the change matrix indicating that surface scattering is removed from all stages when compared to square 1 (flooded soil).

When the crop reaches the advanced vegetative stage in July, more vegetative

structures are added to the scattering scene due to the increase in the plants height and the number of tillers. As a consequence, there is an increase in the power of the returned backscatter and addition of both surface scattering and double bounce is observed. This combination is reflected in the change matrix with purple colour in the intersection between squares 1 to 3 and 2 to 3. On the contrary, the biggest decrease in the intensity of change occurs in the transition between vegetative to reproductive stages (end July to end of August). This is observed due to the plants starting to lose the vigorous vertical structure when entering into the reproductive stage. The change matrix shows at this point, decrease in surface and double bounce in the intersection between squares 3 to 4 in the lower triangular.

At the end of the season (rightmost column) an increase in green color corresponding to volume scattering being added to the scene when the crop reaches maturation can be seen. This is communicating that comparing stage 5 with any stage from 1 to 4, volume scattering is added. This is as a consequence of the plants random orientation and also due to the plants getting drier and therefore more transparent to the SAR signal causing multiple scattering to be present in the scene. Traditional polarimetric analysis has reported similar results with high values of entropy at this stage (Lopez-Sanchez et al., 2014; Lopez-Sanchez et al., 2017).

4.7.2 Other crop and land types

To generalize the usefulness of the change matrix for target dynamics analysis, we obtained the change matrix for other crops included in the test site 2. The obtained results are shown in figures 4.5, 4.6 and 4.7. It is possible to see by visual inspection how different the resulting matrices are for each of these three crop types and to that of the rice crop presented in figure 4.4. This shows how the matrix encodes differently the temporal PolSAR evolution for each crop type characterizing it in a specific way. The analysis correlating the crop morphology at the different growth stages can also be used with these change matrices to understand the interaction of the SAR signal with each crop throughout the season.

It is important to notice that because the matrix contains separately each scattering mechanism (in each channel), the analysis of the parcel evolution can be done for each mechanism separately. For instance, we can compare if the double bounce

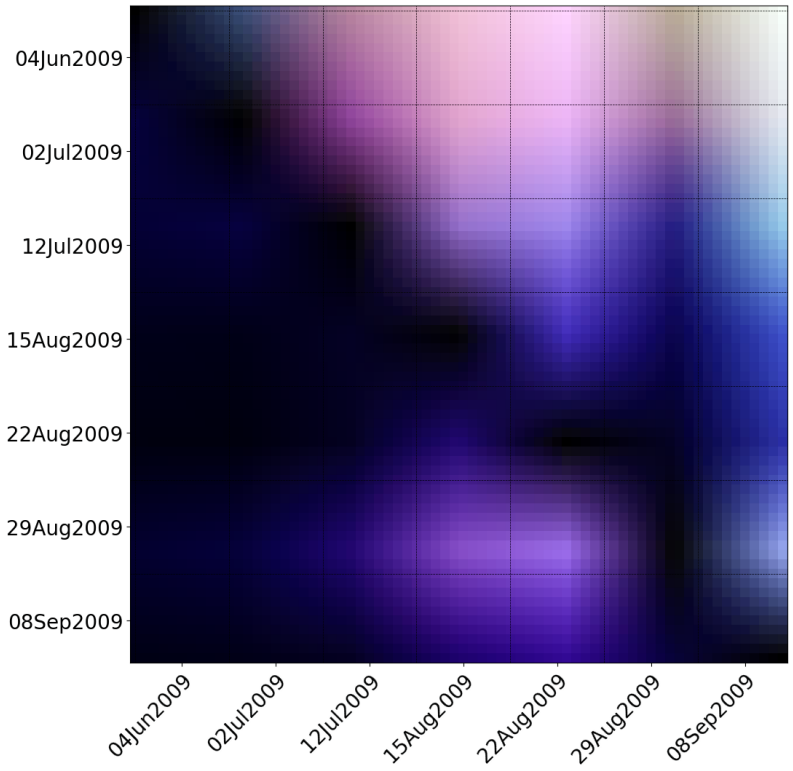

Figure 4.5: Typical Barley change matrix. The added and removed SMs between two dates correspond to their intersecting squares in the upper and lower triangular part, respectively.

in a parcel due to the plants emergence above the water level is delayed in time relative to other parcels or a reference parcel.

On the other hand, similar effects were observed for other land types, such as rivers, forests, cities where each of these land types created a change matrix with specific behaviour. These differences, described by the colours that represent the evolution of scattering mechanisms, the intensity of the change matrix and the times when specific events occur, can be used to characterize a crop type or more generally a land class and, consequently, this information can be exploited as input for image classification.

4.8 Crop type classification

It was shown in section 4.7 how the change matrix can be used to visualize, understand and characterise the interaction and response of the radar signal with a target that evolves over time. This section presents the application of the change

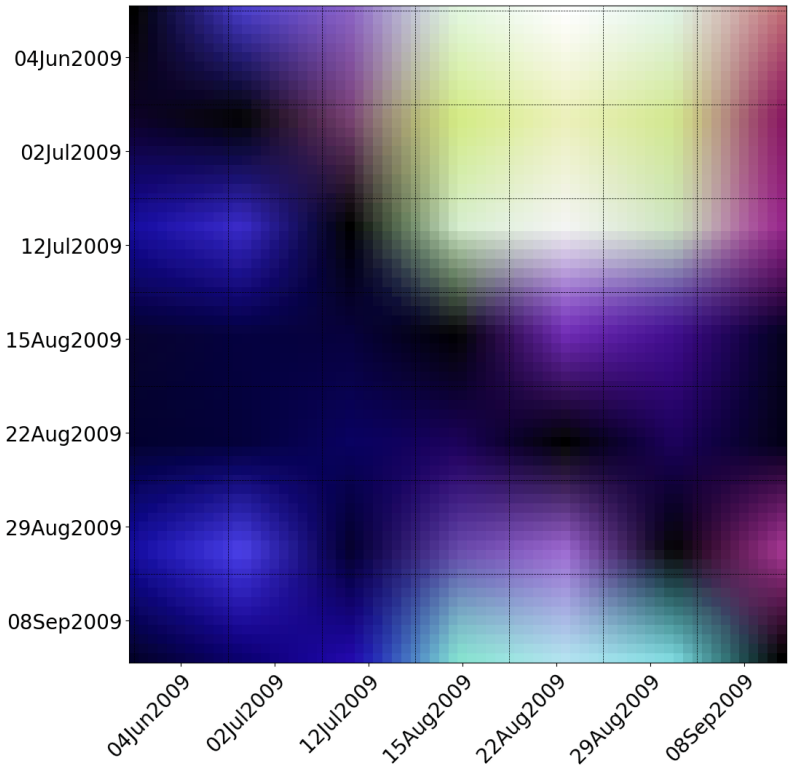

Figure 4.6: Typical Canola change matrix. The added and removed SMs between two dates correspond to their intersecting squares in the upper and lower triangular part, respectively.

matrix for multitemporal image classification. It considers the proven fact that multiple acquisitions provide better performance results than single image classification while also considering the fully polarimetric information measured by the satellite (McNairn & Shang, 2016a; Skriver et al., 2011).

In order to investigate the change matrix potential for image classification, change matrices are used as inputs for a fully connected Neural network (NN) classifier. Its performance is then compared with a classification based on time series of PolSAR features, where the features are derived from covariance matrix decompositions (Lee & Pottier, 2009).

4.8.1 Dataset splits, metrics and classifier

4.8.1.1 Dataset splits

In all cases, the parcels where ground truth is available are divided into three groups: Training (65%), validation (15%) and test parcels (20%) preserving in all cases the

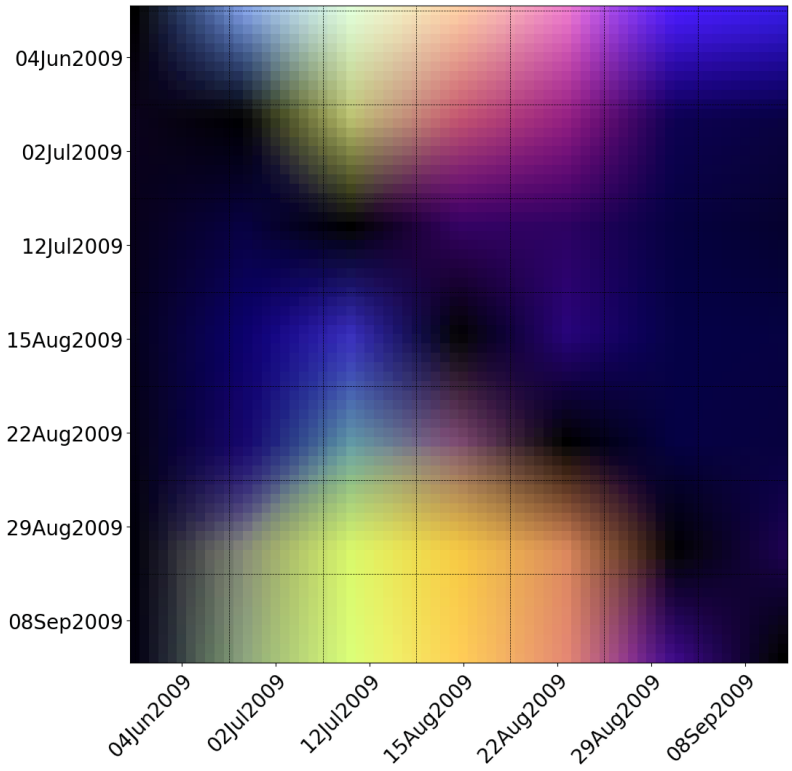

Figure 4.7: Typical Field Pea change matrix. The added and removed SMs between two dates correspond to their intersecting squares in the upper and lower triangular part, respectively.

same proportion of samples per class as in the original dataset. Note that we split the data ensuring that the resolution cells belonging to a parcel are only present in one of the sets (i.e. training parcels independent from validation and test parcels) considering that neighbouring pixels would have correlation due to spatial filters and other pre-processing steps, such as multi-looking, speckle filter and co-registration. Without doing this, the test set would contain samples very similar to those in the training set and the model would give over-optimistic performance after predicting on test set. After splitting the available ground truth and removing the crop types where the data is not enough for training and testing a model, the dataset is reduced to 10 crop types and results in a highly imbalanced distribution of pixels for training, validation and testing in each class. Accordingly, both the classifier and the metrics used are adjusted to account for this effect.

4.8.1.2 Neural network classifiers

A fully connected neural network is used for classification in all the cases presented in the following subsections. Hyperparameter search was performed to select network depth, width and need for dropout layers, and to select the optimizer and learning rate. This resulted in a NN with three hidden layers of 256 neurons each, using batch normalization before every hidden layer and before the output layer, and Nadam optimizer with learning rate of 0.0005. To deal with the class imbalance as previously stated, the model is trained using weighted cross entropy loss function, in which the weights correspond to ratios obtained from the class imbalance. Note that randomly sub-sampling the majority classes before training was also tested, delivering similar or slightly lower performances. On the other hand Random Forest based classifiers were also tested also with lower performance.

4.8.1.3 Metrics

The accuracy metric is traditionally reported to evaluate classifiers performance. However, since it relies on the frequency with which the model predictions on the test set match the ground truth, in imbalanced classification problems the results are dominated by the majority classes and with small contribution by the minority classes (Santos et al., 2018; Sun et al., 2009). To account for this, we report the balanced accuracy metric which is the accuracy adjusted by their corresponding class weight (ratio of samples per class over the total number of samples). We also report the per-class F1 score, recommended for imbalanced classification (Santos et al., 2018; Sun et al., 2009), and compute the macro average F1 measure to average across classes.

To be able to compare the obtained results with other works, we additionally report the traditional overall accuracy which we call imbalanced accuracy, since it does not account for the class imbalance present in the data.

4.8.2 Change matrix based classification

The change matrix (CM) of size NxNx3 derived in section 4.7, where N is the number of dates, is flattened as a one-dimensional array and received by the input layer of

Table 4.3: Classification results using the flattened change matrices and PolSAR features as input for the NN.

Metric	**Change Matrix**	**PolSAR-features**
Balanced accuracy	0.671	0.667
F1 macro	0.623	0.614
Imbalanced accuracy	0.788	0.777

the NN. For the present analysis 7 images corresponding to the dates shown in table 4.2 are used, thus resulting in a 147 input feature vector.

Figure 4.8 shows the confusion matrix obtained after predicting on the test set. It can be noticed that the CM-based classifier performs well predicting crops such as canola, field peas, lentil and mixed pasture and that it under performs predicting crops such as barley, durum wheat, oats and spring wheat, mostly due to confusion in the prediction between these four classes. This is in part explained considering that these crop types have similar biophysical characteristics being all of them part of the family of cereal crops, therefore producing similar PolSAR responses. Table 4.3 shows the corresponding metrics obtained on the test set after training the models. It can be seen in the change matrix column that both the overall balanced accuracy and the F1 macro metrics are relatively low mainly due to the confusions made by the classifier within the cereal crops predictions. Note that the overall imbalanced accuracy gives the impression of a better classifier performance, although in this particular case it can be attributed to the class imbalance in the dataset.

If instead of classifying cereal crops individually but a single class is used for all of them (barley, durum wheat, oats and spring wheat), the classification performance increases significantly as presented in the figure 4.9. In this case most classes are predicted correctly, being flax the crop less accurately predicted with some confusions with the cereal crops and pastures. Also notice that the performance of the classifier predicting canola in the test set is very high since this crop structure and its evolution over time is considerably different with respect to the other crops under analysis.

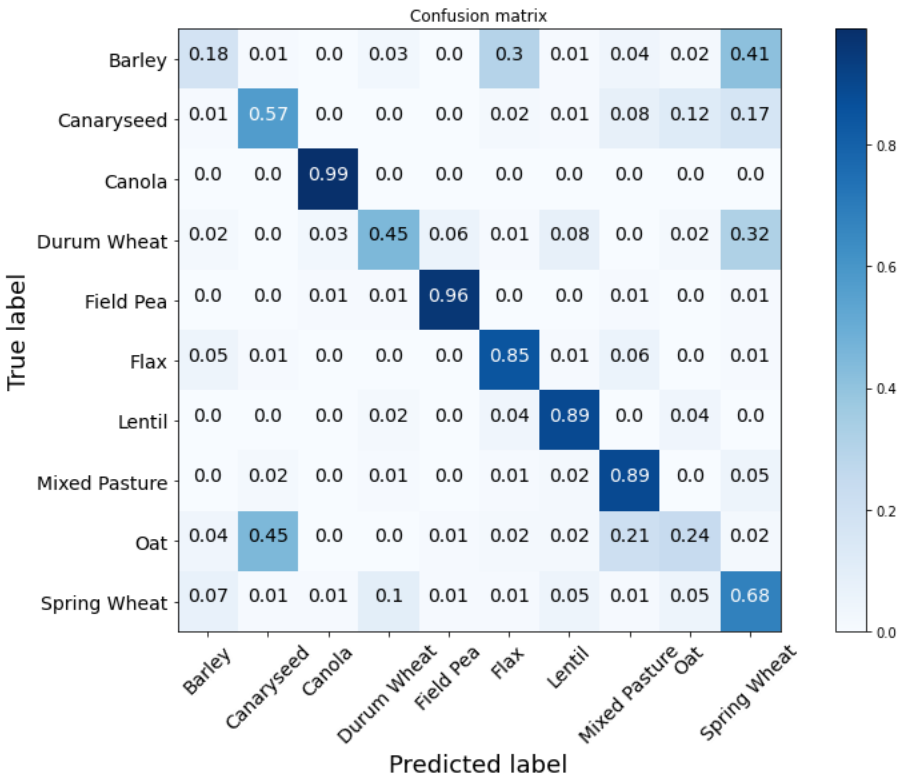

Figure 4.8: Confusion matrix for the change matrix based classification when predicting 10 crop types.

4.8.3 PolSAR-features based classification

Time series of backscatter and PolSAR features derived from the H/A/alpha decomposition of the coherency matrix (S. R. Cloude & Pottier, 1996; Lee & Pottier, 2009), were obtained and used as input for an additional Neural network to compare its performance with that of the CM-based classification. A total of 16 features time series were considered, including the VV, VH, HH backscatter, the ratios VH/VV, HH/VH, and HH/VV, dominant and average eigenvalues, dominant and average alpha angles, dominant beta angle, entropy, anistropy and the magnitude of the scattering mechanisms computed as $\sqrt{\underline{\lambda}} * \cos(\underline{\alpha})$, $\sqrt{\underline{\lambda}} * \sin(\underline{\alpha}) * \cos(\underline{\beta})$, $\sqrt{\underline{\lambda}} * \sin(\underline{\alpha}) * \sin(\underline{\beta})$.

Figure 4.10 shows the confusion matrix for this case, with most classes having a similar performance than the CM-based classification, except for Canary seed and field peas where the CM-based classifier seems to have slightly better performance, and showing that using PolSAR time series features the classifier also has confusions identifying the cereal crops.

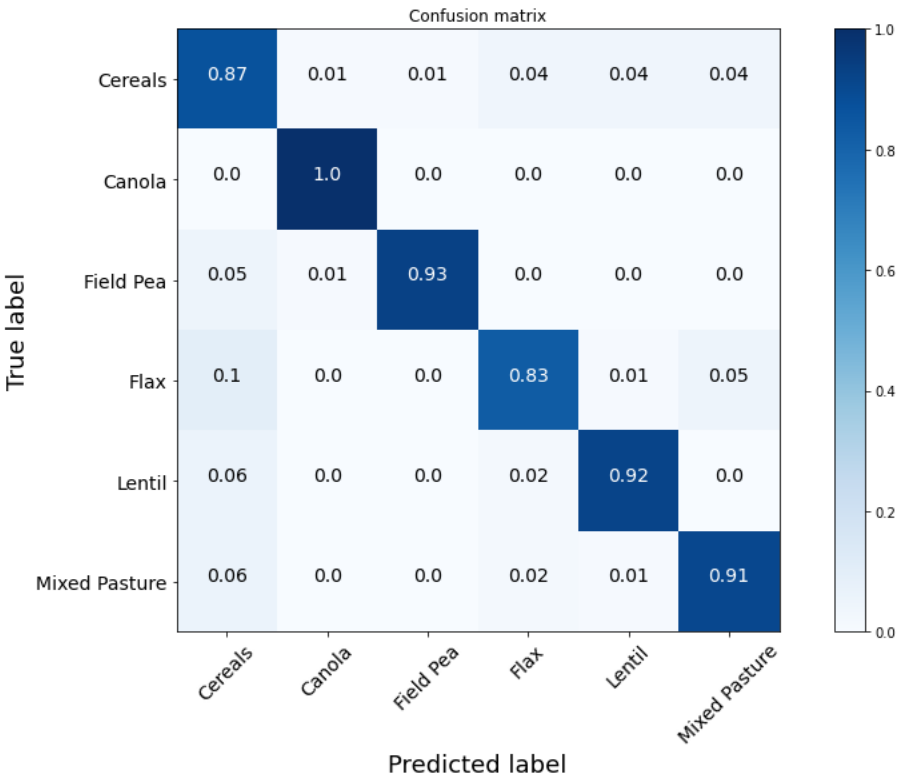

Figure 4.9: Confusion matrix for the change matrix based classification when predicting 6 crop types.

In terms of overall performance, table 4.3 shows that the classifiers using both input data types (i.e. change matrices or PolSAR time series features) seem to have very similar resulting test metrics and the balanced accuracy as well as the F1 macro which are particularly important for imbalanced classification, are slightly better for the change matrix based classifier. Note however that because the differences are not large enough (around 1%) a definite conclusion about which input data type performs best is not possible.

After grouping the cereal crops in a single class and training a NN classifier to predict the reduced set of classes, the results obtained are shown in figure 4.11. Again significant improvements are achieved compared to a classifier predicting the cereal crops separately and improvements in all crops types apart from mixed pasture are also achieved with respect to the CM-based classification. With regards to overall performance, table 4.4 shows that the classifiers using both input data types have similar resulting test metrics, however, note that for this case of the reduced set of classes the balanced accuracy and the F1 macro are both metrics approxi-

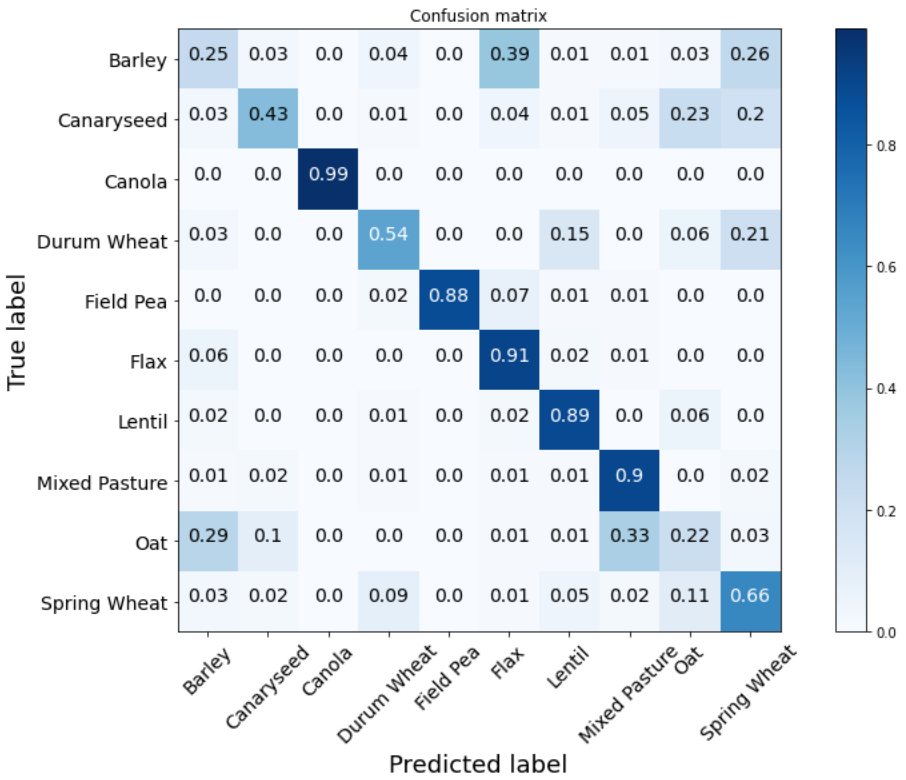

Figure 4.10: Confusion matrix for the PolSAR-features based classification when predicting 10 crop types.

Table 4.4: Classification results when predicting the cereal crops in a single class.

Metric	**Change Matrix**	**PolSAR-features**
Balanced accuracy	0.908	0.928
F1 macro	0.839	0.867
Imbalanced accuracy	0.910	0.933

mately 3% better for the PolSAR time series based classifier than for the CM-based equivalent. This is opposite to the results of table 4.3 where the CM-based outperforms the PolSAR-features based classification. Since neither of the two tables show large differences between metrics a definite conclusion about which input data type performs better is not possible but rather we see that the performances are comparable.

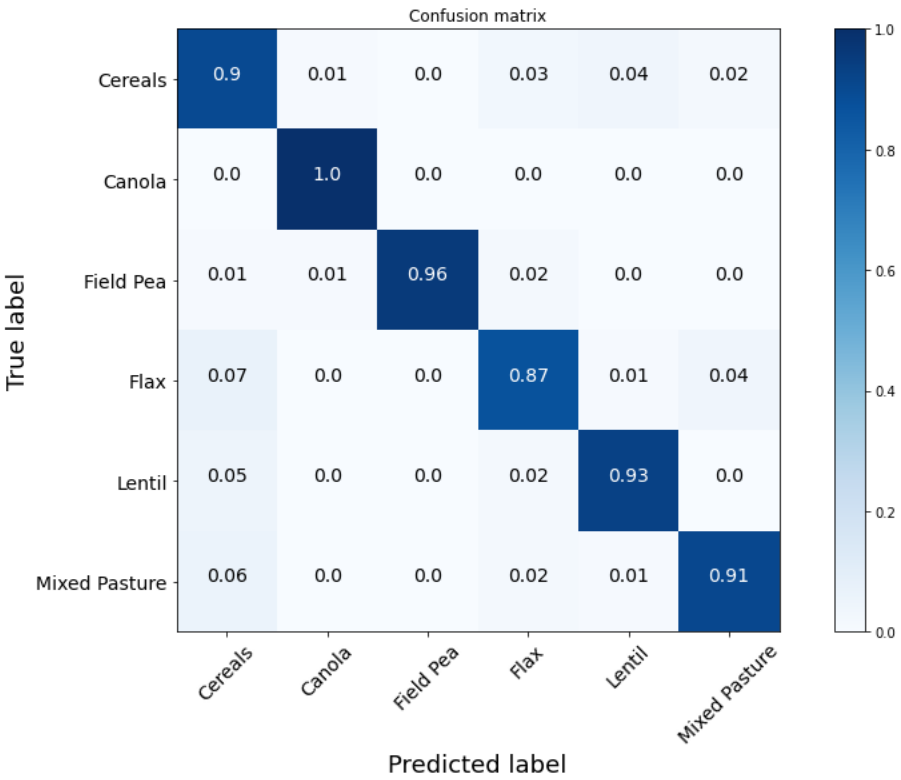

Figure 4.11: Confusion matrix for the PolSAR-features based classification when predicting 6 crop types

4.8.4 Prediction maps

The trained models can now be used for predicting on the whole test site as shown in figures 4.13 and 4.15 for the 10 classes case, that is, the cereals crops as independent classes, and for the 6 classes by combining the cereal crop types, respectively.

We can notice in figure 4.13 similar results to those obtained in the confusion matrices, in which canola, lentil, field peas and mixed pasture have strong agreement with the ground truth, whereas the cereal crops are confused between them. Figure 4.15 also shows the confusion of the model to predict flax as a cereal crop.

4.9 Discussion

This paper addresses a method to process and analyse multitemporal and quad polarimetric SAR data. This aims at developing a methodology that helps reducing the complexity when analysing time series of polarimetric features. As shown in section 4.7, inspired by Alonso-González et al. (2020), we use quad-pol change

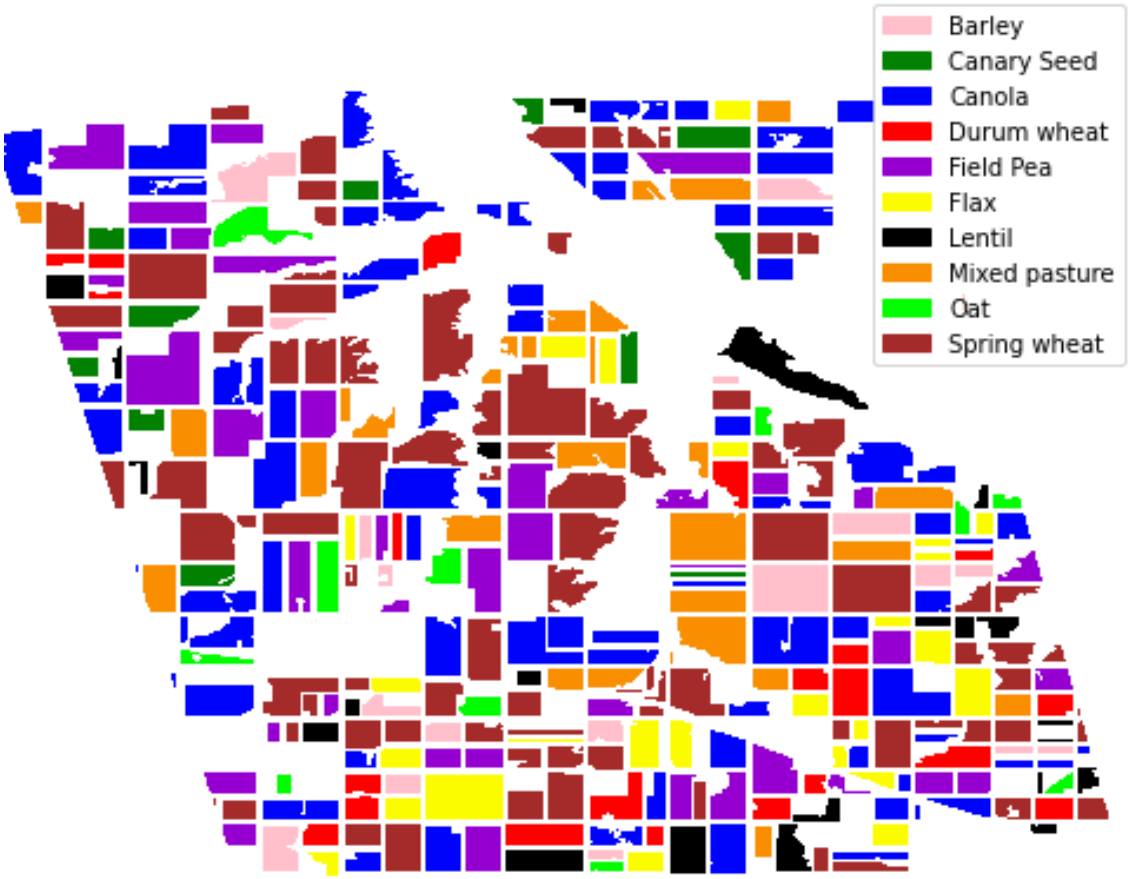

Figure 4.12: Ground truth map when predicting 10 crop types.

detection to encode the evolution of scattering mechanisms over time in a change matrix. The proposed change matrix can be interpreted intuitively by looking at its colours and intensities. Note that in this paper, in order to have a more straight forward interpretation of the scattering mechanisms, a change detector based on the difference of the covariance matrices is used as opposed to the power ratio used by Alonso-González et al. (2020). This is also an improvement compared to previous approaches that propose a multitemporal change detection (Conradsen et al., 2016; A. Nielsen et al., 2017) and change matrices (Lê et al., 2014; Lê et al., 2015), however, only exploiting intensity of changes without using the polarimetric information available.

In section 4.8, we address the performance for image classification using the change matrix as input. This was compared to more traditional classifiers that use multitemporal quad-pol features as inputs. Experimental results indicate that comparable levels can be obtained for image classification purposes when using the

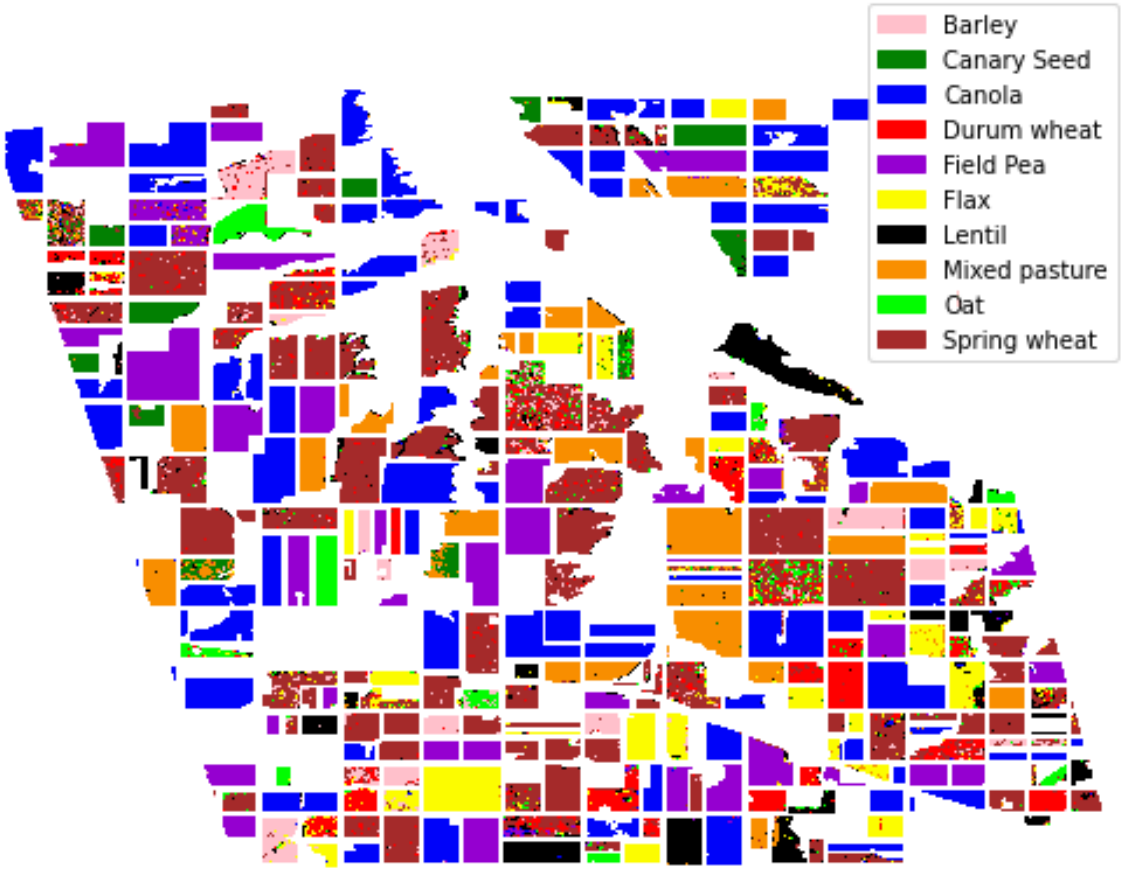

Figure 4.13: Prediction map using the CM-based classifier when predicting 10 crop types.

change matrix as input for a machine learning classifier. Note however, that the change matrix allows one to have an interpretable idea of the input data being used, while simultaneously providing a single method for crop monitoring over time and crop type classification. The crop type classification outcome could be improved further by implementing a post-processing spatial filtering stage such as a majority vote moving window or using morphological filters. This would smooth the predictions at pixel level by considering spatial information. Although it was not implemented in this paper to avoid biases when comparing the proposed change detection methodology and state of the art classifiers, it could increase the accuracy achieved by the predictive models.

Regarding transferability of the methodology presented in this chapter, since the change detection proposed here for crop monitoring does not require ground truth, it can be implemented in other sites where Quad-PolSAR data is available. While having information about the crop being monitored aids the interpretation, the current

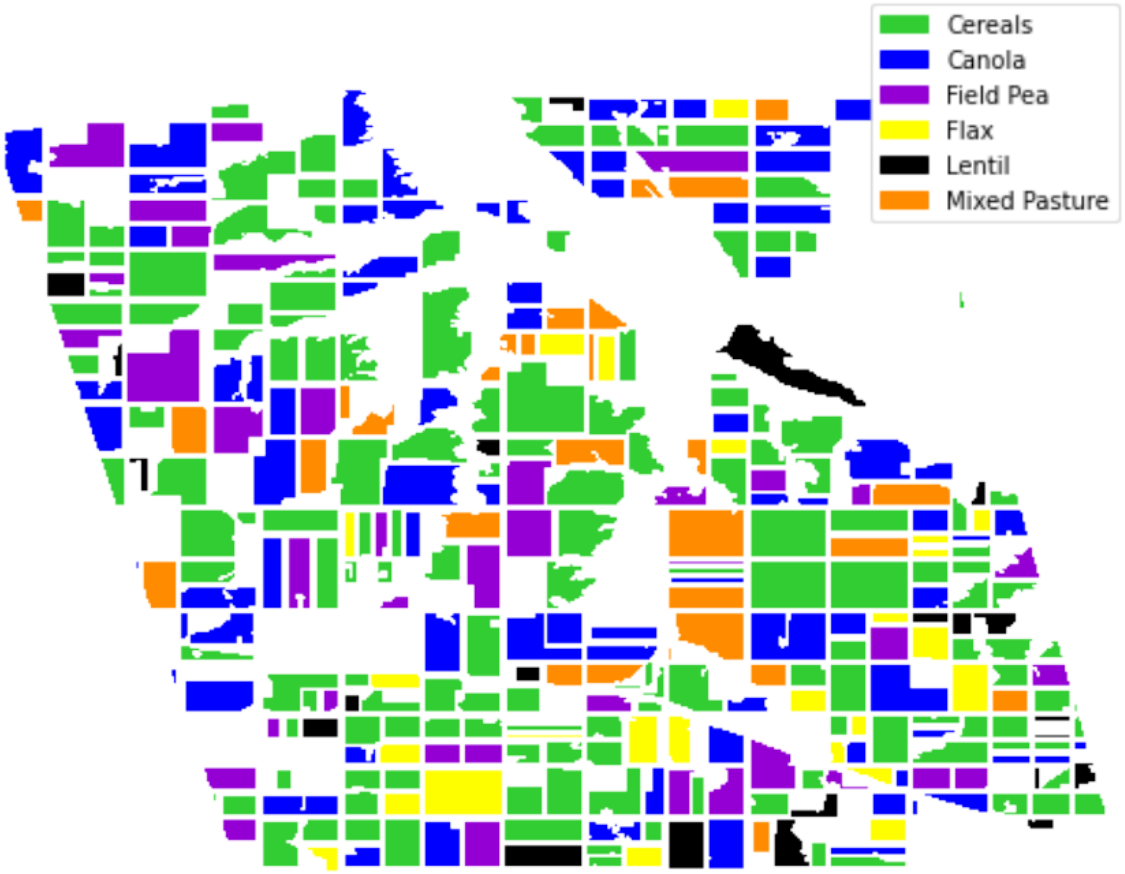

Figure 4.14: Ground truth map when predicting 6 crop types.

method will provide information about the changes in crop scattering mechanisms and which can be then linked to the crop growth stage. It is important to consider the influence of the incidence angle since combining different acquisition geometries currently results in undesired artifacts due to combined detection of changes in both the crop growth and the observation geometry. Using the change matrix for crop growth, a simple solution would be to restrict the detection of changes to the same orbit as in figure 4.3 resulting in increasing the time between images. However, for current constellations this might be acceptable since it can reach times of 6 days, for example for the case of Sentinel-1. A different approach could be to perform incidence angle normalisation before the change detection step as for instance in Bauer-Marschallinger et al., 2018. Note that the influence of the incidence angle when using the change matrix for crop type classification is expected to be less significant. This is because both the training and test pixels (or pixels in the region of interest) contain the effect of the incidence angle. Therefore, a classifier could predict crop types since it receives the same information at training and testing

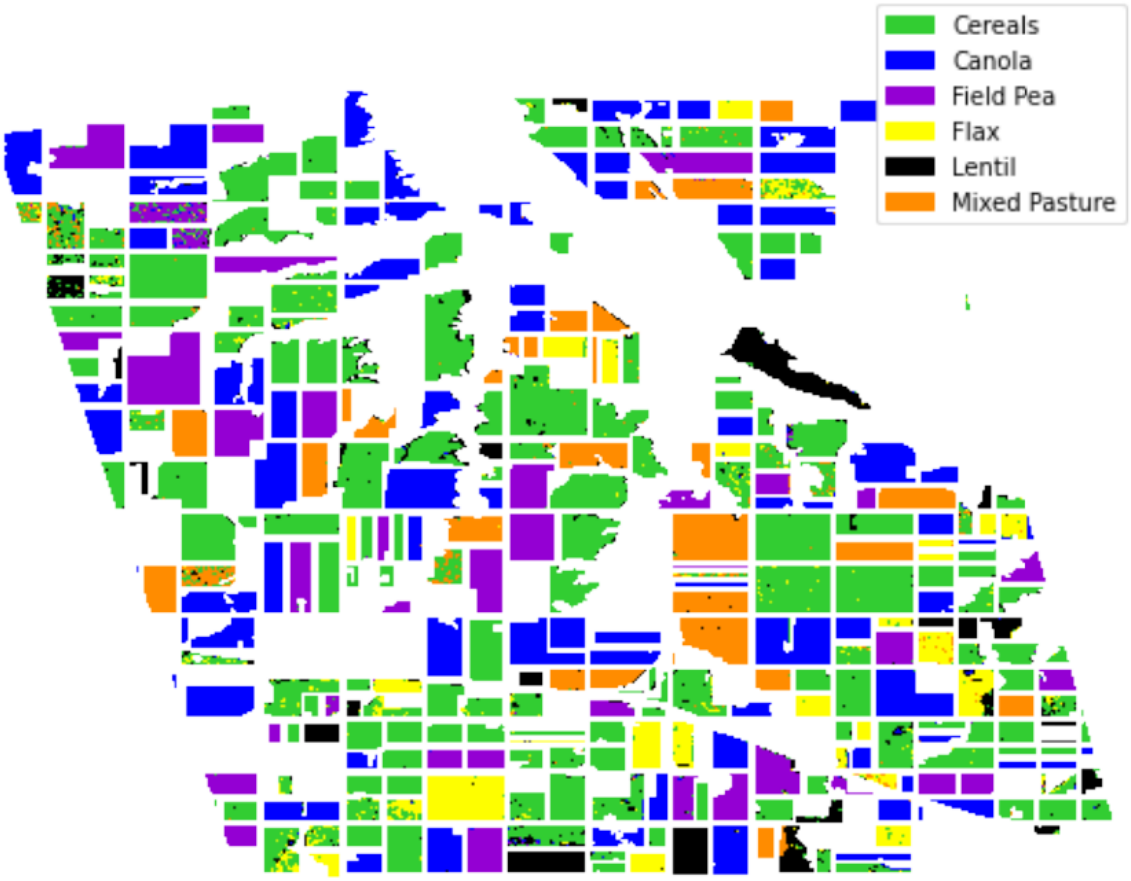

Figure 4.15: Prediction map using the CM-based classifier when predicting 6 crop types.

times. The acquisition geometry, however, requires more detailed consideration and will be addressed in future work. Also for forthcoming investigation, other methods that create multitemporal matrices can be integrated to the present methodology. These methods, recently introduced in the literature, use interferometric coherence between images Jacob et al., 2020; Mestre-Quereda et al., 2020 instead of the polarimetric information. Therefore, combining the PolSAR and InSAR data, may result in complementary information being used as input for the classifier in order to boost performance. Similarly, a next step developing the change matrices methodology is to adapt it to dual pol systems such as the Sentinel-1 satellite. This is done by replacing the 3x3 pixel covariance matrices derived for monostatic Quad-pol systems of equation (4.10), for the 2x2 matrices formed using the two polarisations provided by Sentinel-1. Note, however, that the visualisation and interpretation need to be adaptaded accordingly.

A current limitation of the proposed method is that the crop stage monitoring

was addressed using 5 phenological stages and not a more granular index of phenology. This aspect is currently being addressed and will be shown in future work. In addition, we have noticed that differences in colour and intensity and deviations from a typical change matrix can be identified visually. This can also be used as a tool for in-season crop growth anomaly detection and will be the focus of future research. Lastly, the computational efficiency of the change matrix needs to be increased considering that it grows over time, as new images become available. Investigations in this regard are being undertaken.

4.10 Conclusion

This article presents a change detection-based method to visualise and analyse multitemporal quad polarimetric images. The change detector is derived as the pixelwise difference of covariance matrices between all the co-registered images in a stack, which organised in a matrix form, allows the interpretation of the evolution of scattering mechanisms over time. We showed how growth stages of rice fields can be related to the scattering mechanisms observed and how it differs from other crop types. Based on this property of encoding the scattering mechanisms for each crop type, we tested the performance of the proposed method for image classification to identify several crop types. Results show that this method yields similar performance to traditional classifiers, which use time series of polarimetric features as input with differences in the overall balanced accuracies and F1-macro metrics of around 1% or 2% in favour of one or another based on the number of classes used. The method presented here achieves similar classification performances while providing additional advantages in terms of interpretability and insight into the physical changes of a target over time. It also provides a different view of the change of crop states that could be incorporated to provide a broader view of the whole dynamic system.

Chapter 5

General Discussion and Conclusion

Space-borne earth observation represents a key tool, enabling access to multi-scale and frequent data for stakeholders within the agricultural supply chain. It is considered an important medium for informed decision making that promotes sustainable and profitable crop management practices. The ability of SAR systems to acquire images without interruptions and their capacity to respond differently to geometrical and dielectric properties of objects, shapes and vegetation states, represents a unique opportunity for timely monitoring of crop biophysical variables. In this context, improving our sets of tools and techniques for exploitation of SAR data for croplands monitoring is essential.

The work of this thesis contributes to current state of the art knowledge and methodologies for agricultural fields monitoring, using data derived from SAR satellites. This section provides discussion around this point, by focusing specifically on three aspects:

(a) A synthesis of the main findings of the thesis and their importance in connection with the existing literature in the field.

(b) Future research directions, underpinned by this thesis.

(c) Recommendations and concluding remarks, in terms of the selection of algorithms for near real-time monitoring of agricultural fields from space-borne SAR imagery.

5.1 Synthesis of findings in the context of the existing literature

An important finding of this thesis is that asparagus crop phenology can be monitored from multitemporal SAR data. Chapter two shows that the C-band SAR signal of the Sentinel-1 satellite is sensitive to asparagus crop development as the backscatter temporal response presents clear changes that can be associated with crop growth and/or management practices. We showed that particularly the VH backscatter is sensitive to crop growth, for instance, since the backscatter intensity rapidly increases in response to stem vertical elongation, caused by the double interaction between the SAR signal with the soil and the vertical stems. The backscatter then remains constant after the canopy reaches maturity as the signal mostly interacts with the fully formed canopy which does not suffer major biomass changes until harvest. The significant backscatter drop in both Sentinel-1 polarisation channels was also associated (through ground truth) with the fern mechanical removal at harvest time. The temporal backscatter signature of asparagus tends to follow a similar sequence to the scattering mechanisms observed for other crop types, such as rice (Lopez-Sanchez et al., 2014) and cereal crops (Vicente-Guijalba et al., 2015). In all of these cases, including asparagus, surface scattering is observed at the beginning of the season, then double bounce increases due to interaction of the signal with soil and vertical stems, and finally, volume scattering dominates once a canopy is formed and the crop reaches maturation. Two unique features, however, characterise the SAR response of asparagus from other crops. Firstly, being a perennial crop causes the backscatter to have a strong seasonal component, as a new agricultural season starts immediately after the end of the previous one, without crop rotation. Secondly, most of the changes in the backscatter time series can be observed in the first month of the season, as this is the time taken from emergence to canopy formation. Note that as the Peruvian test site has mild winters, the canopy does not reach senescence naturally and there are not significant changes in the canopy biomass. This is reflected in the backscatter time series which shows minimal change during this period. It is important to mention that before this thesis, only a limited number of studies had considered the use of radar remote sensing for monitoring asparagus

activities. In these cases, authors have specifically focused on asparagus crop identification using SAR imagery (Arias et al., 2020; Bargiel et al., 2010; Sabour et al., 2008; Tavakkoli & Lohmann, 2006). However, none of these studies investigated and interpreted the backscatter response to the crop growth stages and development over time, as was shown in chapter two. As such, it is the first time that evidence is provided to the literature about the potential for asparagus monitoring. Similarly, to the best of our knowledge, none of the previous studies evaluated the possibility of retrieving asparagus crop stage, as was proposed in this thesis using a machine learning approach (section 2.2.7). An important outcome of this was the use of ancillary data, such as multitemporal images, the season starting date or the season accumulated temperature, helps to separate crop stages that have similar backscatter response.

Note, however, that the work on asparagus of chapter two is limited in its scope since it only used one of three possible SAR acquisition geometries and does not have a straight forward integration with other satellite sensors. Similarly, as in several publications presented recently, (Küçük et al., 2016; Lopez-Sanchez, Ballester-Berman, & Hajnsek, 2011; Mascolo et al., 2015; Shang et al., 2013), the model presented for crop stage retrieval is not able to extrapolate predictions forward or backward in time. This means, for instance, that this approach does not allow to forecast when subsequent growth stages would be reached. In this regard, recent studies have shown that a Bayesian Filtering Framework (BFF) can be used to address these issues (De Bernardis et al., 2016b; De Bernardis et al., 2014b; McNairn et al., 2018; Vicente-Guijalba et al., 2015). BFFs enable near real-time crop monitoring by updating the state of the crop variables as soon as a new image is available. Similarly, as an observation model can be used separately for a given sensor, it allows to easily integrate several sensors observing the crop. Indeed, a study by De Bernardis et al. (2016b) fused SAR and optical data from the TerraSAR-X and the LANDSAT satellites for rice phenology tracking. The authors highlighted the benefits of the active passive sensor fusion for improving retrieval accuracy of rice phenology. Similarly, McNairn et al. (2018) fuse multifrequency SAR data using the X-band from TerraSAR-X and C-band from RADARSAT-2 satellites also emphasizing the benefits of the fusion for accuracy and reduction of temporal resolution

for monitoring canola phenology. Note, however, that the dynamic and observation models of these studies limit their transferability to other sites. In the case of De Bernardis et al. (2016b) since it uses parametric models specific for rice crops. In the case of McNairn et al. (2018) since the model relies specifically on temperature for the dynamic models and the observation models are not mentioned in the study. In this context, a key contribution of this thesis is the use of historical data and a data-driven approach to learn the predictive dynamic and observation models and the associated uncertainty with a model prediction. The Gaussian Processes based Extended Kalman filter (GP-EKF) proposed in chapter three of this thesis for asparagus below ground carbohydrates tracking, implement this and expands current state of the art studies for tracking crop variables.

First of all, since it is a learning-based method, it removes the requirement of fitting a parametric function for dynamic and observation models in the Bayesian Filtering Frameworks (i.e. Kalman and particle filters). This is a constrain that can be encountered in recent works (De Bernardis et al., 2016b; McNairn et al., 2018). On this basis, the GP-UKF of chapter three facilitates the transferability of the method to other crop types and regions where ground truth is available. This can be seen for instance with the use of the method for asparagus crops. Parametric dynamic and observation models for asparagus are not as common as those for cereal crops which are the crop types where most of the research in the literature has focused on (i.e. rice, wheat, barley) (De Bernardis et al., 2016b; Vicente-Guijalba et al., 2015). This means that obtaining these models can be time consuming, requires specific crop knowledge and may not be initially accurate. On the contrary, learning the models with Gaussian Processes, simplifies this task. Moreover, since the uncertainty associated with the model predictive accuracy and the training data availability is learnt alongside, their incorporation in Bayesian filtering frameworks is straight forward (Deisenroth et al., 2009; Ko & Fox, 2009; Turner et al., 2010).

In addition, the GP-UKF method was also presented with the use of freely available remote sensing data. Existing studies use quad-polarisation SAR as it provides more information to characterise a crop (De Bernardis et al., 2014b; McNairn et al., 2018; Vicente-Guijalba et al., 2015). This translates in the practice into having more SAR features helpful to separate crop growth states over a season. This is a more

complicated task using the dual-pol backscatter intensities of the free Sentinel-1 data alone as less information is available, and therefore, for this task we proposed to exploit the temporal data dimension. Specifically, we created SAR vectors of observations including the images available in the previous 100 days to characterise a crop state. This way the vector of observations contains more information and is able to discriminate between similar crop conditions. This has important implications since it gives opportunities for freely available data users (such as farmers in developing countries) to implement state of the art techniques.

Most of the work that reports monitoring biophysical variables from spaceborne SAR data, has focused on estimating crop phenology (Küçük et al., 2016; Lopez-Sanchez et al., 2014; Mascolo et al., 2016; McNairn et al., 2018; Shang et al., 2013; Vicente-Guijalba et al., 2015). To a lesser extent, other studies focused on the estimation of variables such as leaf area index (Bériaux et al., 2015; Kweon & Oh, 2014; Tao et al., 2016b), biomass (Hosseini & McNairn, 2017; Mandal, Kumar, McNairn, et al., 2019; Wiseman et al., 2014b) or crop height (Erten et al., 2016a; Xie et al., 2021b; Yuzugullu et al., 2016). However, an investigation reporting below-ground carbohydrates content from SAR observations of above-ground canopy condition of agricultural fields, has not been reported before (to the best of our knowledge). This is a novel contribution of this work, exploring additional capabilities of the exploitation of SAR data for agricultural applications.

It is to be noted that through the Unscented Transform, the GP-EFK approximates the crop states to Gaussian distributions. While this ensures the resulting filtering equations to be tractable or in closed form, the filter may lose representational power and hence accuracy. Compared to the sampling-based particle filters presented by De Bernardis et al. (2014b), De Bernardis et al. (2016b) and McNairn et al. (2018) which can deal with non-Gaussian distributions at expense of higher computational cost, this can be seen as a limitation of the GP-UKF. In addition, the process and observation noise for the two variables monitored are uncorrelated in the current version of the GP-UKF. This is a limitation first recognised in this study, since previous papers report only tracking a single variable. Despite not being implemented here yet, a potential solution using multi-output Gaussian Process models that learn correlated uncertainties is introduced in the discussion section of

chapter three.

In chapter four, a novel quad-PolSAR change detection based method is presented for crop monitoring and crop type classification. It builds upon recent state of the art change detection techniques based on the optimisation of the difference of the covariance matrices (Marino & Alonso-Gonzalez, 2018; Silva et al., 2018), which enables the extraction of information about the intensity and type of changes between a pair of PolSAR images. As mentioned in section 4.2, this is an improvement compared to classical methods that only focus in extracting intensity of changes, as it provides additional tools to infer what physical changes a target on the ground may be suffering. We also designed a novel visualisation method that allows straight forward interpretation of both intensity and type of changes between pairs of SAR images (Silva-Perez et al., 2021). By organizing the multitemporal polarimetric changes in a change matrix formalism, we ensure that it contains the added or removed scattering mechanisms of a scene, not only, from consecutive pairs of images, but also among all the images in a stack. Note that recent methods that focus in multitemporal PolSAR change detection only intent to determine when a given change happened in a time series without interpreting the types of changes in scattering mechanisms that a target undegoes (Conradsen et al., 2016; A. Nielsen et al., 2017). Moreover, other studies present ways to determine whether a target has been added or removed from a scene, for instance, if a strong response coming from a ship in the sea is now present in an image but was not in the previous one (A. A. Nielsen et al., 2019). Interestingly, the change matrix that we proposed, is able to present both, if a target has been added or removed from a scene and also how the scattering mechanisms changed due to the added/removed target. In regards to organising multitemporal changes in a matrix form, some studies have previously presented work upon this idea. These works, however, use only a single polarisation (Lê et al., 2014) or provide information about how dynamic or stable a pixel is (Lê et al., 2015), without providing insight into the kind of process that may be happening in the pixel, as it our change matrix approach can do. In this thesis, these advantages are applied to the observation and interpretation of changes in the PolSAR scattering mechanisms of several crop types over a whole season and validated with relevant field data.

Note that since we strongly emphasise in results interpretability and in results that are highly related to physical changes in the crop, the change matrices method proposed provides a step towards less reliance in ground truth. Due to high costs, this is normally a limitation on the use of remotely sensed data. Interestingly, since we also evaluated the potential of this method for crop type classification and found that its performance is similar to a traditional neural-network based classifier that uses PolSAR time series as input, the change matrices approach contributes to current literature not only with a novel crop monitoring method but also with a novel methodology for crop type identification. This is a crucial result since a single methodology is able to perform satisfactorily for two separate applications. Moreover, since the interpretable change matrices are used for training a classifier, it is also a step towards reducing the black box effect that can often be common in machine learning algorithms trained for crop type mapping.

5.2 Future work

Futures line of research can be devised when considering the current context of the field and the findings of this thesis. In terms of improving state of the art algorithms for crop monitoring, a common point that all current Bayesian filtering algorithms are lacking (including the GP-UKF presented in this thesis), is the implementation of pixel-level monitoring of crop biophysical variables. This can be a challenging task since it is necessary to harmonise the spatial resolution of the different sensors involved (i.e. SAR, optical and ground sensors). Although it can be argued that the parcel level tracking is acceptable since the management practices are normally implemented at this level, pixelwise retrieval could provide farmers more accurate data for informed decision making, for example for intra-field zone management. In addition, for the GP-UKF implemented as part of this thesis, the implementation of other Bayesian filtering methods such as a particle filter could improve the accuracy of the results. This will complement the implementation of the multiple output Gaussian process regression as discussed in the previous section, to account for the correlated uncertainties between state variables and correlated uncertainties between the remote sensing observations.

An additional line of work that is relevant is the design of novel and informative ground truth-free features that extract information about the crop from SAR imagery. This is by, for example, proposing novel SAR vegetation indices, derived from backscatter intensities, Interferometric SAR (InSAR) products or the integration of PolSAR/InSAR or PolInSAR data formats. Such indices support the characterisation of crop states and the gain of crop insights from the SAR response without requiring ground truth. Critically, better understanding of the SAR signal interaction with bare soils and vegetation represent a significant milestone in this field of research. Although this has been widely investigated, even nowadays most algorithms rely heavily on the ground truth to fit statistical or machine learning models. This is a major limitation for the potential of large area coverage offered by remote sensing. In this context, applications such regional or national level monitoring of management practices are limited by a quality, but expensive ground dataset collected in the field.

Crop agronomical models are a tool for retrieving the state and health of crop biophysical variables and for modelling crop yield from the interaction between soil, plants, and meteorological conditions (Kasampalis et al., 2018). However, deployment of these crop models at large scale in operational settings is complex considering that the spatial dimension is not directly embedded in the models but needs a large, expensive and in occasions impractical network of ground sensors to monitor meteorological and ground conditions (Kasampalis et al., 2018). Remote sensing is regarded as a tool to observe and measure input variables that correlate with crop condition. This can be for example by deriving variables such as Leaf Area Index (LAI), soil moisture or biomass from remote sensing data and using them as inputs for the crop agronomical models. It can also be by using SAR based or optical-based vegetation indices directly into the crop model. This way, agronomical models can be scaled up and crop monitoring can be achieved by the synergetic use of knowledge accumulated in both, the crop modelling and the remote sensing communities. Note that recent machine learning approaches aim at deriving this same information directly from remotely sensed data without using crop models. However, these methods require intensive ground truth datasets to train the models. Lack of training data translates in prediction inaccuracies and model uncertainties, since the model

has no capability to extrapolate results when conditions different to those in which the models are trained are used as inputs (Kasampalis et al., 2018). In this context, the use of crop models that use knowledge about soil, plants, and meteorological conditions interactions, represents a valuable tool to fill these potential gaps left by the machine learning models. In addition, applications that involve remote sensing and crop modelling are sometimes referred to as a data assimilation applications (Huang et al., 2019). Considering this, few studies have presented Kalman Filters (Kalman, 1960) as a tool for data assimilation for rice, wheat and potato crops, however, mostly, for optical sensors (De Wit & Van Diepen, 2007; Jiang et al., 2014; Wagner et al., 2020). Therefore, an expansion of machine learning and the Bayesian-filters for data assimilation using multidimensional SAR alone or in fusion with optical data, could bring a new set of opportunities for accurate and timely crop development monitoring.

In the chapter 4 of this thesis, a paradigm different to Bayesian filtering algorithms was presented for crop monitoring. It is based on the concept of change matrices created from multitemporal and polarimetric change detection that can be used for crop monitoring and crop type mapping. The change matrices approach provides a physical interpretation of the changes in target dynamics over time. This is considering that the change matrix illustrates the PolSAR intensity and type of scattering mechanisms that a target suffers over time. As such, the same principle can be used to monitor different applications to those presented in this thesis. In agriculture, cropping management practices such as irrigation type, use of soil tillage, harvest timing, post-harvest activities and knowledge about implementation of crop rotation and agroforesty, are other key aspects of large area crop monitoring. This is to tackle food security problems, payments of indemnities from governments, banks, and insurance companies, and to deal with current agro-environmental challenges. In this regard, the change matrices approach can be adapted to for this purpose. Similarly, the change matrices concept can be easily expanded to monitoring other environmental processes including forest change and logging, wetlands, and flood monitoring. Current efforts are focused on adapting it for flood monitoring.

The change matrix can be further developed for information extraction by using additional features that describe change over time. InSAR coherent changes

have been used recently in a change matrix type of application (Jacob et al., 2020; Mestre-Quereda et al., 2020). This technique can be added to the current approach to increase and complement the representational power of the change matrix to capture more information about a dynamic process. Furthermore, to enhance or complement the change matrices approach developed in this thesis, future work could include other ways to derive multitemporal changes. This can be by using different PolSAR change detection approaches such as that presented in (Alonso-González et al., 2020) or by utilising well-known similarity measurements such as ratio operators (Conradsen et al., 2003) or the Wishart or Geodetic PolSAR distances (Lee et al., 1999). Finally, expansion of the approach for anomaly detection may be achieved by adding an automatic thresholding method to flag in near-real time anomalous change from a typical change behaviour. This is currently under development considering statistical control chart techniques (Woodall & Montgomery, 1999) and online change point detection methods (Aminikhanghahi & Cook, 2017).

5.3 Final recommendations and concluding remarks

Several approaches for retrieving crop biophysical variables from SAR data have been reported in the literature. Modelling approaches based on radiative transfer theory are not as popular nowadays as they were two decades ago. This might be due to the strong theoretical background required, the assumptions about the geometrical shapes of the canopy involved in the modelling as well as the computational cost of running the models. Although machine learning approaches have been significantly utilised recently, the applications presented so far focus on a single task, such as classification or regression settings to estimate a biophysical variable. However, a complete monitoring system that enables near real time monitoring, sensor fusion, gap filling, and the forecasting of crop variables is yet to be presented. Accordingly, it is recommended to use a Bayesian Filtering Framework to accomplish these tasks. A key suggestion proposed in this work is to use a data-driven approach to learn dynamic and observation models (and uncertainty associated with their predictions), so that the BFF can be easily adapted for different state variables, crop types and locations.

With regards to SAR data formats used as input for the algorithms, GRD SAR data was used in chapters 2 and 3 while SLC was used in chapter 4. An increasing number of platforms are focusing on providing the so-called analysis ready data (ARD) (Gorelick et al., 2017; JNCC & NERC, 2021; Truckenbrodt et al., 2019) in which the SAR image pre-processing steps are already applied, as was the case for chapters 2 and 3 of this thesis. Note, however, that only the GRD data format is commonly provided as ARD which limits the use of these platforms for polarimetric or interferometric SAR data exploitation. The methodology presented in chapter 4, for instance, can not be deployed using GRD-ARD, and the pre-processing steps are required. While this increases the computational requirements in terms of storage and processing, it provides more flexibility when choosing the steps undertaken to process the images, as it was, for example, described in section 4.3.3 of this thesis. In this context it is of key importance to recognise the type SAR data to be exploited when designing and applying algorithms for crop development monitoring.

Concerning SAR data types, although pilot applications for PolInSAR data have been developed, the satellite system requirements for data acquisition limit its potential for operational crop monitoring. Since missions in the near future will include both PolSAR and multiple-pass InSAR, it is encouraged to explore these data types for agricultural applications. Currently, most approaches derive PolSAR information from decompositions of SAR pixel covariance matrices. However, it is recommended to also consider change detection methods, both for PolSAR, as presented in chapter four of this thesis, and InSAR coherent change detection (Jacob et al., 2020; Mestre-Quereda et al., 2020). These represent powerful approaches to quantify, visualise and understand changes in a field. Even though some work is still required in this area for operational monitoring, specifically mapping the observed changes to crop condition and how to handle the computational cost of the change matrix, this approach can easily be expanded for different uses in agriculture or other environmental applications.

Exploration of data assimilation techniques is also recommended e.g. the combination of agronomic models with climate variables and with SAR and remote sensing-derived vegetation indices and information about canopy state variables. This allows the possibility of the agronomic models predicting the evolution of bio-

physical variables over time, estimating crop yields, and simulating the impact and effectiveness of different crop growth conditions and management practices on a regional or national scale (based on knowledge of the interaction between the crop and external factors such as weather and soil). Further, machine learning and BFFs can be used in a previous, subsequent or parallel step, or in a hybrid fashion, to increase the accuracy of the results.

5.3.1 Summary and concluding remarks

Increase in food demand due to the increasing population, improvements in quality of life of developing countries and wider access to food, are expected to put additional pressures on society's food production systems. This challenge needs to be overcome in a sustainable manner, mitigating current agro-environmental issues and yet providing a source of profitable work for communities around the world. Uninterrupted crop monitoring helps the promotion of sustainable management practices to achieved this. Remote sensing and particularly, SAR imagery, supported by recent and future satellite constellations that provide free access to data, can make an important contribution in this regard. The crop monitoring applications presented in this thesis, included monitoring of asparagus in Peru, rice in Spain and cereal crops in Canada. We demonstrated how this can be accurate, and how other similar monitoring challenges can be approached. The use of SAR technology is ultimately a tool to provide insight for all of the stakeholders in the agricultural supply chain to allow informed decision making that promotes sustainable food production and trade.

Bibliography

Adams, J. R., Rowlandson, T. L., McKeown, S. J., Berg, A. A., McNairn, H., & Sweeney, S. J. (2013). Evaluating the cloude–pottier and freeman–durden scattering decompositions for distinguishing between unharvested and post-harvest agricultural fields. *Canadian Journal of Remote Sensing*, *39*(4), 318–327.

Agency, C. S. (2021). *What is the rcm?* https://www.asc-csa.gc.ca/eng/satellites/radarsat/what-is-rcm.asp

Agency, E. S. (2021). *Biomass esa's forest mission.* https://www.esa.int/Applications/Observing_the_Earth/Biomass

Agency, E. S. (ESA 2015). *Sentinel-1 online.* https://sentinel.esa.int/web/sentinel/missions/sentinel-1

Ahmad, L., Kanth, R. H., Parvaze, S., & Mahdi, S. S. (2017). Growing degree days to forecast crop stages. *Experimental agrometeorology: A practical manual* (pp. 95–98). Springer.

Akbari, V., Anfinsen, S. N., Doulgeris, A. P., Eltoft, T., Moser, G., & Serpico, S. B. (2016). Polarimetric sar change detection with the complex hotelling–lawley trace statistic. *IEEE Transactions on Geoscience and Remote Sensing*, *54*(7), 3953–3966.

Akbari, V., Doulgeris, A. P., & Eltoft, T. (2013). Monitoring glacier changes using multitemporal multipolarization sar images. *IEEE Transactions on Geoscience and Remote Sensing*, *52*(6), 3729–3741.

Allen, S., Grimshaw, H., Parkinson, J., & Quarmby, C. (1989). Organic constituents. *Chemical Analysis of Ecological Material, Blackwell Scientific Publications, Oxford*, 160–200.

Alonso-Gonzalez, A., Joerg, H., Papathanassiou, K., & Hajnsek, I. (2016). Change analysis and interpretation in polarimetric time series over agricultural fields at c-band. *Proceedings of EUSAR 2016: 11th European Conference on Synthetic Aperture Radar*, 1–6.

Alonso-González, A., Joerg, H., Papathanassiou, K., & Hajnsek, I. (2016). Dual-polarimetric agricultural change analysis of long baseline tandem-x time series data. *2016 IEEE International Geoscience and Remote Sensing Symposium (IGARSS)*, 325–328. https://doi.org/10.1109/IGARSS.2016.7729077

Alonso-González, A., López-Martınez, C., Papathanassiou, K. P., & Hajnsek, I. (2020). Polarimetric sar time series change analysis over agricultural areas. *IEEE Transactions on Geoscience and Remote Sensing*.

Álvarez, M. A., Rosasco, L., & Lawrence, N. D. (2012).

Aminikhanghahi, S., & Cook, D. J. (2017). A survey of methods for time series change point detection. *Knowledge and information systems*, *51*(2), 339–367.

Antropov, O., Rauste, Y., & Hame, T. (2011). Volume scattering modeling in polsar decompositions: Study of alos palsar data over boreal forest. *IEEE Transactions on Geoscience and Remote Sensing*, *49*(10), 3838–3848.

Arias, M., Campo-Bescós, M. Á., & Álvarez-Mozos, J. (2020). Crop classification based on temporal signatures of sentinel-1 observations over navarre province, spain. *Remote Sensing*, *12*(2), 278.

Attema, E., & Ulaby, F. T. (1978). Vegetation modeled as a water cloud. *Radio science*, *13*(2), 357–364.

Baghdadi, N., El Hajj, M., Zribi, M., & Bousbih, S. (2017). Calibration of the water cloud model at c-band for winter crop fields and grasslands. *Remote Sensing*, *9*(9), 969.

Ballester-Berman, J., Lopez-Sanchez, J., & Fortuny-Guasch, J. (2005). Retrieval of biophysical parameters of agricultural crops using polarimetric sar interferometry. *IEEE Transactions on Geoscience and Remote Sensing*, *43*(4), 683–694. https://doi.org/10.1109/TGRS.2005.843958

Bannari, A., Morin, D., Bonn, F., & Huete, A. (1995). A review of vegetation indices. *Remote sensing reviews*, *13*(1-2), 95–120.

Bargiel, D. (2017). A new method for crop classification combining time series of radar images and crop phenology information. *Remote sensing of environment*, *198*, 369–383.

Bargiel, D., Herrmann, S., Lohmann, P., & Sörgel, U. (2010). Land use classification with high-resolution satellite radar for estimating the impacts of land use change on the quality of ecosystem services. *International Archives of the Photogrammetry, Remote Sensing and Spatial Information Sciences:[100 Years ISPRS Advancing Remote Sensing Science, Pt 1] 38 (2010), Nr. 7B*, *38*(7B), 68–73.

Bauer-Marschallinger, B., Freeman, V., Cao, S., Paulik, C., Schaufler, S., Stachl, T., Modanesi, S., Massari, C., Ciabatta, L., Brocca, L., et al. (2018). Toward global soil moisture monitoring with sentinel-1: Harnessing assets and overcoming obstacles. *IEEE Transactions on Geoscience and Remote Sensing*, *57*(1), 520–539.

Bégué, A., Arvor, D., Bellon, B., Betbeder, J., De Abelleyra, D., PD Ferraz, R., Lebourgeois, V., Lelong, C., Simões, M., & R Verón, S. (2018). Remote sensing and cropping practices: A review. *Remote Sensing*, *10*(1), 99.

Bériaux, E., Lambot, S., & Defourny, P. (2011). Estimating surface-soil moisture for retrieving maize leaf-area index from sar data. *Canadian Journal of Remote Sensing*, *37*(1), 136–150.

Bériaux, E., Waldner, F., Collienne, F., Bogaert, P., & Defourny, P. (2015). Maize leaf area index retrieval from synthetic quad pol sar time series using the water cloud model. *Remote Sensing*, *7*(12), 16204–16225.

Bhogapurapu, N., Dey, S., Bhattacharya, A., Mandal, D., Lopez-Sanchez, J. M., McNairn, H., López-Martınez, C., & Rao, Y. S. (2021). Dual-polarimetric descriptors from sentinel-1 grd sar data for crop growth assessment. *ISPRS Journal of Photogrammetry and Remote Sensing*, *178*, 20–35.

Blackburn, G. A. (1999). Relationships between spectral reflectance and pigment concentrations in stacks of deciduous broadleaves. *Remote sensing of environment*, *70*(2), 224–237.

Boschetti, M., Stroppiana, D., Brivio, P., & Bocchi, S. (2009). Multi-year monitoring of rice crop phenology through time series analysis of modis images. *International journal of remote sensing*, *30*(18), 4643–4662.

Bousbih, S., Zribi, M., Lili-Chabaane, Z., Baghdadi, N., El Hajj, M., Gao, Q., & Mougenot, B. (2017). Potential of sentinel-1 radar data for the assessment of soil and cereal cover parameters. *Sensors*, *17*(11), 2617.

Bouvet, A., Le Toan, T., & Lam-Dao, N. (2009). Monitoring of the rice cropping system in the mekong delta using envisat/asar dual polarization data. *IEEE Transactions on Geoscience and Remote Sensing*, *47*(2), 517–526. https://doi.org/10.1109/TGRS.2008.2007963

Bracaglia, M., Ferrazzoli, P., & Guerriero, L. (1995). A fully polarimetric multiple scattering model for crops. *Remote Sensing of Environment*, *54*(3), 170–179.

Breiman, L. (2001). Random forests. *Machine learning*, *45*(1), 5–32.

Breiman, L., Friedman, J., Stone, C. J., & Olshen, R. A. (1984). *Classification and regression trees*. CRC press.

Cable, J. W., Kovacs, J. M., Jiao, X., & Shang, J. (2014). Agricultural monitoring in northeastern ontario, canada, using multi-temporal polarimetric radarsat-2 data. *Remote Sensing*, *6*(3), 2343–2371.

Campbell, J. B., & Wynne, R. H. (2011). *Introduction to remote sensing*. Guilford Press.

Camps-Valls, G., Martino, L., Svendsen, D. H., Campos-Taberner, M., Muñoz-Marí, J., Laparra, V., Luengo, D., & García-Haro, F. J. (2018). Physics-aware gaussian processes in remote sensing. *Applied Soft Computing*, *68*, 69–82. https://doi.org/https://doi.org/10.1016/j.asoc.2018.03.021

Canisius, F., Shang, J., Liu, J., Huang, X., Ma, B., Jiao, X., Geng, X., Kovacs, J. M., & Walters, D. (2018). Tracking crop phenological development using multi-temporal polarimetric radarsat-2 data. *Remote Sensing of Environment*, *210*, 508–518.

Caruana, R. (1997). Multitask learning. *Machine Learning*, *28*(1), 41–75. https://doi.org/10.1023/A:1007379606734

Casas, A. (2004). *El cultivo del espárrago en la costa peruana* [Available at http://www.lamolina.edu.pe/agronomia/dhorticultura/html/apuntesdeclase/Casas/El%20Cultivo%20del%20esp%C3%A1rrago%20en%20la%20Costa%20Peruana.pdf].

Chakraborty, M., Manjunath, K., Panigrahy, S., Kundu, N., & Parihar, J. (2005). Rice crop parameter retrieval using multi-temporal, multi-incidence angle radarsat sar data. *ISPRS Journal of Photogrammetry and Remote Sensing*, *59*(5), 310–322.

Chandrasekhar, S. (2013). *Radiative transfer*. Courier Corporation.

Cloude, S. (2009). *Polarisation: Applications in remote sensing*. Oxford University Press. https://books.google.co.uk/books?id=K1S0kgEACAAJ

Cloude, S. R., & Pottier, E. (1996). A review of target decomposition theorems in radar polarimetry. *IEEE Transactions on Geoscience and Remote Sensing*, *34*(2), 498–518. https://doi.org/10.1109/36.485127

Conradsen, K., Nielsen, A. A., Schou, J., & Skriver, H. (2003). A test statistic in the complex wishart distribution and its application to change detection in polarimetric sar data. *IEEE Transactions on Geoscience and Remote Sensing*, *41*(1), 4–19.

Conradsen, K., Nielsen, A. A., & Skriver, H. (2016). Determining the points of change in time series of polarimetric sar data. *IEEE Transactions on Geoscience and Remote Sensing*, *54*(5), 3007–3024.

Cota, N., Kasetkasem, T., Rakwatin, P., Chanwimaluang, T., & Kumazawa, I. (2015). Rice phenology estimation based on statistical models for time-series sar data. *2015 12th International Conference on Electrical Engineering/Electronics, Computer, Telecommunications and Information Technology (ECTI-CON)*, 1–6. https://doi.org/10.1109/ECTICon.2015.7207072

Cumming, I. G., & Wong, F. H. (2005). Digital processing of synthetic aperture radar data. *Artech house*, *1*(3), 108–110.

Curlander, J. C., & McDonough, R. N. (1991). *Synthetic aperture radar* (Vol. 11). Wiley, New York.

d'Andrimont, R., Taymans, M., Lemoine, G., Ceglar, A., Yordanov, M., & van der Velde, M. (2020). Detecting flowering phenology in oil seed rape parcels with sentinel-1 and-2 time series. *Remote Sensing of Environment*, *239*, 111660.

Davidson, M. W., Le Toan, T., Mattia, F., Satalino, G., Manninen, T., & Borgeaud, M. (2000). On the characterization of agricultural soil roughness for radar remote sensing studies. *IEEE Transactions on Geoscience and Remote Sensing*, *38*(2), 630–640.

De Bernardis, C., Vicente-Guijalba, F., Martinez-Marin, T., & Lopez-Sanchez, J. M. (2016a). Contribution to real-time estimation of crop phenological states in a dynamical framework based on ndvi time series: Data fusion with sar and temperature. *IEEE Journal of Selected Topics in Applied Earth Observations and Remote Sensing*, *9*(8), 3512–3523. https://doi.org/10.1109/JSTARS.2016.2539498

De Bernardis, C., Vicente-Guijalba, F., Martinez-Marin, T., & Lopez-Sanchez, J. M. (2016b). Contribution to real-time estimation of crop phenological states in a dynamical framework based on ndvi time series: Data fusion with sar and temperature. *IEEE Journal of Selected Topics in Applied Earth Observations and Remote Sensing*, *9*(8), 3512–3523. https://doi.org/10.1109/JSTARS.2016.2539498

De Bernardis, C. G., Vicente-Guijalba, F., Martinez-Marin, T., & Lopez-Sanchez, J. M. (2014a). Estimation of key dates and stages in rice crops using dual-polarization sar time series and a

particle filtering approach. *IEEE Journal of Selected Topics in Applied Earth Observations and Remote Sensing*, *8*(3), 1008–1018.

De Bernardis, C. G., Vicente-Guijalba, F., Martinez-Marin, T., & Lopez-Sanchez, J. M. (2014b). Estimation of key dates and stages in rice crops using dual-polarization sar time series and a particle filtering approach. *IEEE Journal of Selected Topics in Applied Earth Observations and Remote Sensing*, *8*(3), 1008–1018.

De Roo, R. D., Du, Y., Ulaby, F. T., & Dobson, M. C. (2001). A semi-empirical backscattering model at l-band and c-band for a soybean canopy with soil moisture inversion. *IEEE Transactions on Geoscience and Remote Sensing*, *39*(4), 864–872.

De Wit, A. d., & Van Diepen, C. (2007). Crop model data assimilation with the ensemble kalman filter for improving regional crop yield forecasts. *Agricultural and Forest Meteorology*, *146*(1-2), 38–56.

Deisenroth, M. P., Fox, D., & Rasmussen, C. E. (2013). Gaussian processes for data-efficient learning in robotics and control. *IEEE transactions on pattern analysis and machine intelligence*, *37*(2), 408–423.

Deisenroth, M. P., Huber, M. F., & Hanebeck, U. D. (2009). Analytic moment-based gaussian process filtering. *Proceedings of the 26th annual international conference on machine learning*, 225–232.

Della Vecchia, A., Ferrazzoli, P., Guerriero, L., Blaes, X., Defourny, P., Dente, L., Mattia, F., Satalino, G., Strozzi, T., & Wegmuller, U. (2006). Influence of geometrical factors on crop backscattering at c-band. *IEEE Transactions on Geoscience and Remote Sensing*, *44*(4), 778–790. https://doi.org/10.1109/TGRS.2005.860489

Della Vecchia, A., Ferrazzoli, P., Guerriero, L., Ninivaggi, L., Strozzi, T., & Wegmuller, U. (2008). Observing and modeling multifrequency scattering of maize during the whole growth cycle. *IEEE Transactions on Geoscience and Remote Sensing*, *46*(11), 3709–3718. https://doi.org/10.1109/TGRS.2008.2001885

DESA, U. (2019). World population prospects 2019. united nations. department of economic and social affairs. *World Population Prospects 2019*.

Doraiswamy, P. C., Moulin, S., Cook, P. W., & Stern, A. (2003). Crop yield assessment from remote sensing. *Photogrammetric engineering & remote sensing*, *69*(6), 665–674.

Erten, E., Lopez-Sanchez, J. M., Yuzugullu, O., & Hajnsek, I. (2016a). Retrieval of agricultural crop height from space: A comparison of sar techniques. *Remote Sensing of Environment*, *187*, 130–144.

Erten, E., Lopez-Sanchez, J. M., Yuzugullu, O., & Hajnsek, I. (2016b). Retrieval of agricultural crop height from space: A comparison of sar techniques. *Remote Sensing of Environment*, *187*, 130–144.

Fan, S., Headey, D., Rue, C., & Thomas, T. (2021). Food systems for human and planetary health: Economic perspectives and challenges. *Annual Review of Resource Economics*, *13*.

Feller, C., & Fink, M. (2007). Refraction as a measure of soluble carbohydrates in storage roots of asparagus. *HortScience*, *42*(1), 57–60.

Fieuzal, R., Baup, F., & Marais-Sicre, C. (2013). Monitoring wheat and rapeseed by using synchronous optical and radar satellite data—from temporal signatures to crop parameters estimation.

Finger, R., Swinton, S. M., El Benni, N., & Walter, A. (2019). Precision farming at the nexus of agricultural production and the environment. *Annual Review of Resource Economics*, *11*, 313–335.

Food, & agriculture organization of the united Nations. (FAO 2019). *Faostat crops* [Available at http://www.fao.org/faostat/en/#data/QC].

Freeman, A., & Durden, S. (1998). A three-component scattering model for polarimetric sar data. *IEEE Transactions on Geoscience and Remote Sensing*, *36*(3), 963–973. https://doi.org/10.1109/36.673687

Fung, A. K., Li, Z., & Chen, K.-S. (1992). Backscattering from a randomly rough dielectric surface. *IEEE Transactions on Geoscience and remote sensing*, *30*(2), 356–369.

Gebbers, R., & Adamchuk, V. I. (2010). Precision agriculture and food security. *Science*, *327*(5967), 828–831.

Gorelick, N., Hancher, M., Dixon, M., Ilyushchenko, S., Thau, D., & Moore, R. (2017). Google earth engine: Planetary-scale geospatial analysis for everyone. *Remote Sensing of Environment*. https://doi.org/10.1016/j.rse.2017.06.031

Graham, A., & Harris, R. (2003). Extracting biophysical parameters from remotely sensed radar data: A review of the water cloud model. *Progress in Physical Geography*, *27*(2), 217–229.

Harfenmeister, K., Itzerott, S., Weltzien, C., & Spengler, D. (2021). Agricultural monitoring using polarimetric decomposition parameters of sentinel-1 data. *Remote Sensing*, *13*(4), 575.

Harfenmeister, K., Spengler, D., & Weltzien, C. (2019a). Analyzing temporal and spatial characteristics of crop parameters using sentinel-1 backscatter data. *Remote Sensing*, *11*(13). https://doi.org/10.3390/rs11131569

Harfenmeister, K., Spengler, D., & Weltzien, C. (2019b). Analyzing temporal and spatial characteristics of crop parameters using sentinel-1 backscatter data. *Remote Sensing*, *11*(13), 1569.

Hodges, T. (1990). *Predicting crop phenology*. Crc Press.

Hosseini, M., & McNairn, H. (2017). Using multi-polarization c-and l-band synthetic aperture radar to estimate biomass and soil moisture of wheat fields. *International journal of applied earth observation and geoinformation*, *58*, 50–64.

Hosseini, M., McNairn, H., Merzouki, A., & Pacheco, A. (2015). Estimation of leaf area index (lai) in corn and soybeans using multi-polarization c-and l-band radar data. *Remote Sensing of Environment*, *170*, 77–89.

Huang, J., Gómez-Dans, J. L., Huang, H., Ma, H., Wu, Q., Lewis, P. E., Liang, S., Chen, Z., Xue, J.-H., Wu, Y., et al. (2019). Assimilation of remote sensing into crop growth models: Current status and perspectives. *Agricultural and forest meteorology*, *276*, 107609.

Inglada, J., & Mercier, G. (2007). A new statistical similarity measure for change detection in multitemporal sar images and its extension to multiscale change analysis. *IEEE transactions on geoscience and remote sensing*, *45*(5), 1432–1445.

Inoue, Y., Sakaiya, E., & Wang, C. (2014). Capability of c-band backscattering coefficients from high-resolution satellite sar sensors to assess biophysical variables in paddy rice. *Remote Sensing of Environment*, *140*, 257–266.

Jacob, A. W., Vicente-Guijalba, F., Lopez-Martinez, C., Lopez-Sanchez, J. M., Litzinger, M., Kristen, H., Mestre-Quereda, A., Ziółkowski, D., Lavalle, M., Notarnicola, C., et al. (2020). Sentinel-1 insar coherence for land cover mapping: A comparison of multiple feature-based classifiers. *IEEE Journal of Selected Topics in Applied Earth Observations and Remote Sensing*, *13*, 535–552.

JAXA, J. S. A. (2021). *Advanced land observing satellite-4 (alos-4).* https://global.jaxa.jp/projects/sat/alos4/

Jiang, Z., Chen, Z., Chen, J., Liu, J., Ren, J., Li, Z., Sun, L., & Li, H. (2014). Application of crop model data assimilation with a particle filter for estimating regional winter wheat yields. *IEEE Journal of Selected Topics in Applied Earth Observations and Remote Sensing*, *7*(11), 4422–4431.

JNCC, J. N. C. C., & NERC, N. E. C. f. E. D. A. (2021). *Jncc sentinel-1 indices analysis ready data (ard) radar vegetation index (rvi)* [Available at https://catalogue.ceda.ac.uk/uuid/22ae54ba3ab14ce8aa6a5271dfddaeb3].

Johnson, J. E., Laparra, V., & Camps-Valls, G. (2019). Accounting for input noise in gaussian process parameter retrieval. *IEEE Geoscience and Remote Sensing Letters*, *17*(3), 391–395.

Johnson, R. W. (2001). An introduction to the bootstrap. *Teaching Statistics*, *23*(2), 49–54.

(JPL), J. P. L. (2021). *Nisar, nasa-isro sar concept mission.* https://nisar.jpl.nasa.gov/mission/mission-concept/

Julier, S. J., & Uhlmann, J. K. (1997). New extension of the kalman filter to nonlinear systems. *Signal processing, sensor fusion, and target recognition VI*, *3068*, 182–193.

Kalman, R. E. (1960). A new approach to linear filtering and prediction problems.

Karthikeyan, L., Chawla, I., & Mishra, A. K. (2020). A review of remote sensing applications in agriculture for food security: Crop growth and yield, irrigation, and crop losses. *Journal of Hydrology*, *586*, 124905.

Kasampalis, D. A., Alexandridis, T. K., Deva, C., Challinor, A., Moshou, D., & Zalidis, G. (2018). Contribution of remote sensing on crop models: A review. *Journal of Imaging*, *4*(4), 52.

Kavats, O., Khramov, D., Sergieieva, K., & Vasyliev, V. (2019). Monitoring harvesting by time series of sentinel-1 sar data. *Remote Sensing*, *11*(21), 2496.

Kersten, P., Lee, J., & Ainsworth, T. (2005). *A comparison of change detection statistics in polsar images* (tech. rep.). NAVAL RESEARCH LAB WASHINGTON DC REMOTE SENSING DIV.

Khabbazan, S., Vermunt, P., Steele-Dunne, S., Ratering Arntz, L., Marinetti, C., van der Valk, D., Iannini, L., Molijn, R., Westerdijk, K., & van der Sande, C. (2019a). Crop monitoring using sentinel-1 data: A case study from the netherlands. *Remote Sensing*, *11*(16). https://doi.org/10.3390/rs11161887

Khabbazan, S., Vermunt, P., Steele-Dunne, S., Ratering Arntz, L., Marinetti, C., van der Valk, D., Iannini, L., Molijn, R., Westerdijk, K., & van der Sande, C. (2019b). Crop monitoring using sentinel-1 data: A case study from the netherlands. *Remote Sensing*, *11*(16), 1887.

Kim, S.-J., Lee, K. B. et al. (2003). Constructing decision trees with multiple response variables. *International Journal of Management and Decision Making*, *4*(4), 337–353.

Ko, J., & Fox, D. (2009). Gp-bayesfilters: Bayesian filtering using gaussian process prediction and observation models. *Autonomous Robots*, *27*(1), 75–90.

Krause, P., Boyle, D., & Bäse, F. (2005). Comparison of different efficiency criteria for hydrological model assessment. *Advances in geosciences*, *5*, 89–97.

Küçük, Ç., Taşkın, G., & Erten, E. (2016). Paddy-rice phenology classification based on machine-learning methods using multitemporal co-polar x-band sar images. *IEEE Journal of Selected Topics in Applied Earth Observations and Remote Sensing*, *9*(6), 2509–2519. https://doi.org/10.1109/JSTARS.2016.2547843

Kweon, S.-K., & Oh, Y. (2014). A modified water-cloud model with leaf angle parameters for microwave backscattering from agricultural fields. *IEEE Transactions on Geoscience and Remote Sensing*, *53*(5), 2802–2809.

Larranaga, A., Alvarez-Mozos, J., Albizua, L., & Peters, J. (2013). Backscattering behavior of rain-fed crops along the growing season. *IEEE Geoscience and Remote Sensing Letters*, *10*(2), 386–390. https://doi.org/10.1109/LGRS.2012.2205660

Lê, T. T., Atto, A. M., Trouvé, E., & Nicolas, J. (2014). Adaptive multitemporal sar image filtering based on the change detection matrix. *IEEE Geoscience and Remote Sensing Letters*, *11*(10), 1826–1830. https://doi.org/10.1109/LGRS.2014.2311663

Lê, T. T., Atto, A. M., Trouvé, E., Solikhin, A., & Pinel, V. (2015). Change detection matrix for multitemporal filtering and change analysis of sar and polsar image time series [Multitemporal remote sensing data analysis]. *ISPRS Journal of Photogrammetry and Remote Sensing*, *107*, 64–76. https://doi.org/https://doi.org/10.1016/j.isprsjprs.2015.02.008

Le Toan, T., Ribbes, F., Wang, L.-F., Floury, N., Ding, K.-H., Kong, J. A., Fujita, M., & Kurosu, T. (1997). Rice crop mapping and monitoring using ers-1 data based on experiment and modeling results. *IEEE Transactions on Geoscience and Remote Sensing*, *35*(1), 41–56.

Leahy, S., Clark, H., & Reisinger, A. (2020). Challenges and prospects for agricultural greenhouse gas mitigation pathways consistent with the paris agreement. *Frontiers in Sustainable Food Systems*, *4*, 69.

Lee, J.-S., Grunes, M., Ainsworth, T., Du, L.-J., Schuler, D., & Cloude, S. (1999). Unsupervised classification using polarimetric decomposition and the complex wishart classifier. *IEEE Transactions on Geoscience and Remote Sensing*, *37*(5), 2249–2258. https://doi.org/10.1109/36.789621

Lee, J.-S., & Pottier, E. (2009). *Polarimetric radar imaging: From basics to applications*. Oxford University Press. https://books.google.co.uk/books?id=K1S0kgEACAAJ

Leiva-Murillo, J. M., Gomez-Chova, L., & Camps-Valls, G. (2013). Multitask remote sensing data classification. *IEEE Transactions on Geoscience and Remote Sensing*, *51*(1), 151–161. https://doi.org/10.1109/TGRS.2012.2200043

Liang, S. (2008). *Advances in land remote sensing: System, modeling, inversion and application*. Springer Science & Business Media.

Lieth, H. (2013). *Phenology and seasonality modeling* (Vol. 8). Springer Science & Business Media.

Lin, H., Chen, J., Pei, Z., Zhang, S., & Hu, X. (2009). Monitoring sugarcane growth using envisat asar data. *IEEE Transactions on geoscience and remote sensing*, *47*(8), 2572–2580.

LIU, C.-a., CHEN, Z.-x., Yun, S., CHEN, J.-s., Hasi, T., & PAN, H.-z. (2019). Research advances of sar remote sensing for agriculture applications: A review. *Journal of integrative agriculture*, *18*(3), 506–525.

Liu, C.-a., CHEN, Z.-x., Yun, S., CHEN, J.-s., Hasi, T., & PAN, H.-z. (2019). Research advances of sar remote sensing for agriculture applications: A review. *Journal of Integrative Agriculture*, *18*(3), 506–525.

Liu, C., Shang, J., Vachon, P. W., & McNairn, H. (2013). Multiyear crop monitoring using polarimetric radarsat-2 data. *IEEE Transactions on Geoscience and Remote Sensing*, *51*(4), 2227–2240. https://doi.org/10.1109/TGRS.2012.2208649

Liu, H., Ong, Y.-S., Shen, X., & Cai, J. (2020). When gaussian process meets big data: A review of scalable gps. *IEEE transactions on neural networks and learning systems*, *31*(11), 4405–4423.

Liu, M., Zhang, H., Wang, C., & Wu, F. (2014). Change detection of multilook polarimetric sar images using heterogeneous clutter models. *IEEE Transactions on Geoscience and Remote Sensing*, *52*(12), 7483–7494.

Liu, P.-W., Bongiovanni, T., Monsivais-Huertero, A., Judge, J., Steele-Dunne, S., Bindlish, R., & Jackson, T. J. (2016). Assimilation of active and passive microwave observations for improved estimates of soil moisture and crop growth. *IEEE Journal of Selected Topics in Applied Earth Observations and Remote Sensing*, *9*(4), 1357–1369.

Liu, Y., Chen, K.-S., Xu, P., & Li, Z.-L. (2016). Modeling and characteristics of microwave backscattering from rice canopy over growth stages. *IEEE Transactions on Geoscience and Remote Sensing*, *54*(11), 6757–6770.

Lopez-Sanchez, J. M., Ballester-Berman, J. D., & Hajnsek, I. (2011). First results of rice monitoring practices in spain by means of time series of terrasar-x dual-pol images. *IEEE Journal of*

Selected Topics in Applied Earth Observations and Remote Sensing, *4*(2), 412–422. https://doi.org/10.1109/JSTARS.2010.2047634

Lopez-Sanchez, J. M., Vicente-Guijalba, F., Ballester-Berman, J. D., & Cloude, S. R. (2014). Polarimetric response of rice fields at C-band: Analysis and phenology retrieval. *IEEE Trans. on Geos. & Rem. Sen.*, *52*(5).

Lopez-Sanchez, J. M., Vicente-Guijalba, F., Erten, E., Campos-Taberner, M., & Javier Garcia-Haro, F. (2017). Retrieval of vegetation height in rice fields using polarimetric SAR interferometry with TanDEM-X data. *Remote Sensing of Environment*, *192*, 30–44.

Lopez-Sanchez, J. M., & Ballester-Berman, J. D. (2009). Potentials of polarimetric sar interferometry for agriculture monitoring. *Radio Science*, *44*(02), 1–20.

Lopez-Sanchez, J. M., Cloude, S. R., & Ballester-Berman, J. D. (2011). Rice phenology monitoring by means of sar polarimetry at x-band. *IEEE Transactions on Geoscience and Remote Sensing*, *50*(7), 2695–2709.

Lu, D. (2006). The potential and challenge of remote sensing-based biomass estimation. *International journal of remote sensing*, (7), 1297–1328.

Macelloni, G., Paloscia, S., Pampaloni, P., Marliani, F., & Gai, M. (2001). The relationship between the backscattering coefficient and the biomass of narrow and broad leaf crops. *IEEE Transactions on Geoscience and Remote Sensing*, *39*(4), 873–884.

Mahalanobis, P. C. (1936). On the generalized distance in statistics.

Mandal, D., Hosseini, M., McNairn, H., Kumar, V., Bhattacharya, A., Rao, Y., Mitchell, S., Robertson, L. D., Davidson, A., & Dabrowska-Zielinska, K. (2019). An investigation of inversion methodologies to retrieve the leaf area index of corn from c-band sar data. *International Journal of Applied Earth Observation and Geoinformation*, *82*, 101893.

Mandal, D., Kumar, V., McNairn, H., Bhattacharya, A., & Rao, Y. (2019). Joint estimation of plant area index (pai) and wet biomass in wheat and soybean from c-band polarimetric sar data. *International Journal of Applied Earth Observation and Geoinformation*, *79*, 24–34. https://doi.org/https://doi.org/10.1016/j.jag.2019.02.007

Mandal, D., Kumar, V., Ratha, D., Dey, S., Bhattacharya, A., Lopez-Sanchez, J. M., McNairn, H., & Rao, Y. S. (2020). Dual polarimetric radar vegetation index for crop growth monitoring using sentinel-1 sar data. *Remote Sensing of Environment*, *247*, 111954.

Marino, A., & Alonso-Gonzalez, A. (2018). Optimisations for different change models with polarimetric sar. *EUSAR 2018; 12th European Conference on Synthetic Aperture Radar*, 1–5.

Marino, A., & Alonso-González, A. (2017). An optimization of the difference of covariance matrices for polsar change detection. *2017 IEEE International Geoscience and Remote Sensing Symposium (IGARSS)*, 5315–5318. https://doi.org/10.1109/IGARSS.2017.8128204

Marino, A., Cloude, S. R., & Woodhouse, I. H. (2012). Detecting depolarized targets using a new geometrical perturbation filter. *IEEE transactions on geoscience and remote sensing*, *50*(10), 3787–3799.

Marino, A., & Hajnsek, I. (2013). A change detector based on an optimization with polarimetric sar imagery. *IEEE Transactions on Geoscience and Remote Sensing*, *52*(8), 4781–4798.

Mascolo, L., Lopez-Sanchez, J. M., Vicente-Guijalba, F., Nunziata, F., Migliaccio, M., & Mazzarella, G. (2016). A complete procedure for crop phenology estimation with polsar data based on the complex wishart classifier. *IEEE Transactions on Geoscience and Remote Sensing*, *54*(11), 6505–6515. https://doi.org/10.1109/TGRS.2016.2585744

Mascolo, L., Forino, G., Nunziata, F., Pugliano, G., & Migliaccio, M. (2019). A new methodology for rice area monitoring with cosmo-skymed hh–vv pingpong mode sar data. *IEEE Journal of Selected Topics in Applied Earth Observations and Remote Sensing*, *12*(4), 1076–1084.

Mascolo, L., Lopez-Sanchez, J. M., Vicente-Guijalba, F., Mazzarella, G., Nunziata, F., & Migliaccio, M. (2015). Retrieval of phenological stages of onion fields during the first year of growth by means of c-band polarimetric sar measurements. *International Journal of Remote Sensing*, *36*(12), 3077–3096.

Mattia, F., Le Toan, T., Picard, G., Posa, F. I., D'Alessio, A., Notarnicola, C., Gatti, A. M., Rinaldi, M., Satalino, G., & Pasquariello, G. (2003). Multitemporal c-band radar measurements on wheat fields. *IEEE transactions on geoscience and remote sensing*, *41*(7), 1551–1560.

McBratney, A., Whelan, B., Ancev, T., & Bouma, J. (2005). Future directions of precision agriculture. *Precision agriculture*, *6*(1), 7–23.

McHutchon, A., & Rasmussen, C. (2011). Gaussian process training with input noise. *Advances in Neural Information Processing Systems*, *24*, 1341–1349.

McMaster, G. S., & Wilhelm, W. (1997a). Growing degree-days: One equation, two interpretations. *Agricultural and forest meteorology*, *87*(4), 291–300.

McMaster, G. S., & Wilhelm, W. (1997b). Growing degree-days: One equation, two interpretations. *Agricultural and forest meteorology*, *87*(4), 291–300.

McNairn, H., Jiao, X., Pacheco, A., Sinha, A., Tan, W., & Li, Y. (2018). Estimating canola phenology using synthetic aperture radar. *Remote Sensing of Environment*, *219*, 196–205. https://doi.org/https://doi.org/10.1016/j.rse.2018.10.012

McNairn, H., & Shang, J. (2016a). A review of multitemporal synthetic aperture radar (sar) for crop monitoring. In Y. Ban (Ed.), *Multitemporal remote sensing: Methods and applications* (pp. 317–340). Springer International Publishing. https://doi.org/10.1007/978-3-319-47037-5_15

McNairn, H., & Shang, J. (2016b). A review of multitemporal synthetic aperture radar (sar) for crop monitoring. *Multitemporal remote sensing*, 317–340.

McNairn, H., Shang, J., Jiao, X., & Champagne, C. (2009). The contribution of alos palsar multipolarization and polarimetric data to crop classification. *IEEE Transactions on Geoscience and Remote Sensing*, *47*(12), 3981–3992.

Meier, U. (1997). *Growth stages of mono-and dicotyledonous plants*. Blackwell Wissenschafts-Verlag.

Mercier, A., Betbeder, J., Rapinel, S., Jegou, N., Baudry, J., & Hubert-Moy, L. (2020). Evaluation of sentinel-1 and-2 time series for estimating lai and biomass of wheat and rapeseed crop types. *Journal of applied remote sensing*, *14*(2), 024512.

Mestre-Quereda, A., Lopez-Sanchez, J. M., Vicente-Guijalba, F., Jacob, A. W., & Engdahl, M. E. (2020). Time-series of sentinel-1 interferometric coherence and backscatter for crop-type mapping. *IEEE Journal of Selected Topics in Applied Earth Observations and Remote Sensing*, *13*, 4070–4084.

Moran, M. S., Alonso, L., Moreno, J. F., Mateo, M. P. C., De La Cruz, D. F., & Montoro, A. (2011). A radarsat-2 quad-polarized time series for monitoring crop and soil conditions in barrax, spain. *IEEE Transactions on Geoscience and Remote Sensing*, *50*(4), 1057–1070.

Nascimento, A. D., Frery, A. C., & Cintra, R. J. (2018). Detecting changes in fully polarimetric sar imagery with statistical information theory. *IEEE Transactions on Geoscience and Remote Sensing*, *57*(3), 1380–1392.

Nasirzadehdizaji, R., Cakir, Z., Sanli, F. B., Abdikan, S., Pepe, A., & Calò, F. (2021). Sentinel-1 interferometric coherence and backscattering analysis for crop monitoring. *Computers and Electronics in Agriculture*, *185*, 106118.

Nasrallah, A., Baghdadi, N., El Hajj, M., Darwish, T., Belhouchette, H., Faour, G., Darwich, S., & Mhawej, M. (2019). Sentinel-1 data for winter wheat phenology monitoring and mapping. *Remote Sensing*, *11*(19), 2228.

Ndikumana, E., Ho Tong Minh, D., Dang Nguyen, H. T., Baghdadi, N., Courault, D., Hossard, L., & El Moussawi, I. (2018). Estimation of rice height and biomass using multitemporal sar sentinel-1 for camargue, southern france. *Remote Sensing*, *10*(9), 1394.

Nielsen, A., Conradsen, K., Skriver, H., & Canty, M. (2017). Visualization of and software for omnibus test-based change detected in a time series of polarimetric sar data. *Canadian Journal of Remote Sensing*, *43*, 582–592.

Nielsen, A. A., Skriver, H., & Conradsen, K. (2019). The loewner order and direction of detected change in sentinel-1 and radarsat-2 data. *IEEE Geoscience and Remote Sensing Letters*, *17*(2), 242–246.

Nielsen, A. A. (2019). Fast matrix based computation of eigenvalues and the loewner order in polsar data. *IEEE Geoscience and Remote Sensing Letters*, *17*(10), 1727–1731.

Novak, L. M., Sechtin, M. B., & Cardullo, M. J. (1989). Studies of target detection algorithms that use polarimetric radar data. *IEEE Transactions on Aerospace and Electronic Systems*, *25*(2), 150–165.

Oh, Y., Sarabandi, K., & Ulaby, F. T. (1992). An empirical model and an inversion technique for radar scattering from bare soil surfaces. *IEEE Transactions on Geoscience and Remote Sensing*, *30*(2), 370–381. https://doi.org/10.1109/36.134086

Oliver, C., & Quegan, S. (2004a). *Understanding synthetic aperture radar images*. SciTech Publishing.

Oliver, C., & Quegan, S. (2004b). *Understanding synthetic aperture radar images*. SciTech Publishing.

Ozer, H. (2003). Sowing date and nitrogen rate effects on growth, yield and yield components of two summer rapeseed cultivars. *European Journal of Agronomy*, *19*(3), 453–463.

Paris, J. (1986). The effect of leaf size on the microwave backscattering by corn. *Remote Sensing of Environment*, *19*, 81–95.

Pedregosa, F., Varoquaux, G., Gramfort, A., Michel, V., Thirion, B., Grisel, O., Blondel, M., Prettenhofer, P., Weiss, R., Dubourg, V., Vanderplas, J., Passos, A., Cournapeau, D., Brucher, M., Perrot, M., & Duchesnay, E. (2021). *Scikit-learn: R^2 score, the coefficient of determination* [Available at https://scikit-learn.org/stable/modules/model_evaluation.html#r2-score].

Phan, H., Le Toan, T., Bouvet, A., Nguyen, L. D., Pham Duy, T., & Zribi, M. (2018a). Mapping of rice varieties and sowing date using x-band sar data. *Sensors*, *18*(1), 316.

Phan, H., Le Toan, T., Bouvet, A., Nguyen, L. D., Pham Duy, T., & Zribi, M. (2018b). Mapping of rice varieties and sowing date using x-band sar data. *Sensors*, *18*(1), 316.

Pipia, L., Muñoz-Marı, J., Amin, E., Belda, S., Camps-Valls, G., & Verrelst, J. (2019). Fusing optical and sar time series for lai gap filling with multioutput gaussian processes. *Remote Sensing of Environment*, *235*, 111452.

Quinonero-Candela, J., & Rasmussen, C. E. (2005). A unifying view of sparse approximate gaussian process regression. *The Journal of Machine Learning Research*, *6*, 1939–1959.

Rasmussen, C. E. (2003). Gaussian processes in machine learning. *Summer school on machine learning*, 63–71.

Richards, J. A. et al. (2009). *Remote sensing with imaging radar* (Vol. 1). Springer.

Rogan, J., & Chen, D. (2004). Remote sensing technology for mapping and monitoring land-cover and land-use change. *Progress in planning*, *61*(4), 301–325.

Romero-Puig, N., & Lopez-Sanchez, J. M. (2021). A review of crop height retrieval using insar strategies: Techniques and challenges. *IEEE Journal of Selected Topics in Applied Earth Observations and Remote Sensing*.

Romero-Puig, N., Marino, A., & Lopez-Sanchez, J. M. (2021). Application of the trace coherence to hh-vv polinsar tandem-x data for vegetation height estimation. *IEEE Transactions on Geoscience and Remote Sensing*.

Rossi, C., & Erten, E. (2015). Paddy-rice monitoring using tandem-x. *IEEE Transactions on Geoscience and Remote Sensing*, *53*(2), 900–910. https://doi.org/10.1109/TGRS.2014.2330377

Ruder, S. (2017). An overview of multi-task learning in deep neural networks. *CoRR*, *abs/1706.05098*. http://arxiv.org/abs/1706.05098

Sabour, S. T., Lohmann, P., & Soergel, U. (2008). Monitoring agricultural activities using multi-temporal asar envisat data. *International Archives of the Photogrammetry, Remote Sensing and Spatial Information Sciences*, *37*, 735–742.

Salepci, N., Eckardt, R., & Richter, N. (2017). *Speckle filtering* [Available at https://eo-college.org/resource/speckle/].

Santos, M. S., Soares, J. P., Abreu, P. H., Araujo, H., & Santos, J. (2018). Cross-validation for imbalanced datasets: Avoiding overoptimistic and overfitting approaches [research frontier]. *ieee ComputatioNal iNtelligeNCe magaziNe*, *13*(4), 59–76.

Särkkä, S. (2013). *Bayesian filtering and smoothing*. Cambridge University Press.

Schlund, M., & Erasmi, S. (2020). Sentinel-1 time series data for monitoring the phenology of winter wheat. *Remote Sensing of Environment*, *246*, 111814.

Schwartz, M. D. et al. (2003). *Phenology: An integrative environmental science*. Springer.

Segal, M., & Xiao, Y. (2011). Multivariate random forests. *Wiley Interdisciplinary Reviews: Data Mining and Knowledge Discovery*, *1*(1), 80–87.

Senamhi. (2021). *Servicio nacional de meteorología e hidrología del perú. monitoreo agroclimático*. https://www.senamhi.gob.pe/?&p=boletin-agro

Shang, J., Jiao, X., McNairn, H., Kovacs, J., Walters, D., Ma, B., & Geng, X. (2013). Tracking crop phenological development of spring wheat using synthetic aperture radar (sar) in northern ontario, canada. *2013 Second International Conference on Agro-Geoinformatics (Agro-Geoinformatics)*, 517–521.

Shang, J., Liu, J., Poncos, V., Geng, X., Qian, B., Chen, Q., Dong, T., Macdonald, D., Martin, T., Kovacs, J., et al. (2020). Detection of crop seeding and harvest through analysis of time-series sentinel-1 interferometric sar data. *Remote Sensing*, *12*(10), 1551.

Shang, J., McNairn, H., Champagne, C., & Jiao, X. (2009). Application of multi-frequency synthetic aperture radar (sar) in crop classification. *Advances in geoscience and remote sensing*. IntechOpen.

Shukla, P., Skea, J., Calvo Buendia, E., Masson-Delmotte, V., Pörtner, H., Roberts, D., Zhai, P., Slade, R., Connors, S., Van Diemen, R., et al. (2019a). Ipcc, 2019: Climate change and land: An ipcc special report on climate change, desertification, land degradation, sustainable land management, food security, and greenhouse gas fluxes in terrestrial ecosystems.

Shukla, P., Skea, J., Calvo Buendia, E., Masson-Delmotte, V., Pörtner, H., Roberts, D., Zhai, P., Slade, R., Connors, S., Van Diemen, R., et al. (2019b). Ipcc, 2019: Climate change and land: An ipcc special report on climate change, desertification, land degradation, sustainable land management, food security, and greenhouse gas fluxes in terrestrial ecosystems.

Siachalou, S., Mallinis, G., & Tsakiri-Strati, M. (2015). A hidden markov models approach for crop classification: Linking crop phenology to time series of multi-sensor remote sensing data. *Remote Sensing*, *7*(4), 3633–3650.

Silva, C., Marino, A., Lopez-Sanchez, J. M., & Cameron, I. (2018). Monitoring agricultural fields using an optimisation of the difference of covariance matrices for polsar. *IGARSS 2018 - 2018 IEEE International Geoscience and Remote Sensing Symposium*, 6619–6622. https://doi.org/10.1109/IGARSS.2018.8519267

Silva-Perez, C., Marino, A., Lopez-Sanchez, J., & Cameron, I. (2021). Multi-temporal polarimetric sar change detection for crop monitoring and crop type classification. *IEEE Journal of Selected Topics in Applied Earth Observations and Remote Sensing*, *1*(j), k–k+1. https://doi.org/...

Silva-Perez, C., Marino, A., & Cameron, I. (2020). Monitoring agricultural fields using sentinel-1 and temperature data in peru: Case study of asparagus (asparagus officinalis l.) *Remote Sensing*, *12*(12), 1993.

Skakun, S., Vermote, E., Franch, B., Roger, J.-C., Kussul, N., Ju, J., & Masek, J. (2019). Winter wheat yield assessment from landsat 8 and sentinel-2 data: Incorporating surface reflectance, through phenological fitting, into regression yield models. *Remote Sensing*, *11*(15), 1768.

Skriver, H., Mattia, F., Satalino, G., Balenzano, A., Pauwels, V. R. N., Verhoest, N. E. C., & Davidson, M. (2011). Crop classification using short-revisit multitemporal sar data. *IEEE Journal of Selected Topics in Applied Earth Observations and Remote Sensing*, *4*(2), 423–431. https://doi.org/10.1109/JSTARS.2011.2106198

Skriver, H., Svendsen, M. T., & Thomsen, A. G. (1999). Multitemporal c-and l-band polarimetric signatures of crops. *IEEE Transactions on Geoscience and Remote Sensing*, *37*(5), 2413–2429.

Smith, P., D. Martino, Z. C., Gwary, D., Janzen, H., Kumar, P., McCarl, B., Ogle, S., O'Mara, F., Rice, C., Scholes, B., & Sirotenko, O. (2007). Agriculture. in climate change 2007: Mitigation. contribution of working group iii to the fourth assessment report of the intergovernmental panel on climate change.

Smith, P., Martino, D., Cai, Z., Gwary, D., Janzen, H., Kumar, P., McCarl, B., Ogle, S., O'Mara, F., Rice, C., et al. (2008). Greenhouse gas mitigation in agriculture. *Philosophical transactions of the royal Society B: Biological Sciences*, *363*(1492), 789–813.

Steele-Dunne, S. C., Khabbazan, S., Vermunt, P. C., Arntz, L. R., Marinetti, C., Iannini, L., Westerdijk, K., & van der Sande, C. (2018). Monitoring key agricultural crops in the netherlands using sentinel-1. *IGARSS 2018 - 2018 IEEE International Geoscience and Remote Sensing Symposium*, 6639–6642. https://doi.org/10.1109/IGARSS.2018.8518953

Steele-Dunne, S. C., McNairn, H., Monsivais-Huertero, A., Judge, J., Liu, P.-W., & Papathanassiou, K. (2017a). Radar remote sensing of agricultural canopies: A review. *IEEE Journal of Selected Topics in Applied Earth Observations and Remote Sensing*, *10*(5), 2249–2273.

Steele-Dunne, S. C., McNairn, H., Monsivais-Huertero, A., Judge, J., Liu, P.-W., & Papathanassiou, K. (2017b). Radar remote sensing of agricultural canopies: A review. *IEEE Journal of Selected Topics in Applied Earth Observations and Remote Sensing*, *10*(5), 2249–2273.

Strang, G., Strang, G., Strang, G., & Strang, G. (1993). *Introduction to linear algebra* (Vol. 3). Wellesley-Cambridge Press Wellesley, MA.

Sun, Y., Wong, A. K., & Kamel, M. S. (2009). Classification of imbalanced data: A review. *International journal of pattern recognition and artificial intelligence*, *23*(04), 687–719.

Tan, B., Morisette, J. T., Wolfe, R. E., Gao, F., Ederer, G. A., Nightingale, J., & Pedelty, J. A. (2008). Vegetation phenology metrics derived from temporally smoothed and gap-filled modis data. *IGARSS 2008-2008 IEEE International Geoscience and Remote Sensing Symposium*, *3*, III–593.

Tao, L., Li, J., Jiang, J., & Chen, X. (2016a). Leaf area index inversion of winter wheat using modified water-cloud model. *IEEE Geoscience and Remote Sensing Letters*, *13*(6), 816–820.

Tao, L., Li, J., Jiang, J., & Chen, X. (2016b). Leaf area index inversion of winter wheat using modified water-cloud model. *IEEE Geoscience and Remote Sensing Letters*, *13*(6), 816–820.

Tavakkoli, M., & Lohmann, P. (2006). Multi-temporal classification of ASAR images in agricultural areas. *ISPRS May*.

team, A. (2009). *Agrisar 2009: "final report vol1 executive summary, data acquisition, data simulation* [Available at https://doi.org/10.5270/esa-jdg5o4g].

Terán-Velazco, C.-A. (2017). *Impactos sociales del espárrago en el perú* [Available at http://repositorio.ulima.edu.pe/bitstream/handle/ulima/6003/Teran_Esparragos_Peru.pdf?sequence=1&isAllowed=y]. Universidad de Lima, Facultad de Ciencias Empresariales y Económicas.

Thenkabail, P. S., Hanjra, M. A., Dheeravath, V., & Gumma, M. (2010). A holistic view of global croplands and their water use for ensuring global food security in the 21st century through advanced remote sensing and non-remote sensing approaches. *Remote sensing*, *2*(1), 211–261.

Toure, A., Thomson, K. P., Edwards, G., Brown, R. J., & Brisco, B. G. (1994). Adaptation of the mimics backscattering model to the agricultural context-wheat and canola at l and c bands. *IEEE Transactions on Geoscience and Remote Sensing*, *32*(1), 47–61.

Truckenbrodt, J., Freemantle, T., Williams, C., Jones, T., Small, D., Dubois, C., Thiel, C., Rossi, C., Syriou, A., & Giuliani, G. (2019). Towards sentinel-1 sar analysis-ready data: A best practices assessment on preparing backscatter data for the cube. *Data*, *4*(3), 93.

Turner, R., Deisenroth, M., & Rasmussen, C. (2010). State-space inference and learning with gaussian processes. *Proceedings of the Thirteenth International Conference on Artificial Intelligence and Statistics*, 868–875.

Ulaby, F. T., Sarabandi, K., Mcdonald, K., Whitt, M., & Dobson, M. C. (1990). Michigan microwave canopy scattering model. *International Journal of Remote Sensing*, *11*(7), 1223–1253.

[UNDP], U. N. D. P. (2021). *The sustainable development goals report 2021.* https://unstats.un.org/sdgs/report/2021/The-Sustainable-Development-Goals-Report-2021.pdf

Valle, S. S., & Kienzle, J. (2020). Agriculture 4.0-agricultural robotics and automated equipment for sustainable crop production. *Integrated Crop Management*, *24*.

Van Tricht, K., Gobin, A., Gilliams, S., & Piccard, I. (2018). Synergistic use of radar sentinel-1 and optical sentinel-2 imagery for crop mapping: A case study for belgium. *Remote Sensing*, *10*(10), 1642.

Veloso, A., Mermoz, S., Bouvet, A., Le Toan, T., Planells, M., Dejoux, J.-F., & Ceschia, E. (2017). Understanding the temporal behavior of crops using sentinel-1 and sentinel-2-like data for agricultural applications. *Remote Sensing of Environment*, *199*, 415–426.

Vicente-Guijalba, F., Martinez-Marin, T., & Lopez-Sanchez, J. M. (2015). Dynamical approach for real-time monitoring of agricultural crops. *IEEE Transactions on Geoscience and Remote Sensing*, *53*(6), 3278–3293. https://doi.org/10.1109/TGRS.2014.2372897

Vicente-Guijalba, F. (2016). *Teledetección multitemporal mediante dinámica de sistemas* (Doctoral dissertation). Universitat d'Alacant-Universidad de Alicante.

Vicente-Guijalba, F., Martinez-Marin, T., & Lopez-Sanchez, J. M. (2014). Crop phenology estimation using a multitemporal model and a kalman filtering strategy. *Ieee Geoscience and Remote Sensing Letters*, *11*(6), 1081–1085.

Vreugdenhil, M., Wagner, W., Bauer-Marschallinger, B., Pfeil, I., Teubner, I., Rüdiger, C., & Strauss, P. (2018). Sensitivity of sentinel-1 backscatter to vegetation dynamics: An austrian case study. *Remote Sensing*, *10*(9), 1396.

Wagner, M. P., Slawig, T., Taravat, A., & Oppelt, N. (2020). Remote sensing data assimilation in dynamic crop models using particle swarm optimization. *ISPRS International Journal of Geo-Information*, *9*(2), 105.

Wali, E., Tasumi, M., & Moriyama, M. (2020). Combination of linear regression lines to understand the response of sentinel-1 dual polarization sar data with crop phenology—case study in miyazaki, japan. *Remote Sensing*, *12*(1), 189.

Wang, H., Magagi, R., Goïta, K., Trudel, M., McNairn, H., & Powers, J. (2019). Crop phenology retrieval via polarimetric sar decomposition and random forest algorithm. *Remote Sensing of Environment*, *231*, 111234. https://doi.org/https://doi.org/10.1016/j.rse.2019.111234

Wang, H., Magagi, R., Goıta, K., Trudel, M., McNairn, H., & Powers, J. (2019). Crop phenology retrieval via polarimetric sar decomposition and random forest algorithm. *Remote Sensing of Environment*, *231*, 111234.

Wang, L.-F., Kong, J., Ding, K., Le Toan, T., Ribbes, F., & Floury, N. (2005). Electromagnetic scattering model for rice canopy based on monte carlo simulation. *Progress In Electromagnetics Research*, *52*, 153–171.

Wang, L., & Qu, J. J. (2009). Satellite remote sensing applications for surface soil moisture monitoring: A review. *Frontiers of Earth Science in China*, *3*(2), 237–247.

Weiß, T., Ramsauer, T., Löw, A., & Marzahn, P. (2020). Evaluation of different radiative transfer models for microwave backscatter estimation of wheat fields. *Remote Sensing*, *12*(18), 3037.

Weiss, M., Jacob, F., & Duveiller, G. (2020a). Remote sensing for agricultural applications: A meta-review. *Remote Sensing of Environment*, *236*, 111402.

Weiss, M., Jacob, F., & Duveiller, G. (2020b). Remote sensing for agricultural applications: A meta-review. *Remote Sensing of Environment*, *236*, 111402.

West, P. C., Gibbs, H. K., Monfreda, C., Wagner, J., Barford, C. C., Carpenter, S. R., & Foley, J. A. (2010). Trading carbon for food: Global comparison of carbon stocks vs. crop yields on agricultural land. *Proceedings of the National Academy of Sciences*, *107*(46), 19645–19648.

Wien, H. C., & Stützel, H. (2020). *The physiology of vegetable crops*. CABI.

Wilson, D., Cloughley, C., Jamieson, P., & Sinton, S. (2001). A model of asparagus growth physiology. *X International Asparagus Symposium 589*, 297–301.

Wilson, D., Cloughley, C., & Sinton, S. (1997). Model of the influence of temperature on the elongation rate of asparagus spears. *IX International Asparagus Symposium 479*, 297–304.

Wilson, D., Cloughley, C., Sinton, S., et al. (2000). Aspirenz: A crop management decision support system for asparagus growers. *Agronomy New Zealand*, *30*, 7–1.

Wilson, D., Sinton, S., Butler, R., Drost, D., Paschold, P.-J., van Kruistum, G., Poll, J., Garcin, C., Pertierra, R., Vidal, I., et al. (2005). Carbohydrates and yield physiology of asparagus–a global overview. *XI International Asparagus Symposium 776*, 413–428.

Wiseman, G., McNairn, H., Homayouni, S., & Shang, J. (2014a). Radarsat-2 polarimetric sar response to crop biomass for agricultural production monitoring. *IEEE Journal of Selected Topics in Applied Earth Observations and Remote Sensing*, *7*(11), 4461–4471. https://doi.org/10.1109/JSTARS.2014.2322311

Wiseman, G., McNairn, H., Homayouni, S., & Shang, J. (2014b). Radarsat-2 polarimetric sar response to crop biomass for agricultural production monitoring. *IEEE Journal of Selected Topics in Applied Earth Observations and Remote Sensing*, *7*(11), 4461–4471.

Woodall, W. H., & Montgomery, D. C. (1999). Research issues and ideas in statistical process control. *Journal of Quality Technology*, *31*(4), 376–386.

Woodhouse, I. H. (2017). *Introduction to microwave remote sensing*. CRC press.

Wu, C., Niu, Z., Tang, Q., & Huang, W. (2008). Estimating chlorophyll content from hyperspectral vegetation indices: Modeling and validation. *Agricultural and forest meteorology*, *148*(8-9), 1230–1241.

Xie, Q., Wang, J., Lopez-Sanchez, J. M., Peng, X., Liao, C., Shang, J., Zhu, J., Fu, H., & Ballester-Berman, J. D. (2021a). Crop height estimation of corn from multi-year radarsat-2 polarimetric observables using machine learning. *Remote Sensing*, *13*(3), 392.

Xie, Q., Wang, J., Lopez-Sanchez, J. M., Peng, X., Liao, C., Shang, J., Zhu, J., Fu, H., & Ballester-Berman, J. D. (2021b). Crop height estimation of corn from multi-year radarsat-2 polarimetric observables using machine learning. *Remote Sensing*, *13*(3), 392.

Xue, J., & Su, B. (2017a). Significant remote sensing vegetation indices: A review of developments and applications. *Journal of sensors*, *2017*.

Xue, J., & Su, B. (2017b). Significant remote sensing vegetation indices: A review of developments and applications. *Journal of sensors*, *2017*.

Yan, W., Yang, B., & Zhang, Y. (2018). Characterizing the c-band backscattering of winter-wheat canopy with a microwave radiative transfer model. *2018 7th International Conference on Agro-geoinformatics (Agro-geoinformatics)*, 1–6.

Yen, Y.-F. (1993). *Growth and physiological responses of asparagus (asparagus officinalis l.) at high temperatures: A thesis presented in partial fulfilment of the requirements for the degree of doctor of philosophy in horticultural science at massey university* (Doctoral dissertation). Massey University.

Yuzugullu, O., Erten, E., & Hajnsek, I. (2016). Estimation of rice crop height from x-and c-band polsar by metamodel-based optimization. *IEEE Journal of Selected Topics in Applied Earth Observations and Remote Sensing*, *10*(1), 194–204.

Yuzugullu, O., Marelli, S., Erten, E., Sudret, B., & Hajnsek, I. (2017). Determining rice growth stage with x-band sar: A metamodel based inversion. *Remote Sensing*, *9*(5), 460.

Zalite, K., Antropov, O., Praks, J., Voormansik, K., & Noorma, M. (2016). Monitoring of agricultural grasslands with time series of x-band repeat-pass interferometric sar. *IEEE Journal of Selected Topics in Applied Earth Observations and Remote Sensing*, *9*(8), 3687–3697. https://doi.org/10.1109/JSTARS.2015.2478120

Zhang, X., Friedl, M. A., Schaaf, C. B., Strahler, A. H., Hodges, J. C., Gao, F., Reed, B. C., & Huete, A. (2003). Monitoring vegetation phenology using modis. *Remote sensing of environment*, *84*(3), 471–475.

Zhang, Y., Liu, X., Su, S., & Wang, C. (2014). Retrieving canopy height and density of paddy rice from radarsat-2 images with a canopy scattering model. *International journal of applied earth observation and geoinformation*, *28*, 170–180.